# Measurement of $W^+W^-$ Production in $pp$ Collisions at $\sqrt{s} = 8\ TeV$ and Probing Anomalous Triple-Gauge-Boson Couplings with the ATLAS Detector

by

Haolu Feng

A dissertation submitted in partial fulfillment
of the requirements for the degree of
Doctor of Philosophy
(Physics)
in the University of Michigan
2015

Doctoral Committee:

Professor Bing Zhou, Chair
Professor James T. Liu
Assistant Professor Thomas A. Schwarz
Assistant Professor Qiong Yang
Assistant Professor Junjie Zhu

To my Parents, Who bought me *10000 Why's* when I was seven.

Also to my wife Jiawen, Who brought me coffee when I was staying up at seven.

## ACKNOWLEDGMENTS

Though only my name appears under the title of this dissertation, a great many people have contributed to its production. I owe my great gratitude to all those people who made this dissertation possible, and changed a plain four years into the best part of my life.

My deepest gratitude is to my advisor, Dr. Bing Zhou. It is amazingly fortunate for me to have an advisor who continuously supports and guides me with vision, motivation, knowledge, expertise, patience, and understanding. She gave me the freedom to explore on my own, and at the same time steer me when my steps faltered. She taught me how to question thoughts and verify ideas, enlightening me with her acute observations, judgements and insights as always. She exemplifies strong work ethic and integrity. Her generous support helped me overcome many crisis situations to finish this dissertation. I could not have imagined having a better advisor and mentor for my Ph.D. study.

I would like to thank other members of my committee, Dr. James Liu, Dr. Thomas Schwarz, Dr. Qiong Yang and Dr. Junjie Zhu, for their timely help, insightful comments, and warmly encouragement during my writing. And for their hard questions as well. I thank Dr. Haijun Yang and Dr. Jianbei Liu as well for their great help during the startup project of my research.

My sincere gratitude also goes to my colleagues in the *WW* Analysis Group, to Dr. Marc-André Pleier, Dr. Dimitra Tsionou, and Dr. Kristin Lohwasser for their dedication in organization and strong support for the analysis; to Dr. Karen Chen, Dr. Jun Gao, Dr. David Hall, Dr. Jiří Hejbal, Dr. Philip Sommer, and Dr. Martin Zeman for their great work and knowledgeable discussions which supports the research and my dissertation; and special thanks to Dr. Yusheng Wu, who was busy as the co-convenor of the analysis group but still provided me with meticulous tutoring at the beginning of the analysis, extraordinary code framework to start with, and patient instructions to trivial technical questions. I will never forget those long but exciting discussions with Yusheng, and the terrific afternoon coffee.

It was my pleasure to work with Dr. Tiesheng Dai, Dr. Claudio Ferretti, Dr.

Jörg Dubbert, Dr. Zhen Yan, Dr. Liang Guan, Dr. Lulu Liu, Dr. Lailin Xu and Dr. Jiaming Yu during my service work at CERN. They are not only great colleagues, but also great friends. I always cherish the memory of working with them like a plumber inside the ATLAS detector, except the knee pain. Tiesheng also provided me with tremendous support for the MC simulation work and the supervising for beam testing and detector commissioning. For me, he is a mentor, a teacher, and an old pal in a home party.

I also thank my friends from USTC, the University of Michigan (UM), and CERN. Thanks to Dr. Lailin Xu and Dr. Lulu Liu for their warmly education in my learning; to Hok-Chuen Cheng for being the best roommate in the world; to Dr. Bing Li, Dr. Shu Li, Hao Liu, and all others for their résonance to the amplitude of my life to make France and Suisse the land of joy.

As always, I owe my great gratitude to Dr. Shawn McKee, Bob Ball and Benjeman Meekhof, for their excellent expertise and instant response to whatever problem the computing systems pop up. I cannot emphasize too much on how important their service is and how remarkable they are. They will be missed by every single Michigan ATLAS Group student, I quote from Dr. Jiaming Yu.

Last but not least, I would like to thank all the staff of the UM Physics Department, for their outstanding support for the students. Special thanks go to Christina Zigulis, who provided me countless help on academic program coordinations, US-Europe life transitions, and altruistic support during my graduation.

In conclusion, I recognize that this research would not have been possible without the financial assistance of the Department of Energy, the National Science Foundation, and the University of Michigan. I express my gratitude to those institutions and agencies.

# TABLE OF CONTENTS


**Dedication** . . . . . . . . . . . . . . . . . . . . . . . . . . . . . . . . . . **ii**

**Acknowledgments** . . . . . . . . . . . . . . . . . . . . . . . . . . . . . . **iii**

**List of Figures** . . . . . . . . . . . . . . . . . . . . . . . . . . . . . . . . **ix**

**List of Tables** . . . . . . . . . . . . . . . . . . . . . . . . . . . . . . . . **xii**

**List of Abbreviations** . . . . . . . . . . . . . . . . . . . . . . . . . . . . **xv**

**Abstract** . . . . . . . . . . . . . . . . . . . . . . . . . . . . . . . . . . **xix**

**Chapter**

**1 Introduction** . . . . . . . . . . . . . . . . . . . . . . . . . . . . . . . **1**

**2 The Standard Model and the $W^+W^-$ Production at the LHC** . . . . . . . . **7**

2.1 The Standard Model . . . . . . . . . . . . . . . . . . . . . . . . . . . 7
2.1.1 Leptons, Quarks, and Gauge Bosons . . . . . . . . . . . . . . . . 8
2.1.2 Gauge Theory . . . . . . . . . . . . . . . . . . . . . . . . . . . 10
2.1.3 Electroweak Theory . . . . . . . . . . . . . . . . . . . . . . . . 12
2.1.4 The Higgs Mechanism . . . . . . . . . . . . . . . . . . . . . . . 16
2.2 $W^+W^-$ Pair Production in the Standard Model . . . . . . . . . . . . . 18
2.2.1 $W^+W^-$ Production and Triple-Gauge-Boson Couplings . . . 19
2.2.2 Experimental Signature of $W^+W^-$ Production . . . . . . . . . . 21

**3 The ATLAS Experiment at LHC** . . . . . . . . . . . . . . . . . . . . . . **23**

3.1 The Large Hadron Collider . . . . . . . . . . . . . . . . . . . . . . . . 23
3.2 The ATLAS Detector . . . . . . . . . . . . . . . . . . . . . . . . . . . 26
3.2.1 Magnet System . . . . . . . . . . . . . . . . . . . . . . . . . . . 27
3.2.2 Tracking Detectors . . . . . . . . . . . . . . . . . . . . . . . . . 29
3.2.3 Calorimeters . . . . . . . . . . . . . . . . . . . . . . . . . . . . 29
3.2.4 Muon Spectrometer . . . . . . . . . . . . . . . . . . . . . . . . . 31
3.2.5 Trigger System . . . . . . . . . . . . . . . . . . . . . . . . . . . 33
3.2.6 Detector Operation and Performance Summary . . . . . . . . 38
3.2.7 Detector Maintenance and Phase 0 Upgrade . . . . . . . . . . . 40
3.3 The ATLAS Computing System . . . . . . . . . . . . . . . . . . . . . . 40
3.3.1 The ATLAS Computing Structure at CERN . . . . . . . . . . . 41

3.3.2 The ATLAS Data Model for Analysis . . . 41

**4 Physics Modeling and Detector Simulation . . . 44**

4.1 Matrix Element Calculation . . . 45
4.2 Parton Showering . . . 47
4.3 Detector Simulation and Digitization . . . 48

**5 Event Reconstruction . . . 51**

5.1 Tracks . . . 51
5.2 Primary Vertices . . . 55
5.3 Electrons . . . 56
5.3.1 Reconstruction . . . 57
5.3.2 Electron Identification . . . 60
5.3.3 Isolation and Impact Parameter Requirement . . . 61
5.3.4 Efficiencies and Scaling Factors . . . 62
5.3.5 Calibration and Corrections . . . 65
5.3.6 Alignment between Inner Trackers and EM Calorimeter . . . 67
5.4 Muons . . . 67
5.4.1 Reconstruction and Identification . . . 67
5.4.2 Inner Detector Track Quality Requirement . . . 70
5.4.3 Isolation and Impact Parameter Requirement . . . 70
5.4.4 Efficiencies and Scaling Factors . . . 71
5.4.5 Corrections . . . 71
5.5 Jets . . . 72
5.5.1 Reconstruction of Calorimeter Jets . . . 73
5.5.2 Calibration and Corrections . . . 75
5.6 Missing Transverse Energy and Momentum . . . 78
5.6.1 Missing Transverse Energy . . . 79
5.6.2 Missing Transverse Momentum . . . 80
5.6.3 Azimuthal Angle between Missing Transverse Energy and Momentum . . . 81
5.7 Object Overlap Removal . . . 81

**6 *WW* Analysis Overview . . . 83**

6.1 Theoretical $W^+W^-$ Cross Section . . . 83
6.2 Signal Monte-Carlo Modelling . . . 86
6.3 Background for $W^+W^-$ signal with $\ell^+\ell^- + \not\!\!E_T$ final state . . . 88
6.3.1 Background MC Modelling . . . 91
6.4 Cross-section Extraction . . . 91

**7 *WW* Signal Event Selection . . . 99**

7.1 Object Selection . . . 100
7.2 Pre-selection . . . 103
7.3 Final Selection . . . 106
7.4 Event Selection Cut-flow . . . 109
7.5 Expected Number of Events from MC . . . 111

7.5.1 MC Event Weights . . . . . . . . . . . . . . . . . . . . . . . . 111
7.5.2 MC Event Prediction Cut-flow . . . . . . . . . . . . . . . . . . 112
7.6 Fiducial Volume Definition . . . . . . . . . . . . . . . . . . . . . . 112
7.7 Acceptance and Corrections . . . . . . . . . . . . . . . . . . . . . . 113

**8 Background Estimation . . . . . . . . . . . . . . . . . . . . . . . . . 115**

8.1 *Z+jets* and Drell-Yan Contributions . . . . . . . . . . . . . . . . . 115
8.1.1 *Z+jets* Estimation with the *ABCD* Method . . . . . . . . . . 116
8.1.2 Systematic Uncertainties . . . . . . . . . . . . . . . . . . . . . . 120
8.2 *W+jets* and *Multijet* Contributions . . . . . . . . . . . . . . . . . . 123
8.2.1 Loose Lepton Definition . . . . . . . . . . . . . . . . . . . . . . 125
8.2.2 Measurement of Lepton Efficiencies . . . . . . . . . . . . . . . . 126
8.2.3 Measurement of Fake-rates . . . . . . . . . . . . . . . . . . . . . 126
8.2.4 Results from the Matrix Method . . . . . . . . . . . . . . . . . . 129
8.3 *Top* Contributions . . . . . . . . . . . . . . . . . . . . . . . . . . . 129
8.4 Di-boson Contributions . . . . . . . . . . . . . . . . . . . . . . . . . 131

**9 Systematic Uncertainties on *WW* Signal Acceptance . . . . . . . . . . . 133**

9.1 Experimental Systematics . . . . . . . . . . . . . . . . . . . . . . . 133
9.1.1 Lepton Detection Systematics . . . . . . . . . . . . . . . . . . . 133
9.1.2 Jet Measurement Systematics . . . . . . . . . . . . . . . . . . . 135
9.1.3 $\not{E}_T$ Determination Systematics . . . . . . . . . . . . . . . . . 136
9.1.4 $\not{p}_T$ Determination Systematics . . . . . . . . . . . . . . . . . 137
9.2 Theoretical Systematics . . . . . . . . . . . . . . . . . . . . . . . . 137
9.2.1 Total Theoretical Uncertainties on $\mathcal{A}_{WW}$, $C_{WW}$ and $\mathcal{A}_{WW} \times C_{WW}$ 137
9.2.2 Fiducial Cross-section Uncertainties . . . . . . . . . . . . . . . 145
9.2.3 Kinematic Distribution Shape Uncertainties . . . . . . . . . . . 145

**10 Cross Section Measurement . . . . . . . . . . . . . . . . . . . . . . . . 149**

10.1 Observation Compared with Predictions . . . . . . . . . . . . . . . . 149
10.2 Cross Section Extraction . . . . . . . . . . . . . . . . . . . . . . . . 150
10.2.1 Cross Section Definition . . . . . . . . . . . . . . . . . . . . . . 150
10.2.2 Maximum Log-likelihood Method . . . . . . . . . . . . . . . . . 150
10.2.3 Cross Section Results . . . . . . . . . . . . . . . . . . . . . . . . 152
10.3 Comparison with the SM Prediction . . . . . . . . . . . . . . . . . . 154

**11 Probing Anomalous Triple-Gauge-Boson Couplings . . . . . . . . . . . 159**

11.1 Effective Field Theory . . . . . . . . . . . . . . . . . . . . . . . . . 159
11.2 Additional Constraints on *WWZ* and *WW*$\gamma$ Couplings Parameters . . 161
11.3 Limit Setting Methodology . . . . . . . . . . . . . . . . . . . . . . . 162
11.3.1 Maximum Likelihood . . . . . . . . . . . . . . . . . . . . . . . . 162
11.3.2 Delta Log Likelihood Limits and Frequentist Limits . . . . . . 164
11.3.3 Optimization . . . . . . . . . . . . . . . . . . . . . . . . . . . . 165
11.4 Limit Setting Procedures . . . . . . . . . . . . . . . . . . . . . . . . 166
11.4.1 MC Samples and Generator Comparisons . . . . . . . . . . . . 166
11.4.2 Re-weighting with **MC@NLO** . . . . . . . . . . . . . . . . . . . . 167

11.4.3 Re-weighting with **BHO** . . . . . 170
11.5 Results of aTGC Limits . . . . . 180
11.5.1 **MC@NLO** Parameterization Results . . . . . 181
11.5.2 **BHO** Parameterization Results . . . . . 183

**12 Summary** . . . . . **186**

**Bibliography** . . . . . **187**

# LIST OF FIGURES

1.1 Elementary particles with mass, charge, and spin, categorized in leptons, quarks, and gauge bosons . . . 2

2.1 Triple-gauge-boson couplings in electroweak theory . . . 16
2.2 LO Feynman diagrams for $W^{+}W^{-}$ pair production at the LHC . . . 20

3.1 The LHC accelerator complex at CERN . . . 24
3.2 Cumulative luminosity and $\langle\mu\rangle$ for the 2011 and 2012 data sets . . . 26
3.3 A longitudinal cut-away view of the ATLAS detector . . . 28
3.4 A longitudinal cut-away view of the ATLAS tracking system . . . 30
3.5 A longitudinal cut-away view of the ATLAS calorimeters . . . 31
3.6 A longitudinal cut-away view of the ATLAS muon spectrometer . . . 32
3.7 Sketch of a barrel ECAL module with visible different layers . . . 35
3.8 Comparison of events with exactly two opposite-charged leptons recorded with single- or di-lepton triggers . . . 37
3.9 Comparison of events with exactly two opposite-charged leptons recorded with single-lepton, di-lepton or a logical **OR** of single- and di-lepton triggers . . . 38
3.10 Diagram of the ATLAS data processes . . . 43

4.1 Schematic view of a hadron-hadron collision process . . . 45
4.2 The PDFs from `MSTW2008` NLO at $Q^2 = 10\ GeV^2$ and $Q^2 = 10^4\ GeV^2$ . . . 46
4.3 Simulation structures of a truth event . . . 49

5.1 Highest $E_T^{rel}$ event ($E_T^{rel} = 196\ GeV$) in $WW$ signal region observed in the $e\mu$ channel in data . . . 52
5.2 A wedge of the transverse plane of the ATLAS detector . . . 53
5.3 Illustration of track reconstruction . . . 54
5.4 A 25-vertex $Z \to \mu\mu$ event showing the high *pile-up* environment for the vertex reconstruction . . . 57
5.5 Illustration of the cross section of an topological cluster in calorimeter . 62
5.6 Four strategies used in muon reconstruction and identification . . . 69
5.7 Jet reconstruction flow for calorimeter jets from towers or clusters . . . 74
5.8 Schematic representation of the JVF discriminant corresponding to the fraction of a jet originating from $vtx_i$ . . . 78
5.9 $E_T^{rel}$ definition . . . 80

6.1 Example of NLO Feynman diagrams for $W^+W^-$ pair production contributed from $q\bar{q}$ initial state at the LHC . . . 84
6.2 Example Feynman diagrams for $W^+W^-$ production backgrounds at the LHC . . . 90

7.1 Kinematic distributions of the selected events at the first cut stage ($M_{\ell\ell}$) 107
7.2 $\not{E}_T^{rel}$ distribution after Z-veto for the $ee$ and $\mu\mu$ and $e\mu$ channels . . . 108
7.3 $\not{p}_T$ distribution after $\not{E}_T^{rel}$ cut for the $ee$ and $\mu\mu$ and $e\mu$ channels . . . 108
7.4 $\Delta\phi(\not{p}_T, \not{E}_T)$ distribution after $\not{p}_T$ cut and in the zero jet bin . . . 108
7.5 Jet multiplicity distribution before the jet-veto for the $ee$ (left) and $\mu\mu$ (middle) and $e\mu$ (right) channels . . . 109
7.6 Distributions for $W^+W^-$ candidates at final selection for combined $ee$, $\mu\mu$ and $e\mu$ channels . . . 110

8.1 The two-dimensional distribution of $\not{E}_T^{rel}$ vs $\Delta\phi(\not{p}_T, \not{E}_T)$ for signal and *Z+jets* MC samples in different channels . . . 117
8.2 The $\not{p}_T$ distribution after $\Delta\phi(\not{p}_T, \not{E}_T)$ cut for signal and *Z+jets* MC samples in different channels . . . 119
8.3 The exponential fits of $\epsilon_{\not{p}_T}$ for *Z+jets* in different channels . . . 120
8.4 Double differential lepton efficiencies used in the matrix method for the $e\mu$-trigger electrons and muons . . . 127
8.5 $p_T$ -binned fake-rates measured in data used in the matrix method for electrons and muons in barrel and end-cap regions . . . 128
8.6 Fake-rates measured on a *W+jets* and di-jet MC samples for electrons and muons shown for two different triggers . . . 129

9.1 The PDFs uncertainties of $qq \rightarrow WW$ signal events in fiducial region for leading lepton $p_T$, $p_T^{\ell\ell}$, $M_{\ell\ell}$, $\Delta\phi_{\ell\ell}$, $|y_{\ell\ell}|$ and $|\cos\theta^*|$ . . . 146
9.2 The QCD scale uncertainties of $qq \rightarrow WW$ signal events in fiducial region for leading lepton $p_T$, $p_T^{\ell\ell}$, $M_{\ell\ell}$, $\Delta\phi_{\ell\ell}$, $|y_{\ell\ell}|$ and $|\cos\theta^*|$ . . . 147
9.3 The comparison of different *GEN+PS* for $qq \rightarrow WW$ signal events in fiducial region for leading lepton $p_T$, $p_T^{\ell\ell}$, $M_{\ell\ell}$, $\Delta\phi_{\ell\ell}$, $|y_{\ell\ell}|$ and $|\cos\theta^*|$ . . . 148
9.4 The comparison of different *GEN+PS* for non-resonant $gg \rightarrow WW$ signal events in fiducial region for leading lepton $p_T$, $p_T^{\ell\ell}$, $M_{\ell\ell}$, $\Delta\phi_{\ell\ell}$, $|y_{\ell\ell}|$ and $|\cos\theta^*|$ . . . 148

10.1 Comparison of the measured cross section from different di-lepton channels with the theoretical calculations of the $W^+W^-$ production cross section at $\sqrt{s} = 8\ TeV$ . . . 158

11.1 Comparison of reconstruction level SM $W^+W^-$ kinematic distributions after all final selection cuts (in the $e\mu$ channel) from using POWHEG+PYTHIA and **MC@NLO**+HERWIG/JIMMY . . . 168
11.2 $p_T^{\ell_1}$ distributions of different samples . . . 169
11.3 Comparison of **BHO** ME-level $p_T^{\ell_1}$ distributions between directly generated events and self-reweighted events from SM (1) . . . 179

11.4 Comparison of **BHO** ME-level $p_T^{\ell_1}$ distributions between directly generated events and self-reweighted events from SM (2) . . . . . . . . . . . . . . . 180
11.5 95% CL limits with form factors with $\Lambda = 2$ to $\Lambda = 10$ *TeV* . . . . . . . . . 183
11.6 $p_T^{\ell_1}$ distributions in the $e\mu$ channel re-weighted from SM to the best fit aTGCs as well as the lower 95% bound and the upper 95% bound . . . 184
11.7 The two-dimensional 95% CL contours for the *LEP* scenario . . . . . . 184

## LIST OF TABLES


2.1 The electric charges ($Q$), isospins ($T_3$) and hypercharges ($Y$) of all the fermions in the SM . . . 16

3.1 Summary of $pp$ collision data during LHC Run I . . . 26
3.2 List of triggers used in the $W^+W^-$ analysis . . . 35
3.3 Main active detector components of the ATLAS detector, from the beam line towards the outside . . . 39
3.4 Operational fraction for ATLAS sub-detectors during Run I . . . 39
3.5 Resolutions of the ATLAS detector components . . . 40

6.1 Predicted cross sections for various $W^+W^-$ production processes . . . 85
6.2 Summary of the possible additional contributions to the $WW$ production cross section that are neglected in the analysis . . . 86
6.3 The $W^+W^-$ signal production processes, cross sections and numbers of fully simulated MC events . . . 87
6.4 **MCFM** cross section predictions for $q\bar{q} + gg \rightarrow W^+W^- \rightarrow \ell^+\nu_\ell\ell^-\bar{\nu}_\ell$ using different PDF sets . . . 88
6.5 Dependence of the **MCFM** cross section predictions for $q\bar{q}+gg \rightarrow W^+W^- \rightarrow \ell^+\nu_\ell\ell^-\bar{\nu}_\ell$ on the variation of the renormalization ($\mu_R$) and factorisation ($\mu_F$) scales by factors of 2 . . . 88
6.6 MC samples/processes used to model $Z$+*jets* background . . . 92
6.7 MC samples/processes used to model $W$+*jets* background . . . 93
6.8 MC samples/processes used to model $W$+*jets* with heavy quark flavor ($b$ and $c$) backgrounds . . . 94
6.9 MC samples/processes used to model *Top* backgrounds ($t\bar{t}$ and $Wt$) . . . 94
6.10 MC samples/processes used to model the di-boson backgrounds $WZ$, $ZZ$, $W\gamma$, and $W\gamma^*$ . . . 95

7.1 Electron definition used in this analysis . . . 101
7.2 Muon definition used in this analysis . . . 102
7.3 Jet definition used in this analysis . . . 103
7.4 Event selection cut-flow for data collected in 2012 at 8 $TeV$ for 20.3 $fb^{-1}$ split in channels . . . 109
7.5 $W^+W^-$ MC event selection cut-flow at final selection . . . 112
7.6 Definitions of fiducial regions for different channels . . . 113
7.7 The $WW$ overall acceptance $\epsilon_{\mathcal{A}}$, fiducial volume acceptance $\mathcal{A}_{WW}$, and correction factor $C_{WW}$ as well as their uncertainties . . . 114

8.1 Comparison of the background yields obtained with the data-driven methods and MC predictions . . . 116
8.2 The B/C/D event yields, $f_{ABCD}$ and $\epsilon_{p\!\!/_T}$ after $\Delta\phi(p\!\!/_T, E\!\!\!/_T)$ cut . . . 119
8.3 $Z$+*jets* background estimation in the signal region for three channels and its comparison to the MC prediction with statistical uncertainties . 120
8.4 Systematic uncertainties of the *ABCD* method due to non-$Z$ MC subtraction 120
8.5 Systematic uncertainties of the *ABCD* method due to $f_{ABCD}$ . . . 121
8.6 Systematics of the *ABCD* method due to $\delta_{p\!\!/_T}$ and $\delta_{E\!\!\!/_T}^{\text{propagated}}$ . . . 122
8.7 Systematic uncertainties of the *ABCD* method due to $\epsilon_{p\!\!/_T}$ . . . 123
8.8 Supporting triggers to study trigger bias effects and to measure fake-rates 126
8.9 Data-driven $W$+*jets* estimate with statistical and systematic uncertainties 130
8.10 Other di-boson background yields and their statistical uncertainties as determined from MC for 20.3 $fb^{-1}$ . . . 131
8.11 Systematic uncertainties for the combined di-boson background processes 132

9.1 Systematic sources and associated relative uncertainties for $W^+W^-$ signal acceptance estimations for $ee$, $e\mu$, $\mu\mu$ and inclusive channels . . . 134
9.2 The sources of Electron scale uncertainties . . . 135
9.3 Jet energy scale uncertainty components for signal samples . . . 136
9.4 Fractional theoretical uncertainties on signal acceptance for $WW$ signal events . . . 138
9.5 Fractional PDFs uncertainties on signal acceptances for $WW$ signal events 139
9.6 Fractional scale uncertainties on signal acceptances for $WW$ signal events from different initial states . . . 140
9.7 Fractional Parton Shower and Generator uncertainties on signal acceptance for $WW$ signal events . . . 142
9.8 Fractional electroweak (EW) correction uncertainties on signal acceptance for $WW$ signal events from $q\bar{q}$ initial state ($qq$) . . . 142
9.9 The inclusive and jet-binned cross sections with different scale variations for $qq \to WW$ process and the jet-veto acceptance calculated with default QCD scales as well as the corresponding fractional jet-veto uncertainties evaluated with *S-T Method* . . . 144
9.10 Fractional jet-veto uncertainties on signal acceptance for $WW$ signal events from $q\bar{q}$ initial state ($qq$) and $gg$-induced ($ggH+gg$) processes . . 144
9.11 The theoretical fiducial cross sections for $ee$, $\mu\mu$ and $e\mu$ channels, as well as associated uncertainties . . . 145

10.1 Summary of observed events and expected signal and background contributions in 3 di-lepton channels . . . 149
10.2 Measured fiducial cross sections for each channel . . . 152
10.3 Measured total cross sections for each channel as well as the combination 152
10.4 Relative systematic uncertainties on the fiducial cross section . . . 155
10.5 Relative systematic uncertainties on the total cross section . . . 156

10.6 Measured fiducial cross sections for each channel compared with the theoretical predictions . . . 157

11.1 Officially produced MC samples for $WW \to \ell\nu\ell\nu$ process with SM or aTGC parameters . . . 167
11.2 Signal aTGC parameterization for the *No Constraint* scenario using 28 **MC@NLO** generator weights . . . 171
11.3 Number of events and statistical uncertainties in signal and backgrounds (using data-driven estimates for *W+jets* and *Top*) in each $p_T^{\ell_1}$ bin in the $e\mu$ channel . . . 172
11.4 Systematic uncertainties on data-driven backgrounds in $p_T^{\ell_1}$ ($GeV$) bins for the $e\mu$ channel . . . 172
11.5 Systematic uncertainties on $WW$ signal ($qq \to WW$) and $WW$ background ($gg \to WW$) events in $p_T^{\ell_1}$ ($GeV$) bins for the $e\mu$ channel . . . 173
11.6 Systematic uncertainties on di-boson background events in $p_T^{\ell_1}$ ($GeV$) bins for the $e\mu$ channel . . . 174
11.7 The 5 aTGC points selected to calculate the re-weighting coefficients for the *HISZ* and *Equal Couplings* scenario . . . 176
11.8 The 20 aTGC points selected to calculate the re-weighting coefficients for the *No Constraint* scenario . . . 176
11.9 The 9 aTGC points selected to calculate the re-weighting coefficients for the *LEP* scenario . . . 177
11.10 Signal anomalous coupling parameterization for *No Constraint* scenario using 3-D re-weighting method . . . 178
11.11 95% CL expected and observed limits on aTGCs for *No Constraint*, *LEP*, *HISZ*, and *Equal Couplings* scenarios with $p_T^{\ell_1}$ bins of [150,250,350,1000]$GeV$ in the $e\mu$ channel . . . 181
11.12 95% CL expected and observed limits on aTGCs for *No Constraint*, *LEP*, *HISZ*, and *Equal Couplings* scenarios with $p_T^{\ell_1}$ bins of [150,250,350,1000]$GeV$ in the $e\mu$ channel . . . 182
11.13 95% CL expected limits on aTGCs for *No Constraint* scenario with $p_T^{\ell_1}$ bins of [150,250,350,1000]$GeV$ in the $e\mu$ channel under different form factors . . . 182
11.14 95% CL observed limits on aTGCs for *No Constraint* scenario with $p_T^{\ell_1}$ bins of [150,250,350,1000] $GeV$ in the $e\mu$ channel under different form factors . . . 183
11.15 95% CL expected and observed limits on aTGCs for *No Constraint* scenario with $p_T^{\ell_1}$ bins of [150,250,350,1000] $GeV$ in the $e\mu$ channel . . . 184
11.16 The interval difference between results obtained by **MC@NLO** re-weighting method and results obtained by 3-D re-weighting method . . . 185

# LIST OF ABBREVIATIONS


| | | |
|---|---|---|
| **ADC** | analogue-to-digital converter | 49 |
| **ALICE** | A Large Ion Collider Experiment | 23 |
| **ANN** | artificial neural network | 68 |
| **AOD** | Analysis Object Data | 42 |
| **aTGCs** | anomalous triple-gauge-boson couplings | 6, 18–22, 47, 83, 159 |
| **ATLAS** | A Toroidal LHC Apparatus | 23 |
| **BR** | branching ratio | 21, 22, 85, 145 |
| **BT** | barrel toroid | 28 |
| **CaloTag** | calorimeter-tagged | 69–71 |
| **CB** | combined | 68, 70–72, 79, 81, 135 |
| **CL** | confidence level | 88, 139, 164, 166, 181–184, 186 |
| **CM** | center-of-mass | 3, 23, 83 |
| **CMS** | Compact Muon Solenoid | 23 |
| **CS** | central solenoid | 28 |
| **CSC** | cathode strip chamber | 32 |
| **DPD** | Derived Physics Data | 42 |
| **DPI** | double parton interaction | 85 |
| **ECAL** | EM calorimeter | 27–31, 33–35, 51, 56–59, 61, 65, 67, 69, 73, 75, 77, 103 |
| **ECT** | endcap toroid | 28 |
| **EE** | endcap-extra | 40 |
| **EF** | event filter | 33, 34, 41 |
| **EFT** | effective field theory | 2, 8, 21, 160, 161 |
| **eID** | electron identification | 60, 61, 63–65, 101, 111, 125 |
| **EM** | electromagnetic | 1, 2, 8, 9, 12, 15, 27, 29, 31, 73, 75, 159, 172 |
| **EMEC** | EM end-cap calorimeter | 31, 59 |
| **ESD** | Event Summary Data | 41, 42 |
| **eV** | electronvolt | 3 |
| **EW** | electroweak | xiii, 2, 7, 8, 12–16, 19, 21, 85, 112, 138, 141, 142, 170–172, 178, 181–184 |

| | | |
|---|---|---|
| **FCAL** | forward calorimeter | 29–31, 59 |
| **FE** | front-end | 33, 34 |
| **FSR** | final state radiation | 47, 49, 76 |
| **GRL** | Good Run List | 83, 104 |
| **GSF** | Gaussian Sum Filter | 59 |
| **HCAL** | hadronic calorimeter | 21, 27, 29–31, 33, 34, 56, 59, 61, 69, 104 |
| **IBL** | insertable B-Layer | 40 |
| **ID** | inner detector | 4, 27, 29, 34, 51, 52, 54, 59, 61, 67–73, 80, 81, 101, 102, 135 |
| **IP** | interaction point | 4, 25, 27–30, 32, 51, 52, 54, 62, 67, 68 |
| **ISR** | initial state radiation | 47, 49, 76 |
| **JER** | jet energy resolution | 75–77, 131, 135, 136 |
| **JES** | jet energy scale | 73, 75, 76, 131, 135 |
| **JVF** | jet vertex fraction | 77, 78, 103 |
| **JVSP** | jet-veto survival probability | 131 |
| **L1** | LV1 trigger | 34 |
| **L2** | LV2 trigger | 34 |
| **LAr** | liquid Argon | 29–31 |
| **LCW** | local cell signal weighting | 73, 74, 76, 103 |
| **LEP** | Large Electron-Position Collider | 23 |
| **LHC** | Large Hadron Collider | 1, 3, 4, 6, 23, 24 |
| **LHCb** | Large Hadron Collider beauty | 23 |
| **LINAC2** | Linear Accelerator 2 | 23, 24 |
| **LO** | leading order | 19, 20, 46, 47, 83, 85, 89, 91, 111 |
| **LS1** | Long Shutdown 1 | 40, 69 |
| **LV1** | level-1 | 33, 34, 38, 40, 50 |
| **LV2** | level-2 | 33, 34 |
| **MC** | Monte-Carlo | 4, 5 |
| **MDT** | muon drift tube | 32 |
| **ME** | matrix element | 44, 45, 47–49, 91, 172, 176, 177, 179, 180 |
| **MLM** | maximum likelihood method | 164 |
| **MPI** | multi-parton interaction | 44, 48, 49 |
| **MS** | muon spectrometer | 4, 27, 31, 32, 34, 40, 51, 67–72, 135 |

| | | |
|---|---|---|
| **MVA** | multivariate analysis | 60 |
| **NLO** | next-to-the-leading order | 19, 46, 47, 83–86, 91, 111, 112 |
| **NNLO** | next-to-next-to-the-leading order | 46, 83–85, 91–94 |
| **nSQP** | new Service Quarter Panel | 40 |
| **PDF** | probability density function | 60, 61 |
| **PDFs** | parton distribution functions | 45, 46, 85–88, 91, 138, 139, 145, 146, 154 |
| **PID** | particle identification | 36, 60, 61, 123–125 |
| **PMT** | photomultiplier tube | 30 |
| **pNNLO** | partial NNLO | 83, 84, 112, 134, 145 |
| **PS** | Proton Synchrotron | 23, 24 |
| **PSB** | Proton Synchrotron Booster | 23, 24 |
| **PV** | primary vertex | 55, 58, 62, 70, 72, 76–78, 81, 96, 105 |
| **QCD** | quantum chromodynamics | 7, 11, 44, 89 |
| **QED** | quantum electrodynamics | 11 |
| **QFT** | quantum field theory | 10 |
| **RAW** | Real Raw Data | 41, 50 |
| **ROD** | readout driver | 34, 50 |
| **RoI** | region of interest | 33, 34, 58 |
| **RPC** | resistive plate chamber | 32, 34 |
| **SA** | stand-alone | 68, 70 |
| **SCT** | silicon-microstrip tracker | 29, 30, 52, 54, 70 |
| **SF** | scaling factor | 36, 63–65, 71, 105, 111, 126, 133 |
| **SIM** | Simulated Event Data | 42 |
| **SM** | Standard Model | 1–5 |
| **SPS** | Super Proton Synchrotron | 23, 24 |
| **ST** | segment-tagged | 68, 70, 71 |
| **TAG** | Tag Data | 42 |
| **TDC** | time-to-digital converter | 49 |
| **TF** | transfer factor | 115, 117 |
| **TGC** | thin gap chamber | 33, 34 |
| **TRT** | transition radiation tracker | 29, 30, 52–54, 58, 59, 70 |
| **UE** | underlying event | 44, 48, 49, 66, 76 |
| **VBF** | vector boson fusion | 86 |
| **VBS** | vector boson scattering | 85 |

| | | |
|---|---|---|
| **WLCG** | Worldwide LHC Computing Grid | 41 |

# ABSTRACT

This thesis presents the measurement of the vector boson pair $W^+W^-$ production cross section in proton-proton collisions at the center-of-mass energy $\sqrt{s} = 8\,TeV$. The leptonic decay channels of the $W^+W^- \rightarrow \ell^+\nu_\ell\ell^-\bar{\nu}_\ell$ ($\ell \in \{e, \mu\}$) are analyzed using data corresponding to $20.3\,fb^{-1}$ of integrated luminosity collected by the ATLAS detector in 2012 at the Large Hadron Collider at CERN (in Geneva, Switzerland). The experimental signature of this measurement is two energetic isolated leptons ($e^+e^-, \mu^+\mu^-, e^\pm\mu^\mp$) and associated large missing transverse energy (due to neutrinos in final states). A total of 6636 $W^+W^- \rightarrow \ell^+\nu_\ell\ell^-\bar{\nu}_\ell$ candidate events is selected in ATLAS data with an estimation of $1547 \pm 28$ background events from non-$WW$ production processes. The measured total production cross section is $71.0^{+1.1}_{-1.1}(\text{stat})^{+5.7}_{-5.0}(\text{syst})^{+2.1}_{-2.0}(\text{lumi})\ pb$, which is comparable with the theoretical prediction of $63.2^{+2.0}_{-1.8}\ pb$ calculated with NNLO QCD and NLO EW corrections. The anomalous triple-gauge-boson couplings ($WWZ$ and $WW\gamma$) could signal new physics beyond the Standard Model at much higher energy scales compared to the directly detectable mass scale at the LHC. An effective Lagrangian is used to generalize the anomalous triple-gauge-boson couplings to describe the $W^+W^-$ productions at the LHC. These anomalous couplings can be experimentally probed by comparing the leading lepton transverse momentum spectrum with the theoretical predictions in different triple-gauge-boson coupling space. No observation of deviations from the Standard Model predicted couplings is found by a maximum likelihood fitting of the leading lepton $p_T$. Therefore, the most stringent limits to date on the anomalous triple-gauge-boson couplings are set from this analysis.

CHAPTER 1

# Introduction

This dissertation presents a measurement of the production cross section of a pair of $W^+W^-$ boson by proton-proton beam collisions at the Large Hadron Collider (LHC) with the ATLAS detector for the first time with the highest colliding energy (8 $TeV$). This measurement is one of the high profile research topics at the LHC, since it provides a stringent test to the Standard Model (SM) at the energy frontier, and crucial background information for searches for new physics beyond SM at the LHC. It is also a very sensitive channel to probe possible new physics through triple-gauge-boson coupling measurements. $W^+W^-$ production has been studied at 7 $TeV$ by the ATLAS and the CMS experiments, both with measured cross sections higher than the SM predictions by $\sim 2\sigma$ [1, 2]. These measurements have attracted a lot of attentions by both theoretical and experimental communities. Therefore, the measurement at 8 $TeV$ will be crucial to understand the nature of the deviations between observations and theoretical predictions at the LHC.

This chapter briefly introduces the particle physics, basic concepts on experiment and analysis, and outlines the structure of this dissertation.

The most profound questions for human beings since the dawn of civilization are, what are the fundamental constituents of matter and how do they interact with each other? Since the time of Ernest Rutherford, a new discipline with defined objectives and systems of research methods has branched out from physics, named particle physics or high energy physics. Over the quests for more than a century, generations of theorists and experimentalists tried to simplify the knowledge of fundamental particles and the interactions between them. The interplay between theories and experiments led to many discoveries. A theoretical framework for particle physics, which is called the SM, had been built about half century ago. It combines three successful quantum field theories that has been developed over the last sixty years, describing three of the four fundamental interactions in nature: electromagnetic (EM), weak, and strong, except gravitational. Furthermore, in the SM the EM and weak forces are successfully unified, called EW theory. Similar to the periodic table of chemical elements, the SM categorizes elementary particles in a very concise way, which is summarized in Figure 1.1. The SM withstood the most rigorous experimental tests with the highest precision ever reached in the history of physical science. A brief summary of the SM will be presented in Chapter 2.

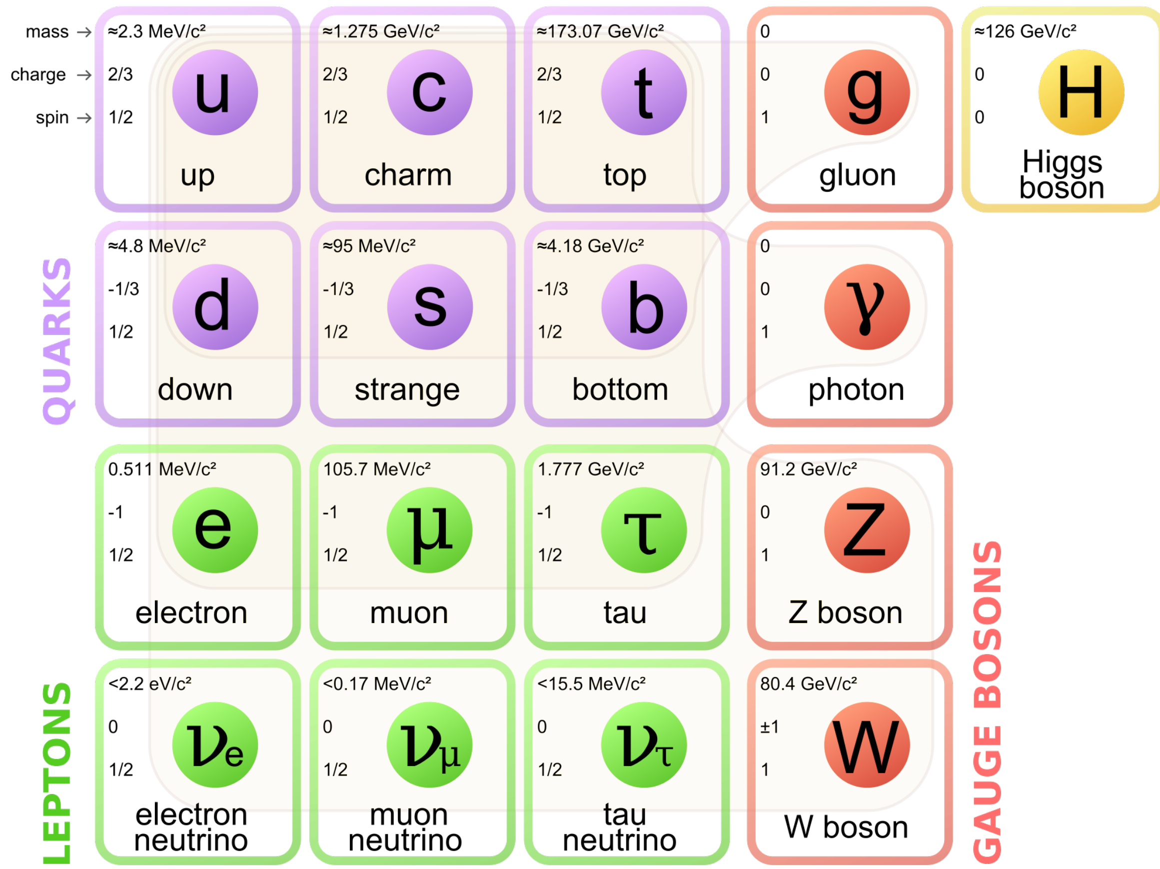


Figure 1.1: Elementary particles with mass, charge, and spin, categorized in leptons, quarks, and gauge bosons. Leptons and quarks are fermions (with non-integer spin), which are elements of matter. Gauge bosons (with integer spin) are force mediators: photon ($\gamma$) mediates EM force, $W$ and $Z$ bosons mediate weak force, gluons ($g$) mediate strong force. The Higgs boson which was discovered in 2012, gives masses to fermions and bosons by the the Higgs mechanism (see Section 2.1.4), completing the final piece of this table.

However, the SM is far from complete. For example, it cannot explain the observed neutrino mass and dark matter. Theorists believe that the SM is an effective field theory (EFT) at low energy scale, and more fundamental theory(ies) could exist at higher energy scales; while experimentalists look for the answers to those observed mysteries through probing the breakdown of the SM at higher energies and search for new phenomena, such as new particles and new forces. This thesis describes a test to the SM by a precision measurement of the cross section of producing a pair of $W^+W^-$ from the colliding protons at the LHC. Furthermore, a thorough study of $W^+W^-$ production would benefit many other studies and measurements. For example, the continuum $W^+W^-$ production is a crucial part of backgrounds to the Higgs boson detection with the $W^+W^-$ decay channel.

The most powerful facilities for particle physics research is high energy colliders. Currently, the unique high energy collider worldwide is the LHC at CERN (the European Organization for Nuclear Research). The necessity of high energy is for two reasons, one is that the spatial resolution of the probed distances of scattered particle beams is inversely proportional to the energy of the beam; the other one is to produce massive particles including undiscovered new particles. The idea of creating new particles from beam collisions is based on the Einstein matter-energy equivalence theorem $E = mc^2$: with $c$ the speed of light in vacuum, provided enough energy $E$, a particle of rest mass $m$ could be produced. There are two kinds of collision experiments. The first kind is to scatter a beam of particles to a heavy nuclei stationary target. The other kind is to make two beams of particles to have a head-on collision. The center-of-mass (CM) energy provided by the fixed target method is $E_{cm} \approx \sqrt{2E_1 m_2}$, where $E_{cm}$ is the CM energy, $E_1$ is the energy of the beam, and $m_2$ is the mass of the target nuclei. The available $E_{cm}$ is limited by $m_2$, for most modern colliders can provide very high $E_1$. In comparison, the CM energy available for head-on collision method is $E_{cm} \approx \sqrt{4E_1 E_2}$, where $E_2$ is the energy of the second beam. For most modern colliders, the head-on collision method maximizes the energy range of the collider, thus provides more powerful ability to probe small distances of particle interactions and produce more massive particles. The energy unit used in particle physics is usually based on *electronvolt($eV$)*: $keV$ ($10^3\ eV$), $MeV$ ($10^6\ eV$), $GeV$ ($10^9\ eV$), and $TeV$ ($10^{12}\ eV$). $1\ TeV = 1.6 \times 10^{-7}\ J$.

In addition to energy, another important parameter for particle accelerator is the intensity of the beams which is referred as *luminosity* in particle physics, for the resemblance of particle beams and light beams if one thinks of light consists of photons. *Instant luminosity* ($d\mathcal{L}/dt$) is the number of particles hitting a unit area per second, thus with the unit of $cm^{-2}s^{-1}$. *Integrated luminosity* ($\mathcal{L}$) is the time integration of instant luminosity, expressing the total number of particles hitting a unit area over time, thus with the unit of $cm^{-2}$.

When beams collide, particles have many possible interaction processes, each of which associates with a certain probability which can be calculated by the SM of particle physics. Such probability of interaction is expressed in the term of *cross section* ($\sigma_{\text{process}}$), which originates from the idea of billiard ball collision: two billiard balls head to each other, if the cross sections of each ball become larger, the probability of the collision also increases correspondingly. The units of cross section is based on barn ($b$): $mb$ ($10^{-3}\,b$), $\mu b$ ($10^{-6}\,b$), $nb$ ($10^{-9}\,b$), $pb$ ($10^{-12}\,b$), and $fb$ ($10^{-15}\,b$). $1\,b = 10^{-24}\,cm^2$, which is actually a very tiny unit. Because barn is in essence a unit of area, for convenience, luminosity often use $b^{-1}$ instead of $cm^{-2}$ in its unit. At the LHC, the most used unit for integrated luminosity is $fb^{-1}$. Thus, for a specific process, the expected number of events produced from a process, $N_{\text{process}}$, is given by the product of cross section and the integrated luminosity: $N_{\text{process}} = \sigma_{\text{process}} \times \mathcal{L}$. In an experiment, the expected number of detected events from a given process therefore can be calculated by:

$$N_{\text{process}}^{\text{expected}} = \sigma_{\text{process}} \times \mathcal{L} \times \mathcal{A} \tag{1.1}$$

where $\mathcal{A}$ denotes the overall experimental acceptance.

To study the probability of one interaction process, particle detectors are used to record the experimental information of the *events* produced in beam collisions. These events will be further reconstructed with computing programs for analysis. There are three major detecting subsystems to record the events: inner detector (ID), calorimeters, and muon spectrometer (MS), ordered by their distances from the interaction point (IP). The chosen order accord with the principle that the inner components should minimize their interference to the detection capability of the outer components. Muons can penetrate most materials without significant energy lost or deflection, thus muon spectrometer is the out-most layer. Calorimeters are designed to absorb energy of particles for measurement, therefore are positioned after ID, which are used to record tracks of charged particles and their interaction vertices. In reality, for a specific process, most of the collision events are not relevant, therefore it is not necessary or possible for detectors to record all of them. E.g., $W^+W^-$ production only occurs once in approximately every $10^9$ $pp$ collisions with 8 $TeV$ collision energy. Hence, *trigger* systems are used in experiment design to record only "interesting" events. The ATLAS detector subsystems, triggers, and their performance parameters, as well as the computing and network systems are described in Chapter 3.

The entire analysis crucially depends on theoretical modeling and detector simulations. Nearly every step of the analysis involves Monte-Carlo (MC) simulations, for both signal and background processes, to calculated the cross sections and kinematic distributions, and to determine the detection acceptance and the associated uncertainties. These MC simulation jobs are carried out with different MC particle generators, parton showerer models and detector simulators. MC simulations are summarized in Chapter 4.

Most of massive particles produced in *pp* collision have very short life-time. For example, the life time of a $W$ boson is an order of $10^{-24}$ $s$. Before directly detected by the detector, they will decay to stable products via different modes (*channels*), each channel with a definite probability (*branching ratios*, *Br*) among all possible decay channels. Therefore, an $W^+W^-$ event can be only identified by analyzing remnants of its decay products. Such objects of interaction remnants are referred to be the physics objects, with its reconstruction details described in Chapter 5. Recorded events contain all reconstructed physics objects and their characteristics (kinematics, geometric positions, detector flags, derivative quantities, etc.). A signal event is tagged by a set of characteristics, determined by the chosen final state particles and channels of the process under investigation. In this dissertation, the final state particles of $W^+W^-$ decay is chosen to be three leptonic decay channels, $W^+W^- \rightarrow e^+\nu_e e^-\bar{\nu}_e$, $\mu^+\nu_\mu\mu^-\bar{\nu}_\mu$, and $e^+\nu_e\mu^-\bar{\nu}_\mu$ or $\mu^+\nu_\mu e^-\bar{\nu}_e$, referred as $ee$, $\mu\mu$ and $e\mu$ channels [1]. However, some other processes other than the $W^+W^-$ production may have the same final state particles, which are considered as backgrounds for this analysis. Selection cuts are designed and optimized to maximize signal and background separation. Different techniques are used to estimate the background contributions in the final selected event samples. An over view of the $W^+W^-$ analysis is provided in Chapter 6, and details of the signal events selection is provided in Chapter 7. Background estimation is detailed in Chapter 8.

The basic connection between theory and experiment is the cross-section calculations and measurements. The cross-section measurement is first conducted in a fiducial phase space which is defined by geometric and kinematic acceptance of an experiment. This measurement is then extrapolated to a total phase space. The *fiducial phase space* or *fiducial volume* is often defined as close as possible to the event selection criteria. The detection efficiency and systematics of analyses are evaluated in this phase space, which is described in Chapter 9. The result of the measured cross section is presented in Chapter 10.

The search for new physics beyond the SM can be conducted by probing the

[1] In convention, the order of the particles matters: the first one is called the "leading lepton" with higher transverse momentum, and the second one is called the "sub-leading lepton" accordingly. In the context of differentiating the two, $e\mu + \mu e$ is a better way to label a channel contains both $e$ and $\mu$.

anomalous triple-gauge-boson couplings (aTGCs) in $W^+W^-$ production at the LHC. The aTGCs could increase the $W^+W^-$ event rate at high energy region. The study of aTGCs with the selected $W^+W^-$ events is described in Chapter 11.

Finally, a summary of this thesis work is given in Chapter 12.

CHAPTER 2

# The Standard Model and the $W^+W^-$ Production at the LHC

This chapter will give a brief description of the particle physics theory, the Standard Model and the $W^+W^-$ production in proton-proton collisions at the LHC.

## 2.1 The Standard Model

The SM is the theory of particle physics. It was a collaborative achievement built upon ground-breaking works by many physicists throughout the latter half of the 20$^{\text{th}}$ century through experiments and theory developments, and was finalized to the current form in the mid-1970s. The SM is a theory based on the ideas of gauge invariance (which naturally introduces the interactions) consisting of the quantum chromodynamics (QCD), the EW theory, and the Higgs mechanism (which internalizes spontaneous symmetry breaking to explain the origin of mass of particles). Because of its rigorous self-consistency and huge power in explaining a wide variety of experimental results in the last 40 years, the SM is thought as the most successful theory of modern physics. The Higgs boson, the last undiscovered particle predicted by the SM, was discovered in 2012 at the LHC, completing the final piece of the theory. A brief history of the making of the SM could be found in the book [3] written by Dr. Steven Weinberg, the 1979 Nobel laureate of Physics.

However, as a theory of "how the world is made of", the SM is far from complete. It does not describe the gravitational interaction (as described by general relativity); it cannot explain what is the origin of dark matter observed in astrophysics experiments; it cannot interpret the origin of neutrino oscillation and their non-zero masses; as an energy and space-time theory, it cannot tell what is the nature of dark energy that causes the universe expansion with acceleration; it treats particles equal to its anti-particle counterparts on existence, yet fails to reveal the mystery for the matter-antimatter asymmetry observed in our universe. In general, it is believed that the SM is an EFT at low energy of some more fundamental theory. Therefore, one of the major motivations of the modern experiments is to search for breakdown of the SM.

### 2.1.1 Leptons, Quarks, and Gauge Bosons

The SM categorizes fundamental particles into what the table shows in Figure 1.1. Elementary particles in this table are grouped into two types according to their intrinsic angular momenta, called spin: the ones with half integer unit of $\hbar$ spin (spin-$\frac{1}{2}$), which are named fermions because they are characterized by Fermi-Dirac statistics; and the ones with integer multiples of $\hbar$ spin, which are named bosons because they obey Bose-Einstein statistics. The relation between spin and statistics was proved by W. Pauli [4]. For fermions, there are six known quarks and six known leptons, all grouped into three generations in Figure 1.1. Each generation of fermions repeat the same charge as the last, but with increasing mass. Along with their antiparticles, fermions are the constituents of all the matter we have known in the universe. On the other hand, bosons are interaction or force mediators, which are grouped into three types according to the interaction they involve: gluons ($g$) which only mediate strong interactions, $W^{\pm}$ and $Z$ which only mediate weak interactions, and photon ($\gamma$) which only mediates EM interactions. In the SM, EM and weak interactions are unified into electroweak theory, which models them into one single electroweak force when interaction energy is above the unification scale ($\sim 100\ GeV$).

Leptons and quarks both participate in EW interactions through the exchange of $W^{\pm}$, $Z$ and $\gamma$. However, only quarks are subject to the strong force through the exchange of gluons, because only quarks and gluons carry color charges. Color charge has no literal meaning but only a descriptive way of the strong charge carried by the described particles. Similar to the "plus" and "minus" assigned to electric charges, colors are categorized into Red ($R$), Green ($G$) and Blue ($B$), as well as the "anticolors" Cyan ($\overline{R}$), Magenta ($\overline{G}$), and Yellow ($\overline{B}$). Because the nature requires particles to be in integer electric charge (including zero charge) and color-neutral, quarks combine into two different kinds of hadrons, or particles consist of quarks, called baryons and mesons. A baryon is a three-quark composite, $qqq$, or a three-antiquark composite, $\overline{qqq}$, while a meson is a quark-antiquark pair, $q\bar{q}$. The color states making hadrons colorless is either a pair as $R\overline{R}$ or a triplet as $RGB$ or $\overline{RGB}$. The fact that no color state particle was ever detected indicates that, quarks are confined in hadrons, bounded by the color carrying force mediator, gluons. The energy of separating a confined quark out of a hadron, if high enough, turns to creating a new pair of $q\bar{q}$. Similar effects happen when a gluon is "radiated" from a final state (real) particle. Such $q\bar{q}$ creation along an outgoing quark leads to a tightly packed sprays of hadrons along the trajectory, named jets, a phenomena commonly seen in particle detectors at high energy particle accelerator facilities.

Gauge bosons are gauge interaction mediators that arise from the requirement of gauge invariance of the theory. There are a total of 12 gauge bosons, including $\gamma$, $W^{\pm}$, $Z$, and eight types of gluons (with different kind of colors). The lighter the bosons are, the longer range the interactions would reach; therefore EM interaction has infinite range, while weak force are short range interactions. Gluons are massless, but they are confined in the particles they help create and have never been directly detected. Other than gauge bosons, the Higgs boson is an elementary scalar boson predicted by the Higgs mechanism. It couples with fermions to generate masses for them (Yukawa coupling), and gives mass to weak vector bosons through spontaneous symmetry breaking. All gauge bosons are electric neutral except $W^{\pm}$; and all bosons are spin $\hbar$ except Higgs boson (spin 0). Besides interacting with fermions, weak gauge bosons, gluons and Higgs are also self-interacting due to the non-Abelian nature of the underlying symmetry of the theory, details of which will be covered in Section 2.1.2.

Just as the photon linking all charged particles, the gluons link all colored particles. The neutral weak gauge boson $Z$ links all the matter and anti-matter fermion pairs, while the charged weak gauge boson $W^{\pm}$ links "up-type" and "down-type" quark and lepton pairs, such as $e \leftrightarrow \nu_e$, $\mu \leftrightarrow \nu_\mu$, $u \leftrightarrow d$, $\bar{c} \leftrightarrow \bar{s}$, $c \leftrightarrow d$ and so on. It is observed that lepton decays are not mixed between generations, but meson decays to quark pairs can be mixed in generations via weak interactions. Nicola Cabibbo introduced the Cabibbo angle, $\theta_C$, to rotate the quark doublets from the mass eigenstates $\begin{pmatrix} d \\ s \end{pmatrix}$ to the weak eigenstates $\begin{pmatrix} d' \\ s' \end{pmatrix}$ with which the weak bosons interact:

$$\begin{pmatrix} d' \\ s' \end{pmatrix} = \begin{pmatrix} \cos\theta_C & \sin\theta_C \\ -\sin\theta_C & \cos\theta_C \end{pmatrix} \begin{pmatrix} d \\ s \end{pmatrix} \tag{2.1}$$

After $c$ quark was discovered, Cabibbo angle was generalized by Kobayashi and Maskawa, to a matrix parameterized for $u$, $d$, $c$, and $s$. The further extended matrix is a $3 \times 3$ one, now called the "CKM matrix", representing the mixing between three quark generations, using a parametrization including three angles and one complex phase. *CP violation* is allowed by the complex phase since CKM matrix elements become their complex conjugates under a CP transformation. The CP violation, such as those amount shown in the weak decays in the $K$ and $B$ mesons, is thought to account for the matter-antimatter asymmetry in our universe; however, current observed CP violations are far from enough to explain the extent of matter-antimatter asymmetry.

### 2.1.2 Gauge Theory

In modern physics, the interactions are naturally introduced by gauge (symmetry) invariance in the Language function. Symmetry implies that physics law is invariant under gauge transformations (space-time, and some internal physical symmetries, such as charge conservation) of the Lagrangian density function $\mathcal{L}$, from which physics law is derived. The underlying physics is represented by the action $\mathcal{I}$ which is defined in four-dimension space $\{q_i, i = 0, 3\}$ as

$$\mathcal{I} = \int \mathcal{L} \, d^4 q \tag{2.2}$$

When the symmetry group depends on space-time, it is called a local symmetry. A continuous symmetry group is called a gauge group. A transformation under the gauge group is called a gauge transformation. The terminology of "gauge", in normal usage, refers to a particular choice, or specification, of the potentials (either vector or scalar) which generates a given field. Therefore, a gauge theory is simply a theory that leaves the action $\mathcal{I}$ invariant under gauge transformations.

According to Noether's theorem, if there is a global gauge symmetry in the action of a physical system, there is a corresponding conservation law corresponding to it. E.g., in quantum field theory (QFT), the global phase invariance is connected to charge conservation [5]. However, a global symmetry is not always available in physical systems, instead, a local gauge symmetry is established in most cases. Since the Lagrangian is required to be Lorentz covariance according to the principle of relativity, local gauge symmetry eventually introduces a gauge field (force carrier) into the system, which is shown by the following generic approach.

For a particle field $\psi(x)$, a global gauge transformation takes the form of

$$\psi(x) \rightarrow \psi'(x) = e^{i\alpha} \psi(x), \tag{2.3}$$

where $\alpha$ is independent of space and time. Apparently the dynamic term of the Lagrangian involving a derivative of the form $\partial_\mu \psi$ is invariant under the global transformation:

$$\partial_\mu \psi \to \partial_\mu \psi' = \partial_\mu e^{i\alpha} \psi = e^{i\alpha} \partial_\mu \psi \tag{2.4}$$

However, if let $\alpha \to \alpha(x)$, $\partial_\mu \psi$ will introduce an extra term, breaking the invariance:

$$\partial_\mu \psi \to \partial_\mu \psi' = e^{i\alpha(x)} \partial_\mu \psi + i e^{i\alpha(x)} \psi \partial \alpha(x) \tag{2.5}$$

This means the operator $\partial_\mu$ is not Lorentz covariant. To bring back the gauge invariance, a covariant derivative operator, $\mathcal{D}_\mu$, is constructed as follows:

$$\mathcal{D}_\mu \equiv \partial_\mu - ieA_\mu, \tag{2.6}$$

where $A_\mu$ is a vector field and transforms as

$$A_\mu \to A'_\mu = A_\mu + \frac{1}{e} \partial_\mu \alpha(x) \tag{2.7}$$

Under such definitions, the gauge invariance of the derivative term of the Lagrangian is restored:

$$\begin{aligned}
\mathcal{D}'_\mu \psi' &= (\partial_\mu - ieA'_\mu) e^{i\alpha(x)} \psi \\
&= \partial_\mu (e^{i\alpha(x)} \psi) - ie \left( A_\mu + \frac{1}{e} \partial_\mu \alpha(x) \right) e^{i\alpha(x)} \psi \\
&= e^{i\alpha(x)} \partial_\mu \psi + i e^{i\alpha(x)} \psi \partial_\mu \alpha(x) - ieA_\mu e^{i\alpha(x)} \psi - i e^{i\alpha(x)} \psi \partial_\mu \alpha(x) \\
&= e^{i\alpha(x)} (\partial_\mu - ieA_\mu) \psi
\end{aligned} \tag{2.8}$$

$$\mathcal{D}_\mu \psi \to \mathcal{D}'_\mu \psi' = e^{i\alpha(x)} \mathcal{D}_\mu \psi \tag{2.9}$$

Therefore, local gauge symmetry introduces a vector field $A_\mu$ into the system. In quantum electrodynamics (QED), the $A_\mu$ vector field represents the photon field that interact with charged particles. The family of phase transformations $U(\alpha(x)) \equiv e^{i\alpha(x)}$ creating the photon field forms the unitary Abelian group $U(1)_{EM}$. The number of gauge fields for $U(1)_{EM}$ symmetry is $dim(U(1)_{EM}) = 1$, therefore there is only one gauge boson coupling to charged particles, the photon. Similarly, QCD has the gauge group $SU(3)_{color}$ and the gauge transformation is $U \in SU(3)_{color}$. The number of gauge fields is $dim(SU(3)_{color}) = 8$, corresponding to the 8 gluons interacting with quarks and holding them together to form hadrons.

By introducing gauge theory, the emergence of gauge bosons become a natural result of the physical system. However, there is one remaining problem: gauge theory requires that gauge bosons are massless, otherwise gauge invariance will be violated. Photons and gluons are massless, but the experimentally observed weak bosons, $W^{\pm}$ and $Z$, are not. To tackle this problem, physicists conceived an idea called spontaneous symmetry breaking, which states that while the underlying law of physics (to be specific, the equation of motion or the Lagrangian) is invariant under a gauge transformation, the system as a whole (to be specific, the lowest-energy state or the vacuum) is not. It is a spontaneous process where a system with symmetric state evolves to an asymmetric state. In this way, the gauge invariance (related to Lagrangian) is conserved but the mass term could emerged for EW interactions. To break the symmetry spontaneously, the Brout-Englert-Higgs-Guralnik-Hagen-Kibble mechanism, or the Higgs mechanism, was introduced. The consequence of the Higgs mechanism is the prediction of the existence of an elementary scalar particle, the Higgs boson. Searching for Higgs boson has been one of the top goals for high energy experiments over the last three decades.

### 2.1.3 Electroweak Theory

The Electroweak theory unifies the EM and weak interactions mediated by the $\gamma$, $W^{\pm}$ and $Z^0$ bosons, which are quanta of gauge fields. For simplicity, we will describe the theory below beginning with the first generation of leptons. The generalization to the other generations should be straight forward. A more complete description of the SM is given in Reference [6].

The framework of the theory begins with the construction of a Lagrangian density function for a free (non-interacting), massless fermion field $\psi(x)$:

$$\mathcal{L} = \overline{\psi} i \gamma^{\mu} \partial_{\mu} \psi \tag{2.10}$$

where $\mu$ is the index of the space-time ($x^{\mu}$) which runs from 0 to 3, $\gamma^{\mu}$ are the $4 \times 4$ Dirac matrices, $\overline{\psi} \equiv \psi^{\dagger} \gamma^0$ and $\partial_{\mu} = \dfrac{\partial}{\partial x^{\mu}} = (\partial_t, \nabla)$.

Experimentally, no right-handed neutrinos are observed (i.e., neutrinos always have their spin pointing in the direction opposite to their momentum), so one writes the electron and neutrino fields as a left-handed doublet and a right-handed singlet:

$$R_e = (e_R), \qquad \text{and} \qquad L_e = \begin{pmatrix} \nu_L \\ e_L \end{pmatrix} \tag{2.11}$$

where the left- and right-handed components of a field $\psi$ are defined by

$$R_e \equiv \psi_R = P_R\psi = \frac{1+\gamma^\mu}{2}\psi, \quad \text{and} \quad L_e \equiv \psi_L = P_L\psi = \frac{1-\gamma^\mu}{2}\psi \tag{2.12}$$

where $\gamma^5$ is a $4 \times 4$ matrix in Dirac representation. So the Lagrangian for free massless leptons is written as

$$\mathcal{L} = \overline{L}_e i\gamma^\mu \partial_\mu L_e + \overline{R}_e i\gamma^\mu \partial_\mu R_e \tag{2.13}$$

The quantum numbers (internal degrees of freedom) are postulated: weak isospin $T$ and hypercharge $Y$. The doublet has $T = \frac{1}{2}$ and the singlet $T = 0$. The upper component of the doublet has weak isospin component $T_3 = +\frac{1}{2}$ and the lower component has $T_3 = -\frac{1}{2}$. The hypercharge $Y$ is related to the electric charge $Q$ and their relation is given below:

$$Q = T_3 + \frac{Y}{2} \tag{2.14}$$

The way of particles behave under the EW symmetry group ($SU(2)$) transformations is familiar because spin also transforms under a (different) $SU(2)$ group. It is known from quantum mechanics that particles with spin 0 are singlets, particles with spin $\frac{1}{2}$ ($J = \frac{1}{2}$) form doublets with $J_3 = +\frac{1}{2}, -\frac{1}{2}$, and so on. All known quarks and leptons are experimentally observed to be either EW singlets or doublets. The theory is required to be invariant under $SU(2)$ phase transformations in the space describing the internal isospin degree of freedom. Since $T = 0$ is for the singlets, the $SU(2)$ group acts non-trivially only on the doublet. The Lagrangian must be invariant under $SU(2)$ transformation of the form

$$L_e \longrightarrow e^{i\frac{\vec{\alpha}(x)\cdot\vec{\tau}}{2}} L_e \tag{2.15}$$

where $\vec{\alpha}(x)$ are the three parameters which specify the rotation and $\vec{\tau}$ are the Pauli matrices, the generators of the isospin $SU(2)$ group. The fact that these matrices do not commute implies that the transformation is non-Abelian, which means that the order of transformation matters.

In a similar way, the theory is required to be invariant under $U(1)$ transformations of the form $\psi \rightarrow e^{i\alpha Y}\psi$. Electroweak singlets have $Y = Y_R = -2$, while doublets have $Y = Y_L = -1$, therefore the $U(1)_Y$ symmetric transformation for doublets and singlets are given below:

$$L_e \longrightarrow e^{-i\alpha(x)} L_e, \quad R_e \longrightarrow e^{-2i\alpha(x)} R_e \tag{2.16}$$

where $\alpha(x)$ specifies the transformation and hypercharge $Y$ is the generator of the $U(1)$ group.

The requirement that gauge symmetries hold locally corresponds to allowing the coefficients $\alpha(x)$ and $\vec{\alpha}$ to be functions of space-time. To remain gauge invariance under local $U(1)_Y$ transformation, one must introduce a gauge field $B_\mu$ which transforms as a four-vector and replace the derivatives by gauge-covariant derivatives. Gauge invariance under local $SU(2)_L$ transformation requires the introduction of three vector fields $W^a_\mu$ ($a = 1, 2, 3$). The covariant derivative is thus introduced as:

$$D^\mu = \partial^\mu - ig_1 \frac{Y}{2} B_\mu - ig_2 \frac{\tau^a}{2} W^a_\mu \tag{2.17}$$

which has the property that $D^\mu \psi$ transforms in the same way as $\psi$, and $g_1$ and $g_2$ here are coupling constants. If we define the field strength tensors

$$F^{\mu\nu} \equiv \partial_\mu B_\nu - \partial_\nu B_\mu \quad \text{and} \quad F^a_{\mu\nu} \equiv \partial_\mu W^a_\nu - \partial_\nu W^a_\mu + g_2 \epsilon^{abc} W^b_\mu W^c_\nu \tag{2.18}$$

where $\epsilon^{abc} = +1(-1)$ if $abc$ is a cyclic (anti-cyclic) permutation of 123 and $\epsilon^{abc} = 0$ otherwise. By replacing $\partial_\mu$ with $D_\mu$ and adding the kinematic term of the gauge fields, the EW Lagrangian is constructed as:

$$\mathcal{L} = \overline{L}_e i\gamma^\mu D_\mu L_e + \overline{R}_e i\gamma^\mu D_\mu R_e + \frac{1}{4} F_{\mu\nu} F^{\mu\nu} + \frac{1}{4} F^a_{\mu\nu} F^{a,\mu\nu} \tag{2.19}$$

which is invariant under the local $U(1)_Y$ symmetry transformations

$$L_e \to e^{-i\alpha(x)} L_e, \quad R_e \to e^{-2i\alpha(x)} R_e, \quad B_\mu \to B_\mu + \frac{2}{g_1} \partial_\mu \alpha(x), \tag{2.20}$$

and under the local $SU(2)_L$ transformations

$$L_e \to e^{i\frac{\vec{\alpha(x)}\cdot\vec{\tau}}{2}} L_e, \quad W^a_\mu \to W^a_\mu + \frac{1}{g_2} \partial_\mu \alpha(x)^a(x) + \epsilon^{abc} \alpha(x)^b W^c_\mu. \tag{2.21}$$

This EW Lagrangian describes massless leptons interacting with four massless vector gauge fields. This process can be generalized to the whole first generation fermions by adding two quarks which are arranged in right-handed singlets and a left-hand doublet:

$$(u_R), \quad (d_R) \quad \text{and} \quad q_L = \begin{pmatrix} u_L \\ d_L \end{pmatrix}. \tag{2.22}$$

If one defines the gauge fields as

$$W^{+}=\frac{-W^{1}+iW^{2}}{\sqrt{2}},\quad W^{-}=\frac{-W^{1}-iW^{2}}{\sqrt{2}},\quad W^{0}=W^{3} \tag{2.23}$$

and

$$A_{\mu}=\frac{g_{2}B_{\mu}+g_{1}W_{\mu}^{0}}{\sqrt{g_{1}^{2}+g_{2}^{2}}},\quad Z_{\mu}=\frac{-g_{2}B_{\mu}+g_{1}W_{\mu}^{0}}{\sqrt{g_{1}^{2}+g_{2}^{2}}} \tag{2.24}$$

the electric charge $e$ and the weak mixing angle $\theta_{w}$ are related to the EW couplings $g_1$ and $g_2$ as below:

$$e=\frac{g_{1}g_{2}}{\sqrt{g_{1}^{2}+g_{2}^{2}}},\quad s_{W}\equiv\sin\theta_{W}=\frac{g_{1}}{g_{1}^{2}+g_{2}^{2}},\quad c_{W}\equiv\cos\theta_{W}=\frac{g_{2}}{g_{1}^{2}+g_{2}^{2}}. \tag{2.25}$$

After some straight forward algebra and adding the quark terms, the EW interaction Lagrange for the first generation leptons and quarks become:

$$\begin{aligned}\mathcal{L}_{SU(2)\otimes U(1)}=&\sum_{f}eQ_{f}\left(\overline{f}\gamma^{\mu}f\right)A_{\mu}\\&+\frac{g_{1}}{c_{W}}\sum_{f}\left[\overline{f}_{L}\gamma^{\mu}f_{L}\left(T_{f}^{3}-Q_{f}s_{W}^{2}\right)+\overline{f}_{R}\gamma^{\mu}f_{R}\left(Q_{f}s_{W}^{2}\right)\right]Z_{\mu}\\&+\frac{g_{2}}{\sqrt{2}}\left[\left(\overline{u}_{L}\gamma^{\mu}d_{L}+\overline{\nu}_{eL}\gamma^{\mu}e_{L}\right)W_{\mu}^{+}+h.c.\right]\end{aligned} \tag{2.26}$$

where $Q_f$ and $T^3_f$ are the EM charge and the third component of isospin, respectively, for each fermion $f$ for $f\in(\nu_e,e,u,d)$, and the $h.c.$ denotes the Hermitian conjugate. In Equation 2.26, the $h.c.$ of $W^+$ is $W^-$. The fields $A_\mu$, $Z_\mu$, $W^+_\mu$ and $W^-_\mu$ are then identified as the photon ($\gamma$), the $Z^0$, and the $W^\pm$ fields, respectively. All fermions which have electric charge interact with the EM field $A_\mu$, regardless of their isospins, with a strength proportional to their electric charges. The neutrino which has $Q_\nu = 0$ interacts only with the $Z^0$ and the $W^\pm$ fields. Also, only left-handed fermions interact with the $W^\pm$ fields. This is due to the fact that right-handed fermions are $SU(2)$ singlets with $T = 0$.

Table 2.1.3 summarizes all the fermion's electric charges ($Q$), isospins ($T_3$) and hypercharges ($Y$).

From the Lagrangian expression 2.19 one should notice that the EW theory is a non-Abelian gauge theory, which predicts the existence of EW gauge boson self-interactions from the $F^a_{\mu\nu}F^{a,\mu\nu}$ term in the Lagrangian. The self-interactions contain

| | Left-handed | $Q$ | $T_3$ | $Y$ | Right-handed | $Q$ | $T_3$ | $Y$ |
|---|---|---|---|---|---|---|---|---|
| Leptons | $\nu_e, \nu_\mu, \nu_\tau$ | 0 | +1/2 | -1 | No interaction (if exist at all) | | | |
| | $e, \mu, \tau$ | -1 | -1/2 | -1 | $e_R, \mu_R, \tau_R$ | -1 | 0 | -2 |
| Quarks | $u, c, t$ | +2/3 | +1/2 | +1/3 | $u_R, c_R, t_R$ | +2/3 | 0 | +4/3 |
| | $d, s, b$ | -1/3 | -1/2 | +1/3 | $d_R, s_R, b_R$ | -1/3 | 0 | -2/3 |

Table 2.1: The electric charges ($Q$), isospins ($T_3$) and hypercharges ($Y$) of all the fermions in the SM.

particular triple-gauge-boson interaction vertices $ZWW$ and $\gamma WW$. By introducing the Higgs Mechanism (see Section 2.1.4), another triple-gauge-boson vertex, $HWW$, also exists. These interactions are shown in Figure 2.1.

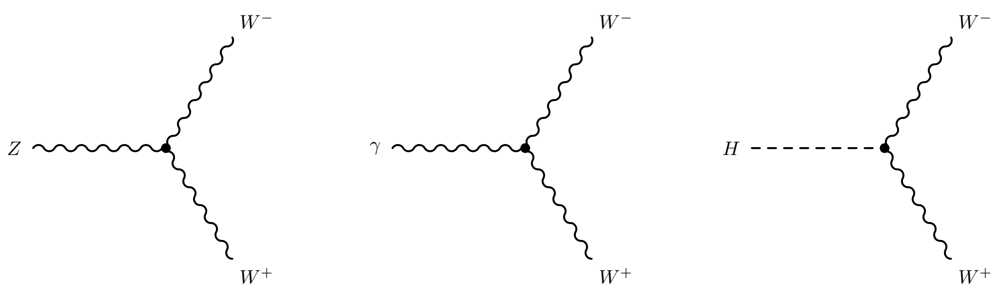


Figure 2.1: Triple-gauge-boson couplings in electroweak theory.

### 2.1.4 The Higgs Mechanism

As described above, the Lagrangian constructed based on the $SU(2)_L \otimes U(1)_Y$ symmetry produces the complete set of EW interactions. However, the weak bosons must be massless within this theoretical framework, and this conflicts with experimental observations: the $Z^0$ and the $W^\pm$ are massive vector bosons. To add masses to the weak bosons and fermions, the *Higgs mechanism* was introduced into the SM around 1964 by three independent theory groups (Brout-Englert, Higgs, and Guralnik-Hagen-Kibble). Through the Higgs mechanism, the EW symmetry is broken spontaneously, and the fermions and weak gauge bosons acquire masses. The idea of the Higgs mechanism is briefly described in this section.

In the SM, an isospin doublet of complex scalar fields with weak hypercharge $Y = 1$, called the Higgs fields $\phi$, is introduced with its potential energy arranged to the general form:

$$V(\phi) = \mu^2\phi^2 + \lambda\phi^4, \tag{2.27}$$

where $\mu^2 < 0$ and $\lambda > 0$, and the $\phi$ is a doublet of complex scalar field:

$$\phi = \begin{pmatrix} \phi^+ \\ \phi^0 \end{pmatrix} = \begin{pmatrix} \frac{\phi_1 + i\phi_2}{\sqrt{2}} \\ \frac{\phi_3 + i\phi_4}{\sqrt{2}} \end{pmatrix} \tag{2.28}$$

The Higgs terms of Lagrangian which arise from the self-interactions of the scalar field is

$$\mathcal{L}_H = (D_\mu\phi)^\dagger(D_\mu\phi) + \mu^2\phi^\dagger\phi - \lambda(\phi^\dagger\phi)^2 \tag{2.29}$$

The potential $V(\phi)$ has a minimum at

$$|\phi^\dagger\phi| = \frac{\mu^2}{2\lambda} \equiv \frac{v}{\sqrt{2}} \tag{2.30}$$

Quantization must therefore start from a ground state, called the *vacuum*, which has a non-zero expectation value $v$. This phenomenon is called spontaneous symmetry breaking: the Lagrangian exhibits a symmetry, but the behavior of the system is determined by the fluctuation of the field around a ground state which does not have the full symmetry of the Lagrangian, and the observable physical system will have a broken symmetry, meaning that the full symmetry of the Lagrangian will not be manifest. One usually makes the particular choice of the vacuum, $\phi_0$, is

$$\phi_0 = \frac{v}{\sqrt{2}}, \tag{2.31}$$

which corresponds to setting $\phi_3 = v$ (the expectation of vacuum) and $\phi_1 = \phi_2 = \phi_4 = 0$ (expression in Equation 2.28). The coupling of the Higgs field with the gauge bosons is then given by the covariant derivative term in $\mathcal{L}_H$:

$$\phi^\dagger \left( ig_1 \frac{Y}{2} B_\mu + ig_2 \frac{\vec{\tau}}{2} \vec{W}_\mu \right)^\dagger \left( ig_1 \frac{Y}{2} B_\mu + ig_2 \frac{\vec{\tau}}{2} \vec{W}_\mu \right) \phi \tag{2.32}$$

Putting $Y = 1$ and $\phi = \phi_0$, writing the Pauli matrices explicitly and using the definition for $W^\pm_\mu$, $A_\mu$ and $Z_\mu$ gives, after some algebra, the following terms in the expression of the $\mathcal{L}_H$:

$$\frac{g_2^2 v^2}{8} \left( \left| W^+_\mu \right|^2 + \left| W^-_\mu \right|^2 \right) + \frac{g_2^2 v^2}{8 c_W^2} \left| Z_\mu \right|^2 . \tag{2.33}$$

Since the expected mass term for a charged boson is $\frac{1}{2}m^2\left|W_\mu\right|^2$, it can be seen that the $W$ acquired mass $M_W = \frac{vg_2}{2}$. For the neutral vector fields, the expected mass terms in the Lagrangian are $\frac{1}{2}M_Z^2 Z_\mu Z^\mu$ and $\frac{1}{2}M_\gamma A_\mu A^\mu$. Since there is no $A_\mu A^\mu$ term, we see that the photon remains massless, while $M_Z = \frac{vg_2}{2c_W}$. Therefore the SM predicts the mass ratio $\frac{M_W}{M_Z} = c_W$, which has been verified experimentally.

The fermions also acquire mass by interacting with the Higgs field. The Lagrangian term is given by

$$\mathcal{L}_{\text{Yukawa}} = -g_f\left(\overline{L}_f\phi R_f + \overline{R}_f\phi^\dagger L_f\right) \tag{2.34}$$

All fermions have similar terms. The coupling here $g_f$ is arbitrary and are called Yukawa coupling. Inserting the vacuum expression of $\phi$ into Equation 2.34, one can obtain the fermion mass as

$$m_f = \frac{vg_f}{\sqrt{2}}. \tag{2.35}$$

Finally, after introducing the Higgs mechanism, the gauge theory also predicts self-interactions of the Higgs field due to the non-Abelian nature of the symmetry. This leads to the existence of the massive scalar Higgs boson, the mass of which is a free parameter in the SM. The Higgs boson couples to particles proportional to their masses, and imports higher order correction to the cross section of certain processes. In 2012, the Higgs boson was announced being discovered by both the ATLAS and CMS collaboration at CERN, making it the final discovered fundamental particle predicted by the SM.

## 2.2 $W^+W^-$ Pair Production in the Standard Model

The $W^+W^-$ pair production is one of the most experimentally accessible di-boson production processes predicted by the SM at hadron colliers. At the LHC the major $W^+W^-$ production mechanisms are shown in Figure 2.2. The non-resonant continuum productions are through the processes in Figure 2.2(a)-2.2(d), while the production through the Higgs boson resonant production is shown in Figure 2.2(e). A sensitive test of the SM can be conducted by measuring the $W^+W^-$ production cross section and by probing the aTGCs of $WW\gamma$ and $WWZ$ (see $s$-channel diagram in Figure 2.2(a)). Study of $W^+W^-$ production is critical for the Higgs boson detection since the continuum $W^+W^-$ production is one of the major backgrounds for $H \to WW$ detection, and for search for new phenomena beyond the SM involving $W^+W^-$ decay mode. Experimentally, the leptonic decay channel provides very clear signals for $W^+W^-$ detection.

### 2.2.1 $W^+W^-$ Production and Triple-Gauge-Boson Couplings

The leading order (LO), or tree-level, Feynman diagrams for the $W^+W^-$ production are shown in Figure 2.2. The contributions of the continuum $W^+W^-$ productions come from initial states of quarks $q\bar{q}$ and gluons $gg$. The resonance $W^+W^-$ production comes from the Higgs decays, dominantly through the gluon-gluon fusion process as shown in Figure 2.2(e). At the next-to-the-leading order (NLO), there is also contribution from quark-gluon interaction $qg$. Furthermore, gluon-gluon induced processes shown in Figure 2.2(d) and 2.2(e) (for off-shell Higgs production) have large destructive interferences at large $W^+W^-$ mass range. The triple gauge-boson-vertices are shown in the $q\bar{q}$ process as in Figure 2.2(a). If only the $t$- and $u$-channel are included in the production cross-section calculations, each of them contributes a divergent term for the $W^+W^-$ cross section, which indicates that the cross section of each diagram will increase linearly with increasing $\sqrt{s}$, the center-of-mass energy of the interaction point. This implies that at sufficient high energy, the sum of the probabilities of the production modes will be greater than one (unitarity violation). By adding the $s$-channel process, which involves the triple-gauge-boson couplings, the cross terms (interference terms) resulting from the squaring of the sum of amplitudes deliberately cancel the divergence, bringing back the unitarity. Thus, any deviation from the $W^+W^-$ cross section predicted by the SM is very sensitive to the aTGCs.

Arise from the non-Abelian nature of the gauge structure of EW theory, the most general Lorentz-invariant effective Lagrangian describing the TGCs, without considering gauge invariance and $CP$ conservations, can be written as Equation 2.36 [7]:

$$\begin{aligned}\frac{\mathcal{L}_{WWV}}{g_{WWV}} =& ig_1^V(W^\dagger_{\mu\nu}W^\mu V^\nu - W^\dagger_\mu V_\nu W^{\mu\nu}) + i\kappa_V W^\dagger_\mu W_\nu V^{\mu\nu} \\ &+ \frac{i\lambda_V}{M_W^2} W^\dagger_{\lambda\mu}W^\mu_\nu V^{\nu\lambda} - g_4^V W^\dagger_\mu W_\nu(\partial^\mu V^\nu + \partial^\nu V^\mu) \\ &+ g_5^V \epsilon^{\mu\nu\rho\sigma}(W^\dagger_\mu(\partial_\rho W_\nu) - (\partial_\rho W^\dagger_\mu)W_\nu)V_\sigma \\ &+ \frac{1}{2} i\tilde{\kappa}_V \epsilon^{\mu\nu\rho\sigma}W^\dagger_\mu W_\nu V_{\rho\sigma} + \frac{1}{2M_W^2} i\tilde{\lambda}_V \epsilon^{\nu\lambda\rho\sigma} W^\dagger_{\lambda\mu} W^\mu_\nu V_{\rho\sigma},\end{aligned} \tag{2.36}$$

where $V \in (\gamma, Z)$, $W^\mu$ is the $W^\pm$ field, $W_{\mu\nu} = \partial_\mu W_\nu - \partial_\nu W_\mu$, $V_{\mu\nu} = \partial_\mu V_\nu - \partial_\nu V_\mu$, while the SM couplings are $g_{WW\gamma} = -e$ and $g_{WWZ} = -e\cot\theta_W$. In Equation 2.36, $g_4$ is odd under $CP$ and $C$ symmetry (violating $CP$), $\tilde{\kappa}_V$ and $\tilde{\lambda}_V$ are odd under $CP$ and $P$ (violating

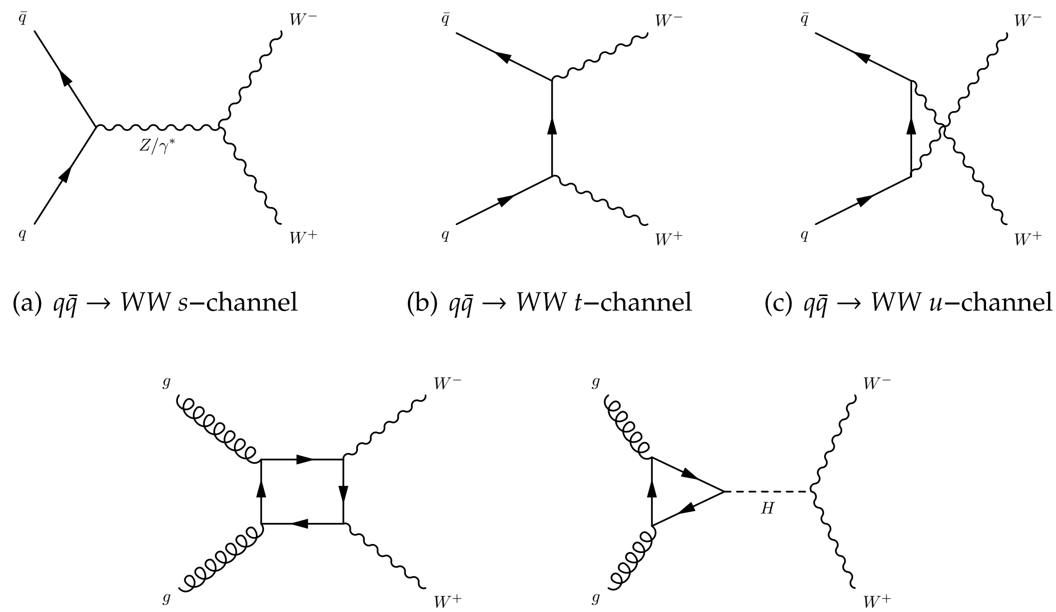


(a) $q\bar{q} \to WW$ $s-$channel (b) $q\bar{q} \to WW$ $t-$channel (c) $q\bar{q} \to WW$ $u-$channel

(d) $gg \to WW$ Continuum (e) $ggH \to WW$

Figure 2.2: LO Feynman diagrams for $W^+W^-$ pair production at the LHC. Three different sources dominantly contributed to this process: quark-antiquark pair ($qq$), gluon-gluon continuum ($gg$), and gluon fusion produced Higgs decay ($ggH$).

$CP$), $g_5$ is odd under $C$ and $P$ (violating $C$ and $P$ but conserving $CP$), while $g_1^V$, $\kappa_V$ and $\lambda_V$ are $C$ and $P$ conserving. In the SM, $g_1^V = \kappa_V = 1$, and all other triple-gauge-boson couplings are zero. Thus the Lagrangian in Equation 2.36 is reduced to the SM Lagrangian shown in Equation 2.37:

$$\begin{aligned} \mathcal{L}_{\text{SM}} = &- ie(W_{\mu\nu}^{\dagger} W^{\mu} A^{\nu} - W_{\mu}^{\dagger} A_{\nu} W^{\mu\nu} + W_{\mu}^{\dagger} W_{\nu} A^{\mu\nu}) \\ &- ie \cot\theta_W (W_{\mu\nu}^{\dagger} W^{\mu} Z^{\nu} - W_{\mu}^{\dagger} Z_{\nu} W^{\mu\nu} + W_{\mu}^{\dagger} W_{\nu} Z^{\mu\nu}), \end{aligned} \tag{2.37}$$

where $A_\mu$ is the photon field and $Z_\mu$ is the $Z$ field.

The SM fixed the TGCs values; any deviation from those values will change the production cross section of the process $qq \to Z/\gamma^* \to WW$. Such modification due to aTGCs would be more significant in high mass region. As the center-of-mass energy grows, the anomalous coupling $\kappa_V$ terms will cause the $W^+W^-$ cross section to increase proportionally to $\sqrt{s}$, while the $\lambda_V$ and $g_1^V$ terms will increase as $s$ [8]. Therefore, if introduced alone, any finite anomalous coupling constant will cause an nonphysical large cross section as $\sqrt{s}$ grows, eventually violating unitarity. The unitarity requires aTGCs must be introduced with a form factor so that the coupling constant will go to zero as $\sqrt{s}$ increases [9], therefore the aTGCs are rewritten as:

$$A(s) = \frac{A_0}{\left(1 + \frac{s}{\Lambda^2}\right)^2} \tag{2.38}$$

where $A_0$ is aTGCs constant, and $\Lambda$ is the form factor, which is related to but not necessarily identical to the regularization scale at which new physics becomes not negligible in the EW sector, meaning new physical cause must be introduced to maintain the unitarity at that energy scale. Although the choice of $\Lambda$ is arbitrary in the EFT, the most reasonable and sensible one to test, is the energy scale of the experiment, which is $\sim 8\ TeV$ at the LHC (Run I).

Theoretically it is difficult to calculate the analytical $W^+W^-$ cross section due to the composite nature of the protons. A MC approach is used to solve this problem. Event generators (MC programs) are used to calculate numerical results for the $W^+W^-$ production. Chapter 4 will provide details about MC generators, parton showerers, and detector simulators. The theoretical predictions for the cross sections of the $W^+W^-$ production as well as backgrounds from non-$WW$ processes are presented in Chapter 6.

### 2.2.2 Experimental Signature of $W^+W^-$ Production

The $W^+W^-$ has three distinctive decay channels:

1. both $W$'s decay hadronically (fully hadronic)
2. one $W$ decays hadronically and the other $W$ decays leptonically (semi-leptonic)
3. both $W$'s decay leptonically (fully leptonic)

The fully hadronic decay channel, $WW \rightarrow q\bar{q}q\bar{q}$, produces four energetic jets as the final state, possessing the largest branching ratio (BR) among all decay modes. However, this advantage is far out-weighed by the disadvantages. First of all, the determination of the primary vertices where the jets are from is very difficult due to the finite energy resolution of the hadronic calorimeter (HCAL) and inherent difficulty of charge sign determination of jets. Secondly, the limited jet energy resolution also makes it hard to distinguish jets from $W$ decays and jets from $Z$ decays, due to the close masses of the two bosons, leading to the $WW \rightarrow jjjj$ process inseparable from the processes of $WZ \rightarrow jjjj$ and $ZZ \rightarrow jjjj$. Finally, large backgrounds from QCD *multijet* production as well as single $W$ or $Z$ productions makes it impractical to select the signal jets of $W^+W^-$ production

The semi-leptonic decay channel, $WW \rightarrow \ell\nu q\bar{q}$, has the second largest BR, where $\ell \in (e, \mu)$ and $q(\bar{q})$ produces a jet. As in the fully hadronic channel, it is impossible to distinguish $WW \rightarrow \ell\nu jj$ from $WZ \rightarrow \ell\nu jj$. The backgrounds are still very high, contributing from QCD *multijet* production and single $W$ production associate with jets ($W$+*jets*).

The fully leptonic decay channel, $WW \rightarrow \ell\nu\ell\nu$, has the smallest BR, with $BR(W \rightarrow \ell\nu) = 0.108$ for each $W$. The $\ell \in (e, \mu)$, excluding $\tau$ due to its short life time as well as many modes decaying into hadrons which requires different techniques for its identification. However, the final state $\ell$'s will include $e$'s and $\mu$'s from the process of $\tau \rightarrow \nu_\tau W \rightarrow \nu_\tau \ell \nu_\ell$ for $\ell \in (e, \mu)$. The $\tau$ contributions are corrected by MC simulations in cross section measurement. The advantage of using the fully leptonic decay channel in this measurement is it's unique clean signature of the $W^+W^-$ signals: two energetic leptons with high transverse momentum ($p_T$) plus large transverse missing energy ($\not{E}_T$) (due to neutrinos) in the final state. Most of the backgrounds come from instrumental misidentification of leptons, and badly reconstructed large $\not{E}_T$ due to *pile-up* (multiple interactions in the same beam bunch crossing), which will be detailed in Chapter 8.

In conclusion, the purely leptonic decay channels have the most separable signals from the background, providing the most sensitive measurement of the $W^+W^-$ production as well as the probing of aTGCs. This thesis will focus the data analysis to the purely leptonic final states in the measurements of $W^+W^-$ production.

**CHAPTER 3**

# The ATLAS Experiment at LHC

The ATLAS collaboration, which consists of 2,800 scientists, has designed, built, maintained, and operated the ATLAS detector located at Geneva under the administration of CERN. The ATLAS detector is a general-purpose particle detector for broad physics studies of head-on collisions of very high energy, very high rate proton beams provided by the LHC, the ever largest man-made machine. A brief description of the LHC is provided in Section 3.1. Section 3.2 describes the ATLAS detector in details. Finally, Section 3.3 summarizes the computing structure of the experiment.

## 3.1 The Large Hadron Collider

The Large Hadron Collider (LHC) is the world's largest and most powerful particle accelerator. It consists of a 27 $km$ ring of superconducting magnets installed in a tunnel with mean depth of 100 $m$ beneath the French-Swiss boarder between Geneva Lake and Jura Mountains, which was previously occupied by the Large Electron-Position Collider (LEP). It accelerates beams of protons or lead ions and collides them within four detectors which are located at different sites along the LHC tunnel: A Toroidal LHC Apparatus (ATLAS), Compact Muon Solenoid (CMS), Large Hadron Collider beauty (LHCb), and A Large Ion Collider Experiment (ALICE). The design CM collision energy is 14 $TeV$, while it operated at 7 $TeV$ and 8 $TeV$ during Run I and will raise the collision energy to 13 $TeV$ at the early stage of Run II starting in 2015.

As shown in Figure 3.1, all LHC colliding protons started from a standard bottle of hydrogen gas. With orbital electrons of the hydrogen atoms being stripped by a strong electric field, the left over protons are injected into the Proton Synchrotron Booster (PSB) from Linear Accelerator 2 (LINAC2) at an energy of 50 $MeV$. The beam is boosted to 1.4 $GeV$ then fed to Proton Synchrotron (PS) where it is accelerated to 25 $GeV$. Then the beam is sent to the Super Proton Synchrotron (SPS) where it is accelerated to 450 $GeV$. Finally, the protons are injected in both clockwise and anticlockwise direction into the LHC, where they are accelerated to the designed energy. Beams circulate in the LHC ring for hours (a typical run lasts for about 10 hours) during normal operating conditions.

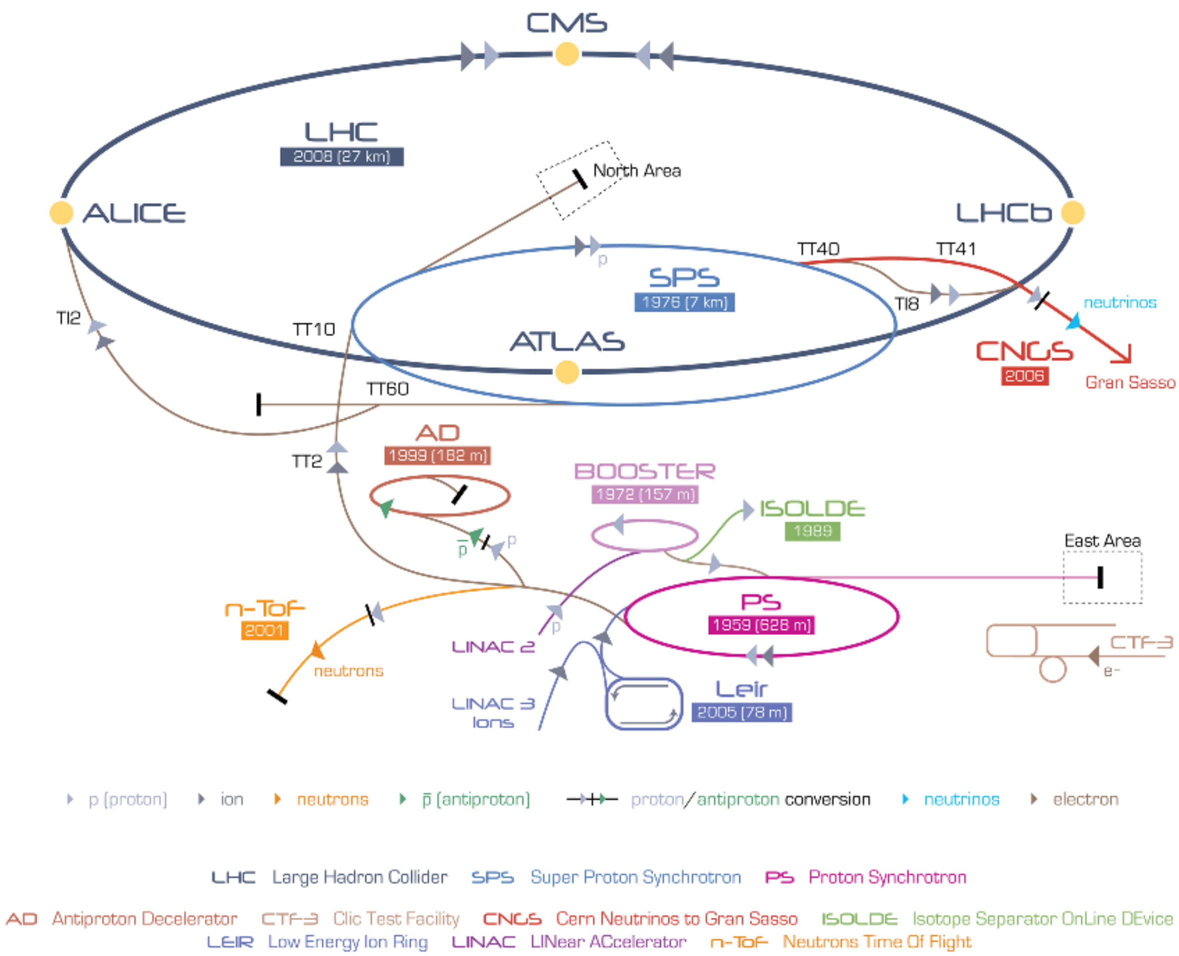


Figure 3.1: The LHC accelerator complex at CERN. The successive accelerators are: LINAC2, PSB, PS, SPS, and finally the LHC. The 4 main LHC detectors are also shown.

Collision energy is one figure of merits for colliders, and instant luminosity is the other one. To accumulate sufficient number of events to analyze rare processes with small cross sections, the detectors must record a large integrated luminosity. The relation between expected number of events and process cross section is

$$N = \sigma \int \dot{\mathcal{L}} dt \tag{3.1}$$

where $\sigma$ is the cross section of a process and $\dot{\mathcal{L}} = d\mathcal{L}/dt$ is the instant luminosity. $\dot{\mathcal{L}}$ depends only on beam parameters and can be expressed as:

$$\dot{\mathcal{L}} = \frac{N_b^2 n_b f_{\text{rev}} \gamma_r}{4\pi\epsilon_n\beta^*} F = \frac{N_b^2 n_b f_{\text{rev}} \gamma_r}{4\pi\Sigma_x\Sigma_y} F \tag{3.2}$$

where $N_b$ is the number of particles per bunch, $n_b$ is the number of bunches per beam, $f_{\text{rev}}$ is the revolution frequency, $\gamma_r$ is the relativistic $\gamma$ factor of the beam, $\epsilon_n$ is the normalized transverse beam emittance, $\beta^*$ is the beta function at the collision point, $\Sigma_{x,y}$ are the beam size in $x$- and $y$-directions, and $F$ is the geometric luminosity reduction factor due to the crossing angle at the IP. The LHC is designed to hold $n_b = 2808$ which corresponding to 25 $ns$ bunch spacing, $N_b = 1.15 \times 10^{11}$, $f_{\text{rev}} = 11.25\ kHz$, $\Sigma_{x,y} = 16.7\ \mu m$. All these figures yield to the design luminosity of $\dot{\mathcal{L}} \approx 10^{34}\ cm^{-2}s^{-1}$ [10], which means almost $10^9$ collisions per second.

The high instant luminosity comes with a trade-off: a large number of additional interactions, known as *pile-up*. While only interesting events will trigger detector readout, *pile-up* events, most of them uninteresting, are recorded simultaneously as well, obscuring interesting physics and degrading detector performance. Large $N_b$ will cause the interactions per bunch crossing increased, known as *in-time pile-up*. Large $n_b$ may cause the bunch spacing shorter than the detector latency, resulting to interactions from other bunch crossings interfering with current measurement, known as *out-of-time pile-up*. Small $\Sigma_{x,y}$ will increase both types of *pile-up*. At the LHC, the number of inelastic $pp$ collision per bunch crossing follows a Poisson distribution, with a mean value $\langle\mu\rangle$ calculated as

$$\langle\mu\rangle = \frac{\mathcal{L} \times \sigma_{\text{inelastic}}}{n_b \times f_{\text{rev}}} \tag{3.3}$$

where $\sigma_{\text{inelastic}} = 71.5(73.0)\ mb$ at $\sqrt{s} = 7(8)\ TeV$. Thus, $\langle\mu\rangle$ can be used as a gauge to describe the gravity of *pile-up*. Since the data used in this analysis were accumulated with 50 $ns$ bunch spacing, besides in-time *pile-up*, out-of-time *pile-up* plays an important role as well, to which the $\langle\mu\rangle$ is more sensitive.

The data-taking during Run I of LHC was incredibly successful. Important parameters of $pp$ data sets are summarized in Table 3.1 [11] and Figure 3.2. The majority of data was obtained in the year of 2012, however it came with the expense of higher *pile-up*, which brings huge challenge for data analysis using 2012 data.

| | 2010 | 2011 | 2012 | Design |
|---|---|---|---|---|
| CM Energy ($TeV$) | 7 | 7 | 8 | 14 |
| Minimum bunch spacing ($ns$) | 150 | 50 | 50 | 25 |
| Peak luminosity ($10^{34}cm^{-2}s^{-1}$) | 0.2 | 3.5 | 7.7 | 10 |
| Delivered luminosity ($fb^{-1}$) | 0.047 | 5.46 | 22.8 | - |
| Recorded luminosity ($fb^{-1}$) | 0.044 | 5.08 | 21.3 | - |
| Good for physics ($fb^{-1}$) | 0.021 | 4.57 | 20.3 | - |
| Luminosity uncertainty ($\delta\mathcal{L}/\mathcal{L}$) | 3.5% | 1.8% | 2.8% | - |

Table 3.1: Summary of *pp* collision data during LHC Run I. Luminosities use the offline calibration. [12]

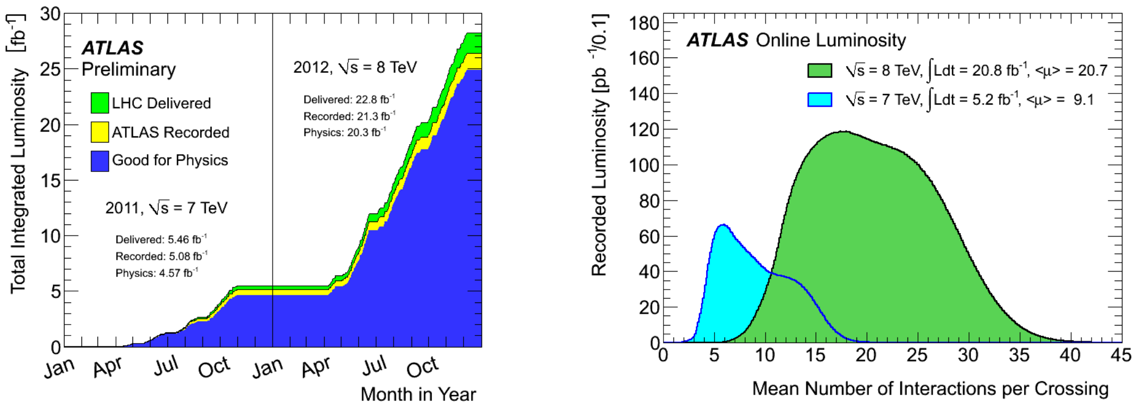


(a) Cumulative Luminosity (b) Pile-up

Figure 3.2: Cumulative luminosity and $\langle\mu\rangle$ for the 2011 and 2012 data sets. (a) The luminosity of 7 TeV data and 8 TeV data are calibrated offline. (b) The luminosity of 7 TeV data and 8 TeV data are calibrated online

## 3.2 The ATLAS Detector

As mentioned above, the ATLAS detector was designed as a general-purpose apparatus. It provides sensitive detection of many kinds of signatures (signals indicating interesting physics), which is very important in the harsh collision environment of the LHC. Such objective brings stringent requirement for the detector to be robust and redundant, with the ability of internal consistency and probing sensitivity.

Experimental signatures consist of particles as decay products, as well as their kinematical and geometrical properties. Such information allows reconstruction of collision events, e.g. the production of Higgs bosons. Final state particles, either stable or decaying in a known way, includes photons ($\gamma$), electrons ($e$), muons ($\mu$), tau's ($\tau$),

$W^{\pm}$ and $Z^0$ bosons, and jets($j$). Neutrinos ($\nu$), as neutral weakly interacting leptons, leave no direct trace in the detector, which makes the conservation of momentum in the transverse plane (the plane perpendicular to the beam axis) appears to be broken. This missing counterpart of transverse momentum is referred to be the "missing transverse energy" ($\not{E}_T$ ). All those signature particles are also called "physical objects" in event reconstruction.

Therefore, to achieve the physics probing objectives, the detector design criteria could be summarized as follows:

- Powerful magnets and efficient charged particle tracking system in high luminosity environment for momentum measurements of high transverse momentum ($p_T$) leptons, electron and photon identification, $\tau$-lepton and heavy flavor identification; and full event reconstruction capability in low luminosity environment.

- Large coverage in geometry, i.e. in pseudorapidity ($\eta$) and in azimuthal angle ($\phi$). $\phi$ is measured around the beam axis, while $\eta$ is defined to be $\eta = -\ln\left(\tan\frac{\theta}{2}\right)$ where $\theta$ is the polar angle from the $z$-direction.

- Excellent EM calorimeter (ECAL) for electron and photon identification and full-coverage HCAL for accurate jet and $\not{E}_T$ measurements.

- High-precision MS for accurate measurements of $\mu$ momenta at high rates;

- Efficient triggering system to record interesting physics events at low energy threshold while persist efficiency at high *pile-up*.

The overall detector layout is shown in Figure 3.3. From the IP which is located at the center of the detector, all subsystems of the detector are indicated.

The following subsections will describe each subsystem with details.

### 3.2.1 Magnet System

The magnet subsystem has two components: one thin superconducting solenoid surrounding the inner tracker cavity; and one eight-fold air-core superconducting toroids consisting of independent coils enclosing the calorimeters with symmetry. The solenoid generates an axial magnetic field for the ID, while the toroids, with a long barrel and two inserted end-cap components, provide a large magnetic field in an open structure for the MS. This configuration of magnet system is unique in the

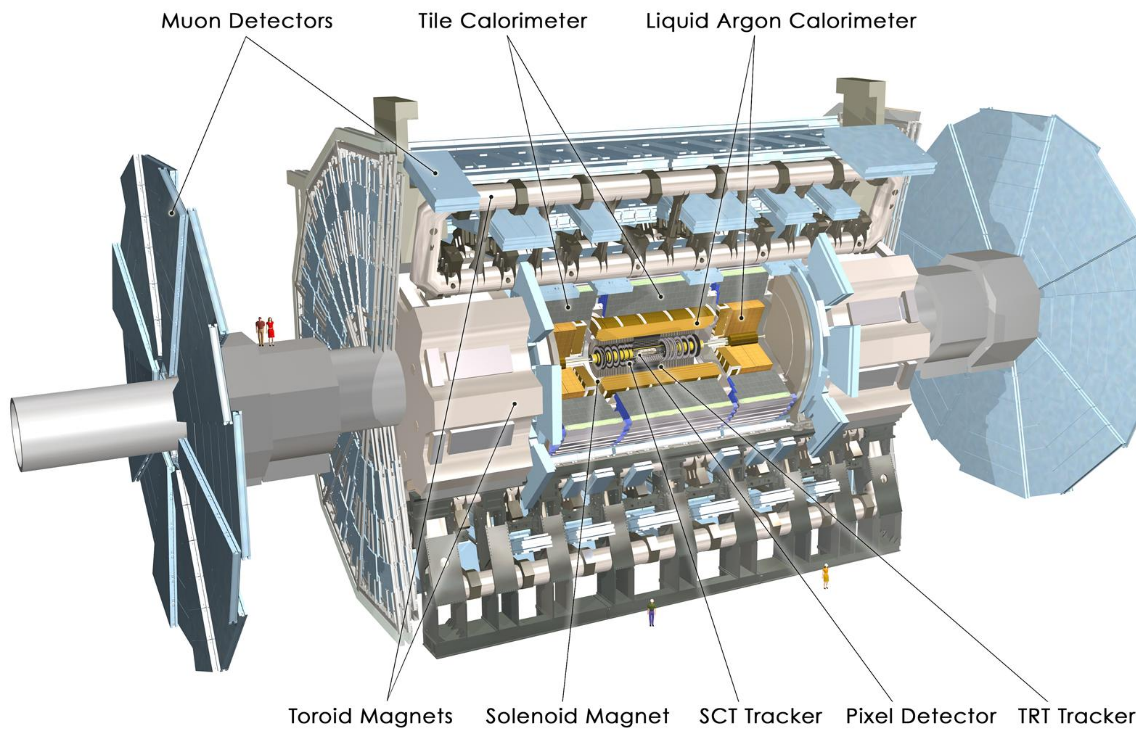


Figure 3.3: A longitudinal cut-away view of the ATLAS detector. The IP is at the center of the detector. Different layers of subsystems around the beam line are shown.

history of large particle detectors. The longitudinal dimension of the magnet system is 26 $m$ and the transverse dimension is 20 $m$ [13].

In terms of the bending power, the central solenoid (CS) provides a central longitudinal field of 2 $T$ with a peak field of 2.6 $T$ [13]. To cope with the fact that the CS is in between the inner tracker and the calorimeters which might degrade the calorimeter performance, the CS and ECAL share one common vacuum vessel of cryostat, therefore minimizing the materials in between.

The barrel toroid (BT) and the two endcap toroids (ECTs) has peak fields of 3.9 $T$ and 4.1 $T$ [13], respectively. The ECT coils are rotated by 22.5° [13] with respect to the BT in order to obtain radial overlap (see Figure 3.3). All toroids are connected in series electrically, and equipped with control systems for fast and slow energy dumps. To safely dissipate the stored energy (1.6 $GJ$ total energy [13]) without overheating the coils, a quench protection system has been designed and installed.

### 3.2.2 Tracking Detectors

The inner tracker system, or the inner detector (ID), provides pattern recognition, momentum measurements and electron-photon identification. The very high energy of the LHC comes with a very tough challenge: the track density near the IP sets a record. Therefore, fine granularity tracker components are demanded for high resolution vertex finding and momentum measurements. Pixel and silicon-microstrip tracker (SCT) semiconductor detectors provide such features. Restricted by materials and high cost, the total layers of semiconductors are limited, thereby a third straw-tub tracking detector named transition radiation tracker (TRT) with much less material per point and lower cost is integrated to the inner tracker system to provide additional track-following capability and enhanced electron-photon identification ability due to their transition radiation through the Xenon-based gas straw tubes.

The layout of the tracking detector is shown in Figure 3.4. Mechanically, the inner tracker system has three units: a barrel part extending over ±80 *cm* of IP [13] which is concentric cylinder arrangement, and two identical end-caps covering the rest of the cylindrical detector which are mounted on disks perpendicular to the beam axis. Typically, a charged particle will cross 3 layers of pixel and 8 layers of SCT, followed by about 36 tracking points of TRT [13]. The innermost layer of pixels, at a radius of about 4 *cm* [13] which is practical to the beam pipe, enhances the measurement of secondary vertices. This layer is referred to be the *B-Layer*.

### 3.2.3 Calorimeters

The ATLAS calorimeters, as shown in Figure 3.5, have three subsystems: a high granular sampling EM calorimeter (ECAL) covering the range of $|\eta| < 3.2$, a hadronic calorimeter (HCAL) covering $|\eta| < 1.7$ for the barrel part and $1.5 < |\eta| < 3.2$ for the end-caps, and a forward calorimeter (FCAL) covering $3.1 < |\eta| < 4.9$ [13]. The calorimetry system provides very good measurements of jets and $\not{E}_T$. The ECAL is a sampling calorimeter using lead plate as absorber (typically 2 *mm* thick) and filling liquid-argon between the gaps of absorbers (2.1 *mm*) as sampling layers, with readout electrodes in the middle [13]. The lead plates are shaped in an accordion geometry, covering full azimuthal angles without dead region and providing fast signal response as well. The barrel ECAL has 3 layers with different granularity as shown in Figure 3.7. The LAr technology demands cryogenic installations, with the operating temperature to be 87 *K* [13]. As mentioned in Section 3.2.1, the solenoid which supplies the 2 *T* magnetic field to the tracker is integrated into the vacuum

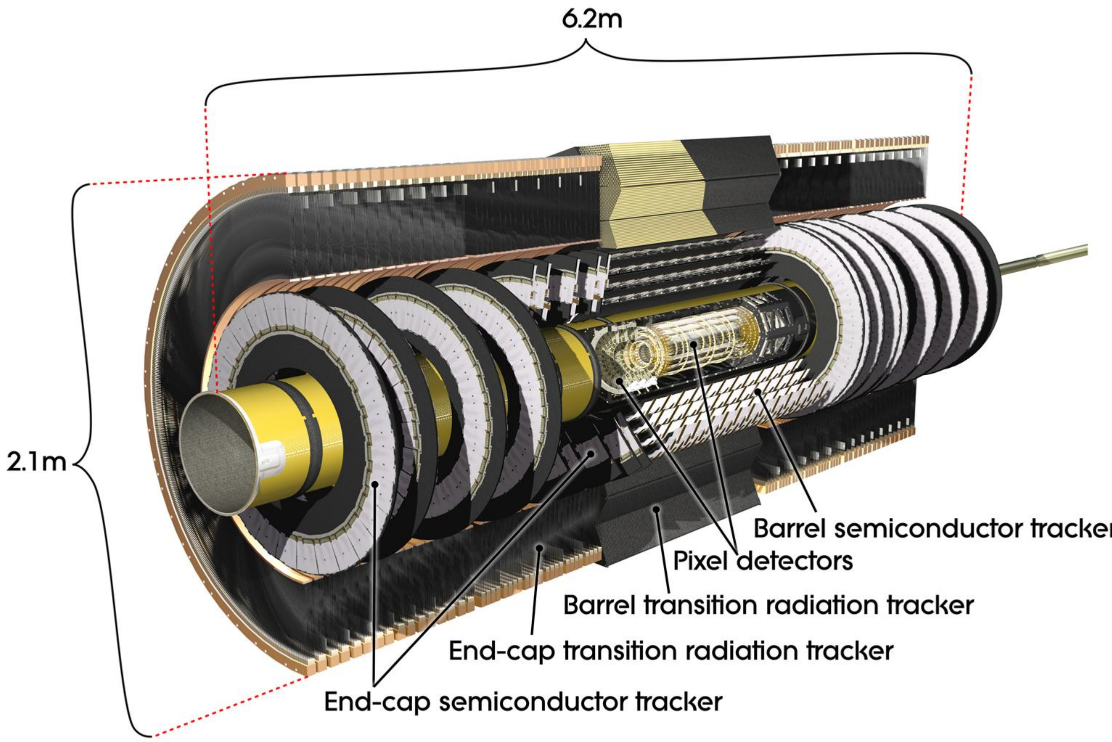


Figure 3.4: A longitudinal cut-away view of the ATLAS tracking system. The IP is at the center of the detector. Outwards from the beam pipe, pixel detectors, SCT and TRT are indicated. The barrel part and two end-caps are clearly shown as well.

vessel of the barrel ECAL cryostat to eliminate two vacuum walls. The solenoid is placed in front of the ECAL. A pre-sampler detector is installed right behind the cryostat cold wall, and is used to correct for the energy loss in the materials.

The HCAL also uses sampling technique, with iron tiles as absorber and plastic scintillator tiles embedded in between as sampler. The tiles are placed radially and staggered in depth, repeated periodically along the beam line. Wavelength shifting fibers are installed on both sides of the scintillating tiles for read out into two separate photomultiplier tubes (PMTs). The barrel and extended barrel HCAL serves as the support for the ECAL cryostats as well as the main solenoid flux return. At large $\eta$, the end-cap HCAL uses LAr technology as well by virtue of its intrinsically radiation-hard characteristics. It uses copper as absorber and is shaped into parallel-plate geometry.

The FCAL covers a range of merely $\theta \leqslant 0.85°$ [13], thus using the LAr technology as well for facing the same high radiation as the end-cap HCAL during operation. It fills LAr into a tungsten matrix with rod-shaped electrodes.

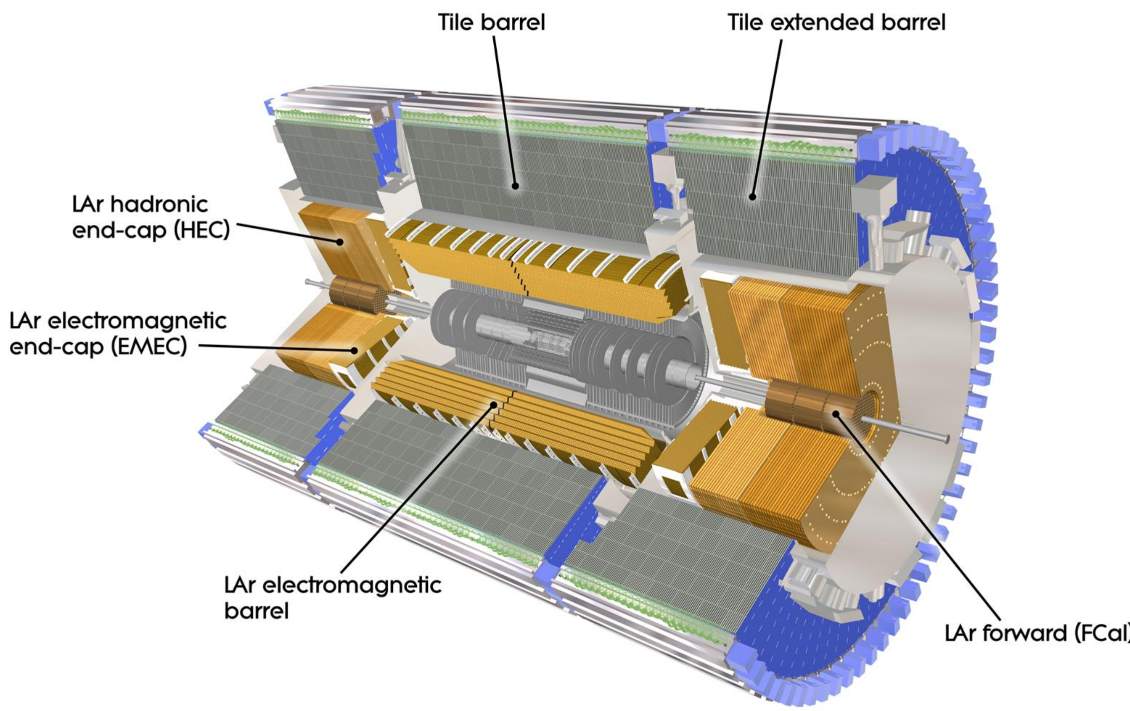


Figure 3.5: A longitudinal cut-away view of the ATLAS calorimeters. The smaller radial regions (2.25 $m$ radius, ±6.65 $m$ length) is the lead/LAr ECAL, and the outer (4.25 $m$ outer radius, ±6.10 $m$ length) is the scintillator-tile HCAL [13]. The FCAL use LAr technology as well. The whole calorimetry is divided into three sections: a barrel and two end-caps. The end-caps can be moved along the beam pipe to create access space for the barrel region maintenance.

The end-cap cryostats integrate the EM end-cap calorimeter (EMEC), HCAL and FCAL into one single piece, each of which is the heaviest single piece of parts of the ATLAS detector.

### 3.2.4 Muon Spectrometer

The muon spectrometer (MS) is the largest sub-detector of the ATLAS detector after complete assemble thus defines the overall dimension of the whole detector. The layout, Figure 3.6, shows its dimension and components.

The instrumentation of the MS is based on the measurements of $\mu$ tracks in the toroidal magnetic field which is almost orthogonal to the trajectories with minimized multiple scattering in materials. The anticipated high flux of particles impacted

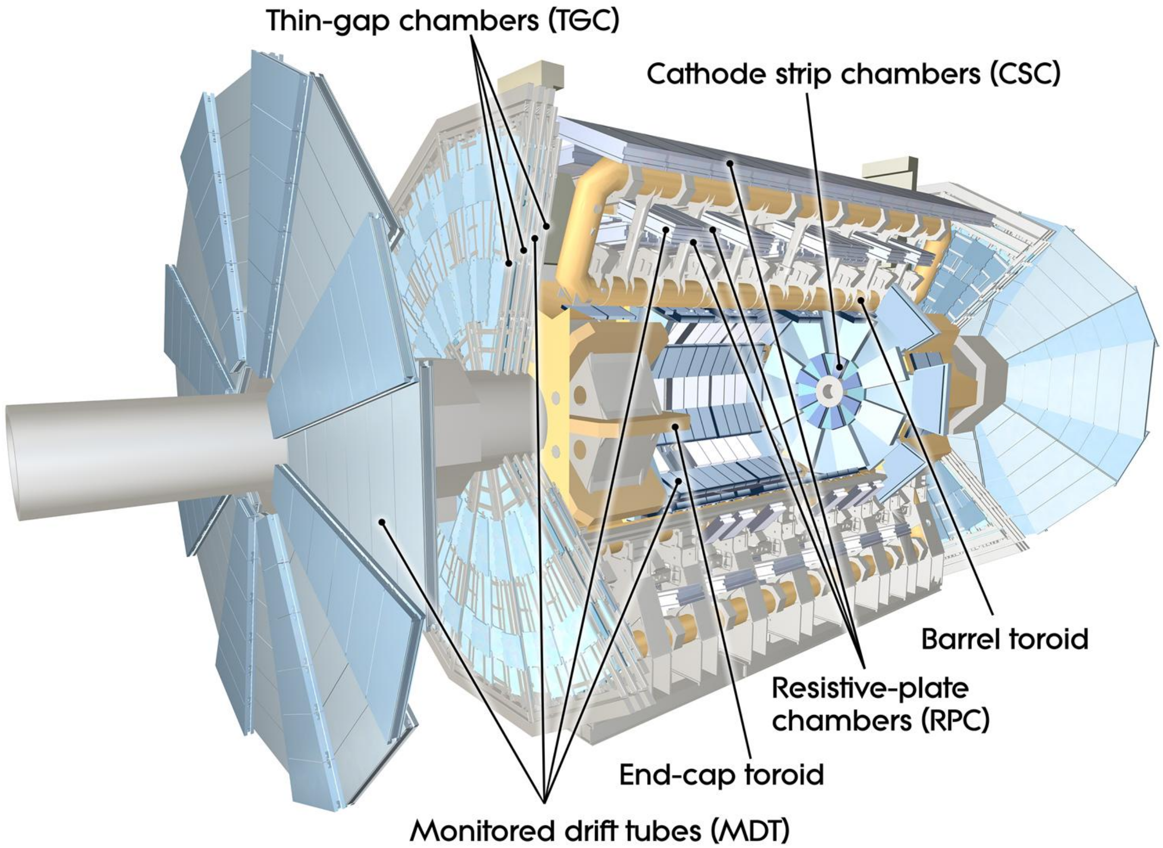


Figure 3.6: A longitudinal cut-away view of the ATLAS muon spectrometer. Three stations of chambers are installed concentrically in the barrel region, and three stations of chambers are installed vertically in the end-cap region. Precision chambers cover almost all $\eta$ region, while triggering chambers only provide $\eta$ coverage up to 2.4. The outer wheel is 23 $m$ distant from the IP and has a diameter of 25 $m$, mounted on the detector cavern wall [13].

on the design, affecting performance parameters such as rate capacity, granularity, ageing properties and radiation hardness. The MS uses gas chambers categorized in two groups, the fast triggering chambers and precision measurement chambers, and optimizes the triggering algorithm to cope with the difficult background conditions resulting from penetrating hadrons from the calorimeters.

The muon drift tubes (MDTs) are used as precision measurement chambers, covering the $\eta$ range up to 2.7. They provide a single-wire resolution of $\sim 80\ \mu m$ when operated at designed gas pressure (3 bar). Closed to the beam axis and near the IP, cathode strip chambers (CSCs) with high granularity are used, which withstand the demanding radiation environment. For triggering chambers, resistive plate chambers

(RPCs) are used in the barrel region and thin gap chambers (TGCs) are used in the end-cap regions, covering a range of $|\eta| < 2.4$ for muon triggers [13].

The geometrical configuration in the barrel region is three concentric cylindrical layers ("stations") of triggering and precision chambers around the beam line, while in the end-cap region three stations of parallel chambers are installed vertically as seen in Figure 3.6, referred to be the small wheel, the big wheel and the outer wheel, respectively. The precision measurement of muon tracks is made in the $R - z$ plane, where $R$ is the radial coordinate defined to be $R = \sqrt{\eta^2 + \phi^2}$. The $z$ is measured in the barrel and the $R$ is measured in the transition and end-cap regions.

Finally, to achieve the stringent requirements of chamber position accuracy and the survey of the precision chambers, optical (laser) alignment systems are designed and integrated inside the muon spectrometer. The alignment system calibrates the chamber position and provide knowledge of accuracy to be 40 $\mu m$.

### 3.2.5 Trigger System

The ATLAS detector receives large volumes of data within nanosecond timescales. At LHC designed intensities, $10^9$ events occur in every second within the ATLAS detector but only one Higgs boson is produced in every 10 seconds. Therefore, a trigger system is designed to quickly and efficiently select interesting events and to reject large numbers of uninteresting events. There are three successive stages in the system called as: level-1 (LV1), level-2 (LV2) and the event filter (EF) triggers.

The LV1 trigger reduces the event rate from 40 $MHz$ to 75 $kHz$ (upgradable to 100 $kHz$) within 2.5 $\mu s$ [13] by finding energetic objects (leptons, photons, and jets) with specialized hardware. It consists of two systems: the LV1 calorimeter trigger and the LV1 muon trigger. The LV1 calorimeter trigger receives reduced granular analog signals from the ECAL and HCAL to search for expected patterns of electrons, photons, $\tau$'s and jets as well as to calculates the $\not{E}_T$. The LV1 muon trigger finds muon tracks by measuring hits in one station then search for additional hits in nearby stations along pre-determined patterns. The LV1 system find interesting objects and identify a region of interest (RoI). The number of identified objects above different energy thresholds is sent to the central trigger processer to determine if a sufficient number of energetic objects has been found in the current event. If the event passes 1 of the 128 different central trigger criteria, a so-called LV1 accept is sent back to the detector. In parallel with the working LV1 triggers, the analog signals from the interesting particles are processed by the front-end (FE) electronics for all the sub-detectors before digitized (as digital form) and stored (as analog form) in the so-called LV1 buffer. Once the LV1 accept arrives, the FE electronics will send the data from the LV1 buffer to the readout drivers (RODs) for further processing; otherwise, the data is removed from the LV1 buffer. Unlike FE electronics, RODs is located in a room outside of the detector hall shielded from radiation.

The LV2 trigger reduces the event rate from 75 $kHz$ to 3.5 $kHz$ within 10 $\mu s$ by running more complex object identification algorithms with commercial computers. It only uses information within RoIs specified by LV1, from the ID, the MS and full granular information of calorimeters. Once the event passes 1 of the 256 different LV2 event criteria, the data in RODs is sent to EF for final selection with commercial computers. There, the event rate is further reduced to 200 ~ 300 $Hz$ within 1 $s$. If the event is selected by the EF, the data is transferred to permanent storage at the CERN computing center; otherwise, it is deleted from the RODs.

For this analysis, the $W^+W^- \to \ell^+\nu_\ell\ell^-\bar{\nu}_\ell$ events are selected online by di-lepton ($e$ or $\mu$) or single-lepton triggers.

A summary of ATLAS electron triggers can be found in Reference [14]. Electron LV1 trigger (L1) uses reduced granularity signals covering $\Delta\eta \times \Delta\phi \sim 0.1 \times 0.1$ from calorimeters, named trigger towers, to identify the RoIs positions and compute their $E_T$, which is shown in Figure 3.7. For each trigger tower, the cells of the ECAL and HCAL are summed. At LV2 trigger (L2), the $e/\gamma$ calorimeter algorithms build cell clusters within the RoI identified by the L1 and obtain final cluster positions. At the EF, offline-like algorithms are used for the reconstruction of calorimeter quantities and apply all the offline based corrections.

A summary of ATLAS muon triggers can be found in Reference [15]. Muon L1 uses the spatial and temporal coincidence of hits in the RPC or TGC to identify RoIs and estimate the $p_T$ of the muons within RoIs. The L2 refines $p_T$ measurements of the muon candidates. The muon EF uses offline and full event information to confirm or discard the L2 candidates, by two complementary methods: the *RoI-based method* focusing on the RoIs defined by L1 and L2, and the *full-scan method* searches the full detector without using RoIs.

All the trigger menus for electrons and muons can be found in [16] and [15] for 2012 run, respectively. For this analysis, events are required to be triggered by di-lepton triggers in the $ee$ and $\mu\mu$ channels and by either di- or single-lepton triggers in the $e\mu/\mu e$ channels, as shown in Table 3.2.

Typically, the $E_T$ threshold for di-electron trigger is 12 $GeV$; and for di-muon trigger, it is combined with one muon with $p_T > 18\,GeV$, and the other with $p_T > 8\,GeV$.

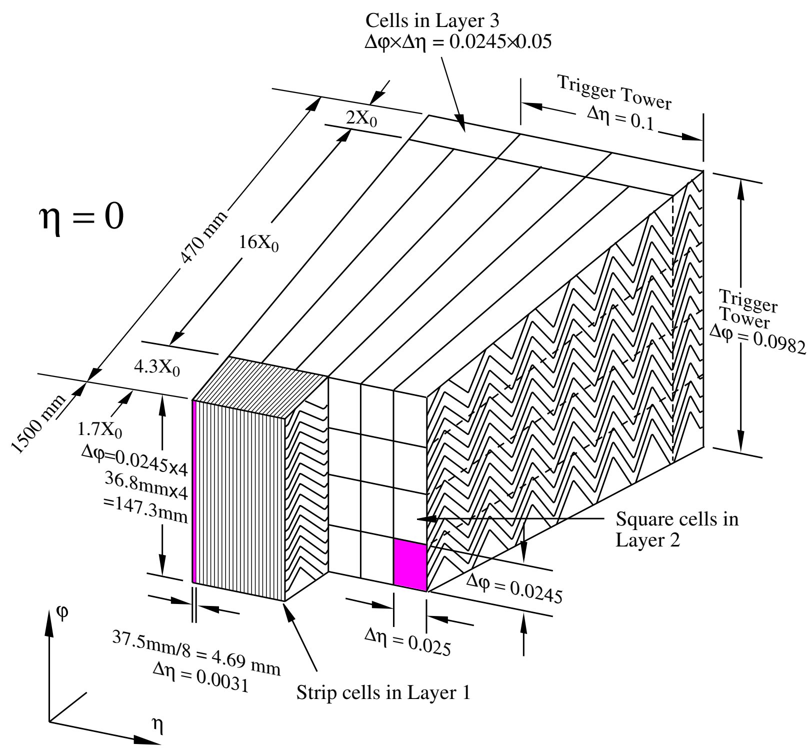


Figure 3.7: Sketch of a barrel ECAL module with visible different layers [13]. The granularity in $\eta$ and $\phi$ of the cells of each of the three layers and of the trigger towers is also shown.

| | $ee$ | $\mu\mu$ | $e\mu$ |
|---|---|---|---|
| Single-lepton | - | - | **EF_e24vhi_medium1**<br>**EF_e60_medium1**<br>**EF_mu24i_tight**<br>**EF_mu36_tight** |
| Di-lepton | **EF_2e12Tvh_loose1**<br>**EF_2e12Tvh_loose1_L2StarB** | **EF_mu18_tight_mu8_EFFS** | **EF_e12Tvh_medium1_mu8** |

Table 3.2: List of triggers used in the $W^+W^-$ analysis.In the $e\mu$ channel any of the single-lepton triggers or the combined $e\mu$ trigger is used.In the same-flavour channels only a single di-lepton trigger is used.

For single electron and muon triggers, the $p_T$ threshold are 24 $GeV$.

For the $ee$ channel, the typical efficiency for either leg to trigger an electron with $p_T > 25$ $GeV$ is > 98(95)% in the barrel(end-cap) region. In contrast, to reach comparable efficiencies, the single-electron triggers have to trigger electrons with $p_T > 60$ $GeV$ [17]. Below that $p_T$ threshold the single-electron trigger exhibits a turn-on starting at 25 $GeV$ with an efficiency of > 90(80)% in the barrel(end-cap) region, which results in a significant loss of events where the sub-leading lepton lies at $20 < p_T < 25$ $GeV$ (Figure 3.8).

For the $\mu\mu$ channel, the efficiency for the leading leg ($p_T > 18$ $GeV$) is $60 - 90(80 - 95)\%$ for barrel(end-cap); and for the other leg it is $> 98(95)\%$ in barrel(end-cap) region. A similar turn-on starting at 25 $GeV$ is observed for single-muon triggers as well (Figure 3.8).

For the $e\mu$ channel, the combined trigger di-lepton trigger ($p_T^e > 12$ $GeV$ and $p_T^\mu > 8$ $GeV$) is used, but is only $\sim 80\%$ efficient for an $e\mu$ event. Hence, a strategy of adding single-lepton triggers to makes sure a higher efficiency (according to Equation 3.5) is chosen for the $e\mu$ channels. Events passing the single-lepton triggers are also allowed. The combination of single- and di-lepton triggers gives higher event yields for leading leptons of $25 < p_T < 60$ $GeV$. As shown in Figure 3.9, this offers a 15% higher yield than the cases using single-lepton triggers only or using di-lepton triggers only.

In our analysis, the lepton trigger efficiency is defined as the fraction of identified offline leptons that fire a given trigger. In the cases of di-lepton triggers, the trigger efficiency $\epsilon_{2trig}^{2\ell}$ is defined as:

$$\epsilon_{di}^{2\ell}(\vec{x_1}, \vec{x_2}) = \epsilon_{mono}^{\ell_1}(\vec{x_1}) \times \epsilon_{mono}^{\ell_2}(\vec{x_2}) \tag{3.4}$$

where $\vec{x_i}$ is offline parameters (e.g. $p_T$ and $\eta$), and $\epsilon_{mono}$ is the single-leg trigger efficiency. For logical conjunction (**OR**) of multiple triggers, the combined trigger efficiency $\epsilon_{\text{total}}$ is calculated as:

$$\epsilon_{\text{total}} = 1 - \prod_i \left(1 - \epsilon_{trig_i}^{\ell_i}\right) \tag{3.5}$$

where $trig_i$ is the single- or di-lepton trigger for lepton $\ell_i$ used in the combined multiple triggers. Clearly, $\epsilon_{\text{total}}$ is higher than any of the $\epsilon_{trig_i}^{\ell_i}$. A *tag-and-probe* method is used to determine trigger efficiencies. The electron trigger efficiency is measured double-differentially in the $\eta - p_T$ plane, while the muon trigger efficiency is measured in $\eta - \phi$. Trigger efficiencies also depend on offline particle identification (PID) for leptons.

According to Equation 3.5, we compute the trigger scaling factor (SF) to correct

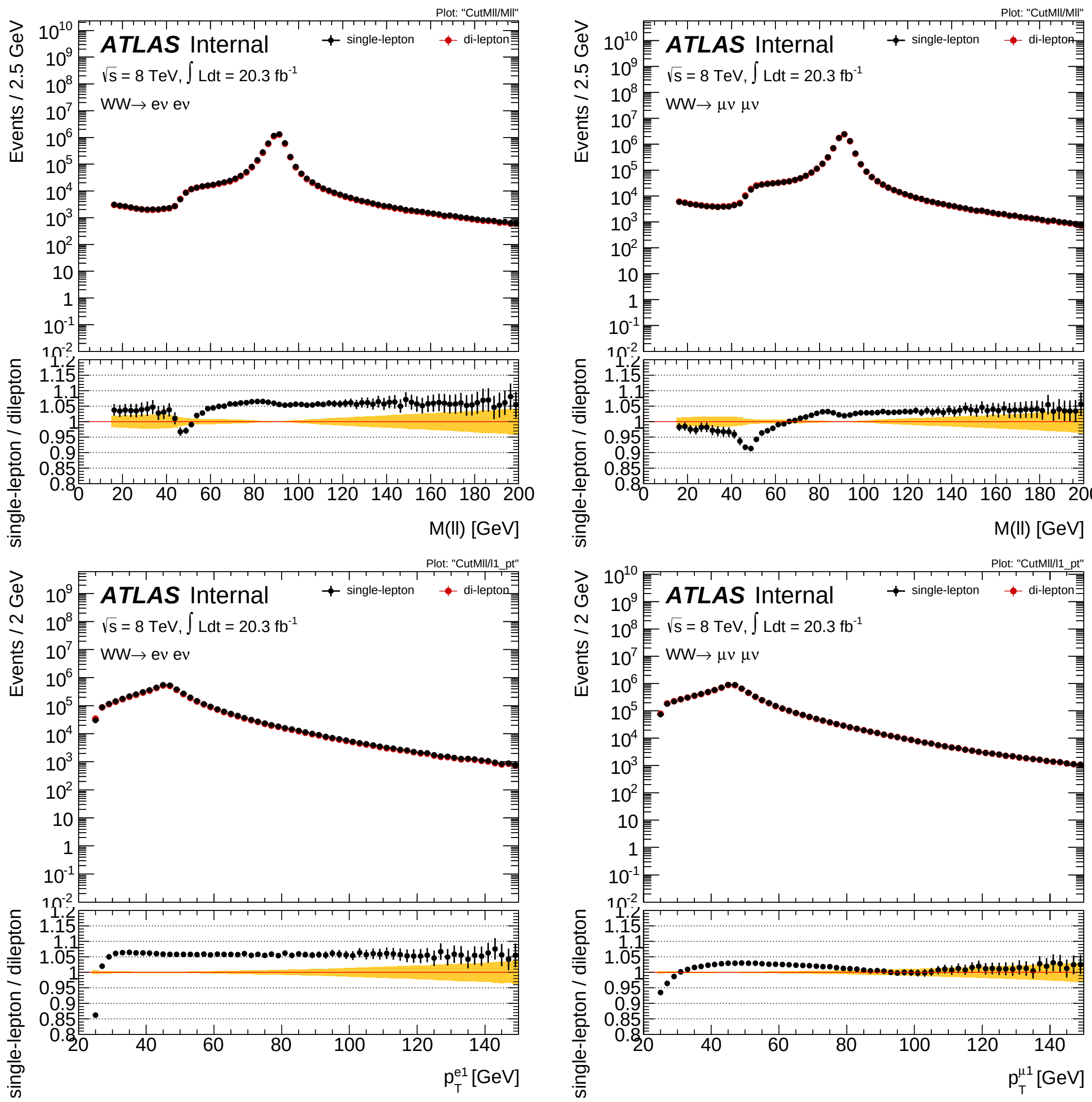


Figure 3.8: Comparison of events with exactly two opposite-charged leptons recorded with single- or di-lepton triggers. The $M_{\ell\ell}$ and leading lepton $p_T$ distributions are shown for the $ee$ and $\mu\mu$ channels. The di-lepton triggers are $\sim 5\%$ less efficient to trigger the events. The turn-on of the single lepton triggers is visible for $M_{\ell\ell} \sim 45\ GeV$ and $p_T^{\ell_1} \sim 25\ GeV$. Note that this figure shows mainly $Z \to \ell\ell$ events. For present analysis the $75 < M_{\ell\ell} < 105\ GeV$ is cut, the leading lepton $p_T$ ($p_T^{\ell_1}$) distribution is shifted to lower ends compared to $Z$.

the trigger efficiencies determined from MC simulations as:

$$SF = \frac{1 - \prod_i \left(1 - \epsilon_i^{\text{data}}\right)}{1 - \prod_i \left(1 - \epsilon_i^{\text{MC}}\right)} \tag{3.6}$$

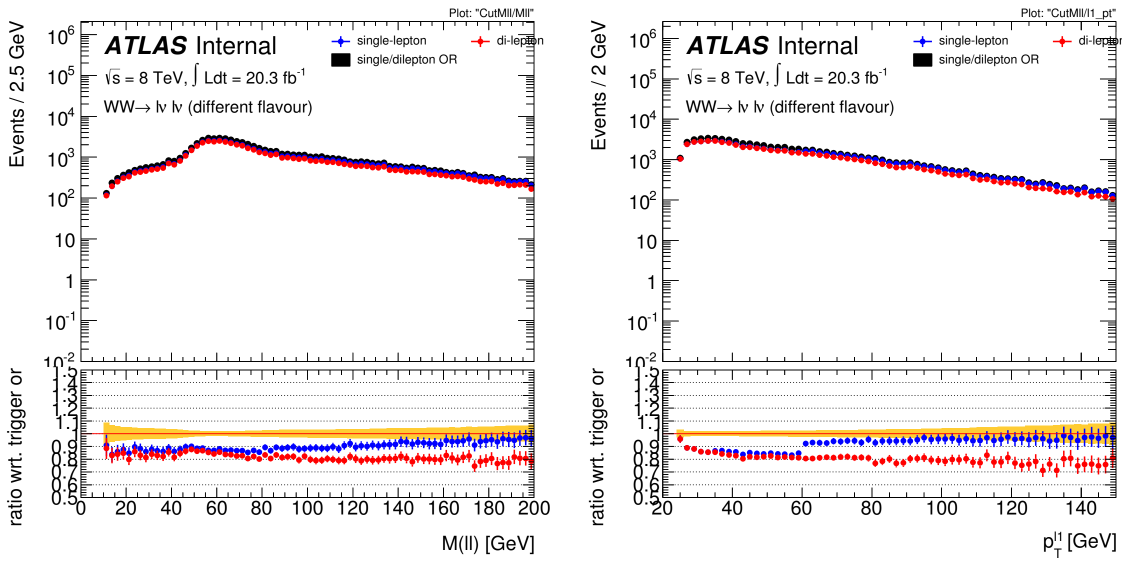


Figure 3.9: Comparison of events with exactly two opposite-charged leptons recorded with single-lepton, di-lepton or a logical **OR** of single- and di-lepton triggers. The $M_{\ell\ell}$ and leading lepton $p_T$ distributions are shown for the combined $e\mu + \mu e$ channels. The single-lepton triggers are more efficient than di-lepton triggers at $p_T > 60\ GeV$ and $M_{\ell\ell} > 60\ GeV$. Both sets of triggers are rather inefficient in $20 < p_T < 60\ GeV$ which is why they are combined for higher event yields.

where the product runs over all selected leptons $i$ in the event. The uncertainties are evaluated with data collected from different data taking periods and with lepton energy and momentum uncertainties. Details of these uncertainties (typically 1-2%) will be given in Chapter 9 for systematic uncertainty calculations.

### 3.2.6 Detector Operation and Performance Summary

The whole ATLAS detector had extraordinary operation performance during Run I. Table 3.3 summarizes the positions, channels, and geometry coverage of active detector components of the ATLAS detector, from the beam line towards outside [13]. Table 3.4 shows the overall operational fraction for sub-detectors as a public result provided by the ATLAS collaboration.

To calibrate the ATLAS detector, beam tests were performed on sub-systems of the detector to determine both the energy and momentum scale using $Z$ invariant mass distribution. Cosmic ray commissioning after final assembly was performed to align the tracking and muon systems, which is also a critical test of the full readout system from the LV1 trigger to the data on the Grid. Within 3 years of LHC running,

| Detector component | Position | Channels (total) | $\eta$-coverage |
|---|---|---|---|
| **Tracking** | | | |
| Pixel | 4 cylindrical barrel layers<br>3 end-cap disks on each side<br>Radial envelope 45.5 - 242 mm | 80,363,520 | ±2.5 |
| SCT | 4 cylindrical barrel layers<br>9 end-cap disks on each side<br>Radial envelope 251 - 610 mm | 6,279,168 | ±2.5 |
| TRT | 73 barrel straw planes<br>80 end-cap straw planes<br>Radial envelope 554 - 1106 mm | 350,848 | ±2.0 |
| **Calorimetry** | | | |
| EM pre-sampler | Barrel | 7,808 | ±1.52 |
| | End-caps | 1,536 | $1.5 < \lvert\eta\rvert < 1.8$ |
| EM LAr calorimeter | 3 depth samples barrel | 101,760 | ±1.48 |
| | 3 depth layers end-caps | 62,208 | $1.375 < \lvert\eta\rvert < 3.2$ |
| Hadronic tile calorimeter | 3 depth samples barrel | 5,760 | ±1.0 |
| | 3 depth samples extended barrel | 4,092 | $0.8 < \lvert\eta\rvert < 1.7$ |
| LAr hadronic end-caps | 4 depth layers | 5,632 | $1.5 < \lvert\eta\rvert < 3.2$ |
| LAr forward hadronic calorimeter | 3 depth layers | 3,524 | $3.1 < \lvert\eta\rvert < 4.9$ |
| **Muon Spectrometer** | | | |
| MDT precision tracking | 3 multi-layer stations | 354,000 | ±2.7 |
| CSC precision tracking | 1 innermost station end-caps | 31,000 | $2.0 < \lvert\eta\rvert < 2.7$ |
| RPC trigger chambers | 2 multi-layer stations barrel | 373,000 | ±1.05 |
| TGC trigger chambers | 2 multi-layer stations end-caps | 318,000 | $1.05 < \lvert\eta\rvert < 2.4$ |

Table 3.3: Main active detector components of the ATLAS detector, from the beam line towards the outside.

| | Subdetector | Number of Channels | Approximate Operational Fraction |
|---|---|---|---|
| Inner Detector | Pixels | 80 M | 95.0% |
| | SCT | 6.3 M | 99.3% |
| | TRT | 350 k | 97.5% |
| Calorimeter | LAr ECAL | 170 k | 99.9% |
| | Tile HCAL (Barrel) | 9800 | 98.3% |
| | LAr HCAL (Endcap) | 5600 | 99.6% |
| | LAr FCAL | 3500 | 99.8% |
| | L1 Calo | 7160 | 100% |
| Muon Spectrometer | L1 Muon RPC | 370 k | 100% |
| | L1 Muon TGC | 320 k | 100% |
| | MDT | 350 k | 99.7% |
| | CSC | 31 k | 96.0% |
| | RPC Barrel | 370 k | 97.1% |
| | TGC Endcap | 320 k | 98.2% |

Table 3.4: Operational fraction for ATLAS sub-detectors during Run I.

designed goals for calibration and performance of the detector has been achieved. Table 3.5 shows that the relative resolution for electrons, photons and muons is at the percent level over large momentum and energy ranges.

| Detector component | Resolution |
|---|---|
| Tracker | $\sigma_{p_T}/p_T = 0.05\% p_T \oplus 1\%$ |
| EM calorimeter | $\sigma_E/E = 10\%/\sqrt{E} \oplus 0.7\%$ |
| Hadronic calorimeter - barrel and end-caps | $\sigma_E/E = 50\%/\sqrt{E} \oplus 3\%$ |
| Hadronic calorimeter - forward | $\sigma_E/E = 100\%/\sqrt{E} \oplus 10\%$ |
| Muon spectrometer | $\sigma_{p_T}/p_T = 10\%$ at $p_T = 1\ TeV$ |

Table 3.5: Resolutions of the ATLAS detector components. The units for energy $E$ and $p_T$ are in $GeV$. $\oplus$ means quadrature sum.

### 3.2.7 Detector Maintenance and Phase 0 Upgrade

During the Long Shutdown 1 (LS1) from 2013 to 2015 after the LHC Run I, the phase 0 detector upgrades and major maintenance have been carried out at CERN by each sub-system working team. Myself was one of the team members for muon system upgrade and maintenance.

The beryllium beam pipe was replaced with a smaller radius one; new aluminum forward pipes are installed. With a smaller beam pipe, a fourth layer of pixel detector, the insertable B-Layer (IBL), was placed in the innermost layer of the tracker along with new Service Quarter Panel (nSQP) to provide more tracking points. The trigger electronics of both calorimeters were upgraded to provide better trigger capability. Previously staged endcap-extra (EE) layers of chambers of the MS and additional chambers in detector feet positions in barrel region were tested and installed with sharpen (LV1) muon trigger. New LV1 trigger processors were also installed. Defected components were fixed or replaced in accessible regions; commissionings of new and replaced components were performed. The upgrade and maintenance plan for the ATLAS detector during LS1s was fulfilled with success at the time of this thesis writing.

## 3.3 The ATLAS Computing System

Computing system is one of the key elements for large experiments. It enables physicists to process huge data set collected from the beam collisions promptly and produce physics analysis results with fast turnaround. This section briefly describe the ATLAS computing system and data process procedures.

### 3.3.1 The ATLAS Computing Structure at CERN

While the LHC sets a record in the collision energy and luminosity, the computing system faces unprecedented challenges as well. It must promptly process high volumes of data and distribute it to the entire ATLAS collaboration around the world. Computing power, storage space, and transmission network is structured as a pyramid model based on the grid technology, named the Worldwide LHC Computing Grid (WLCG), which consists of 4 tiers of computing centers: `Tier-0`, `Tier-1`, `Tier-2`, and `Tier-3`.

The `Tier-0`, simply the CERN Data Center, processes all the data for the first time. The conditions of the detector is monitored here, such as failure of a signal channel or malfunction of a power supply. Shifters monitor the data live in the ATLAS control room. A small set of data is processed within one hour so that analyzers can study the data and identify any problem within the next 24 hours. Unusable data is flagged for physics analyzers to reject in their analysis. But the majority of data, 95%, is usable for physics analysis. `Tier-0` is the safe keeper of all LHC raw data, and the first reconstruction from raw data is also performed in this central hub.

The `Tier-1`'s are 13 large computing centers located worldwide, which receive raw and reconstructed data from `Tier-0` and can re-process them when needed. There are roughly 155 `Tier-2`'s located mainly at universities and research institutes, which store sufficient data, being the most convenient data access sites as well as analysis task computing power for ATLAS members. They are also the main production sites for MC event generation and simulation. There is no formal engagement between WLCG and `Tier-3`'s, which are local computing resources (departmental clusters or even a personal computer).

### 3.3.2 The ATLAS Data Model for Analysis

Detailed description of the ATLAS computing model can be found in [18]. This sub-section briefly summarizes the data preparation of the experiment.

The data types produced are listed by the processing precedence as follows:

- Real Raw Data (RAW): Data output from the EF trigger in bytestream format, which is used for reconstruction.
- Event Summary Data (ESD): Data output of reconstruction process in object-oriented format, which is usually unnecessary for physics applications other than calibration or reconstruction.

- Analysis Object Data (AOD): Reduced event derived from ESD, suitable for physics analysis. It contains physics objects and other interesting parameters stored in object-oriented format.

- Derived Physics Data (DPD): AOD-like, n-tuple style representation of event data for end-user analysis and histogramming, suitable for direct analysis and display. The contents are minimized by means of skimming (selecting only interesting objects), thinning (keeping only interesting objects) and slimming (reducing physics information of selected objects). DPD can be further categorized as:

  – `D1PD`: Centrally produced (working group level) DPD from AOD or AOD made with working group DPD maker.

  – `D2PD`: Privately made or customized DPD produced from `D1PD` or AOD.

  – `D3PD`: N-tuple made from `D1PD`, `D2PD`, or AOD.

- Tag Data (TAG): Event-level metadata supporting efficient identification and event selection to a given analysis, which is stored in a relational database.

- Simulated Event Data (SIM): A range of data types from MC event simulation, including generator level events, parton showered generator level events, full simulation events (interfaced with detector simulation and digitization). It could be any level of the formats mentioned above.

Data processes from detector to tired computing structure are shown in Figure 3.3.2. Detailed physics objects reconstruction will be described in the next Chapter of this thesis.

For Run I physics analysis, officially produced data samples and simulated events were used in data analysis. This thesis work is mainly using the `D3PD` with `Tier-3` computing for event selections and final physics interrelations.

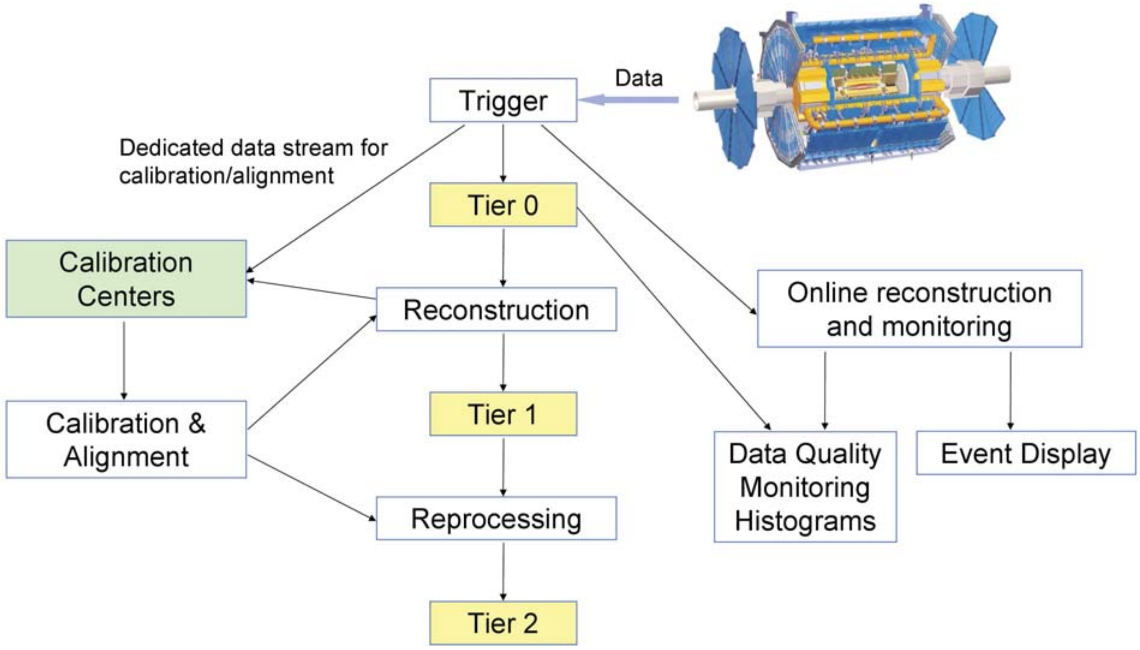


Figure 3.10: Diagram of the ATLAS data processes.

CHAPTER 4

# Physics Modeling and Detector Simulation

Monte-Carlo simulations for different physics processes, both for theoretical modeling and for detector responses, are crucial for modern particle experiments, thus are used to design detectors, to study their performances, and to compare experimental results with theoretical predictions.

The underlying theory for *pp* collision and particle scattering is QCD. Depending on the momentum transferred between interacting particles, scattering processes can be classified as *soft* (low momentum transferred) and *hard* (deep inelastic, high momentum transferred). For *soft* processes, the cross sections and event properties are not well understood, due to the intrinsically non-perturbative QCD effects; while for hard processes, such predictions can be calculated with good precision using perturbative QCD. Soft processes often occur along with hard processes, called underlying events (UEs), which essentially comes from the multi-parton interactions (MPIs) between the remnants of the proton from collisions. In most cases, interesting physics lies in hard processes since they reach high energy scale, while soft interactions are not ignorable when considering total cross section for specific processes.

To generate an event for a process with MC method, there are 3 steps which are illustrated in Figure 4.1.

1. Partonic cross section calculation (matrix element (ME) calculation) and kinematic distributions;

2. Parton showering (including initial and final state radiation);

3. Detector simulation for MC generated events.

Each step will be detailed in the following sections. The ATLAS simulation program is integrated into the ATHENA framework [19].

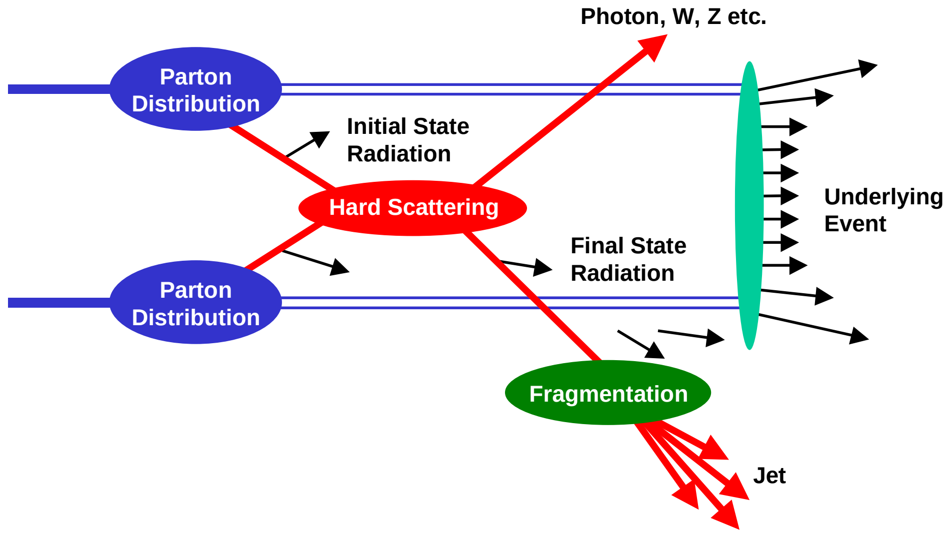


Figure 4.1: Schematic view of a hadron-hadron collision process. The ME calculation accounts for the hard scattering, while parton showering accounts for the fragmentation and hadronization (jets). Detector simulation is not included here.

## 4.1 Matrix Element Calculation

All information at this step is at parton level. For hard scattering, complications in analytical calculations come from the compositive protons in the initial state: only *partons* inside protons participate in interactions. The scattering ME of the process is calculated here to determine the cross sections and kinematic distributions for physics processes based on the *Factorization Theorem* expressed in formula below:

$$\sigma_{pp\to X} = \sum_{i,j} \int dx_i dx_j f_i^p(x_i, \mu_F^2) f_j^p(x_j, \mu_F^2) \times \hat{\sigma}_{i,j}(\alpha_s, \mu_R, \mu_F) \tag{4.1}$$

where $\sigma_{pp\to X}$ is the cross section for a given physics process of $pp \to X$; $f_i^p(x_i, \mu^2)$ is the parton distribution functions (PDFs); and $\hat{\sigma}_{i,j}$ is the short distance partonic reaction cross section in which $\alpha_s$ is the strong interaction coupling, $\mu_F$ is the factorization energy scale of the hard interaction, and $\mu_R$ is the renormalization scale for the QCD running coupling used in calculations. Each of those terms is explained below.

PDFs $f_i^p(x_i, Q^2)$ describes the probability, in the proton $p$, of finding a parton of flavor $i$ (quarks or gluons) carrying a fraction $x_i$ of the proton energy under the interaction energy scale $Q$, which is often chosen to be $\mu_F$. PDFs cannot be calculated from perturbative QCD due to the intrinsic non-perturbative effect, thus they are determined by fits to data in various processes from experimental measurements worldwide. In this analysis, the major PDFs used are `CT10` [20], `MSTW` [21], and `NNPDF` [22], wrapped in the **LHAPDF** library [23]. An NLO PDF constrained by new ATLAS measurements, referred as `ATLAS-epWZ` [24], is also used. An example of PDFs from `MSTW2008` NLO is shown in Figure 4.2.

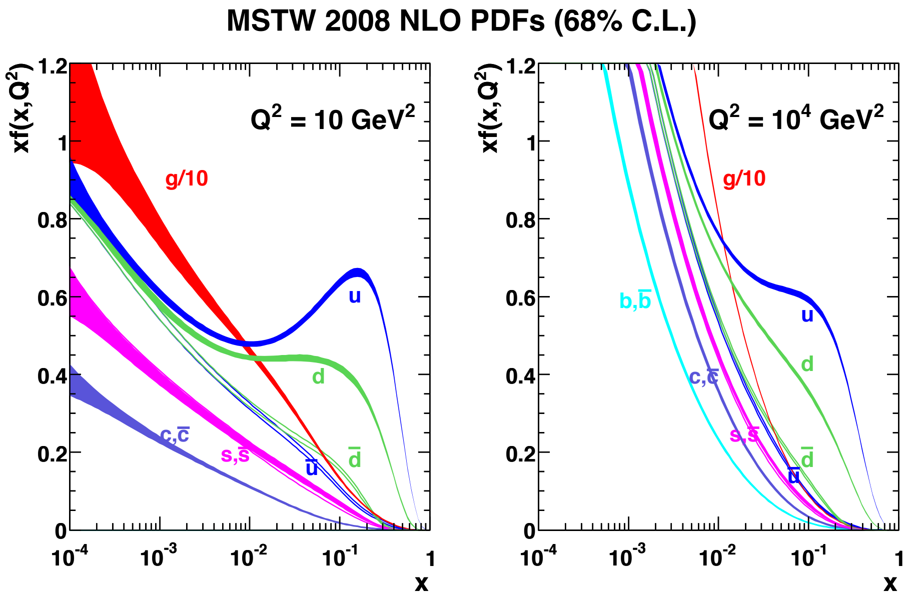


Figure 4.2: The PDFs from `MSTW2008` NLO at $Q^2 = 10\ GeV^2$ and $Q^2 = 10^4\ GeV^2$. The gluon distributions are scaled down by a factor of 10. The uncertainties are shown as bands.

The parton level hard scattering cross section $\hat{\sigma}_{i,j}$ can be calculated perturbatively in QCD in form of the fixed-order expansion in $\alpha_s$. The calculation with tree-level diagrams gives the LO partonic cross section. For LHC physics analysis, most of the theoretical calculations are performed with higher order corrections, including the NLO and the next-to-next-to-the-leading order (NNLO). These calculations involve the choice of scales, $\mu_F$ and $\mu_R$, as well as PDFs, which is one of the major sources of the uncertainties of the theoretical predictions. The choices of $\mu_F$ and $\mu_R$ are arbitrary. In convention, $\mu_F$ and $\mu_R$ are selected to be of the order of the typical energy scales of the hard scattering process to avoid unnaturally large logarithms in the calculation of perturbation series, and $\mu_F = \mu_R$ is assumed in most cases. For example, $\mu_F = \mu_R = \dfrac{M_{WW}}{2}$ for $W^+W^-$ production, which is the invariant mass of the $W$ pair system.

The incoming or outgoing partons carrying color charges can emit QCD radiations in form of gluons while the ones carrying electric charges can emit QED radiations in form of photons, known as initial state radiation (ISR) or final state radiation (FSR). They are also included in the ME calculation step.

Major MC generators for ME calculations used in this analysis are

- **POWHEG BOX** (POWHEG) [25]: used to generate the $q\bar{q} \rightarrow W^+W^-$ and $gg \rightarrow H \rightarrow W^+W^-$ events and kinematic distributions at NLO in QCD,
- **gg2WW** [26]: used to generate the $W^+W^-$ events from the off-shell Higgs and continuum productions with the gluon-gluon fusion at LO in QCD,
- **MCFM** [27]: used to calculate various cross sections including the $W^+W^-$ production; not used in event generation,
- ALPGEN [28]: used to generate events at LO including additional partons in the $2 \rightarrow 2$ hard scattering process (e.g., $Z$+*jets* and $W$+*jets* ),
- **MC@NLO** [29]: used to generate events and kinematic distributions at NLO in QCD; implemented with the ability of storing aTGCs parameterized event weights, which can be used in probing of aTGCs,
- **AcerMC** [30]: dedicated to generate the SM background processes for *Top* physics at the LHC,
- SHERPA [31]: used for $W\gamma^*$ production modeling, including hadronization implementation (see Section 4.2),
- **BHO** [32]: a parton level generator to calculate both LO and NLO cross sections for all five di-boson final states ($W^+W^-$ , $W^{\pm}Z$, $ZZ$, $W^{\pm}\gamma$, $Z\gamma$) with aTGCs parameters; it does not include parton showers automatically.

## 4.2 Parton Showering

The final state partons usually emit soft photons (carrying electric charges) or gluons (carrying color charges). Also, due to color confinement of QCD, quarks and gluons must convert to hadrons, called hadronization, or interchangeably, fragmentation. MC programs are used in this step for this purpose. Fragmentation leads to cascades (showers) of particles, which are beyond the parton level. All partons go through fragmentation except the *Top* quark, which will decay to $W + b$ promptly before hadronization. Most of the particles produced in $pp$ collisions have short life time, such as massive bosons: $W^{\pm}$, $Z$ and $H$. These particles will decay to final state particles in MC simulation programs based on theoretical predictions.

In addition to the hard scattering processes, UEs also produce many soft final state particles in an collision event. Such phenomena are simulated by parton showerers as well, using the algorithms called *tuning*.

Major MC programs and algorithms for parton showering and UE tunings are

- Pythia [33, 34]: Multi-purpose generator often used for parton showering and UE simulations.
- Herwig/Herwig++ [35, 36]: alternative to Pythia program for parton showering; Herwig is based on `Fortran` while Herwig++ is based on `C++`.
- Jimmy [37]: a library of routines which should be linked with Herwig. Jimmy allows to generates MPI events in $qq$, $\gamma\gamma$ and $q\gamma$ collision events, usually used for UE simulations.
- **`AUET2`** [38]: an UE tuning, often interfaced with Herwig/Jimmy.
- **`AU2`** [39]: an UE tuning, often interfaced with Pythia.
- **`Photos/Photos++`** [40]: an algorithm interfaced with a "host" MC generator (e.g., Pythia) for QED radiative corrections in decays of any resonances.
- **`Tauola/Tauola++`** [41]: an algorithm interfaced with a "host" MC generator (e.g., Pythia) for simulating polarized $\tau$ decays with spin correlations.

The ME events (partion-level) gone through parton showering (particle-level) are called *truth events* and are usually used in theoretical studies, such as signal acceptance determination and theoretical systematic uncertainty evaluation. Figure 4.3 provides a full illustration of a *truth* hard collision event associating with UEs breaking down into simulation steps.

## 4.3 Detector Simulation and Digitization

The generated MC events with the truth particle information will be input into MC detector simulation program to simulate the final state particle interactions with the detector materials, and to emulate the detector electronics responses such as detection timing and deposit charge in the detector due to the interactions (digitization).

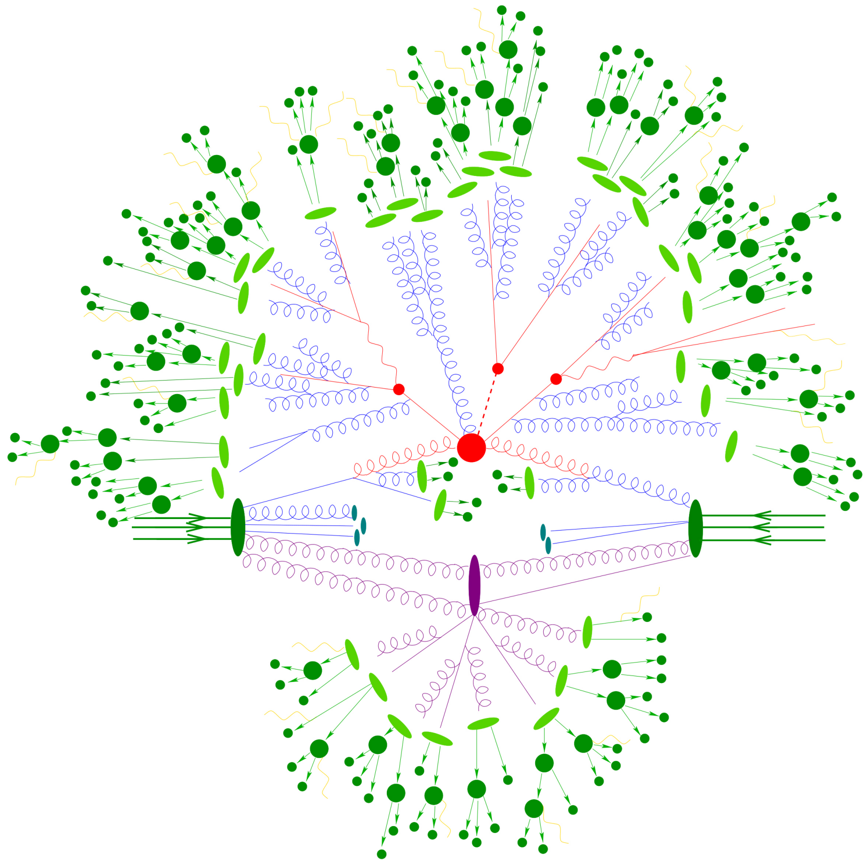

Figure 4.3: Simulation structures of a truth event. Red blobs are the hard scattering (including ISR and FSR), which is simulated by ME generators. Red and blue tree structure is the additional QCD radiation; light green blobs are the fragmentation for QCD partons – both are simulated by parton showerers. Purple blobs are underlying MPIs, which is simulated by UE tuning interfaced with host MC generators. Dark green blobs are hadron decays (into other hadrons and leptons); yellow curves are additional QED radiations – both are simulated by algorithms interfaced with host MC generators.

The ATLAS detector simulation is based on **`Geant4`** framework [42, 43]. In this program, the MC generator produced particles will pass through different detector layers and interact with matter of the detector. Strict detector geometry limitations are applied at this step, which is considered in truth event generation (for acceptance studies), if any.

The signals (deposited energies and hit positions) will be *digitized* as same as the real experimental signals in units of analogue-to-digital converter (ADC) hits (collected charges) and time-to-digital converter (TDC) hits (timing). All kinds of simulation events are considered: hard scattering signal, minimum bias (keep UEs without any explicit hard-scattering cut-off), beam-halo (beam interactions far away from the detector), beam-gas (beam collides with residual gas within the beam pipe), and cosmic-ray events. The *pile-up* is simulated at this step: before the detector signal is generated, events of any kind can be overlaid at a user-specified rate. LV1 trigger is also simulated, with no events disregarded but different trigger menus evaluated. The constructed digital signals are fed into emulated ROD in the detector electronics, then output as RAW format data file.

All the digitization parameters are obtained from test beam experiments prior to the ATLAS detector assembly. The output format of the simulated events is *bytestream*, the same as the data from real *pp* collisions collected by the ATLAS detector. The only difference of MC data and real data is that MC events have truth particle information in underlying physics process. The event reconstruction and physics object reconstructions are exactly the same for MC events as data, which will be described in details in Chapter 5.

## CHAPTER 5

# Event Reconstruction

Events recorded by the ATLAS detector or using MC simulations from $pp$ collisions are reconstructed for physics analysis. This is done by reconstructing individual *Physics Objects* in an event. Objects reconstructed in this analysis include charged particle tracks, interaction vertices from the $pp$ collision, electrons, muons, hadronic jets, and $\not{E}_T$. Figure 5.1 is an actual event display for a $WW \to e\mu e\mu$ event candidate recorded by ATLAS in 2012. The light-blue track is a reconstructed muon, the yellow energy cluster is a reconstructed electron, and the red dashed line indicate the missing transverse energy direction. Other color reconstructed tracks in the inner tracker are from underlying events.

Figure 5.2 shows a wedge of the transverse plane of the ATLAS detector, which illustrates "signals" left by all kinds of physics objects in the detector with distinct characteristics. For example, the muons penetrate the whole detector and leave tracks in both ID and MS, while electrons only leave tracks in the ID and deposit all the energies in the ECAL. The details of how these objects are reconstructed in the ATLAS experiment are described in this Chapter.

## 5.1 Tracks

A track is a trajectory of a charged particle leaves, from the IP outward the ID. In the algorithm of track reconstruction [44], particles associated with tracks are classified into two types: primary particles and secondary particles. Primary particles are long-lived (lifetime greater than $3\times10^{11}$ $s$) particles directly produced in a $pp$ interaction, or subsequent particles decayed or produced from short-lived particles (lifetime shorter than $3 \times 10^{11}$ s). Secondary particles are particles decayed from primary (or other secondary) particles. From raw data of ID, space points representing hits and holes are reconstructed. A **hit** is a track measurement point left in ID layers. A **hole** is an

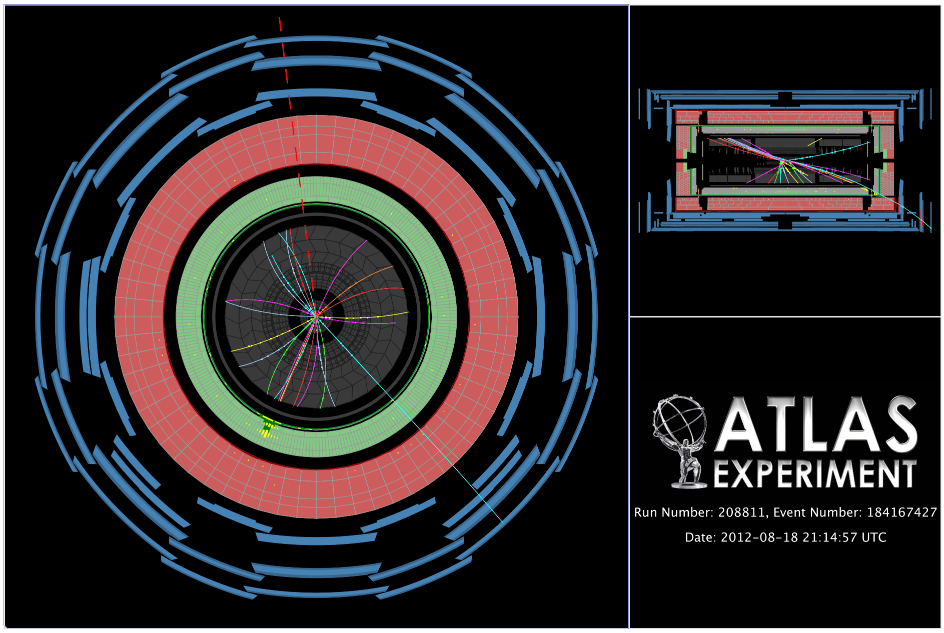


Figure 5.1: Highest $\not{E}_T^{rel}$ (see Section 5.6.1) event ($\not{E}_T^{rel} = 196\ GeV$) in $WW$ signal region observed in the $e\mu$ channel in data. Cross-sectional (left) and side (top right) views are shown. The electron (green cluster) and muon (cyan) have $p_T = 104\ GeV$ and $97\ GeV$, respectively, and the $\not{E}_T$ (hashed red) is $196\ GeV$. Only tracks with $p_T > 1\ GeV$ are displayed.

expected but non-existing measurement point along a track. To reconstruct tracks of the primary and secondary particles, a sequence of algorithms using progressive fitting are used as described below [44, 45].

The algorithm used for primary track reconstruction is called *inside-out*, with requirement of track transverse momentum $p_T > 400\ MeV$. It sets some silicon detector (Pixel and SCT) space points as seeds, then adds hits outward from the IP using a filter algorithm. In the track extension stage, track candidate ambiguities are handled with another algorithm, until the tracks are extended into TRT. After that, the track candidate is refitted using full information of the ID (Pixel, SCT, TRT). If the quality of the refit candidate is worse than the silicon-only (no extension) candidate, the refit candidate is labeled as an **outlier** and the TRT hits are labeled as **TRT outliers**, which may be useful in other object selection requirements (see Section 5.4.2).

The secondary track reconstruction algorithm follows an opposite direction, called *outside-in*. With TRT hits, it finds track segments using a pattern recognition algorithm, followed by a successive back tracking into the silicon detector. Besides secondary particles, the *outside-in* algorithm can also deal with primary tracks without initial

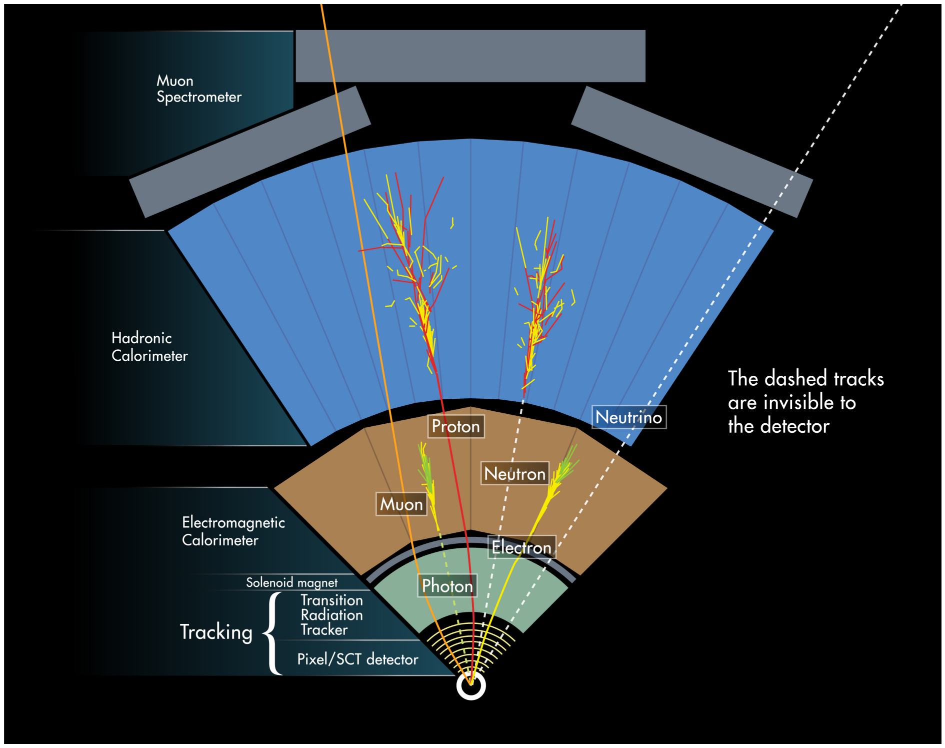


Figure 5.2: A wedge of the transverse plane of the ATLAS detector. Hadrons, leptons and photons have different signatures left in the detector. With algorithms dealing with such different characteristics, physics objects are reconstructed for following analysis.

seeds due to ambiguous hits. Finally, tracks with a TRT segment but no extension into the silicon detectors are referred to as **TRT-standalone** tracks. They may come from the photon conversion.

An illustration of the track reconstruction with different reconstructed candidates is shown in Figure 5.3.

A primary track has a larger fraction of hits located in the silicon detectors than a secondary track does. When track candidates are reconstructed, they are matched to primary or secondary particles based on that criterion. Fake tracks are candidates that could not be matched to either a primary or secondary particle. The main contribution to fake tracks are *pile-up*, because it increases hits from other particles near a candidate track, confusing the pattern recognition algorithm – this effect is called **shadowing**. To suppress fake tracks, a robust quality requirement is provided for track candidates, in contrast to the default quality requirement. Both quality requirements are summarized below, with the hits and holes defined in previous context.

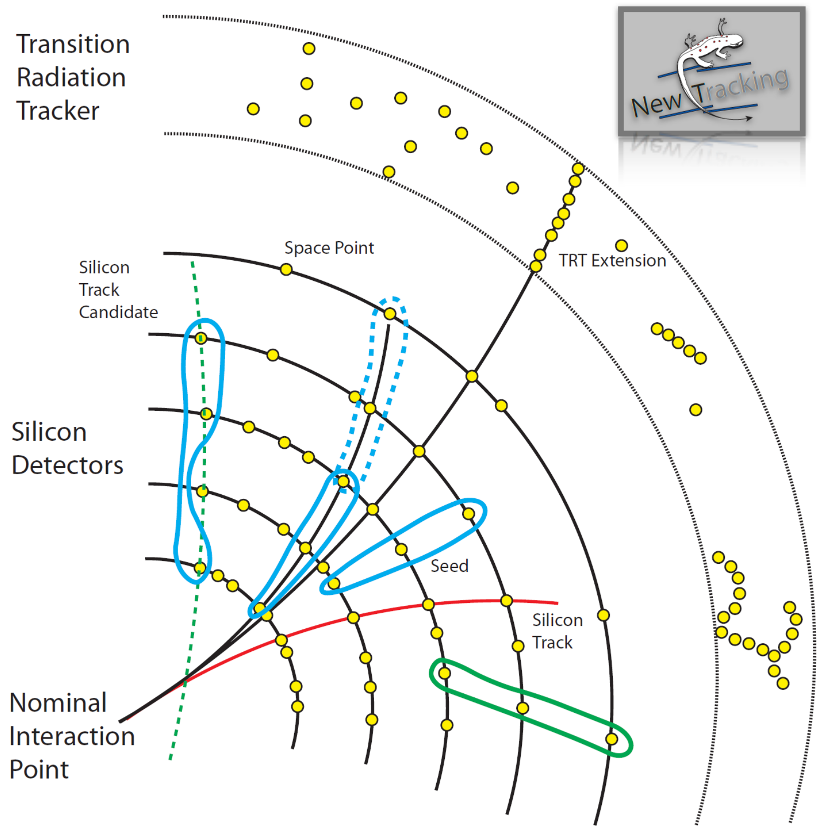


Figure 5.3: Illustration of track reconstruction. The ID layers here are not shown in scale. Yellow dots are space points representing hits by charged particles; blue circles are track seeds (possibly primary track), with dotted blue circles representing the progressive extrapolation; green circles are track seeds which probably could not trace back to IP (secondary track); the green dotted line is a silicon track candidate, possibly a secondary track; black lines are reconstructed primary tracks, one of which is matched to a TRT segment; the red line is a primary track (extrapolation unfinished) with opposite charge to the black tracks.

- *Robust quality requirement*:
  - At least 9 hits in the silicon detectors (Pixel and SCT), including 1 hit in B-Layer (defined in Section 3.2.2)
  - 0 hole in the Pixel
- *Default quality requirement*:
  - At least 7 hits in the silicon detectors
  - At most 2 holes in the Pixel

The primary track reconstruction efficiency is defined as the fraction of primary particles with $p_T > 400$ $MeV$ and $|\eta| < 2.5$ matched to a reconstructed track. With increased *pile-up*, the efficiencies of both primary and secondary tracks changes very little; but the robust requirement globally reduces the primary and secondary track reconstruction efficiency by 5% and 1-2%, respectively [44]. Though the robust requirement is proved to be extremely effective at controlling the non-primary fraction, it comes with a considerable costcertain specific topologies, such as $e$ and $\tau$ reconstructions, are suffered from the corresponding 5% efficiency loss. In this analysis, the robust track quality is chosen to define a good track.

Nevertheless, physics analysis has the freedom to choose the most appropriate track quality requirement by balancing different considerations, being not limited to choose from either the default or the robust one defined above. This analysis has implemented different track quality requirements for different physics object reconstructions. They will be elaborated in the following sections.

## 5.2 Primary Vertices

A vertex is a spatial point where an interaction happens and out-going particle originates. A primary vertex (PV) is where the $pp$ collision happens, while a secondary vertex is where successive interactions or decays happen on the out-going particles from a PV or another secondary vertex. Experimentally, a PV is the vertex with the largest $\sum p_T^2$ of its associated tracks. In many analysis, PVs attract most interest since that's where most of the final state particles are from. However, in analysis relating to the reconstruction and identification of $\tau$'s and $b$'s, secondary vertices are also used because the two particles are short-lived compared to other stable particles (e.g., $e$ and $\mu$) but are long-lived enough to "fly" over a detectible distance in the detector, then decay into other particles, hence forming a secondary vertex. This analysis does not use any $\tau$ or $b$ as final state particles, so only focusing on the reconstruction of PVs.

The reconstruction of vertices relies on reconstructed tracks, using two algorithms: *finding* algorithm dedicated to associate tracks to vertex candidates, and *fitting* algorithm dedicated to determine the vertex position along with uncertainties [46]. The tracks used in $finding$ must fulfil requirements listed in Reference [46]. With the pre-selected tracks, $finding$ determines vertex seeds, by looking for the global maximum in the distribution of $z$ coordinates of the tracks. Then $fitting$ determines the position of the vertex with an adaptive algorithm, by performing a $\chi^2$ fit using the seeds and its nearby tracks. Depending on the $chi^2$ of the fit, each track is assigned a weight measuring its compatibility with the fitted vertex seed. Outlying tracks (displaced by more than $7\sigma$) are used to seed a new vertex. The $fitting$ algorithm repeats itself until no additional vertex is found or all tracks are associated. After all tracks are associated to vertices, vertices are matched to interactions, by summing the weights of the tracks associated to the vertex candidate. If the sum is greater than 50%, the interaction is considered matched to that vertex. This criterion ensures that the vertex positions are dominated by "good-fitted" tracks.

The vertex reconstruction efficiency is calculated with the same track-to-particle matching used to calculate the tracking efficiency. The efficiency of reconstructible interactions (interactions with at least two primary charged particles with $p_T >$ 400 $MeV$ and $|\eta| < 2.5$) is ~90% [44]. The vertex efficiency decreases with increasing $\langle\mu\rangle$ to ~50% at $\langle\mu\rangle = 41$ [44]. Also, the probability to reconstruct a fake vertex increases in high *pile-up* environment (7% fake-rate at $\langle\mu\rangle = 41$ [44]), with a vertex defined fake if the leading contribution to the total weight is from a fake track. During reconstruction, vertices are required to contain at least two tracks. However, to suppress *pile-up*, vertices are required to have 3 tracks for robustness, coming with a loss of vertex reconstruction efficiency due to the shadowing effect (see Section 5.1). In addition, the robust requirement of tracks (see Section 5.1) also reduces vertex efficiency. Figure 5.4 shows a typical 25-vertex $Z \to \mu\mu$ event recorded by ATLAS in 2012 data taking.

## 5.3 Electrons

Electrons are reconstructed based on the energy deposits (clusters) in the ECAL, then matched to reconstructed tracks of charged particles in the inner tracker, and vetoed if HCAL has significant activity along the direction of the clusters. Besides true isolated electrons, this reconstruction method inevitably introduces large background, including typical processes such as misidentified hadrons, photon converted electrons, and non-isolated electrons from heavy flavour hadron decays. Therefore, additional identification requirements are applied to reject backgrounds. Additional isolation requirement are also used to improve the quality of selected electrons. The electron reconstruction, identification, and isolation methods are described in this subsection. The overall electron selection efficiency in this analysis ranges from 70-90% in the central region ($|\eta| < 1.37$), and 5-10% less in the forward region ($1.52 < |\eta| < 2.47$). These measurements have an accuracy of $< 0.5\%$ and is dominated by the uncertainty

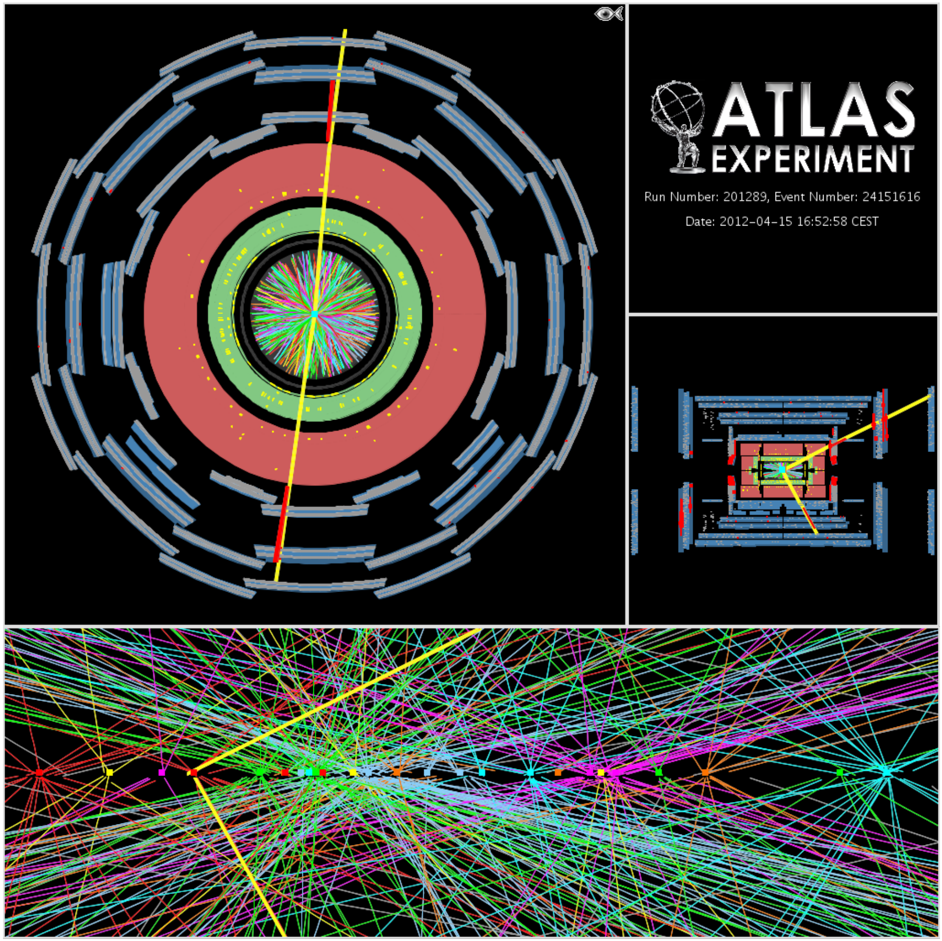


Figure 5.4: A 25-vertex $Z \to \mu\mu$ event showing the high *pile-up* environment for the vertex reconstruction.

on the background estimate in the *tag-and-probe* (see Section Section 5.3.4) samples [47].

### 5.3.1 Reconstruction

The ECAL granulates its accordion middle layer into towers in units of $\eta \times \phi = 0.025 \times 0.025$, named *trigger towers*, as illustrated in Figure 3.7. For electrons in the central region ($|\eta| < 2.47$), the reconstruction contains 3 main steps as follows [47]:

1. *Seed-Cluster reconstruction*:
   An EM cluster is seeded by using a sliding-window algorithm [48], with a duplicate-removal algorithm applied on close-by seed clusters. The seed cluster position is defined to be the barycentre of the cluster. For each seed cluster

passing loose shower shape requirements [47], a RoI with a cone-size of $\Delta R = 0.3$ around the seed cluster barycenter is defined. The collection of these EM cluster RoIs is retained for use in the track reconstruction.

2. *Track candidate reconstruction and track-cluster association*:
   Electron track reconstruction contains two steps, *pattern recognition* and *track fit*. The electron track reconstruction uses information of silicon hits and RoIs defined above.

   - *Pattern recognition*:
     Two algorithms are used based on different hypothesis for energy loss on material surfaces: the standard pattern recognition [45] using the *pion hypothesis* and the modified pattern recognition [49] using the *electron hypothesis* which allows at large as 30% energy loss for possible bremsstrahlung. The default approach to reconstruct track candidates is to use the *pion hypothesis*, by extending a track seed (consisting of 3 silicon hits) to a full track (at least 7 silicon hits) falling within one EM cluster RoI. If the *pion hypothesis* fails, it is retried with the *electron hypothesis*. In this way, pattern recognition performance is improved while the interference with the main track reconstruction is minimized.
   - *Track fit*:
     The parameters of the track candidates found by pattern recognition are then fitted with the same hypothesis used in pattern recognition, using the *ATLAS Global $\chi^2$ Track Fitter* [50]. Again, if a track candidate fails in *pion hypothesis* fit, it is refitted with the *electron hypothesis*.

   After track fit, electron tracks (with fitted parameters) are loosely associated to an EM cluster based on the following criteria:

   - Silicon tracks with at least 4 silicon hits are extrapolated from the point of closest approach with respect to the PV to the middle layer of the ECAL. A silicon track is considered matched to an EM cluster if the spatial distances of the two is within $(|\Delta\eta|, |\Delta\phi|) = (0.05, \varphi)$, where $\varphi$ is depending on which side of the track the EM cluster falls into: $\varphi = 0.2$ on the side the track is bending towards and $\varphi = 0.05$ on the opposite side.
     TRT-only tracks with less than 4 silicon hits are extrapolated from the last measurement point to the middle layer of the ECAL. A TRT-only track is considered matched to an EM cluster if it meets the same $|\Delta\phi|$ requirement

above, but there is no $|\Delta\eta|$ requirement due to the poor precision of $\eta$ measurement.

- For low momentum tracks (both silicon and TRT-only) suffering from significant energy loss before reaching ECAL, their momenta is re-scaled to the cluster energy, and the $|\Delta\phi|$ matching requirement is modified to be $\varphi = 0.1(0.05)$ on the (opposite) side the track is bending towards. $|\Delta\eta|$ is the same for both silicon and TRT-only tracks.

3. *Electron candidate reconstructed*:
   In this final step, the track parameters of silicon tracks obtained from the *Global $\chi^2$ Track Fit* is re-estimated with an optimized track fitter, the *Gaussian Sum Filter (GSF)* [51], accounting for non-linear bremsstrahlung effects. TRT-only and silicon tracks keep the parameters from the *Global $\chi^2$ Track Fit* if they failed in the GSF ($\sim$0.01% [47]). In addition, tighter ($|\Delta\eta|, |\Delta\phi|$) requirements are applied:

   - For silicon tracks, $|\Delta\phi| = 0.1$ on the side the track is bending towards
   - For TRT-only tracks, $|\Delta\eta| = 0.35(0.2)$ in the TRT barrel(end-cap) and $|\Delta\phi| = 0.03(0.02)$ on the (opposite) side the track is bending towards.

   In this procedure more than one track can be associated with a cluster, with the primary track chosen by the following criteria: the track with at least 1 Pixel hit; or the track with the smallest $\Delta R = \sqrt{(\Delta\eta)^2 + (\Delta\phi)^2}$ if more than one tracks pass the first criteria.
   An electron candidate is considered reconstructed if at least one track is matched to the seed cluster; otherwise, the cluster is classified as an unconverted photon candidate. The cluster energy of the electron candidate is rebuilt with calibrations and corrections (See Section 5.3.5). The four-momentum of the electron candidate is determined from both the final cluster and its primary track. For silicon tracks, cluster energy and ($\eta_{\text{track}}, \phi_{\text{track}}$) are used; for TRT-only tracks, cluster energy and ($\eta_{\text{cluster}}, \phi_{\text{cluster}}$) are used.

For forward region electrons ($2.47 < |\eta| < 4.9$), only the EMEC and the FCAL are used for reconstruction since the ID loses coverage in this region. Therefore, distinction is impossible for electrons and photons in this region. A different cluster reconstruction algorithm is used in forward region [48]. An forward region electron with $E_T > 5$ *GeV* and low hadronic leakage (energy deposited in the HCAL) is considered reconstructed, with its position defined by the barycentre of the cells belonging to the cluster. In this analysis, only central electrons are used, thus no further details of forward electrons is provided.

### 5.3.2 Electron Identification

In previous di-boson analysis, a cut-based electron identification (eID) is used [52]. This thesis uses a likelihood-based eID by exploiting the advantages of multivariate analysis (MVA) techniques. MVA technique is widely used in physics analysis to separate signal from background by simultaneously evaluating several discriminating variables, in contrast to cut-based technique which solely relies on successive cuts. Likelihood method uses discriminating variables for signal and background probability density functions (PDFs), and combine them into a discriminant on which an operating point is applied to decide an event or object to be signal or background. Unlike cut-based menus, likelihood uses full shape information, and are more sensitive to small shape differences, therefore can use a broader range of discriminating variables including those with large overlap between signal and background. By introducing the likelihood method, the resulting PID has an improved rejection of light-flavor jets and photon conversions, compared to the cut-based menus.

A given electron has a set of eID variables with discriminating power, called likelihood variables, denoted by $\vec{x}$. The likelihood eID is constructed by first creating a set of PDFs from $\vec{x}$, then giving the electron a score, or discriminant $d_{\mathcal{L}}$ as the form below [52]:

$$d_{\mathcal{L}} = \frac{\mathcal{L}_S}{\mathcal{L}_S + \mathcal{L}_B}, \qquad \mathcal{L}_{S,B}(\vec{x}) = \prod_{i=1}^{n} P_{S,B;i}(x_i) \tag{5.1}$$

where $\mathcal{L}_{S,B}$ is the likelihood function for signal or background, and $P_i(x_i)$ is the PDF of $x_i$ in $\vec{x}$. Note that, $x_i$ could be a cut-based variable or not, as explained in the above paragraph.

Constructing a likelihood eID menu consists of three steps:

1. Choose the specific variables $\vec{x}$ to be used in likelihood.
2. Choose additional variables, if any, to be applied as cuts on top of the likelihood.
3. Choose an operating point for the likelihood discriminant $d_{\mathcal{L}}$.

Such a menu combining a likelihood with traditional cuts is called *effective PID*, which is used as the eID for this analysis. The efficiency of the menu is the combined efficiency of $d_{\mathcal{L}}$ and the additional cuts. The likelihood method is ideal when $x_i$ is completely uncorrelated with each other. As a result, some variables used in cut-based PID are not used in likelihood. The chosen likelihood variables and additional cuts as well as their definitions in the eID menu are listed in Table 1 and Table 3 in Reference [52].

After the effective eID menu is chosen, the next importing step is to determine the PDFs of the chosen variables. $P_i(x_i)$ are very sensitive to mis-modeling, therefore both signal and background PDFs are derived from data, using a *tag-and-probe* method in $Z \to ee$ events [52]. The PDF function is differentially binned in $(E_T, |\eta|)$ to accommodate the large shape variations in both variables. Special treatments are used to deal with low statistics caused by rugged shape of PDF and background contamination in low $E_T$ bins [52]. All PDFs are hand-tuned to ensure optimization.

Five criteria are provided by the likelihood eID: `VeryTight`, `Tight`, `Medium`, `Loose`, and `VeryLoose`. Electrons passing tighter selection criteria are almost able to pass looser ones, with non-overlap ratio no larger than 0.05% between any two categories [52]. The measured performance of each operating point is shown in Table 2 in Reference [52]. This analysis uses the likelihood `VeryTight` menu, denoted by `VeryTightLH`.

### 5.3.3 Isolation and Impact Parameter Requirement

To further suppress electrons mis-identified from hadron jets, additional isolation cuts are applied on top of the eID described above. Tow main isolation alternatives are:

- Calorimeter based isolation: The calorimetric isolation quantity $\sum E_T^{\Delta R<r}$ is the sum of the transverse energy $E_T$ deposited in the calorimeter cells in a cone of $\Delta R < r$ (named isolation cone) around the cluster barycenter, excluding the contribution of the particle itself, which is defined to be the deposited energy within $\Delta\eta \times \Delta\phi = 0.125 \times 0.175$ around the particle. Cells from the ECAL and HCAL are all used within the cone. The more isolated is the particle from adjacent environment, the smaller is the contribution of $\sum E_T^{\Delta R<r}$ to the total energy deposited within the isolation cone. To achieve *pile-up* robustness, *Topological Clusters* are used as shown in Figure 5.5.

- Track based isolation: The track isolation quantity $\sum p_T^{\Delta R<r}$ is the sum of the transverse momentum $p_T$ of the ID tracks in a cone of $\Delta R < r$ around the primary track, excluding the track momentum of the particle itself. The tracks in the sum must share the same PV with the considered track (by implementing impact parameter constraints), and pass the robust track quality requirement (see Section 5.1). This variable is quite *pile-up* robust.

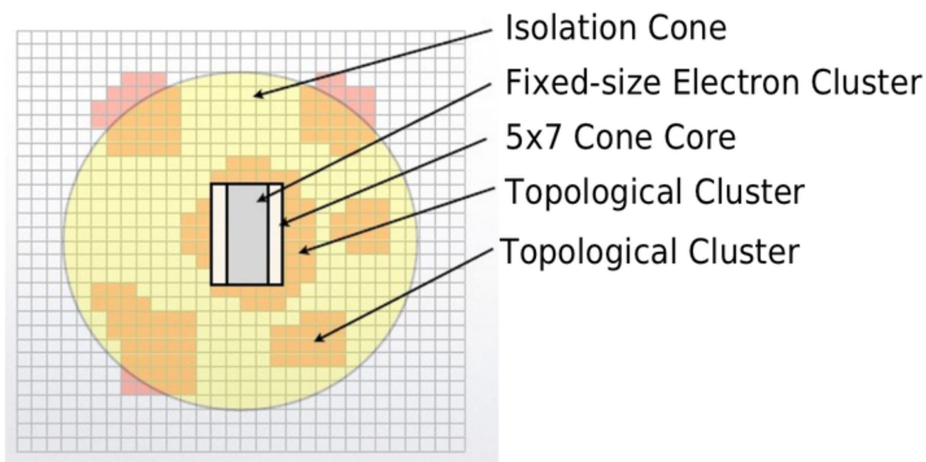


Figure 5.5: Illustration of the cross-section of an topological cluster in calorimeter. The yellow circle is the cone size. The pink cells are topological clusters. Only topological clusters falls within the cone size are summed. The $5 \times 7$ square is the $0.125 \times 0.175$ cone core, which is subtracted from the isolation quantity.

Besides used in electron reconstruction, these isolation cuts are also used in the *tag-and-probe* method to tighten the selection criteria of the tag particles for efficiency measurements (see Section 5.3.4).

In addition to isolation cuts, a final requirement on transverse and longitudinal impact parameters is also applied to ensure the electron candidates come from PVs. $d_0$ and $z_0$ denote the transverse and longitudinal impact parameters of tracks with respect to the center of the luminous region (also called beam spot), respectively; and $\sigma(d_0)$ and $\sigma(z_0)$ denote the corresponding uncertainties estimated by the track fit. The beam spot is simply where the two incoming beams collide, which is spatially a long thin ellipsoid region surrounding IP. Generally, $d_0$ and $z_0$ are small if the tracks come from the center of the beam spot, indicating they are real primary tracks.

### 5.3.4 Efficiencies and Scaling Factors

The accuracy of MC modeling plays an important role in cross section measurements and searches for new physics. The electron efficiency $\epsilon_e$, which is generally different between data and MC samples, is conceptually defined as:

$$\epsilon_e = \frac{N_e^{\text{selected}}}{N_e^{\text{pool}}} \tag{5.2}$$

where $N_e^{\text{selected}}$ is the number of electrons passing some selection criterion (e.g., reconstruction requirement, eID requirement), and $N_e^{\text{pool}}$ is the total number of "real" electrons. Full electron efficiency $\epsilon_{\text{total}}$ can break down into different components:

$$\epsilon_{\text{total}} = \epsilon_{\text{reco}} \times \epsilon_{\text{id}} \times \epsilon_{\text{trig}} \times \epsilon_{\text{other}} \tag{5.3}$$

where $\epsilon_{\text{reco}}$, $\epsilon_{\text{id}}$, and $\epsilon_{\text{trig}}$ are efficiencies for reconstruction, eID, and electron trigger, respectively. They can be separately determined by Equation 5.2 with corresponding $N_e^{\text{selected}}$ and $N_e^{\text{pool}}$. The trigger efficiency is discussed in Section 3.2.5. As the electron reconstruction, eID and electron trigger have fixed menus and are generally independent of analyses, these 3 efficiencies are also independent of analyses as long as the menus are chosen. In contrast, $\epsilon_{\text{other}}$ is dependent on specific analysis, corresponding to additional selection criteria, e.g. the isolation and impact parameter (*Iso/Ip*) requirements.

In order to achieve reliable physics results, the MC efficiencies need to be corrected by correction factors, or SFs, defined as the ratios of the measured efficiencies in data to those in MC:

$$SF = \frac{\epsilon_{\text{data}}}{\epsilon_{\text{MC}}} \tag{5.4}$$

The SFs are usually close to 1, while deviations may be caused by mis-modeling of tracking parameters or shower shapes in calorimeters. The merit of using SFs is that, systematics in the efficiency measurement of both data and MC are expected to cancel out in SFs. Therefore, the combination of different efficiency measurements is carried out by using the SFs instead of the efficiencies themselves:

$$SF_{\text{total}} = SF_{\text{reco}} \times SF_{\text{id}} \times SF_{\text{trig}} \times SF_{\text{other}} \tag{5.5}$$

As efficiencies (therefore SFs) have dependence on $E_T$ and $\eta$, they are all measured differentially (binned) in $(E_T, \eta)$.

Measuring the eID and reconstruction efficiency requires a clean and unbiased sample of electrons. The problem is that, while the $N_e^{\text{selected}}$ is easy to determined in Equation 5.2, the $N_e^{\text{pool}}$ is almost impossible to know in priori according to its definition. A solution to that is to construct a representative sub-sample of the original electron pool and do the selection based on it. With sufficient statistics, the efficiency calculated based on the sub-sample should approximate the real efficiency. Such sub-sample is prepared by applying a widely used data-driven method, called *tag-and-probe* method, on large-statistics $Z \to ee$ or $J/\psi \to ee$ samples. In the *tag-and-probe* method, strict selection criteria are applied to select a $Z$ or $J/\psi$ decayed electron (called *tag*); by requiring the second electron coming from the same $Z$ or $J/\psi$ but with looser selection criteria, a *probe* electron is defined. The probe sample forms a representative sub-sample of the original electron pool. The full efficiency is then defined as the fraction of probe electrons passing the tested criteria. In order to minimize the bias of the probe sample, the roles of *tag* and *probe* can be switched for a pair of $e$ coming from the same $Z$ (or $J/\psi$) as long as they fit the selection requirements. Due to the looser criteria, the probe samples are contaminated by background (mis-identified jets, secondary electrons, photon converted electrons) especially at low $E_T$ regions. This contamination is estimated using background template method, or using simultaneous fits of signal and background. The *tag-and-probe* method is elaborated is Reference [47].

Using the *tag-and-probe* method, the efficiency of eID, $\epsilon_{\text{id}}$, is defined as:

$$\epsilon_{\text{id}} = \frac{N_e^{\text{eID}}}{N_e^{\text{reco}}} \tag{5.6}$$

where $N_e^{\text{eID}}$ is the number of electrons passing a certain eID menu (*tag*), and $N_e^{\text{reco}}$ is the number of reconstructed electrons (*probe*) passing the "electron track quality" (associated with tracks having at least 7 silicon hits and at least 1 Pixel hit). The detailed measurement of $\epsilon_{\text{id}}$ is documented in Reference [47]. For `VeryTightLH` menu, $\epsilon_{\text{id}} = 78\%$ for electrons with $E_T > 15\ GeV$, and the uncertainty $\sigma(\epsilon_{\text{id}}) = 5 - 6\%(1 - 2\%)$ for $E_T < (>)25\ GeV$.

Similarly, the reconstruction efficiency, $\epsilon_{\text{reco}}$, is defined as:

$$\epsilon_{\text{reco}} = \frac{N_e^{\text{reco}}}{N_{\text{cluster}}^{\text{reco}}} \tag{5.7}$$

where $N_e^{\text{reco}}$ is defined the same as in Equation 5.6, and $N_{\text{cluster}}^{\text{reco}}$ is the number of reconstructed cluster seeds. The detailed measurement of $\epsilon_{\text{reco}}$ is documented in Reference [47]. For electrons with $E_T > 15\ GeV$, $\epsilon_{\text{reco}}$ varies from 99% at low $\eta$ to 95% at high $\eta$ for both data and MC. The uncertainty is $\sigma(\epsilon_{\text{reco}}) = 0.5 - 1.5\%$ for $E_T < 25\ GeV$ and $\sigma(\epsilon_{\text{reco}}) < 0.5\%$ for $E_T > 25\ GeV$. The $E_T - \eta$ binned SFs are shown in Reference [47] and are applied to MC samples for correction.

The *Iso/Ip* efficiency, $\epsilon_{\text{Iso/Ip}}$, is derived in this analysis, by using the *tag-and-probe* method on $Z \rightarrow ee$ samples as well. The *tag* and *probe* electrons are defined as:

- *tag*:
  - $p_T > 25$ $GeV$, $|\eta| < 2.47$ excluding the crack region $|\eta| = [1.37, 1.52]$
  - Matched to single electron trigger and pass the `tight++` cut-based eID
- *probe*:
  - Opposite charges with the tag
  - Invariant mass of *tag-probe* pair must consistent with $M_Z$
  - Apply all nominal electron selection cuts (see Table 7.1) except *Iso/Ip* cuts

By adding *Iso/Ip* cuts to the probe sample, $\epsilon_{\text{Iso/Ip}}$ can be derived as defined in Equation 5.8:

$$\epsilon_{\text{Iso/Ip}} = \frac{N_{\text{full}}}{N_{\text{full}}^{\text{no Iso/Ip}}} \tag{5.8}$$

The detailed measurement of $\epsilon_{\text{Iso/Ip}}$ as well as the SF is documented in Reference [53].

### 5.3.5 Calibration and Corrections

**Absolute Energy Scale Calibration** The absolute energy scale of the ECAL need to be calibrated from MC. Precise calibration of the energy measurement of electrons and photons is a fundamental input to many physics measurements. The energy of an electron or photon candidate is built from the energy of a EM cluster using multivariate algorithms. After all corrections, the $Z$ resonance is used to set the absolute energy scale for measured di-electron mass in binned $\eta$ regions. Procedures to calibrate the energy response of electrons and photons are summarized in Reference [54]. The final calibrated energy is used as the energy of electrons and photons for data.

**Data-MC Energy Scale Correction** The energy scales in Data and MC are not exactly the same. To bring back the agreement, an energy scale correction for electron energy is needed, which is parameterized as below:

$$E^{\text{data}} = E^{\text{MC}} (1 + \alpha_i) \tag{5.9}$$

where $E^{\text{data}}$ and $E^{\text{MC}}$ are raw energy of data and MC, and $\alpha_i$ is the energy scale correction factor in the $i$-th bin of $\eta$. The systematic uncertainty variations of $\alpha_i$ is defined to be $\alpha_i^{\text{var}}$, then the difference between $\alpha_i^{\text{var}}$ and the nominal correction factor and $\alpha_i^{\text{nom}}$ is defined as $\delta\alpha_i^{\text{var}} = \alpha_i^{\text{var}} - \alpha_i^{\text{nom}}$. In this analysis, $\alpha_i^{\text{nom}}$ is applied to correct $E^{\text{data}}$ only, and $\delta\alpha_i^{\text{var}}$ for different variations are applied to $E^{\text{MC}}$ for systematic studies:

$$E^{\text{data}}_{\text{correction}} = \frac{E^{\text{data}}}{1 + \alpha_i^{\text{nom}}} \tag{5.10}$$

$$E^{\text{MC}}_{v_i} = E^{\text{MC}}\left(1 + \delta\alpha_i^{v_i}\right), \quad \text{for variation } v_i \tag{5.11}$$

**Energy Resolution Correction** The electron energy resolution of MC simulation, $\sigma_E^{\text{MC}}$, is not the same as that of data, $\sigma_E^{\text{data}}$. Therefore $E^{\text{MC}}$ also needs to be corrected according to the data energy resolution $\sigma_E^{\text{data}}$. The resolution correction is also called **smearing**. Define

$$\delta\sigma_E^2 = \left(\sigma_E^{\text{data}}\right)^2 - \left(\sigma_E^{\text{MC}}\right)^2 \tag{5.12}$$

Then the resolution corrected $E^{\text{MC}}$ is simply:

$$E^{\text{MC}}_{\text{reso}} = E^{\text{MC}}\left(1 + N\left(0, \delta\sigma_E\right)\right) \tag{5.13}$$

where $N\left(0, \delta\sigma_E\right)$ is a Gaussian distribution.

**Calorimeter Isolation Energy Correction** Isolation correction quantities are defined in 5.3.3. For calorimeter isolation quantity, (at least) two effects bring in unwanted changes to $\sum E_T^{\Delta R<r}$ : signal leakage and *pile-up*. Signal leakage refers to the signal particle (electron or photon) leaks its energy outside of the cone core, causing the $\sum E_T^{\Delta R<r}$ grows as a function of $E_T$. *pile-up* makes $\sum E_T^{\Delta R<r}$ contaminated from soft energy deposited by UEs, causing the $\sum E_T^{\Delta R<r}$ dependent on current event ("in-time *pile-up*") or previous events ("out-of-time *pile-up*"). Hence, a correction algorithm is implemented to correct the calorimeter isolation energy. In contrast, because the tracks used in $\sum p_T^{\Delta R<r}$ are constrained by the impact parameter cuts ensuring they come from the same vertex associated to the electron, there is no need to correct $\sum p_T^{\Delta R<r}$ in general.

### 5.3.6 Alignment between Inner Trackers and EM Calorimeter

As an electron going out from IP, it leaves a bent track in the ID and a cluster (energy deposit) in the ECAL (Figure 5.2). The cluster, as well as the impact point of the track extrapolation to the inner surface of the ECAL, records spatial coordinates $(\eta, \phi)$ of the electron, respectively. However, due to the precision tolerance of detector assembly, the two recorded $(\eta, \phi)$ coordinates may differ. Therefore, the two detector sub-systems need to be aligned for electrons.

The alignment of the two sub-detector systems is measured using prompt decayed electrons (electrons decayed from $W$ or $Z$) selected with transverse energy $E_T > 20\,GeV$ and strict identification criteria (see Section 5.3). The relative displacements are indicated by the difference between the two $(\eta, \phi)$ coordinates defined above. The derived alignment constants are applied to correct both the $\eta$ and $\phi$ electron cluster coordinates.

## 5.4 Muons

The efficient identification of muons and the accurate measurement of their momenta are two of the main features of the ATLAS detector. Muons ($\mu$) are reconstructed and identified with the MS, the ID and the calorimeters (to a lesser extent) of the ATLAS detector. The MS is a stand-alone muon tracker, where muon tracks are reconstructed in two steps: firstly local track segments are sought within each muon station; and then track segments from different stations are combined to form MS tracks. The ID provides an independent measurement of the muon track close to the IP. The calorimeters assist to muon identification, covering approximately 100 to 190 radiation lengths (depending on $\eta$) of muons, corresponding to materials between the IP and the MS. Details about muon reconstruction can be found in Reference [55].

### 5.4.1 Reconstruction and Identification

Unlike electron reconstruction, the muon reconstruction and identification algorithms are incorporated. Two independent algorithm families implementing different strategies (named "Chains") are used in the reconstruction and identification: *Chain 1* (*STACO*) [56] and *Chain 2* (*MUID*) [57]. According to different reconstruction criteria, based on available information of MS, ID and calorimeters, muons are reconstructed and identified into 4 types [55]:

- Stand-alone (SA) muons: Muon tracks are reconstructed using information in the MS only, with each track required to cross at least 2 layers of MS chambers. Then the muon tracks are extrapolated back to the IP taking into account the energy loss in calorimeters. The *STACO*-family uses *MuonBoy* [58] algorithm for SA muon reconstruction and identification, assigning energy loss based on the material crossed in the calorimeters [59]. The *MUID*-family uses *MOORE* [60] at the first stage (find tracks and performs inward extrapolation), assigning energy loss with similar strategy to *MuonBoy/STACO*, additionally making use of the calorimeter energy measurement if they are significantly larger than the most likely value and the muon appears to be isolated [59]. Both *MuonBoy/STACO* and *MOORE/MUID* carry out a least-squares fit to form tracks [59]. Muons produced in the calorimeter (e.g. from $\pi$ and $K$ decays) are likely to enter the MS and serve as a background of "fake" muons [61]. SA muons are mainly used to extend the acceptance to $2.5 < |\eta| < 2.7$ since the ID coverage is limited to $|\eta| < 2.5$.

- Combined (CB) muons: For *STACO*, MS tracks reconstructed by *MuonBoy* and ID tracks reconstructed by progressive fitting (see Section 5.1) are statistically combined to form CB muon tracks, using the parameters of the reconstructed tracks and their covariance matrices [61]. The *MUID* accesses ID tracks from *iPatRec* track fitter [56] and MS tracks from *MOORE* to produce CB tracks by doing a global refit [61]. Both *iPatRec/MUID* and *MOORE/MUID* adopt least-squares fitting for track finding. CB muon is the main type of reconstructed muons and has the highest muon purity, but with coverage limited to $|\eta| < 2.5$.

- Segment-tagged (ST) muons: An ST muon is identified if an ID track extrapolated to the inner station of MS matches to at least 1 local track segment which is not yet associated with a CB track. The reconstruction and identification algorithm for this type of muons is *MuTag* [56] in the *STACO*-family and *MuGirl* [62] in the *MUID*-family. *MuTag/STACO* defines a tag $\chi^2$ using the difference between any nearby segment and the prediction from the extrapolated track. *MuGirl/MUID* uses an artificial neural network (ANN) to define a discriminant [61]. In either case, if a segment is sufficiently close to the predicted track position, the ID track is tagged as corresponding to a muon. ST muons are mainly used to increase acceptance in cases the muon crosses only one layer of the MS, either due to its low $p_T$ or because it falls in regions with limited MS acceptance. [1]

[1] Part of the MS chambers were not installed in $1.1 < |\eta| < 1.3$ during 2012. Those chambers are

- Calorimeter-tagged (CaloTag) muons: A CaloTag muon is identified if an ID track is matched to a minimum ionizing particle (energy deposit complied with certain requirements) in the calorimeter, by algorithms described as follows [59]. Two calorimeter-seed algorithms are used to search for muons: the *LArMuID* finds muon with ECAL information and the *TileMuId* used for triggering with HCAL information. Then, a track-seed algorithm, *CaloMuonTag*, extrapolates ID tracks through the calorimeter identifying those matching the energy deposition pattern of a muon. No MS information is used by *CaloMuonTag*. Another track-seed algorithm, *CaloMuonLikelihoodTool*, builds a likelihood ratio to discriminate $\mu$ from $\pi$. CaloTag muon has the lowest purity of all the muon types but it recovers acceptance in the uninstrumented regions of the MS, e.g. for region $|\eta| < 0.1$ where the MS is only partially equipped with muon chambers in order to provide space for the services of the ID and the calorimeters.

Figure 5.6 illustrates the 4 categories of muon reconstructed and identified as described above.

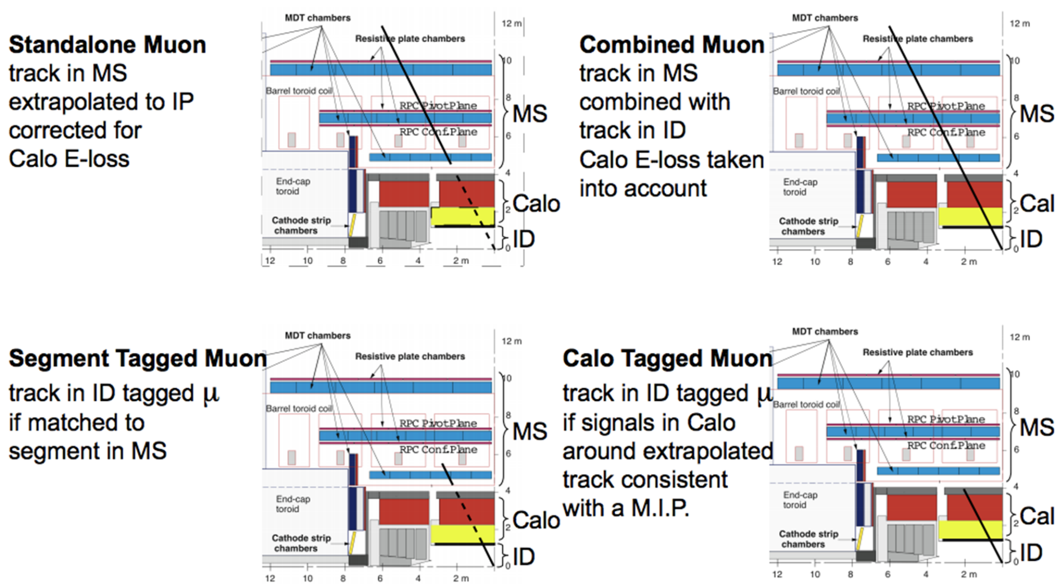


Figure 5.6: Four strategies used in muon reconstruction and identification.

The two independent algorithm families provide cross-checks and yield similar reconstruction efficiency, with *Chain 1* more robust against background while *Chain 2* having a slightly higher efficiency. Incorporating the best features of the two chains, a unified algorithm *Chain 3*, or *MUONS* [55], has been developed and used in parallel

installed during LS1 in 2013.

to the other two chains in the muon reconstruction of 2012 data. *Chain 3* performs an ID-MS combined momentum fit including muons traversing only one MS layer, eliminating the distinction between CB and ST muons. It is planned to use only *Chain 3* for future data taking. This analysis uses CB muons reconstructed with the *STACO* algorithm.

### 5.4.2 Inner Detector Track Quality Requirement

Hits in the ID are used to assure the quality of the muon tracks. The ID tracks used in CB, ST, and CaloTag muons have different track quality requirements other than the ones used in track reconstruction as mentioned in 5.1. The ID track quality criteria required by muon reconstruction is [55]:

- At least 1 hit in Pixel. Hits in dead Pixel sensors are counted.
- At least 5 hits in SCT. Hits in dead SCT sensors are counted.
- At most 2 holes in active sensors of silicon trackers.
- Define $n_{\mathrm{TRT}}^{\mathrm{hit}}$ as the number of TRT hits of the muon track, $n_{\mathrm{TRT}}^{\mathrm{outlier}}$ as the number of TRT outliers (see Section 5.1) of the muon track, and $n \equiv n_{\mathrm{TRT}}^{\mathrm{hit}} + n_{\mathrm{TRT}}^{\mathrm{outlier}}$.
  In the region of full TRT acceptance, $0.1 < |\eta| < 1.9$, require $n > 5$ and $\frac{n_{\mathrm{TRT}}^{\mathrm{outlier}}}{n} < 0.9$.

The numbers of hits required in the first two bullets are reduced by 1 if the track traverses a sensor known to be inefficient according to a time-dependent database. The above requirements are dropped for $|\eta| > 2.5$, where short ID track segments can be matched to SA muons to form a CB muon.

### 5.4.3 Isolation and Impact Parameter Requirement

To reject secondary muons from hadronic jets, isolation requirements are applied to the ID tracks of muons. To further reduce background, calorimeter isolation requirements are applied to the muon candidates as well. To ensure the muons are coming from PVs, impact parameter requirements are applied. The definitions of isolation quantities and impact parameters are the same as in Section 5.3.3, with the electrons replaced by muons in all cases.

### 5.4.4 Efficiencies and Scaling Factors

For each type of muon in $|\eta| < 2.5$, the total reconstruction efficiency, $\epsilon^{\text{Type}}_{\text{total}}$, is given by [55]:

$$\epsilon^{\text{Type}}_{\text{total}} = \epsilon(\text{Type}|\text{ID}) \times \epsilon(\text{ID}) \simeq \epsilon(\text{Type}|\text{ID}) \times \epsilon(\text{ID}|\text{MS}) \tag{5.14}$$

where $\epsilon(\text{ID})$ is the efficiency that a muon has its ID track reconstructed, $\epsilon(\text{Type}|\text{ID})$ is the probability that a muon reconstructed by the ID is also reconstructed by the MS. However, the $\epsilon(\text{ID})$ cannot be measured directly, hence a *probe* sample is selected by a *tag-and-probe* method (see Section 5.3.4) to yield an approximation of $\epsilon(\text{ID})$. The *probe* sample is chosen to be the muons reconstructed by the MS. $\epsilon(\text{ID}|\text{MS})$ is the probability that a muon reconstructed by the MS is also reconstructed by the ID, which can serve as the approximation of $\epsilon(\text{ID})$ with the *tag-and-probe* method. Alternatively, $\epsilon(\text{Type}|\text{ID})$ is also derived using a *probe* sample chosen to be the muons reconstructed by the ID, for Type∈(CB,ST).

Similar to the case of electrons, SFs for muons are also defined as Equation 5.4, with the same consideration of cancelling possible systematics in the efficiency measurement of data and MC. The SFs are then used to correct MC samples in physics analysis.

$Z \to \mu\mu$ events (at high $p_T$ regions) and $J/\psi \to \mu\mu$ events (at low $p_T$ regions) are used to measure the reconstruction efficiencies of all muon types with the *tag-and-probe* method. Results [55] show that $\epsilon^{\text{Type}}_{\text{total}}$ is a function of $\eta$. The combination of CB, ST, and CaloTag muons gives a uniform muon reconstruction efficiency of about 99% over most detector regions. The efficiency measured in data and MC are in good agreement, well within 1% in general.

The muon isolation efficiency and its SF is optimized and measured with the *tag-and-probe* method applied on $Z \to \mu\mu$ samples, as described in Reference [63, 64].

### 5.4.5 Corrections

Similar to the electron case, the reconstructed muon momenta from MC samples need to be corrected for both scale and resolution. Note that (see Section 5.3.5), while smearing is applied to MC for both electrons and muons, the scale correction is applied to data for electron but to MC for muons.

**Correction for Momentum Scale and Resolution** To correct CB muon momenta, scale and resolution corrections are applied to the muon $p_T$'s reconstructed by the

ID and the MS separately, then are propagated to the CB muon to get the corrected transverse momentum, $p_T^{\mathrm{Cor,CB}}$, using a weighted average [55] formula:

$$p_T^{\mathrm{Cor,CB}} = f \cdot p_T^{\mathrm{Cor,ID}} + (1 - f) \cdot p_T^{\mathrm{Cor,MS}} \tag{5.15}$$

where $f$ is solved from uncorrected MC simulated samples:

$$p_T^{\mathrm{MC,CB}} = f \cdot p_T^{\mathrm{MC,ID}} + (1 - f) \cdot p_T^{\mathrm{MC,MS}} \tag{5.16}$$

and the $p_T^{\mathrm{Cor,Det}}$ for Det∈(ID,MS) are corrected using the following equation:

$$p_T^{\mathrm{Cor,Det}} = \frac{p_T^{\mathrm{MC,Det}} + \sum_{n=0}^{1} s_n^{\mathrm{Det}}\left(\eta,\phi\right)\left(p_T^{\mathrm{MC,Det}}\right)^n}{1 + \sum_{m=0}^{2} \Delta r_m^{\mathrm{Det}}\left(\eta,\phi\right)\left(p_T^{\mathrm{MC,Det}}\right)^{m-1} g_m}, \quad \text{with } s_0^{\mathrm{ID}} = 0 \text{ and } \Delta r_0^{\mathrm{ID}} = 0 \tag{5.17}$$

where $s_n^{\mathrm{Det}}\left(\eta,\phi\right)$ and $\Delta r_m^{\mathrm{Det}}\left(\eta,\phi\right)$ are momentum scale corrections and resolution smearings depending on $(\eta,\phi)$, respectively; and $g_m = N(0,1)$, the normal distribution. The MS and ID correction parameters contained in Equation are extracted from data for $Z \to \mu\mu$ and $J/\psi \to \mu\mu$ events, using an MC template maximum likelihood fit method [55].

With details described in Reference [55], the scale corrections for MC muon ID tracks is always below 0.1%, and the scale correction for MC muon MS tracks is $\lesssim$ 0.1% except for some $\eta$ regions. Depending on $p_T$, total resolution smearing corrections below 10% and below 15% are needed for the simulated ID and MS track reconstructions.

**Calorimeter Isolation Correction** Isolation correction quantities are defined in 5.3.3. A correction based on the number of reconstructed PVs in the event is made to $\sum E_T^{\Delta R<r}$ that compensates for extra energy due to *pile-up* [64].

## 5.5 Jets

Jets are collimated sprays of energetic hadrons, produced via the fragmentation of quarks and gluons (see Section 4.2). They are the dominant signature of high-energy, hard $pp$ collisions at the LHC as well as key ingredients for many physics measurements and searches for new physics. In ATLAS, jets are reconstructed by two algorithms: the *track jets* which uses ID tracks as input to the jet finding algorithm, and the *calorimeter jets* which uses energy deposits in calorimeter in stead. This analysis chooses the latter method. Calorimeter jets are reconstructed from energy deposited in groups of topologically adjacent calorimeter cells with significant signals above noise, called *topo-clusters* [48]. In addition, MC simulated jets are reconstructed with the same algorithm as observed jets, referred as *truth jets* or *particle-level jets*. Figure 5.7 illustrates the jet reconstruction flow for calorimeter jets, with details elaborated in the following sections.

### 5.5.1 Reconstruction of Calorimeter Jets

Jet reconstruction starts from the deposited energy in the calorimeter cells, which have been calibrated at the EM scale. This scale is set in test beams and is defined to reproduce correctly the electron energy in the beams.

Before reconstructing jets, *topo-clusters* are identified by an algorithm with raised noise threshold [65] by use of signal-to-noise significance, in the purpose of suppressing the increased cell noise due to *pile-up*. The *topo-clusters* are seeded from the EM clusters, the showers particles producing in ECAL. If jet finding algorithm is implemented at this step, these jets are called *EM-scale* jets. Alternatively, if the *topo-cluster* seeds are calibrated before jet-finding to correct for the calorimeter response to hadrons in purpose of resolution improvement and fluctuation reduction, using the so-called LCW method (see Section 5.5.2.1), then these jets are called *LCW-scale* jets. This analysis uses LCW-scale jets as shown in Type-III flow in Figure 5.7.

After *topo-clusters* are found and calibrated by LCW, jets are reconstructed by the anti-$k_T$ jet-finding algorithm [66] with distance parameters $R = 0.4$ utilizing the FastJet software package [67], followed by jet energy scale (JES) and in-situ calibration (see Section 5.5.2) to form refined physics jets which is ready for use in physics analysis, as shown in Figure 5.7. Reconstructed physics jets are classified into three categories:

- *Bad*: Jets from background events or faked by detector effects, need to be removed
- *Ugly*: Jets in problematic calorimeter regions (e.g the transition region) that are not well measured
- *Good*: Jets to be used in physics analysis

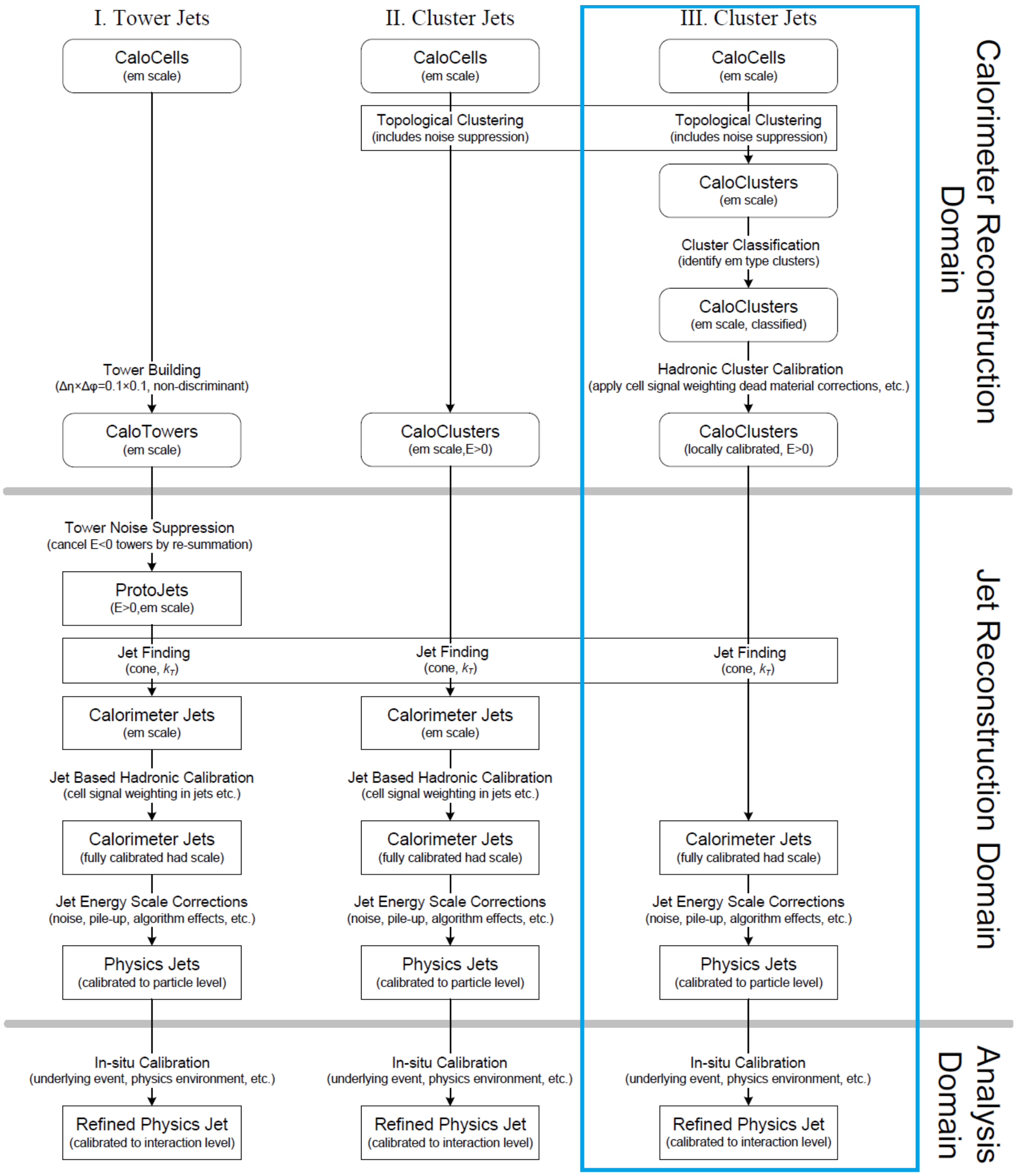


Figure 5.7: Jet reconstruction flow for calorimeter jets from towers or clusters. Flow-II is for the EM-scale jets, and Flow-III is for the LCW-scale jets (see Section 5.5.1). This analysis adopts Flow-III scheme: starting from EM-scale calorimeter cells, *topo-clusters* (CaloClusters in the Figure) are built and calibrated by LCW for detector effects (local hadronic scale); secondly jet finding algorithm is applied to form LCW-scale calorimeter jets, followed by JES calibration for physics effects to form physics jets; finally physics jets are calibrated in-situ to final-scale to form refined physics jets, ready for use in physics analysis.

Different analysis requires different quality of jets. The tighter is the jet quality, the lower is the jet efficiency; while the lower is the jet quality, the more likely that the jet is fake. Four sets of jet quality criteria – `Looser`, `Loose`, `Medium` and `Tight` — are defined in order to reject fake jets [68]. The jet quality and category are complementary in selections for "good jet".

### 5.5.2 Calibration and Corrections

Precise measurement of the jet energy is a fundamental ingredient of many physics analyses at the LHC; moreover, the jet reconstruction performance has a direct impact on the measurement quality of the missing transverse energy, $\not{E}_T$ , which plays a decisive role in this analysis. The systematic uncertainty in the jet energy measurement is the dominant experimental uncertainty for numerous physics results including this one. Jet uncertainties mainly come from the JES and jet energy resolution (JER), which are described in this section.

#### 5.5.2.1 Energy Scale Calibration

The ultimate goal of the jet energy measurement is to reconstruct the initial parton momentum. However, the measured energy scale suffers from both detector and physics effects, which needs to be calibrated. All the JES corrections are derived from MC simulations. The JES calibrations in the reconstruction stage are performed in the following procedures [61], as shown in Figure 5.7:

1. Correct for detector effects: calorimeter non-compensation[2], cell noise threshold, energy losses in dead material and uninstrumented regions, longitudinal energy leakage, particle deflection in the magnetic field, etc. This step of calibration contains [69]:

    - Cluster classification: clusters are classified as EM or hadronic with assigned probability
    - Hadronic weighting: correct calorimeter cell for hadronic responses
    - Out-of-cluster corrections: correct for energy depositions not passing the noise threshold in clustering

[2] The detector non-compensation refers to the effect that the signal per unit of incoming energy recorded by the detector is smaller for hadrons compared to electrons. E.g., for energy deposited by hadrons in ECAL, a typical 30% loss is observed in the jet energy measurement compared to the $e/\gamma$ with the same energy.

- Dead material corrections: correct for energy deposited in materials outside the calorimeter

After this step, the JES at particle-level is obtained.

2. Correct for physics effects: cell clustering, parton fragmentation, ISR and FSR, UEs, *pile-up*, etc. This step of calibration specializes in [69]:

   - Pile-up correction: correct for the energy offset due to *pile-up*. The *hadronic scale* is **not** restored until this correction is applied.
   - Vertex (origin) correction: correct the direction of *topo-clusters* back to the PV from the geometrical centre of the detector. JES is not affected by this correction.
   - Jet energy and direction correction: correct the $E$ and $\eta$ of reconstructed jets to those of truth jets. Note that *pile-up* effect has been subtracted.

   After this step, the obtained JES is calibrated to parton-level *hadronic scale*.

ATLAS has developed several JES calibration schemes [61] with different levels of complexity and different sensitivity to systematic effects. This analysis adopts the so-called *LCW+JES* scheme, with the merit of better JER and lower sensitivity to the flavor of the parton including the jet than other schemes. In the *LCW+JES* scheme, the *topo-clusters* are firstly found and calibrated by the LCW method which applies corrections for the detector effects; then jets are built from these locally calibrated clusters by a jet algorithm as mentioned in Section 5.5.1. This correction for *topo-clusters* is "local" since it is applied at cluster level without referencing to any jet definition or considering the jet context. After calorimeter jet reconstruction, corrections for physics effects are applied.

After MC-based corrections, JES calibration can be validated in-situ by using a well calibrated object in suitable physics processes as reference and comparing data to the nominal MC simulation. This in-situ validation, or in-situ calibration, determines the systematic uncertainty of the *hadronic energy scale* (including contributions from ISR/FSR and UEs) as well as the JER (see Section 5.5.2.2). The in-situ calibration has two procedures [61]:

1. Check the uniformity of the JES calibration as a function in $\phi - \eta$ plane, using QCD *dijet* events

2. Obtain absolute *hadronic energy scale* with a $p_T$-balance method, using $Z/\gamma + jet$ events. The final state of $Z/\gamma + jet$ can be seen as a two-body system, where $p_T^j$ is exactly balanced by $p_T^{Z/\gamma}$. In other words, $p_T^j$ can be calibrated by $p_T^{Z/\gamma}$, which in turn can be measured by ECAL if using $Z/\gamma \to \ell\ell$ decay. Eventually, the $p_T$-balance method propagates the well-understood knowledge of the EM scale of leptons to the *hadronic scale* of jets.

The above in-situ calibration is only applicable to central rapidity region. For high $p_T$ region or forward region where jet statistics is limited in $Z/\gamma + jet$ events, *multijet* events are used along with modified balancing methods [61, 69]. The in-situ calibration is the last step for jet reconstruction(see Figure 5.7), after which the refined physics jets are corrected to *final scale*.

#### 5.5.2.2 Energy Resolution Correction

The *dijet* balance method is used for the determination of the JER, based on the momentum conservation in the transverse plane [70]. The asymmetry between the $p_T$'s of two leading jets in a *dijet* system is defined as

$$A(p_T^{j_1}, p_T^{j_2}) = \frac{p_T^{j_1} - p_T^{j_2}}{p_T^{j_1} + p_T^{j_2}} \tag{5.18}$$

where $p_T^{j_1}$ and $p_T^{j_2}$ are randomly ordered. The resolution of $A(p_T^{j_1}, p_T^{j_2})$, $\sigma_A$, is chosen to be the width of a Gaussian fit to the distribution of $A(p_T^{j_1}, p_T^{j_2})$. If the event has exactly two back-to-back jets that satisfying momentum conservation in the transverse plane, and requiring both jets to be in the same $\eta$ region, the relation between $\sigma_A$ and the fractional $p_T$ resolution is given by

$$\sigma_A = \frac{\sqrt{\sigma^2_{p_T^{j_1}} + \sigma^2_{p_T^{j_2}}}}{\left\langle p_T^{j_1} + p_T^{j_2} \right\rangle} \simeq \frac{1}{\sqrt{2}} \frac{\sigma_{p_T}}{p_T} \tag{5.19}$$

where $\sigma_{p_T^{j_1}} = \sigma_{p_T^{j_2}} = \sigma_{p_T}$. The JER, $\frac{\sigma_E}{E}$, is then equivalent to $\frac{\sigma_{p_T}}{p_T}$.

#### 5.5.2.3 Correction for Jet Vertex Fraction

To further suppress *pile-up* effects, a discriminant jet vertex fraction (JVF) is defined for each jet with respect to each PV [71]. Tracks are matched to each jet within

$\Delta R(track, jet) \leqslant 0.4$ then used to calculate the fraction of track $p_T$ from each PV. For a single jet $j_a$, the JVF with respect to the vertex $v_b$ in the event is written in Equation 5.20. Figure 5.8 shows a scheme of the JVF definition.

$$JVF\left(j_a, v_b\right) = \frac{\sum_k p_T\left(trk_k^{j_a}, v_b\right)}{\sum_n \sum_l p_T\left(trk_l^{j_a}, v_n\right)} \tag{5.20}$$

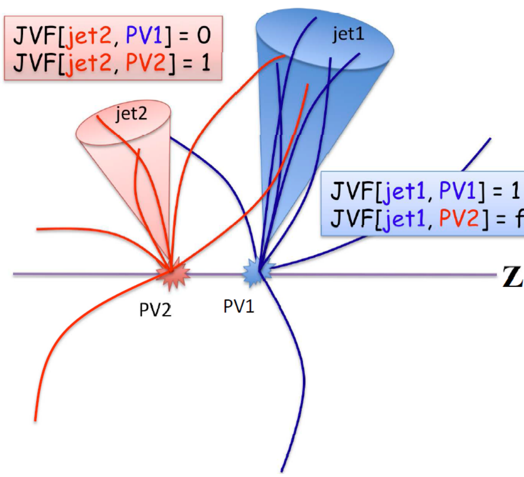


Figure 5.8: Schematic representation of the JVF discriminant corresponding to the fraction of a jet originating from $vtx_i$.

## 5.6 Missing Transverse Energy and Momentum

The reconstructed missing transverse energy ($\not{E}_T$) has two constituents — one that is produced by particles weakly interacting with the detector (true $\not{E}_T$, $\not{E}_T{}^{\text{true}}$), such as $\nu$ or escaping particles; and the other one due to detector inefficiencies and resolution (fake $\not{E}_T$, $\not{E}_T{}^{\text{fake}}$). A very good measurement of the $\not{E}_T$ is essential for many physics studies in ATLAS. An event with large $\not{E}_T$ is the key signature in this analysis. An important requirement on the measurement of $\not{E}_T$ is to minimize the effect that produces $\not{E}_T{}^{\text{fake}}$, such as detector inefficiencies, resolution limits, and *pile-up* challenge. During reconstruction, the calorimeter plays a crucial role, based on which two $\not{E}_T$ reconstruction algorithms are developed, *Cell-based* and *Object-based*. The cell-based algorithm directly makes use of energy deposits in calorimeter cells that passes a noise suppression procedure, while the object-based algorithm relies on the reconstructed, calibrated, and identified objects in the event. It is proved that the object-based method is more reliable to reconstruct events with abundant low-$p_T$ objects, such as in the case of high *pile-up* [61]. Thus, this analysis adopts the object-based algorithm as the $\not{E}_T$ reconstruction method.

### 5.6.1 Missing Transverse Energy

The object-based reconstruction algorithm firstly define *topo-clusters* in calorimeter as in the jet reconstruction [48], then apply a noise suppression method based on defined *topo-clusters* [61]. The cells that constitute the *topo-clusters* are hereafter called *topo-cells*.

Secondly, the algorithm uses the *topo-clusters* to calculate all contribution to identified and calibrated objects, following this specific order [72]: $e$, $\gamma$, hadronically decaying $\tau$, jets and $\mu$, which are reconstructed with information from all the sub-detectors. Each *topo-cluster* only matches to the first object that associates to it. *Topo-clusters* and tracks not associated to the above high-$p_T$ objects are further identified as low-$p_T$ objects (e.g. mini-jets). The final remaining *topo-cells* are calibrated and added to the $\not{E}_T$ calculation as well. Products of low-$p_T$ objects are generally called "SoftTerms".

Finally, the $\not{E}_T$ is calculated as the negative vectorial sum of all the momenta in the transverse plane, under the assumption of momentum conservation, which is expressed as:

$$\not{E}_{T\,x,y} = -\left(E^{e}_{x,y} + E^{\gamma}_{x,y} + E^{\tau}_{x,y} + E^{j}_{x,y} + E^{\mu}_{x,y} + E^{\text{SoftTerm}}_{x,y}\right) \tag{5.21}$$

where $E^{\mu}_{x,y}$ removes energy loss in calorimeter to avoid double counting, if CB muons are used. $\not{E}_T$ is reconstructed by the `METRefFinal` algorithm (provided by the performance group) in this analysis, using all reconstructed and calibrated physics objects described in previous sections, in full $\phi$-angle and $|\eta| < 4.9$

In order to reduce the sensitivity to mis-measured leptons or jets, this analysis uses a modified $\not{E}_T$ called relative missing transverse energy ($\not{E}_T^{rel}$), which is the projection of the $\not{E}_T$ to the closest selected lepton or jet in the transverse plane, as defined in Equation 5.22 and illustrated in Figure 5.9.

$$\not{E}_T^{rel} = \begin{cases} \not{E}_T \times \sin\left(\Delta\phi_{\ell,j}\right) & \text{if } \Delta\phi_{\ell,j} < \pi/2 \\ \not{E}_T & \text{if } \Delta\phi_{\ell,j} \geq \pi/2 \end{cases} \tag{5.22}$$

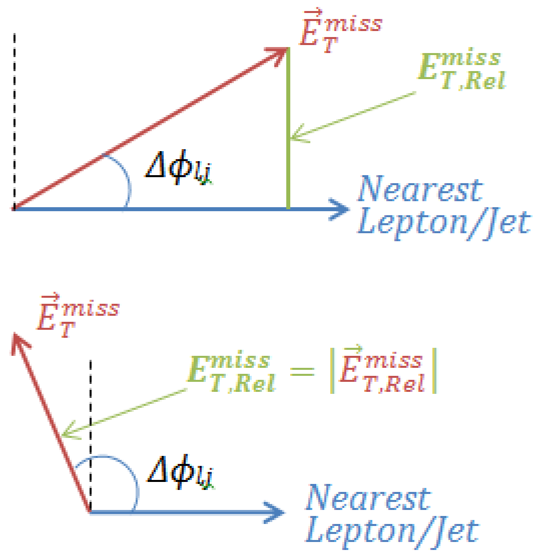


Figure 5.9: $\not{E}_T^{rel}$ definition

Since $\not{E}_T$ sums the $E_T$ of all recorded objects, the energy scale and resolution corrections of each object ($e$, $\mu$, $jet$) must be propagated to $\not{E}_T$ , including: the energy scale correction applied to observed electron as well as the energy smearing applied to simulated electrons as described in Section 5.3.5, the momentum smearing applied to MC muons as described in Section 5.4.5, and the jet calibration corrections applied to observed jets as described in Section 5.5.2.1.

### 5.6.2 Missing Transverse Momentum

The calorimeter based measurement of $\not{E}_T$ suffers a lot from *pile-up* in the form of large amount of low-$p_T$ deposits in the calorimeter. This worsens the resolution of the $\not{E}_T$ measurement and the suppression of $Z$+*jets* background (see Section 8.1). Therefore, the missing transverse momentum ($\not{p}_T$) is defined using ID information, providing an alternative to $\not{E}_T$ with higher resolution for low-$p_T$ objects and uncorrelated systematic effects. It is defined analogously to the $\not{E}_T$ as the negative vectorial sum of all ID tracks satisfying:

- $p_T > 500\ MeV$
- $|\eta| < 2.5$

- $|d_0| < 1.5\ mm$
- $|z_0 \sin\theta| < 1.5\ mm$
- $n^{\text{hit}}_{\text{Pixel}} \geq 1$
- $n^{\text{hit}}_{\text{SCT}} \geq 6$

The ID tracks from the signal leptons are included regardless of their quality. For signal electrons, the ID-track based $p_T$ is replaced by the EM-cluster based $E_T$; while for signal muons, the ID track is replaced by the CB track.

The $\not{p}_T$ relies on the ID therefore only includes charged particles within $|\eta| < 2.5$. However, it is expected to be more *pile-up* robust since it uses tracks originating from the PV; also it excludes track-free photons and neutral hadrons which lower the $\sum p_T$, thus improves resolution. It is often used in parallel with $\not{E}_T$ to discriminate *pile-up* suffered backgrounds, such as $Z$+*jets* and *Top*.

### 5.6.3 Azimuthal Angle between Missing Transverse Energy and Momentum

The azimuthal angle between $\not{E}_T$ and $\not{p}_T$, $\Delta\phi(\not{p}_T, \not{E}_T)$, is defined to further suppress the $Z$+*jets* background. Generally, if the $\not{E}_T$ and $\not{p}_T$ are real, they are not the same vector but their directions are collinear, yielding a concentrated $\Delta\phi(\not{p}_T, \not{E}_T)$ around 0. However, in a high *pile-up* environment, the reconstructed $\not{E}_T$ for $Z \to ee$ and $Z \to \mu\mu$ events are generally fake, thus $\Delta\phi(\not{p}_T, \not{E}_T)$ in such events loses polarization, tending to be uniformly distributed. On the contrary, $WW$ signal events contain real $\not{E}_T$ due to the escaping neutrinos, thus both the $\not{E}_T$ and $\not{p}_T$ tend to remain collinear, leading to concentrated $\Delta\phi(\not{p}_T, \not{E}_T)$ at small values.

## 5.7 Object Overlap Removal

When all physics object are reconstructed, an overlap removal procedure is applied to avoid double counting, in which case one real particle is reconstructed to two or more objects . 4 schemes of object overlap removal are considered: $e/e$, $\mu/e$, $e/jet$ and $\mu/jet$. This procedure is usually done after object selection.

By far the most important one is the $e/jet$ overlap removal: any calorimeter cluster associated with a high-$p_T$ electron will also be reconstructed by the anti-$k_T$ algorithm. So jets inside a cone of $\Delta R < 0.3$ around the selected electrons need to be removed.

However, when considering calorimeter isolation for electrons, the jet energy from remaining clusters is not ignored.

The other 3 overlap removal schemes are meant to deal with rare problems, hence have little effect with the current selection, except in the case of loosened object quality criteria (e.g. in the *tag-and-probe* method). Detailed overlap removal rules are listed at the end of Section 7.1.

CHAPTER 6

# $WW$ Analysis Overview

This measurement of $W^+W^-$ production cross section uses data collected in 2012 at a CM energy of $\sqrt{s} = 8\ TeV$ in $pp$ collisions by the ATLAS experiment. Data events were used based on a data-quality flag, the Good Run List (GRL) definition, per luminosity block. The corresponding total integrated luminosity passing GRL in this analysis is 20.3 $fb^{-1}$ , as determined by the standard ATLAS tool for luminosity calculation. According to the The ATLAS Luminosity Measurement Task Force, the uncertainty of the integrated luminosity is 2.8% and is dominated by the knowledge of the LHC beam currents.

In this Chapter, an overview of the $WW$ analysis is presented, including the theoretical cross section calculations and modeling, the dominated background and simulations, the method for cross section measurements, and the strategy of probing aTGCs.

## 6.1 Theoretical $W^+W^-$ Cross Section

The theoretical cross section of $W^+W^-$ production at leading order (LO) included all the Feynman diagrams shown in Figure 2.2. NLO and NNLO calculations were performed for more precise predictions. Figure 6.1 shows some examples of NLO Feynman diagrams for $q\bar{q} \to W^+W^-$ processes. The NNLO cross section for on-shell $W^+W^-$ pair production has been presented in a recent paper [73]. Table 6.1 summarizes the predicted cross sections for various $W^+W^-$ production processes.

The partial NNLO (pNNLO) cross section for total $W^+W^-$ production includes the NLO $qq$ and LO continuum $gg$ cross sections, while the full NNLO cross section incorporates the NNLO $qq$ cross section. In addition, the NNLO $gg \to H \to WW$ cross section is included in both cases. The corresponding calculations with **MCFM** are presented in details in Section 6.2.

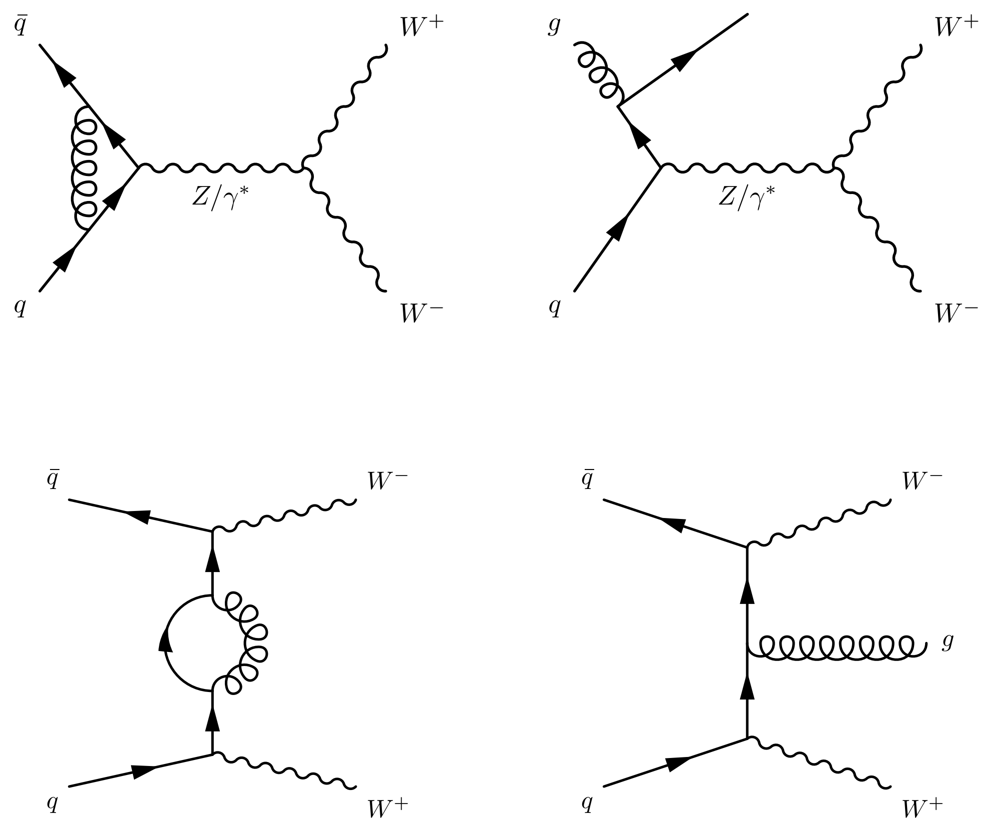


Figure 6.1: Example of NLO Feynman diagrams for $W^+W^-$ pair production contributed from $q\bar{q}$ initial state at the LHC.

The full NNLO cross section is used as a reference and compared with the measured total cross section. The pNNLO calculation provided by the available MC generators to date is the best option by far for the MC event normalization, fiducial measurements and the extrapolation from fiducial region to total phase space (Section 6.2).

In addition to the chosen $W^+W^-$ production processes as shown in Figure 2.2, there are several additional small contributions which are not included in this analysis. These contributions are listed in Table 6.2 with detailed description below.

- Higher-order corrections to the $gg \to W^+W^-$ could increase its cross section by a factor of 2-3 [75] (based on $gg \to H \to WW$ calculations), resulting in a total cross section higher by 2.8 $pb$. Nevertheless, this high-order correction has not been available and is not covered by the quoted scale uncertainty, since it is

| Process | $\sigma$ [$pb$] | $\Delta_\sigma^{Total}$ [$pb$] | $\Delta_\sigma^{\text{Scale}}$ | $\Delta_\sigma^{\text{PDF}}$ | $\Delta_\sigma^{\text{Br}}$ | Calculation |
|---|---|---|---|---|---|---|
| (1) $q\bar{q} \to WW$ | 53.2 | $^{+2.5}_{-2.2}$ | $^{+2.3}_{-1.9}$ | $^{+1.0}_{-1.1}$ | - | NLO MCFM |
| (2) $gg \to WW$ | 1.4 | $^{+0.3}_{-0.2}$ | $^{+0.3}_{-0.2}$ | $^{+0.1}_{-0.1}$ | - | LO MCFM |
| (3) $q\bar{q} \to WW$ | 59.1 | $^{+1.6}_{-1.7}$ | $^{+1.2}_{-1.0}$ | $^{+0.9}_{-0.9}$ | | NNLO [73] |
| (4) $gg \to H \to WW$ | 4.1 | $\pm 0.5$ | $\pm$ 0.3 | $\pm 0.3$ | $\pm 0.2$ | NNLO [73, 74] |
| $W^+W^-$ production (pNNLO) | 58.7 | $^{+3.0}_{-2.7}$ | $^{+2.7}_{-2.3}$ | $^{+1.3}_{-1.4}$ | | (1)+(2)+(4) |
| $W^+W^-$ production (NNLO) | 63.2 | $^{+2.0}_{-1.8}$ | $^{+1.6}_{-1.4}$ | $^{+1.2}_{-1.2}$ | | (3)+(4) |

Table 6.1: Predicted cross sections for various $W^+W^-$ production processes. The first row gives the predicted cross sections for the non-resonant $q\bar{q} \to W^+W^-$ production with the uncertainty from scales, PDFs and $\alpha_s$ variations shown in $pb$. The second and fourth rows show the predicted cross section for the non-resonant $gg \to W^+W^-$ and the resonant $gg \to H \to W^+W^-$ with error decomposition. The NNLO cross section and its uncertainties for $q\bar{q} \to W^+W^-$ production are given in the third row, with the scale uncertainty coming from the NNLO paper while the PDFs uncertainty taken from the corresponding NLO calculation. The partial and full NNLO cross sections for $W^+W^-$ production are shown in the fifth and sixth rows, the uncertainties of non-resonant ($qq + gg$) and resonant (through Higgs decays) $W^+W^-$ productions are combined linearly. Notice that, the BR uncertainty of (4) is assimilated into the scale uncertainty in quadrature during combination.

only evaluated at LO, therefore might be underestimated.

- The effect of NLO EW corrections on the $W^+W^-$ production cross section is neglected [76] in expected event yield normalization. Note that the EW correction is considered in the signal acceptance calculation on NLO MC samples so that this known effect is propagated into the extraction of measured cross sections.

- The contribution of $\gamma\gamma$-induced $W^+W^-$ production is expected to be negligible [76, 77].

- The contribution of vector boson scattering (VBS) is neglected due to the small production rate [78].

- The contribution of double parton interactions (DPIs) is found to be negligible [79]. An alternative check using Pythia generated samples with full $W^+W^-$ selection applied found that, the contribution is at per-mil level.

- Besides $gg \to H \to WW$, there are additional Higgs processes producing $WW$ pairs: vector boson fusion (VBF) Higgs production, and associated Higgs productions of $WH$, $ZH$ and $t\bar{t}H$. The relative event rate from these processes is expected very low [73, 74]. The final contribution in fiducial volume is found to be at per-mil level.

| **Total prediction for $WW$ production** | | |
|---|---|---|
| Process | cross section [$pb$] | Calculation |
| Total $WW$ (pNNLO) | $58.7^{+3.0}_{-2.7}$ | see Table 6.1 |
| Total $WW$ (NNLO) | $63.2^{+2.0}_{-1.8}$ | see Table 6.1 |
| **Neglected estimated contributions to $WW$ production:** | | |
| Process | Estimated change in $\sigma^{\text{total}}$ [$pb$] | Calculation |
| $gg \to W^+W^-$ | up to +2.8 | see Reference [75] |
| $WW$ (NLO EW Corr.) | -0.5 | see Reference [76] |
| $\gamma\gamma$-induced $WW$ | +0.5 | see Reference [76, 77] |
| VBS topology | <+0.5 | see Reference [78] |
| DPI | +0.3 | see Reference [80] |
| VBF Higgs, $WH$, $ZH$ | +0.6 | see Reference [73, 74] |

Table 6.2: Summary of the possible additional contributions to the $WW$ production cross section that are neglected in the analysis. The quoted total $W^+W^-$ production cross sections in this analysis are listed in top rows for reference.

## 6.2 Signal Monte-Carlo Modelling

The NLO MC generator Powheg is used to model $q\bar{q} \to W^+W^- \to \ell^+\nu_\ell\ell^-\bar{\nu}_\ell$ and is interfaced to Pythia for parton showering. The **gg2WW** program is used to model $gg \to W^+W^- \to \ell^+\nu_\ell\ell^-\bar{\nu}_\ell$ and is interfaced to Herwig/Jimmy program for parton showering. To be consistent with other ATLAS di-boson analyses and to prepare for a future consistent SM cross section combination with CMS, the $qq/gg$ signal-yield normalization is derived using **MCFM** and CT10 PDFs. The $gg \to H \to W^+W^- \to \ell^+\nu_\ell\ell^-\bar{\nu}_\ell$ is modelled again with Powheg interfaced to Pythia, which is normalized following the recommendations of the *LHC Higgs Cross Section Working Group*, yielding a cross section of $19.27 \pm 2.9$ $pb$ [73, 74] and a $H \to W^+W^-$

branching ratio of 21.5 ± 0.9% [81] at $M_H = 125\ GeV$. Adding the uncertainties in quadrature yields a $gg \to H \to WW$ cross section of 4.1 ± 0.5 $pb$. For these signal samples, the **AU2-CT10** underlying-event tune is used for Pythia, while **AUET2-CT10** is used for Herwig.

A summary for the above mentioned $W^+W^-$ production cross sections is provided in Table 6.3. The resulting total signal cross section is $58.7^{+3.0}_{-2.7}\ pb$, where the non-resonant-$WW$ ($qq + gg$) and resonant production cross section uncertainties have been added linearly.

| Process | $\sigma$ [$pb$] | $\epsilon_{\text{filter}}$ | $N_{\text{MC}}$ | Generator | $\mu_R = \mu_F$ | Parton Showerer |
|---|---|---|---|---|---|---|
| $q\bar{q} \to W^+W^- \to e^+\nu e^-\nu$ | 0.62 | 1.0 | 299700 | Powheg | $M^*_W$ | Pythia |
| $q\bar{q} \to W^+W^- \to \mu^+\nu\mu^-\nu$ | 0.62 | 1.0 | 300000 | Powheg | $M^*_W$ | Pythia |
| $q\bar{q} \to W^+W^- \to e^+\nu\mu^-\nu$ | 0.62 | 1.0 | 299999 | Powheg | $M^*_W$ | Pythia |
| $q\bar{q} \to W^+W^- \to \mu^+\nu e^-\nu$ | 0.62 | 1.0 | 300000 | Powheg | $M^*_W$ | Pythia |
| $q\bar{q} \to W^+W^- \to e^+\nu\tau^-\nu$ | 0.62 | 1.0 | 299996 | Powheg | $M^*_W$ | Pythia |
| $q\bar{q} \to W^+W^- \to \mu^+\nu\tau^-\nu$ | 0.62 | 1.0 | 299999 | Powheg | $M^*_W$ | Pythia |
| $q\bar{q} \to W^+W^- \to \tau^+\nu\mu^-\nu$ | 0.62 | 1.0 | 300000 | Powheg | $M^*_W$ | Pythia |
| $q\bar{q} \to W^+W^- \to \tau^+\nu e^-\nu$ | 0.62 | 1.0 | 299999 | Powheg | $M^*_W$ | Pythia |
| $q\bar{q} \to W^+W^- \to \tau^+\nu\tau^-\nu$ | 0.62 | 1.0 | 299999 | Powheg | $M^*_W$ | Pythia |
| $gg \to W^+W^- \to e^+\nu e^-\nu$ | 0.017 | 1.0 | 30000 | **gg2WW** | $M_W$ | Herwig/Jimmy |
| $gg \to W^+W^- \to \mu^+\nu\mu^-\nu$ | 0.017 | 1.0 | 30000 | **gg2WW** | $M_W$ | Herwig/Jimmy |
| $gg \to W^+W^- \to e^+\nu\mu^-\nu$ | 0.017 | 1.0 | 30000 | **gg2WW** | $M_W$ | Herwig/Jimmy |
| $gg \to W^+W^- \to \mu^+\nu e^-\nu$ | 0.017 | 1.0 | 30000 | **gg2WW** | $M_W$ | Herwig/Jimmy |
| $gg \to W^+W^- \to e^+\nu\tau^-\nu$ | 0.017 | 1.0 | 30000 | **gg2WW** | $M_W$ | Herwig/Jimmy |
| $gg \to W^+W^- \to \mu^+\nu\tau^-\nu$ | 0.017 | 1.0 | 30000 | **gg2WW** | $M_W$ | Herwig/Jimmy |
| $gg \to W^+W^- \to \tau^+\nu\mu^-\nu$ | 0.017 | 1.0 | 30000 | **gg2WW** | $M_W$ | Herwig/Jimmy |
| $gg \to W^+W^- \to \tau^+\nu e^-\nu$ | 0.017 | 1.0 | 30000 | **gg2WW** | $M_W$ | Herwig/Jimmy |
| $gg \to W^+W^- \to \tau^+\nu\tau^-\nu$ | 0.017 | 1.0 | 30000 | **gg2WW** | $M_W$ | Herwig/Jimmy |
| $gg \to H \to W^+W^- \to \ell\nu\ell\nu$ | 0.43492 | 0.49105 | 500000 | Powheg | $M_H/2$ | Pythia |

Table 6.3: The $W^+W^-$ signal production processes, cross sections and numbers of fully simulated MC events. The MC simulation "filter" is an event selection at the generator level. The corresponding filter efficiencies $\epsilon_{\text{filter}}$ are given in the table. `CT10` PDFs is used for all $WW$ generators here. Renormalization and Factorization scales without star sign indicate fixed scales are used. The starred version represents that the scales used by the generator are dynamic, which are set to be half the invariant mass of the final state lepton system. The $M_H$ is set to be 125 $GeV$.

To assess the systematic uncertainties of the theoretical prediction for $W^+W^-$ production, different contributions from PDFs, scales, and the strong coupling constant $\alpha_S$ are considered. **MCFM** is again used in this uncertainty study. The impact from different PDF sets on the prediction provides the PDF uncertainty, which is given in Table 6.4. The PDF uncertainties are $^{+1.8}_{-2.0}\%$ with respect to the central value of the cross section.

| | CT10 | NNPDF | MSTW2008 | ATLAS-epWZ |
|---|---|---|---|---|
| $q\bar{q} + gg$ xsec $[fb]$ | $637 \pm 1$ | $641 \pm 1$ | $649 \pm 2$ | $671 \pm 1$ |
| Deviation from CT10 [%] | 0.0 | 0.6 | 1.9 | 5.3 |
| $gg$ contribution [%] | 2.65 | 2.80 | 2.75 | 2.27 |
| PDF uncertainty $[fb]$ | $^{+12}_{-13}$ | $\pm 10$ | $^{+12}_{-9}$ | $^{+9}_{-10}$ |
| PDF uncertainty [%] | $^{+1.8}_{-2.0}$ | $\pm 1.5$ | $^{+1.9}_{-1.4}$ | $^{+1.3}_{-1.4}$ |

Table 6.4: **MCFM** cross section predictions for $q\bar{q} + gg \to W^+W^- \to \ell^+\nu_\ell\ell^-\bar{\nu}_\ell$ using different PDF sets. Cross section uncertainties given are statistical only. The CT10 PDF uncertainties have been divided by 1.645 to scale from 90% CL to 68% CL.

The impact of renormalization ($\mu_R$) and factorization ($\mu_F$) scales are varied *independently* by a factor of 2 to determined the scale uncertainty, which is shown in Table 6.5, yielding uncertainties of $^{+4.0}_{-3.5}\%$ with respect to the central value of the cross section.

| | $0.5 * \mu_R$ | $1 * \mu_R$ | $2 * \mu_R$ |
|---|---|---|---|
| $0.5 * \mu_F$ | 3.25% | -0.39% | -3.48% |
| $1 * \mu_F$ | 3.52% | 0.00% | -2.79% |
| $2 * \mu_F$ | 3.99% | 0.31% | -2.42 % |

Table 6.5: Dependence of the **MCFM** cross section predictions for $q\bar{q} + gg \to W^+W^- \to \ell^+\nu_\ell\ell^-\bar{\nu}_\ell$ on the variation of the renormalization ($\mu_R$) and factorisation ($\mu_F$) scales by factors of 2. Using the maximum and minimum values to construct the uncertainty envelope yields a scale uncertainty of +4.0% and −3.5%. The default scales used in **MCFM** are the dynamic scale of half the invariant mass of the final state system $0.5m(3456)$.

To assess the impact of $\alpha_S$ used in the PDFs, the $\alpha_S$ is varied by $\pm 0.001$ from its default value of 0.118. This yields a variation of the cross section by $^{+0.5}_{-0.3}\%$, small compared to the PDF uncertainty of $^{+1.8}_{-2.0}\%$.

Adding scale, PDF and $\alpha_S$ uncertainties in quadrature yields a total uncertainty of $^{+4.4\%}_{-4.0\%}$. Then dividing the **MCFM** prediction by $Br(W \to \ell\nu)^2 = 0.108^2$ yields the total cross section prediction $54.6^{+2.4}_{-2.2}\ pb$.

## 6.3 Background for $W^+W^-$ signal with $\ell^+\ell^- + \not{E}_T$ final state

As discussed in Section 2.2.2, the fully leptonic decay channel, $W^+W^- \to \ell^+\nu_\ell\ell^-\bar{\nu}_\ell$ for $\ell \in \{e, \mu\}$, has been chosen for the $W^+W^-$ production cross section measurement. The experimental signal signature is two energetic leptons (including $\tau$ decayed $e$ or $\mu$ from $WW \to \tau\nu\tau\nu$ or $WW \to \ell\nu\tau\nu$ for $\ell \in \{e, \mu\}$) with high transverse momentum ($p_T$) and large transverse missing energy ($\not{E}_T$) in the final state. The background events from $t\bar{t}$ and $Wt$ processes will also have two $W$ bosons with associated $b$-jets in final state. Events from these processes are not considered as the $W^+W^-$ signal, and can be suppressed by vetoing on the presence of any jets (jet-veto).

Other background processes can produce $\ell^+\ell^- + \not{E}_T$ final states, either from genuine physics process or detector effects. The background contributions from different processes for $W^+W^-$ detection are listed below. Figure 6.2 shows the LO Feynman diagrams for those background processes.

- Drell-Yan: jet associated $Z$ production (Figure 6.2(a)) decaying leptonically with $\not{E}_T$ due to mis-measurement, *pile-up* or particles escaping down the beam line;
- *Top*: $t\bar{t}$ (Figure 6.2(c)) and single-*Top* ($Wt$, Figure 6.2(d)) production generating real $W$ pairs but without high energetic jets detected, thus passing jet-veto requirement;
- $W$+*jets*: jet associated $W$ production (Figure 6.2(b)) decaying leptonically ($\ell + \nu$) with an associated jet mis-identified as a lepton;
- Di-boson production (Figure 6.2(e)):
  - $WZ \to \ell\ell\ell\nu$ with one lepton not detected;
  - $W\gamma$: $W\gamma$ production with the $\gamma$ identified as an electron;
  - $W\gamma^* \to \ell\nu\ell\ell$ with one lepton not detected, where the $\gamma^*$ is a virtual massive photon and decays to $\ell^+\ell^-$ (internal conversion) [82];
  - $ZZ \to \ell\ell\nu\nu, \ell\ell\ell\ell$ with leptons poorly or not detected;
- *Multijet* production: QCD *multijet* process (Figure 6.2(f)) with $\not{E}_T$ and both leptons mis-identified from jets.

The signal and background contributions expected from the data are mainly modelled with MC simulations corrected using control data samples of $Z \to \ell^+\ell^-$ and $W^\pm \to \ell^\pm\nu$. The multi-jets and $W$+*jets* background are estimated from data since the rare fragmentation effects leading to a jet-misidentified lepton are not reliably modelled in the simulation, thus a fully data-driven method is used (see Section 8.2). The Drell-Yan background and *Top* background are also estimated using data-driven techniques (see Section 8.1 and Section 8.3), and compared with MC estimated results.

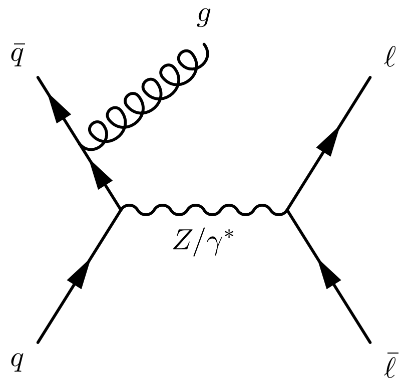


(a) $Z$+*jets*

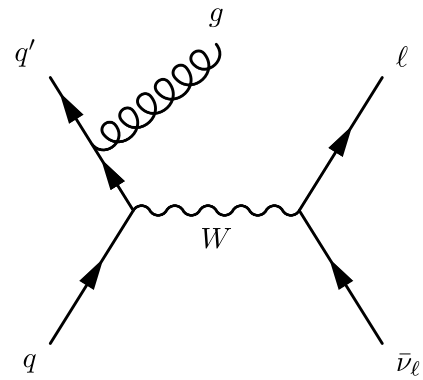


(b) $W$+*jets*

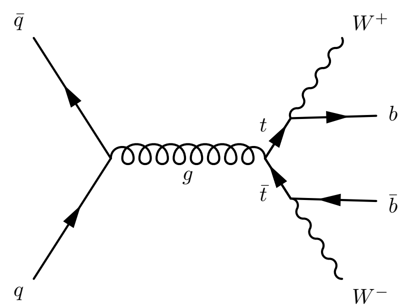


(c) $t\bar{t}$

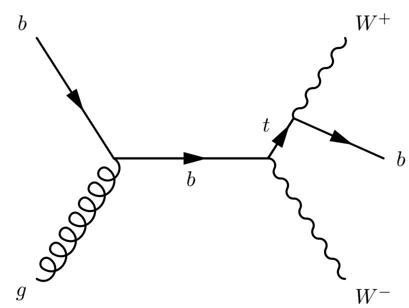


(d) $Wt$

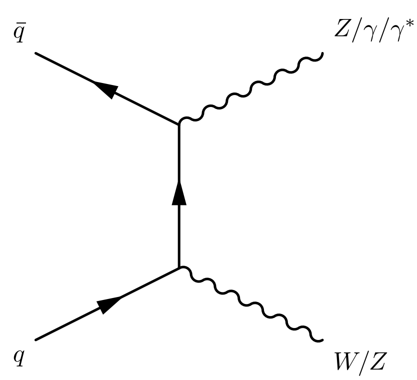


(e) Di-boson $t$-channel

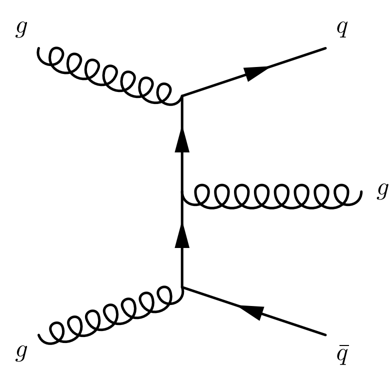


(f) Multijet

Figure 6.2: Example Feynman diagrams for $W^+W^-$ production backgrounds at the LHC.

### 6.3.1 Background MC Modelling

The cross sections of major backgrounds from different processes, with the used generators, $\epsilon_{\text{filter}}$'s and total number of simulated events are described in this section. Whenever LO event generators are used, the cross sections are corrected by using k-factors to NLO or NNLO (if available) ME calculations.

The $V + jets$ for $V \in (W, Z)$ samples are categorized into two types: light-flavor jets and heavy-flavor ($b$ and $c$) jets. The ALPGEN generator with CTEQ6L1 PDFs is used for $V + jets$, then interfaced to HERWIG/JIMMY for parton showering with **AUET2-CT10** tuning. Specifically for the $Z$+$jets$ samples which has large cross section, the LO PDF CTEQ6L1 is re-weighted to the NLO PDF CT10 in order to better model the lepton $\eta$ distributions at pre-selection level. In the produced heavy-flavor samples, ALPGEN does not match heavy-flavor jets explicitly, causing the same heavy-flavour jets appearing in multiple samples when they are combined together; therefore a heavy flavour overlap removal tool is applied (see Section 7.2). Tables 6.6 and 6.7 summarize the light-flavor samples for $Z$+$jets$ and $W$+$jets$, respectively. Table 6.8 summarize the heavy-flavour jet samples.

The $Top$ samples are listed in Table 6.9, including both $t\bar{t}$ and $Wt$ quark production. **MC@NLO** is the generator for $Top$ events, with the exception of $t$-channel $Wt$ events modelled with **AcerMC**.

The di-boson processes $WZ$, $ZZ$ and $W\gamma$ are modelled with POWHEG, POWHEG and ALPGEN, respectively (Table 6.10). For $W\gamma^*$, in the internal conversion scenario, $e^+e^-$, $\mu^+\mu^-$ and even $\tau^+\tau^-$ decays occur with substantial probability, yielding a significant background. To correctly describe high lepton $p_T$ behavior, $W\gamma^*$ samples are generated with SHERPA including up to one additional parton in the ME for each of the three photon leptonic final states. The $W\gamma^*$ production with SHERPA potentially includes events generated in the POWHEG + PYTHIA samples of $WZ$ events. To avoid double counting, the $W\gamma^*$ events are required a limit of $M_{\gamma^*} < 7\ GeV$ while the $WZ$ samples are required a limit of $M_{\gamma^*} > 7\ GeV$ (see Section 7.2).

## 6.4 Cross-section Extraction

A *fiducial cross section* is determined from the measurement within the experimental fiducial volume, which will be defined in Section 7.6. The uncertainty of the fiducial cross section measurement is mainly from the experimental uncertainties. To obtain a total cross section, the fiducial cross section is extrapolated into the full phase space,

| Process | $\sigma$ [$pb$] | k-factor | $\epsilon_{\text{filter}}$ | $N_{\text{MC}}$ |
|---|---|---|---|---|
| $Z(\rightarrow ee)$ + Np0($M > 60$ $GeV$) | 718.89 | 1.18 | 1 | 6619984 |
| $Z(\rightarrow ee)$ + Np1($M > 60$ $GeV$) | 175.6 | 1.18 | 1 | 1329498 |
| $Z(\rightarrow ee)$ + Np2($M > 60$ $GeV$) | 58.849 | 1.18 | 1 | 404998 |
| $Z(\rightarrow ee)$ + Np3($M > 60$ $GeV$) | 15.56 | 1.18 | 1 | 109999 |
| $Z(\rightarrow ee)$ + Np4($M > 60$ $GeV$) | 3.9322 | 1.18 | 1 | 30000 |
| $Z(\rightarrow ee)$ + Np5($M > 60$ $GeV$) | 1.1994 | 1.18 | 1 | 10000 |
| $Z(\rightarrow \mu\mu)$ + Np0($M > 60$ $GeV$) | 718.91 | 1.18 | 1 | 6608490 |
| $Z(\rightarrow \mu\mu)$ + Np1($M > 60$ $GeV$) | 175.81 | 1.18 | 1 | 1334697 |
| $Z(\rightarrow \mu\mu)$ + Np2($M > 60$ $GeV$) | 58.805 | 1.18 | 1 | 404995 |
| $Z(\rightarrow \mu\mu)$ + Np3($M > 60$ $GeV$) | 15.589 | 1.18 | 1 | 110000 |
| $Z(\rightarrow \mu\mu)$ + Np4($M > 60$ $GeV$) | 3.9072 | 1.18 | 1 | 30000 |
| $Z(\rightarrow \mu\mu)$ + Np5($M > 60$ $GeV$) | 1.1933 | 1.18 | 1 | 10000 |
| $Z(\rightarrow \tau\tau)$ + Np0($M > 60$ $GeV$) | 718.85 | 1.18 | 1 | 6615490 |
| $Z(\rightarrow \tau\tau)$ + Np1($M > 60$ $GeV$) | 175.83 | 1.18 | 1 | 1334998 |
| $Z(\rightarrow \tau\tau)$ + Np2($M > 60$ $GeV$) | 58.63 | 1.18 | 1 | 405000 |
| $Z(\rightarrow \tau\tau)$ + Np3($M > 60$ $GeV$) | 15.508 | 1.18 | 1 | 108999 |
| $Z(\rightarrow \tau\tau)$ + Np4($M > 60$ $GeV$) | 3.9526 | 1.18 | 1 | 30000 |
| $Z(\rightarrow \tau\tau)$ + Np5($M > 60$ $GeV$) | 1.1805 | 1.18 | 1 | 10000 |
| $Z(\rightarrow ee)$ + Np0($10 < M < 60$ $GeV$) | 3477.9 | 1.19 | 0.01045 | 6994180 |
| $Z(\rightarrow ee)$ + Np1($10 < M < 60$ $GeV$) | 108.72 | 1.19 | 0.20383 | 4497280 |
| $Z(\rightarrow ee)$ + Np2($10 < M < 60$ $GeV$) | 52.837 | 1.19 | 0.13841 | 1468393 |
| $Z(\rightarrow ee)$ + Np3($10 < M < 60$ $GeV$) | 11.291 | 1.19 | 0.20806 | 438397 |
| $Z(\rightarrow ee)$ + Np4($10 < M < 60$ $GeV$) | 2.5852 | 1.19 | 0.25262 | 108930 |
| $Z(\rightarrow ee)$ + Np5($10 < M < 60$ $GeV$) | 0.6937 | 1.19 | 1.0 | 112180 |
| $Z(\rightarrow \mu\mu)$ + Np0($10 < M < 60$ $GeV$) | 3477.7 | 1.19 | 0.01086 | 6984686 |
| $Z(\rightarrow \mu\mu)$ + Np1($10 < M < 60$ $GeV$) | 108.74 | 1.19 | 0.21096 | 4491587 |
| $Z(\rightarrow \mu\mu)$ + Np2($10 < M < 60$ $GeV$) | 52.814 | 1.19 | 0.14253 | 1503397 |
| $Z(\rightarrow \mu\mu)$ + Np3($10 < M < 60$ $GeV$) | 11.299 | 1.19 | 0.21385 | 439699 |
| $Z(\rightarrow \mu\mu)$ + Np4($10 < M < 60$ $GeV$) | 2.5793 | 1.19 | 0.25869 | 108890 |
| $Z(\rightarrow \mu\mu)$ + Np5($10 < M < 60$ $GeV$) | 0.69373 | 1.19 | 0.69373 | 115000 |
| $Z(\rightarrow \tau\tau)$ + Np0($10 < M < 60$ $GeV$) | 3477.9 | 1.19 | 0.00002 | 27969 |
| $Z(\rightarrow \tau\tau)$ + Np1($10 < M < 60$ $GeV$) | 108.71 | 1.19 | 0.00136 | 30000 |
| $Z(\rightarrow \tau\tau)$ + Np2($10 < M < 60$ $GeV$) | 52.827 | 1.19 | 0.00174 | 27610 |
| $Z(\rightarrow \tau\tau)$ + Np3($10 < M < 60$ $GeV$) | 11.311 | 1.19 | 0.00387 | 29600 |
| $Z(\rightarrow \tau\tau)$ + Np4($10 < M < 60$ $GeV$) | 2.592 | 1.19 | 1.0 | 365497 |
| $Z(\rightarrow \tau\tau)$ + Np5($10 < M < 60$ $GeV$) | 0.6929 | 1.19 | 1.0 | 114420 |

Table 6.6: MC samples/processes used to model $Z$+*jets* background. The corresponding cross sections, generator level filter efficiencies and total numbers of events are shown in this table. ALPGEN is used with `NpX` (`X`=0...5) in the process name referring to the number of additional partons in the final state. The k-factors are calculated according to the NNLO inclusive $W/Z$ production cross sections [83], and are assigned for each `NpX` samples.

| Process | $\sigma$ [$pb$] | k-factor | $\epsilon_{\text{filter}}$ | $N_{\text{MC}}$ |
|---|---|---|---|---|
| $W(\to e\nu)$ + Np0 | 8037.1 | 1.19 | 1 | 3459894 |
| $W(\to e\nu)$ + Np1 | 1579.2 | 1.19 | 1 | 2499491 |
| $W(\to e\nu)$ + Np2 | 477.2 | 1.19 | 1 | 3769487 |
| $W(\to e\nu)$ + Np3 | 133.93 | 1.19 | 1 | 1009997 |
| $W(\to e\nu)$ + Np4 | 35.622 | 1.19 | 1 | 249999 |
| $W(\to e\nu)$ + Np5 | 10.533 | 1.19 | 1 | 70000 |
| $W(\to \mu\nu)$ + Np0 | 8040 | 1.19 | 1 | 3469692 |
| $W(\to \mu\nu)$ + Np1 | 1580.3 | 1.19 | 1 | 2499694 |
| $W(\to \mu\nu)$ + Np2 | 477.5 | 1.19 | 1 | 3769886 |
| $W(\to \mu\nu)$ + Np3 | 133.94 | 1.19 | 1 | 1006698 |
| $W(\to \mu\nu)$ + Np4 | 35.636 | 1.19 | 1 | 254999 |
| $W(\to \mu\nu)$ + Np5 | 10.571 | 1.19 | 1 | 69900 |
| $W(\to \tau\nu)$ + Np0 | 8035.8 | 1.19 | 1 | 3419992 |
| $W(\to \tau\nu)$ + Np1 | 1579.8 | 1.19 | 1 | 2499793 |
| $W(\to \tau\nu)$ + Np2 | 477.55 | 1.19 | 1 | 3765989 |
| $W(\to \tau\nu)$ + Np3 | 133.79 | 1.19 | 1 | 1009998 |
| $W(\to \tau\nu)$ + Np4 | 35.583 | 1.19 | 1 | 249998 |
| $W(\to \tau\nu)$ + Np5 | 10.54 | 1.19 | 1 | 65000 |

Table 6.7: MC samples/processes used to model $W$+*jets* background. The corresponding cross sections, generator level filter efficiencies and total numbers of events are shown in this table. ALPGEN is used with `NpX` (`X`=0...5) in the process name referring to the number of additional partons in the final state. The k-factors are calculated according to the NNLO inclusive $W/Z$ production cross sections [83], and are assigned for each `NpX` samples.

| Process | $\sigma$ [$pb$] | k-factor | $\epsilon_{\text{filter}}$ | $N_{\text{MC}}$ |
|---|---|---|---|---|
| $W(\to \ell\nu) + c + \text{Np0}$ | 807.89 | 1.19 | 1 | 6499580 |
| $W(\to \ell\nu) + c + \text{Np1}$ | 267.61 | 1.19 | 1 | 2069796 |
| $W(\to \ell\nu) + c + \text{Np2}$ | 69.823 | 1.19 | 1 | 519998 |
| $W(\to \ell\nu) + c + \text{Np3}$ | 20.547 | 1.19 | 1 | 110000 |
| $W(\to \ell\nu) + c + \text{Np4}$ | 4.3069 | 1.19 | 1 | 19900 |
| $W(\to \ell\nu) + b\bar{b} + \text{Np0}$ | 55.682 | 1.19 | 1 | 474997 |
| $W(\to \ell\nu) + b\bar{b} + \text{Np1}$ | 45.243 | 1.19 | 1 | 359500 |
| $W(\to \ell\nu) + b\bar{b} + \text{Np2}$ | 23.246 | 1.19 | 1 | 174898 |
| $W(\to \ell\nu) + b\bar{b} + \text{Np3}$ | 11.144 | 1.19 | 1 | 50000 |
| $W(\to \ell\nu) + c\bar{c} + \text{Np0}$ | 150.19 | 1.19 | 1 | 1274900 |
| $W(\to \ell\nu) + c\bar{c} + \text{Np1}$ | 132.68 | 1.19 | 1 | 1049994 |
| $W(\to \ell\nu) + c\bar{c} + \text{Np2}$ | 71.807 | 1.19 | 1 | 524900 |
| $W(\to \ell\nu) + c\bar{c} + \text{Np3}$ | 30.264 | 1.19 | 1 | 169500 |

Table 6.8: MC samples/processes used to model $W$+*jets* with heavy quark flavor ($b$ and $c$) backgrounds. The corresponding cross sections, generator level filter efficiencies and total numbers of events are shown in this table. ALPGEN is used with `NpX` (`X`=0...5) in the process name referring to the number of additional partons in the final state. The k-factors are calculated according to the NNLO inclusive $W/Z$ production cross sections [73, 74], and are assigned for each `NpX` samples.

| Process | $\sigma$ [$pb$] | k-factor | $\epsilon_{\text{filter}}$ | $N_{\text{MC}}$ | Generator |
|---|---|---|---|---|---|
| $t\bar{t}$ | 21.806 | 1.2177 | 1 | 9977338 | **MC@NLO** |
| $W(\to \ell\nu) + t$ | 20.67 | 1.082 | 1 | 1999194 | **MC@NLO** |
| $t \to e(t\text{-chan})$ | 9.48 | 1 | 1 | 299899 | **AcerMC** |
| $t \to \mu(t\text{-chan})$ | 9.48 | 1 | 1 | 300000 | **AcerMC** |
| $t \to \tau(t\text{-chan})$ | 9.48 | 1 | 1 | 293499 | **AcerMC** |
| $t \to e(s\text{-chan})$ | 0.606 | 1 | 1 | 199899 | **MC@NLO** |
| $t \to \mu(s\text{-chan})$ | 0.606 | 1 | 1 | 199899 | **MC@NLO** |
| $t \to \tau(s\text{-chan})$ | 0.606 | 1 | 1 | 199799 | **MC@NLO** |

Table 6.9: MC samples/processes used to model *Top* backgrounds ($t\bar{t}$ and $Wt$). The corresponding cross sections, generator names, generator level filter efficiencies and total numbers of events are shown in the table.

| Process | $\sigma$ [$pb$] | k-factor | $\epsilon_{\text{filter}}$ | $N_{\text{MC}}$ | Generator |
|---|---|---|---|---|---|
| $W^+Z \to e^+\nu e^+e^-$ | 1.407 | 1 | 0.29456 | 190000 | Powheg |
| $W^+Z \to e^+\nu\mu^+\mu^-$ | 0.9328 | 1 | 0.35211 | 190000 | Powheg |
| $W^+Z \to e^+\nu\tau^+\tau^-$ | 0.1746 | 1 | 0.16682 | 76000 | Powheg |
| $W^+Z \to \mu^+\nu e^+e^-$ | 1.399 | 1 | 0.29351 | 189999 | Powheg |
| $W^+Z \to \mu^+\nu\mu^+\mu^-$ | 0.9537 | 1 | 0.35132 | 190000 | Powheg |
| $W^+Z \to \mu^+\nu\tau^+\tau^-$ | 0.1746 | 1 | 0.16863 | 76000 | Powheg |
| $W^+Z \to \tau^+\nu e^+e^-$ | 1.399 | 1 | 0.14289 | 75400 | Powheg |
| $W^+Z \to \tau^+\nu\mu^+\mu^-$ | 0.9382 | 1 | 0.18256 | 76000 | Powheg |
| $W^+Z \to \tau^+\nu\tau^+\tau^-$ | 0.1719 | 1 | 0.058517 | 19000 | Powheg |
| $W^-Z \to e^-\nu e^+e^-$ | 0.9795 | 1 | 0.29694 | 189899 | Powheg |
| $W^-Z \to e^-\nu\mu^+\mu^-$ | 0.639 | 1 | 0.35302 | 190000 | Powheg |
| $W^-Z \to e^-\nu\tau^+\tau^-$ | 0.1125 | 1 | 0.15969 | 76000 | Powheg |
| $W^-Z \to \mu^-\nu e^+e^-$ | 0.9359 | 1 | 0.29766 | 76000 | Powheg |
| $W^-Z \to \mu^-\nu\mu^+\mu^-$ | 0.6488 | 1 | 0.35414 | 190000 | Powheg |
| $W^-Z \to \mu^-\nu\tau^+\tau^-$ | 0.1125 | 1 | 0.16023 | 190000 | Powheg |
| $W^-Z \to \tau^-\nu e^+e^-$ | 0.9359 | 1 | 0.14803 | 76000 | Powheg |
| $W^-Z \to \tau^-\nu\mu^+\mu^-$ | 0.638 | 1 | 0.18657 | 76000 | Powheg |
| $W^-Z \to \tau^-\nu\tau^+\tau^-$ | 0.1107 | 1 | 0.056651 | 19000 | Powheg |
| $ZZ \to 4e$ | 0.0735 | 1.0 | 0.90765 | 1099997 | Powheg |
| $ZZ \to 2e2\mu$ | 0.1708 | 1.0 | 0.82724 | 1599696 | Powheg |
| $ZZ \to 2e2\tau$ | 0.1708 | 1.0 | 0.58278 | 599899 | Powheg |
| $ZZ \to 4\mu$ | 0.0735 | 1.0 | 0.91241 | 1099798 | Powheg |
| $ZZ \to 2\mu2\tau$ | 0.1708 | 1.0 | 0.58725 | 600000 | Powheg |
| $ZZ \to 4\tau$ | 0.0735 | 1.0 | 0.10604 | 300000 | Powheg |
| $ZZ \to 2e2\nu$ | 0.168 | 1.0 | 1.0 | 299400 | Powheg |
| $ZZ \to 2\mu2\nu$ | 0.168 | 1.0 | 1.0 | 300000 | Powheg |
| $ZZ \to 2\tau2\nu$ | 0.168 | 1.0 | 1.0 | 299999 | Powheg |
| $W(\to \ell\nu) + \gamma + \text{Np0}$ | 229.88 | 1.15 | 0.31372 | 14296258 | Alpgen |
| $W(\to \ell\nu) + \gamma + \text{Np1}$ | 59.518 | 1.15 | 0.44871 | 5393984 | Alpgen |
| $W(\to \ell\nu) + \gamma + \text{Np2}$ | 21.39 | 1.15 | 0.54461 | 2899389 | Alpgen |
| $W(\to \ell\nu) + \gamma + \text{Np3}$ | 7.1203 | 1.15 | 0.62974 | 859697 | Alpgen |
| $W(\to \ell\nu) + \gamma + \text{Np4}$ | 2.1224 | 1.15 | 1.0 | 364999 | Alpgen |
| $W(\to \ell\nu) + \gamma + \text{Np5}$ | 0.46612 | 1.15 | 1.0 | 60000 | Alpgen |
| $W\gamma^* \to \ell\nu ee$ ($M_{\gamma^*} < 7$ $GeV$) | 10.17487 | 1.0 | 1.0 | 2008998 | Sherpa |
| $W\gamma^* \to \ell\nu\mu\mu$ ($M_{\gamma^*} < 7$ $GeV$) | 2.53518 | 1.0 | 1.0 | 504996 | Sherpa |
| $W\gamma^* \to \ell\nu\tau\tau$ ($M_{\gamma^*} < 7$ $GeV$) | 0.22830 | 1.0 | 1.0 | 50000 | Sherpa |

Table 6.10: MC samples/processes used to model the di-boson backgrounds $WZ$, $ZZ$, $W\gamma$, and $W\gamma^*$. The corresponding cross sections, generator names, generator level filter efficiencies and total numbers of events are shown in this table. `NpX` (`X`=0...5) in the process name refers to the number of additional partons in the final state.

where theoretical uncertainties will be evaluated and included in this extrapolation. Therefore, fiducial cross section provides a common ground for different theoretical predictions, and constitutes a measurement which minimizes theoretical uncertainties. Equation 6.1 is used to determine the fiducial cross section:

$$\sigma^{\text{fiducial}}_{WW\to\ell\nu\ell\nu} = \frac{N_{\text{obs}} - N_{\text{bkg}}}{C_{WW}\mathcal{L}} \tag{6.1}$$

where $N_{\text{obs}}$ is the number of observed events in fiducial volume, $N_{\text{bkg}}$ is the number of estimated background in fiducial volume, $\mathcal{L}$ is the integrated luminosity, and $C_{WW}$ is the signal efficiency correction factor. Dominant uncertainties of fiducial cross section measurements come from detector efficiencies and resolution corrections. Specifically, $C_{WW}$ is decomposed into the following contribution terms:

$$C_{WW} = \epsilon_{\text{trig}} \times \epsilon_{\text{select}} \times \epsilon_{\text{lep}} \times \alpha_{\text{reco}} \tag{6.2}$$

where $\epsilon_{\text{trig}}$ is the trigger efficiency (see Section 3.2.5), $\epsilon_{\text{select}}$ is the event-level selection efficiency (e.g. the PV selection efficiency), $\epsilon_{\text{lep}} = \epsilon_{\ell_1} \times \epsilon_{\ell_2}$ is the lepton reconstruction efficiency, and $\alpha_{\text{reco}}$ is the fiducial volume correction factor explained as follows. The fiducial volume is realized at both the reconstruction level (representing experimental measurement) and generator level (representing theoretical calculation), but the generator simulation is, in most cases, incapable per se for accurate reproduction of such fiducial volume defined at the reconstruction level. So $\alpha_{\text{reco}}$ accounts for the acceptance difference between them, including resolutions as well as smearing corrections. $C_{WW}$ is practically calculated by:

$$C_{WW} = \frac{N^{\text{reco}}_{\text{fiducial}}}{N^{\text{gen}}_{\text{fiducial}}} \tag{6.3}$$

where $N^{\text{gen}}_{\text{fiducial}}$ is the number of events selected at the generator-level (with the fiducial cuts) in fiducial volume, and $N^{\text{reco}}_{\text{fiducial}}$ is the number of events selected at the reconstruction-level (with the analysis cuts) in fiducial volume. The fiducial cuts are chosen to be similar to the analysis cuts, though (in most cases) the two are not exactly the same, for example the lepton isolation requirements are not included in the fiducial requirements. The same signal MC samples are used for Equation 6.3 to calculate $N^{\text{reco}}_{\text{fiducial}}$ and $N^{\text{gen}}_{\text{fiducial}}$. For $N^{\text{gen}}_{\text{fiducial}}$, the truth particle information (`D3PD` truth branches) **before** detector simulation is used; while for $N^{\text{reco}}_{\text{fiducial}}$, full simulated information (`D3PD` reconstruction branches) is used. Considering that the MC samples do not replicate data, MC to data corrections (*pile-up* re-weighting, lepton smearing, muon scale correction, etc.) have to be applied before the $C_{WW}$ calculation. An accurate evaluation of $C_{WW}$ is crucial in the comparison between experimental results and theoretical predictions.

Using MC simulations, the fiducial acceptance ($\mathcal{A}_{WW}$) of the fiducial volume from the full phase space can be determined. Using Equation 6.4, the fiducial cross section is extrapolated to determine the total cross section:

$$\sigma_{WW}^{\text{total}} = \frac{\sigma_{WW\to\ell\nu\ell\nu}^{\text{fiducial}}}{\mathcal{A}_{WW} Br} = \frac{N_{\text{obs}} - N_{\text{bkg}}}{C_{WW} \times \mathcal{A}_{WW} \times \mathcal{L} \times Br} \tag{6.4}$$

where $\mathcal{A}_{WW}$ is the acceptance factor to the full phase space, $Br$ is the branching fraction of di-leptonic $W^{+}W^{-}$ decays which has been measured precisely by previous experiments. Part of the systematics of $\sigma_{WW}^{\text{total}}$ is purely caused by the theoretical modelling of the $WW$ signal, which is encapsulated in $\mathcal{A}_{WW}$. The rest is contributed by the systematics of $C_{WW}$. The calculation of $\mathcal{A}_{WW}$ is as follows:

$$\mathcal{A}_{WW} = \frac{N_{\text{fiducial}}^{\text{gen}}}{N_{\text{full}}^{\text{gen}}} \tag{6.5}$$

where $N_{\text{full}}^{\text{gen}}$ is the **MC simulated** events at the generator-level in **full phase space** , and $N_{\text{fiducial}}^{\text{reco}}$ has exactly the same definition as in Equation 6.3. Similarly, the same signal MC samples are used for the calculation. Since both the numbers are extracted in generator-level, `D3PD` truth branches are used in both cases, and there is no need to correct the MC to data.

Notice that, the $\mathcal{A}_{WW} \times C_{WW}$ yields:

$$\epsilon_{\mathcal{A}} \equiv \mathcal{A}_{WW} \times C_{WW} = \frac{N_{\text{fiducial}}^{\text{reco}}}{N_{\text{full}}^{\text{gen}}} \tag{6.6}$$

By considering $\epsilon_{\mathcal{A}}$, all systematics contained in $N_{\text{fiducial}}^{\text{gen}}$ are eliminated, which brings a simpler consideration of systematics for the total cross section.

Equation 6.4 is only applicable to one single channel. To combine the cross section results across all channels, a maximum likelihood fitting method is used. The extraction of the fiducial cross section and total cross section is detailed in Chapter 10.

Finally, with selected $W^{+}W^{-} \to \ell^{+}\nu_{\ell}\ell^{-}\bar{\nu}_{\ell}$ candidate events and estimated background events, the leading lepton $p_T$ ($p_T^{\ell_1}$) spectrum is measured and compared to theoretical predictions with different triple-gauge-boson couplings to probe the anomalous couplings. A maximum likelihood fitting method is also used to fit the coupling parameters which have already described in Equation 2.36 in Section 2.2.1.

# CHAPTER 7

# *WW* Signal Event Selection

This chapter presents details of the $W^+W^- \to \ell^+\nu_\ell\ell^-\bar{\nu}_\ell$ event selection criteria (cuts) used in this analysis, along with the cut-flows and event yields for both data and MC, which are also compared graphically at different selection stages.

The analysis includes three final states, $e^+e^- + \not{E}_T$, $\mu^+\mu^- + \not{E}_T$ and $e^\pm\mu^\mp + \not{E}_T$. The `Egamma` and `Muons` data streams are used for the *ee* and $\mu\mu$ channels, respectively. The inclusive $e\mu$ sample is obtained using both data streams where duplicate events are removed. Selection cuts are applied to detect signal against backgrounds, therefore an improvement on signal significance is the critical goal for cut optimization studies. The event selection cuts were chosen and optimized as follows.

In a cut-based analysis, a *cut* consists of a chosen variable (discriminant) with a discriminating value. The implementation of a cut is to require the discriminant in reconstructed events to be larger or smaller than the cut value. To avoid potential selection bias, the chosen discriminants should be well modelled in MC simulation and minimally correlated with each other. Furthermore, it is desirable to keep adequate signal statistics in a measurement , as larger signal size benefits not only the data-theory comparison but also the search for new physics.

The cuts used for this analysis is based on the cuts used in 7 *TeV* analysis [1], optimized by adding or removing certain cuts as well as adjusting original cut values to adapt to 8 *TeV* conditions. MC samples are used in the optimization study. Most of the background processes have sufficient statistics for the study except the same-flavor channel of *W+jets* samples; however, the contribution of it is tiny for the final selected events, thus has little impact on final selection. Generally, two major steps of event selection with different strategies are defined: the *pre-selection* which aims to trim as much backgrounds as possible without sacrificing many signal events, and the *final selection* which aims to increase signal significance, which is defined in

Equation 7.1:

$$S_{\text{signal}} = \frac{N_S}{\sqrt{N_S + N_B + \sum_{i=0}^{n} \left(\sigma_{\text{syst}}^{B_i}\right)^2}} \cdot \Theta(N_S) \tag{7.1}$$

with

$$\Theta(N_S) = \begin{cases} 1 & \text{if } N_S \geqslant N_{\text{critical}} \\ 0 & \text{Otherwise} \end{cases} \tag{7.2}$$

where $S_{\text{signal}}$ is the signal detection significance, $N_S$ and $N_B$ are the number of signal and background events after final selection, $n$ is the number of background processes. $\sigma_{\text{syst}}^{B_i}$ is the systematic uncertainty for a given background $B_i$. In the signal significance calculation during optimization study, the fractional background systematic uncertainties are set to be 30%, 30%, 30% and 10% for $Z$+*jets*, *Top*, $W$+*jets* and di-boson backgrounds, respectively, based on previous experience. $\Theta(N_S)$ is a step function, and the $N_{\text{critical}}$ is set to be 900 (2500) for same-flavor (opposite-flavor) channels. $\Theta(N_S)$ is introduced to guarantee a reasonable size of the selected signal events (3 ~ 4 times larger than that in the 7 *TeV* analysis considering the increased integrated luminosity), since the figure of merit for $S_{\text{signal}}$ tends to be maximized toward small signal size with tiny background contribution. The details of cut optimization is documented in the Appendix A in the supporting note of this analysis [53].

Before the event selection step, physics objects has to be reconstructed according to some requirements since object-related cuts are used in both event selection steps. The following sections detail the cuts required in the step of object selection, event pre-selection and event final selection.

## 7.1 Object Selection

As elaborated in Chapter 5, the object selection criteria for electrons, muons, and jets are listed as Table 7.1, Table 7.2, and Table 7.3, respectively.

The principle for $E_T^{miss}$ reconstruction is detailed in Section 5.6.1. `METUtility` tool is used to build the $E_T^{miss}$ variable. And $E_T^{miss,rel}$ is constructed according to Equation 5.22. The reconstruction of $p_T^{miss}$ is very straight-forward: it is the negative vectorial sum of all tracks fulfilling the requirements listed in Section 5.6.2. Notice that, since $E_T^{miss}$ and $p_T^{miss}$ are fully correlated to other physics objects, any calibration and corrections to other objects will be propagated to $E_T^{miss}$ and $p_T^{miss}$.

**Electron Selection**

| | |
|---|---|
| Reconstructed by either standard algorithm (cluster based or cluster-and-track based) | `Author == 1 or 3` |
| Geometrical Acceptance: | $\|\eta\| < 2.47$, excluding the transition region $1.37 \leqslant \|\eta\| \leqslant 1.52$ |
| Object Quality: | outside regions with LAr readout problems |
| Kinematic Acceptance: | $E_T > 7\ GeV$ |
| Identification Criteria: | `VeryTight` likelihood |
| Calorimeter Isolation Requirement: | for $p_T < 15\ GeV$: $\left(\sum E_T^{\Delta R<0.3} - E_T\right)/E_T < 0.20$<br>for $15 < p_T < 20\ GeV$: $\left(\sum E_T^{\Delta R<0.3} - E_T\right)/E_T < 0.24$<br>for $p_T > 20\ GeV$: $\left(\sum E_T^{\Delta R<0.3} - E_T\right)/E_T < 0.28$ |
| Track Isolation Requirement: | for $p_T < 15\ GeV$: $\left(\sum p_T^{\Delta R<0.4} - p_T\right)/p_T < 0.06$<br>for $15 < p_T < 20\ GeV$: $\left(\sum p_T^{\Delta R<0.3} - p_T\right)/p_T < 0.08$<br>for $p_T > 20\ GeV$: $\left(\sum E_T^{\Delta R<0.3} - E_T\right)/E_T < 0.10$ |
| Transverse Impact parameter requirement: | $\frac{\|d_0\|}{\sigma(d_0)} < 3$ |
| Longitudinal Impact parameter requirement: | $\|z_0 \times \sin(\theta_{trk})\| < 0.4\ mm$ |

Table 7.1: Electron definition used in this analysis. `Author` is a `D3PD` variable indicating the eID algorithm. $\sum E_T^{\Delta R<r}$ and $\sum p_T^{\Delta R<r}$ are defined in Section 5.3.3. $d_0$ and $z_0$ denote the transverse and longitudinal impact parameters of tracks with respect to the centre of the beam spot. $\theta_{trk}$ is the longitudinal included angle between the ID track and the beam line. More forward tracks have a longer projection on the z-axis and thus a larger uncertainty; hence the $|z_0|$ cut is changed to $|z_0 \times \sin(\theta_{trk})|$ to reduce the effect of such increased uncertainty.

**Muon Selection**

| | |
|---|---|
| Reconstructed combined *STACO* muon | `Author == 6` |
| Geometrical Acceptance: | $\|\eta\| < 2.47$ |
| Kinematic Acceptance: | $p_T > 7\ GeV$ |
| Inner Detector Requirements: | $n^{\text{hit}}_{\text{Pixel}} + n^{\text{DeadSensor}}_{\text{Pixel}} > 0$<br>$n^{\text{hit}}_{\text{SCT}} + n^{\text{DeadSensor}}_{\text{SCT}} \geqslant 5$<br>$n^{\text{hole}}_{\text{Pixel}} + n^{\text{hole}}_{\text{SCT}} < 3$<br>for $0.1 < \|\eta\| < 1.9$: $\left(n^{\text{outliers}}_{\text{TRT}} + n^{\text{hits}}_{\text{TRT}}\right) > 5$ and<br>$n^{\text{outliers}}_{\text{TRT}} / \left(n^{\text{outliers}}_{\text{TRT}} + n^{\text{hits}}_{\text{TRT}}\right) < 0.9$ |
| Calorimeter Isolation Requirement: | for $p_T < 15\ GeV$: $\sum E_T^{\Delta R<0.3}/p_T < 0.06$,<br>for $15 < p_T < 20\ GeV$: $\sum E_T^{\Delta R<0.3}/p_T < 0.12$,<br>for $20 < p_T < 25\ GeV$: $\sum E_T^{\Delta R<0.3}/p_T < 0.18$ and<br>for $p_T > 25\ GeV$ : $\sum E_T^{\Delta R<0.3}/p_T < 0.30$ |
| Track Isolation Requirement: | for $p_T < 15\ GeV$: $\sum p_T^{\Delta R<0.4}/p_T < 0.06$,<br>for $15 < p_T < 20\ GeV$: $\sum p_T^{\Delta R<0.3}/p_T < 0.08$ and<br>for $p_T > 20\ GeV$: $\sum p_T^{\Delta R<0.3}/p_T < 0.12$ |
| Transverse Impact parameter requirement: | $\frac{\|d_0\|}{\sigma(d_0)} < 3$ |
| Longitudinal Impact parameter requirement: | $\|z_0 \times \sin\theta_{\text{STACO}}\| < 1mm$ |

Table 7.2: Muon definition used in this analysis. `Author` is a `D3PD` variable, indicating the $\mu$-ID algorithm. $\sum E_T^{\Delta R<r}$ and $\sum p_T^{\Delta R<r}$ are defined in Section 5.3.3. The variables used in ID requirements are defined in Section 5.4.2. $d_0$ and $z_0$ denote the transverse and longitudinal impact parameters of tracks with respect to the centre of the beam spot. $\theta_{\text{STACO}}$ is the longitudinal included angle between the *STACO* track and the beam line. More forward tracks have a longer projection on the z-axis and thus a larger uncertainty; hence the $|z_0|$ cut is changed to $|z_0 \times \sin\theta_{\text{STACO}}|$ to reduce the effect of such increased uncertainty.

**Jet Selection**

| Reconstructed from *topo-clusters* with anti-$k_T$ algorithm under *LCW+JES* scheme, $\Delta R = 0.4$ | |
|---|---|
| Geometrical Acceptance: | $\lvert\eta^{\text{EM-scale}}\rvert < 4.5$ |
| Kinematic Acceptance: | $p_T^{\text{calibrated}} > 25\ GeV$ |
| Jet Quality: | Reject `Looser` and *ugly* jets |
| JVF: | $JVF > 0.5$ for jets with<br>$\lvert\eta^{\text{EM-scale}}\rvert < 2.4$ and<br>$p_T^{\text{calibrated}} < 50\ GeV$ |

Table 7.3: Jet definition used in this analysis. The definition of *topo-clusters* and *LCW+JES* scheme, as well as the calibration details are defined in Section 5.5.2.1. As different calibration schemes only differ in energy corrections, most geometry parameters are still measured by ECAL, so EM-scale $\eta$ is used. Jet quality definitions are in Section 5.5.1. The definition and purpose of JVF cut is explained in Section 5.5.2.3.

After object selections, there is possibility of double- or triple-counting for independently reconstructed objects. Three steps of object-overlap removal are prioritized as follow (see Section 5.7):

1. Selected muons with $\Delta R(\mu, j) < 0.3$ is removed, where $\Delta R(\mu, j) = \sqrt{(\eta_\mu^{\text{STACO}} - \eta_j^{\text{EM-scale}})^2 + (\phi_\mu^{\text{STACO}} - \phi_j^{\text{EM-scale}})^2}$
2. Selected electrons with $\Delta R(e, \mu) < 0.1$ is removed, where $\Delta R(e, \mu) = \sqrt{(\eta_e^{\text{trk}} - \eta_\mu^{\text{STACO}})^2 + (\phi_e^{\text{trk}} - \phi_\mu^{\text{STACO}})^2}$
3. Selected jets with $\Delta R(j, e) < 0.3$ is removed, where $\Delta R(j, e) = \sqrt{(\eta_j^{\text{EM-scale}} - \eta_e^{\text{cl}})^2 + (\phi_j^{\text{EM-scale}} - \phi_e^{\text{cl}})^2}$

Note that different versions (track-based and cluster-based) of electron dynamic variables are used in different removal steps. Also, as different jet calibration schemes only differ in energy corrections, and geometry measurement of jets is performed by ECAL, EM-scale geometry parameters are used for jets, instead of those reconstructed at LCW-scale.

## 7.2 Pre-selection

The pre-selection is an event-level selection in order to improve the data quality and reject most of the backgrounds without compromising the signal acceptance. This analysis follows the standard recommendation by data quality and performance groups and proceeds as follows, with an indication of what sample the cut is applied to:

1. **Heavy Flavor Overlap Removal** (MC): Reject events in heavy-flavor $W$+*jets* MC samples if the `D3PD` variable `top_hfor_type==4` (See Section 6.3.1).

2. **Mass Overlap Removal** (MC): Reject events with truth $M_Z < 7$ *GeV* in $WZ$ samples to remove overlap events between $WZ$ and $W\gamma^*$ MC Samples (see Section 6.3.1).

3. **Data Quality** (data): Data events must be in the GRL, reflecting luminosity blocks with fully functional sub-detectors during data taking.

4. **Stream Overlap Removal** (data): Reject events in `Egamma` stream if the `D3PD` variable `streamDecision_Muons==1`. Overlapped events are only kept in `Muons` stream.

5. **Physics Object Selection** (MC+data): Refer Section 7.1 for details.

6. **Object Overlap Removal** (MC+data): Refer Section 7.1 for details.

7. **Event Cleaning**: Remove problematic events in data and MC. The problems are listed as follows:

   - **Hot Tile Cell** (data): In the data taking periods B1 and B2 there was a hot HCAL cell that had not been masked in the reconstruction. Events are removed if a jet points to that region.
   - **Tile Trip** (data): The HCAL has suffered from frequent module trips since 7 *TeV* running. These trips are considered a tolerable data quality defect as long as the trip is accounted for during off-line reconstruction, but it is recommended to remove the affected events to better control the event quality.
   - **HCAL Correction** (MC+data): In 2012, there was one HCAL module masked for the full data set, but it turned out that the correction used for masked cells was unable to properly handle all dead modules. It is important to remove events where jets fall into such masked regions, as otherwise the jet is poorly reconstructed in addition to large amounts of fake $\not\!\!E_T$. The jet definition follows Table 7.3 but adopts `Medium` quality criterion.

- $\not{E}_T$ (MC+data): Events with at least one `Looser` jet, which is $p_T \geqslant 20\ GeV$ (calibrated in *EM+JES* scheme) and not overlapping with a selected electron, will have adverse effects on $\not{E}_T$. Such events are removed.
- **Detector Flag** (data): Miscellaneous events are removed due to detector error flags or corrupted events recorded [53].

8. **Primary Vertex Selection** (MC+data): The reconstructed PV is required to have least 3 good associated tracks (see Section 5.2).

9. **Trigger Selection** (MC+data): Events must pass selected trigger requirements (see Section 3.2.5).

10. **Di-lepton Selection** (MC+data): An event is selected if there are:

    - Exactly two isolated, opposite-charged leptons with $p_T > 25(20)\ GeV$ for leading (sub-leading) leptons. Leptons follow the selection criteria in physics object selection. This requirement ensures the selected leptons are on or proximate to the trigger plateau and enables the use of the official trigger SFs (see Section 3.2.5). It also strongly reduces the $W{+}jets$ and $Multijet$ backgrounds due to the $p_T$ dependence of the muon fake-rate.
    - No additional leptons with $p_T > 7\ GeV$. It suppresses di-boson backgrounds.

11. **Trigger Matching** (MC+data): This requirement tests if the selected leptons did fire the selected triggers. For same-flavor channel, both leptons have to be matched to the di-lepton trigger. For opposite-flavor channel, two scenarios are counted as "matched": at least one of the leptons (with $p_T > 25\ GeV$) has to be matched to any of the single-lepton triggers; or both leptons have to be matched to the di-lepton trigger.

Based on MC studies, after the pre-selection, the dominant contribution (> 99%) to $ee$ and $\mu\mu$ events comes from the inclusive $Z/\gamma^* \rightarrow \ell^+\ell^-$ process (Drell-Yan). The $W^+W^-$ signal only contributes $\sim 0.14\%$ of the selected events. For the $e\mu$ final state, the $W^+W^-$ signal contributes 11.7%, where the major background are Top (60.7%), $Z \rightarrow \tau\tau$ (22.6%) and QCD ($W{+}jets$ and di-jets) (5%).

The following figures show the kinematic distributions at the pre-selection level detailed above. The MC has been normalized to the integrated luminosity of the data set (20.3 $fb^{-1}$) using NLO SM cross sections. Figure 7.1 shows the di-lepton invariant mass $M_{\ell\ell}$ along with leading and sub-leading lepton $p_T$ distributions. Data and MC agree well in all these distributions for pre-selected di-lepton events, illustrating good understanding of the detector performance.

## 7.3 Final Selection

The final $W^+W^-$ event selection cuts are chosen to optimize the signal significance according to Equation 7.1, and are prioritized as below.

1. $\mathbf{M}_{\ell\ell}$: The invariant mass cut for di-lepton pairs: $M_{\ell\ell} > 15(10)$ $GeV$ for $ee/\mu\mu$ ($e\mu$) channels. It further removes events from $Multijet$ and the low mass spectrum not modelled by MC.

2. **Z-veto**: $|M_{\ell\ell} - M_Z| > 15$ $GeV$ for the same-flavor channels only. It remove events from Drell-Yan.

3. $\not{E}_T^{rel}$: $\not{E}_T^{rel} > 45(15)$ $GeV$ for the $ee/\mu\mu(e\mu)$ channels. It further suppresses the Drell-Yan. Figure 7.2 shows the $\not{E}_T^{rel}$ distributions for $ee$, $\mu\mu$ and $e\mu$ channels prior to the $\not{E}_T^{rel}$ cut applied.

4. $\not{p}_T$: $\not{p}_T > 45(20)$ $GeV$ for $ee/\mu\mu$ ($e\mu$) channels. It further suppresses the Drell-Yan (see Section 5.6.2). Figure 7.3 shows the $\not{p}_T$ distributions for $ee$, $\mu\mu$ and $e\mu$ channels prior to the $\not{p}_T$ cut applied.

5. $\mathbf{\Delta\phi}(\not{p}_T, \not{E}_T)$: $|\Delta\phi(\not{p}_T, \not{E}_T)| < 0.3(0.6)$ for $ee/\mu\mu$ ($e\mu$) channels. This variable is another powerful discriminant against Drell-Yan. Figure 7.4 shows the distribution just before the final cut stage.

6. **Jet-veto**: $N_j = 0$, which is the final cut. The number of good jets (see Table 7.3) is required to be zero. This cut efficiently removes inclusive $Top$ events ($t\bar{t}$ and $Wt$) with leptonic decay modes. Figure 7.5 shows the jet multiplicity distribution prior to the jet-veto cut is applied.

After all the selections, a total of 6636 candidates events is observed in data. The distributions of different kinematic variables for the selected candidate events including the estimated backgrounds (see Chapter 8) are shown in Figure 7.6, associated with data statistical uncertainties and systematic uncertainties of the predictions (see Chapter 9).

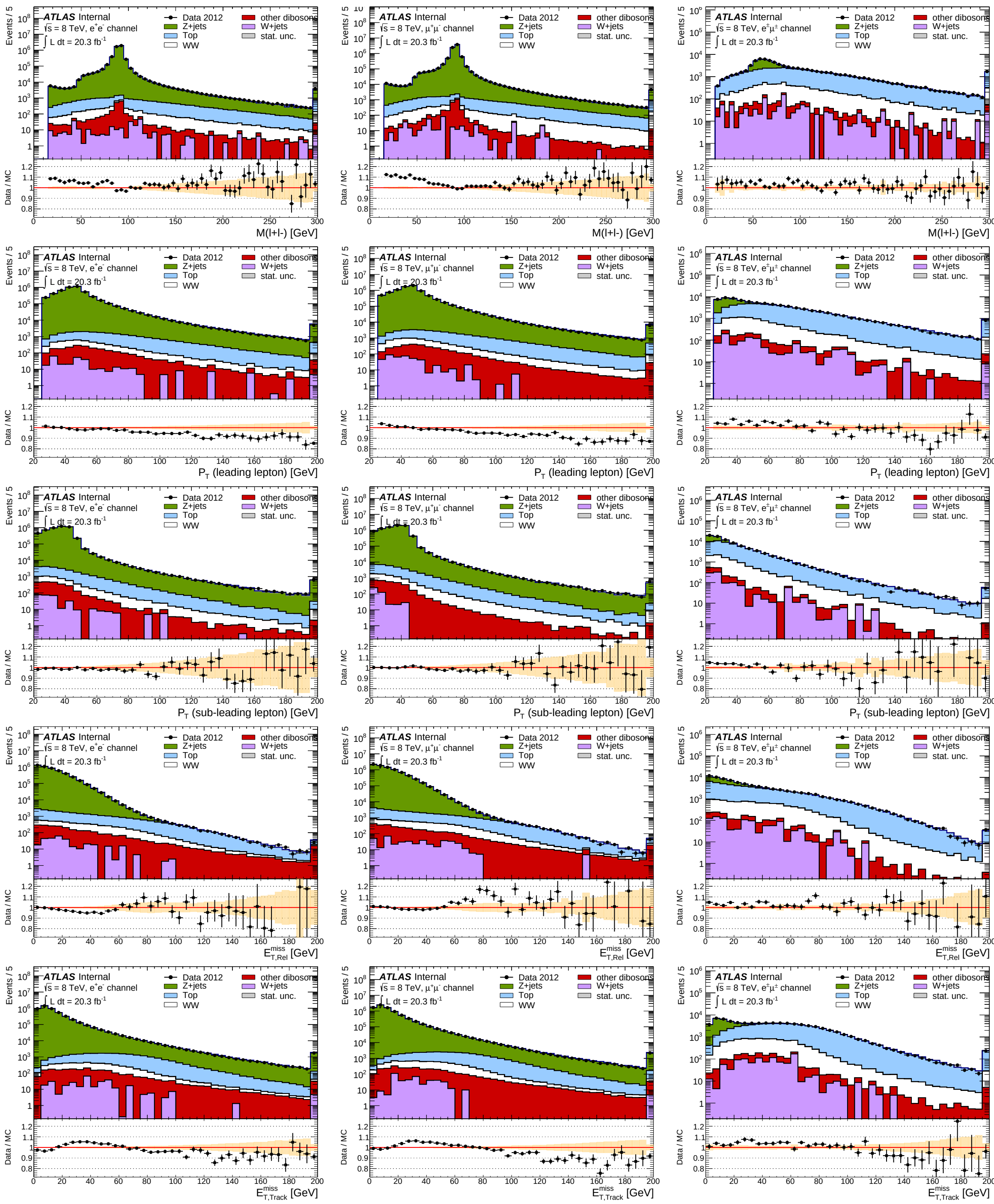


Figure 7.1: Kinematic distributions of the selected events at the first cut stage ($M_{\ell\ell}$). Data are shown together with the processes predicted by MC and scaled to 20.3 $fb^{-1}$ . From left to right the $ee$, $\mu\mu$ and $e\mu$ channels are shown. The top row shows di-lepton invariant mass $M_{\ell\ell}$, the second row shows the $p_T^{\ell_1}$ with $\ell_1$ being the leading lepton, the third row the $p_T^{\ell_2}$ with $\ell_2$ being the sub-leading lepton, the fourth row the $\not{E}_T^{rel}$ , and the bottom row the $\not{p}_T$ . Statistical uncertainties are shown as gray bands in the main plot or as orange bands on the ratio plot.

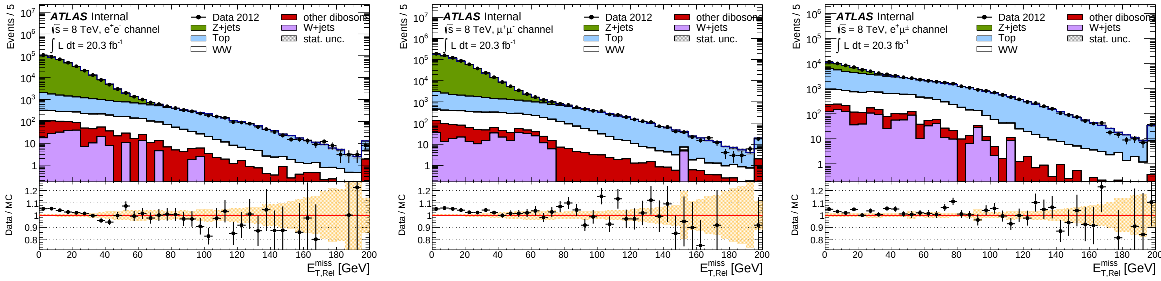


Figure 7.2: $\not\!\!E_T^{rel}$ distribution after $Z$-veto for the *ee* (left) and $\mu\mu$ (middle) and $e\mu$ (right) channels. Data are shown together with the processes predicted by MC and scaled to 20.3 $fb^{-1}$ . Statistical uncertainties are shown as gray bands in the main plot or as orange bands on the ratio plot.

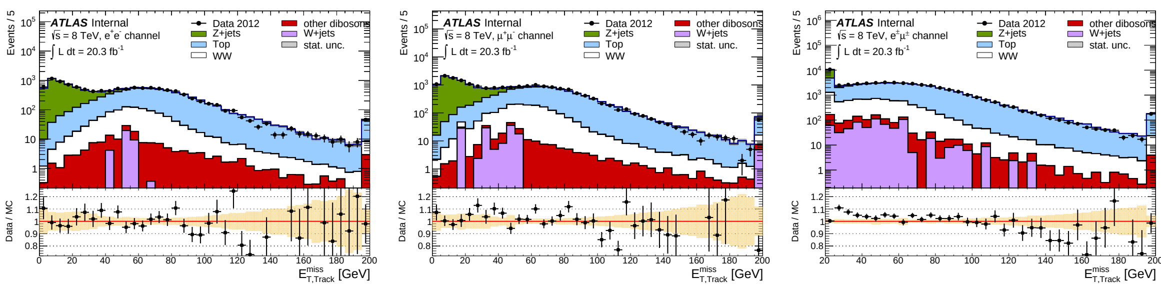


Figure 7.3: $\not\!p_T$ distribution after $\not\!\!E_T^{rel}$ cut for the *ee* (left) and $\mu\mu$ (middle) and $e\mu$ (right) channels. Data are shown together with the processes predicted by MC and scaled to 20.3 $fb^{-1}$. Statistical uncertainties are shown as gray bands in the main plot or as orange bands on the ratio plot.

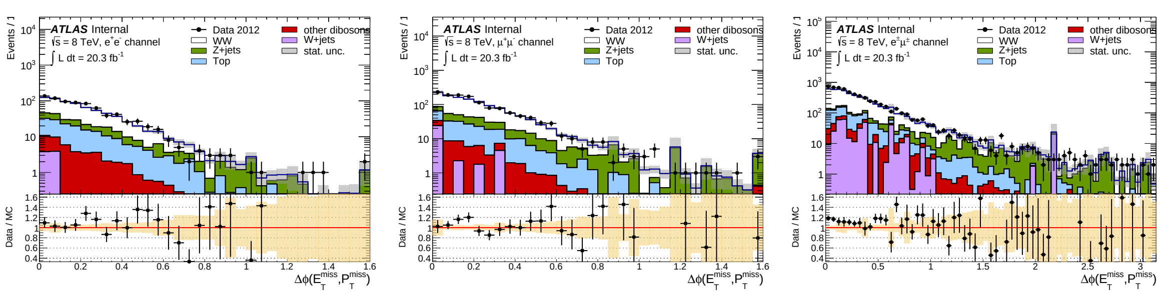


Figure 7.4: $\Delta\phi(\not\!p_T, \not\!\!E_T)$ distribution after $\not\!p_T$ cut and in the zero jet bin. From left to right the *ee* and $\mu\mu$ and $e\mu$ channels are shown. Data are shown together with the processes predicted by MC and scaled to 20.3 $fb^{-1}$. Statistical uncertainties are shown as gray bands in the main plot or as orange bands on the ratio plot.

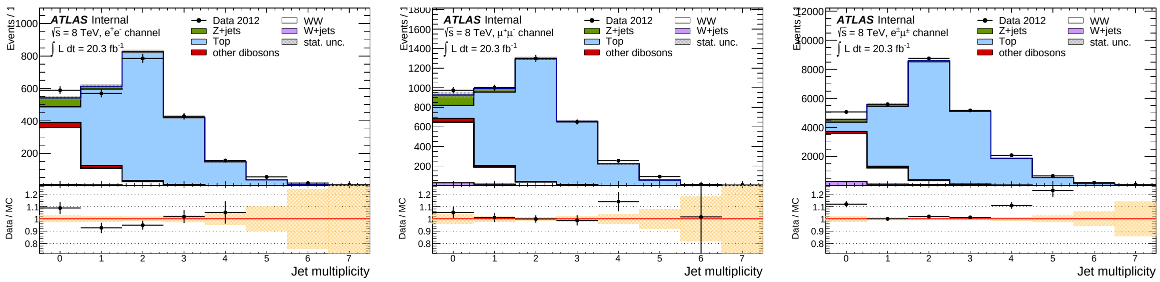


Figure 7.5: Jet multiplicity distribution before the jet-veto for the $ee$ (left) and $\mu\mu$ (middle) and $e\mu$ (right) channels. Data are shown together with the processes predicted by MC and scaled to 20.3 $fb^{-1}$. Statistical uncertainties are shown as gray bands in the main plot or as orange bands on the ratio plot.

## 7.4 Event Selection Cut-flow

The $W^+W^-$ event selection cut-flow for data is shown in Table 7.4. 6636 candidate events were observed after final selection in 20.3 $fb^{-1}$ of data, where the total prediction is 5745, including 4197 expected SM $W^+W^-$ events.

| Cuts | $ee$ | $\mu\mu$ | $e\mu$ | Combined |
|---|---:|---:|---:|---:|
| 2 leptons | 6011503 | 10414698 | 167682 | 16593883 |
| Opposite-sign | 5996645 | 10410426 | 157280 | 16564351 |
| $p_T^{\ell_1}$, trigger-match | 4945211 | 8406743 | 84698 | 13436652 |
| BCH Cleaning | 4929115 | 8380532 | 83086 | 13392733 |
| $M_{\ell\ell} > 15(10)\ GeV$ | 4918726 | 8357583 | 83042 | 13359351 |
| $\lvert M_{\ell\ell} - M_Z\rvert > 15\ GeV$ | 412853 | 721978 | — | 1217873 |
| $\not{E}_T^{rel} > 45(15)\ GeV$ | 11594 | 19887 | 52142 | 83623 |
| $\not{p}_T > 45(20)\ GeV$ | 5762 | 9152 | 43718 | 58632 |
| $\Delta\phi(\not{p}_T, \not{E}_T) < 0.3(0.6)$ | 2613 | 4291 | 27591 | 34495 |
| Jet-Veto | 594 | 975 | 5067 | 6636 |

Table 7.4: Event selection cut-flow for data collected in 2012 at 8 $TeV$ for 20.3 $fb^{-1}$ split in channels. For the $M_{\ell\ell}$, $\not{E}_T^{rel}$, $\not{p}_T$, and $\Delta\phi(\not{p}_T, \not{E}_T)$ cuts, two cut values are presented in first column, with the first one for same-flavor channel and the second one for $e\mu$ channel.

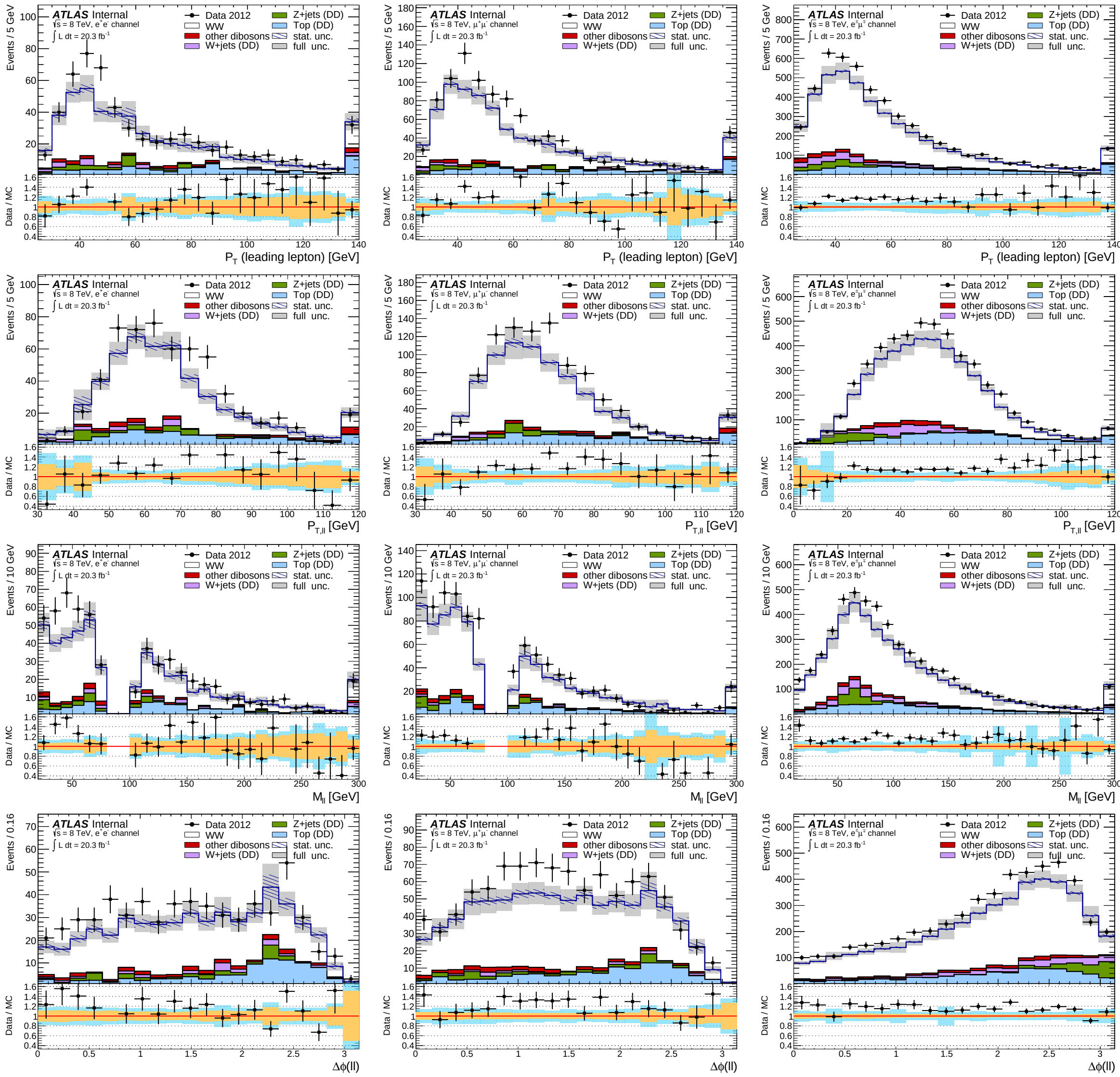


Figure 7.6: Distributions for $W^+W^-$ candidates at final selection for combined $ee$, $\mu\mu$ and $e\mu$ channels: the left column shows the $ee$ channel, the middle column the $\mu\mu$ channel and the right column the $e\mu$ channel. The first row shows the leading lepton $p_T$, the second row the transverse momentum of di-lepton pair $p_T^{\ell\ell}$, the third row shows the invariant mass of the di-lepton pair $M_{\ell\ell}$ distributions, and the fourth row shows the $\Delta\phi_{\ell\ell}$ distributions. The points represent data and the stacked histograms describe the signal and backgrounds separately. Signal and "other di-bosons" are modeled by MC, $Z$+*jets* is estimated by the simultaneous fit, top is estimated by JVSP method and the $W$+*jets* distribution has been obtained using the matrix method (indicated by the DD – data-driven label). The uncertainty includes statistical uncertainties and systematics on the signal and backgrounds and is shown as grey bands in the main plot and in blue on the ratio plot. Statistical uncertainty itself is indicated by the line pattern in the main plot or the orange band in the ratio plot. The histograms are normalised by SM cross sections to 20.3 $fb^{-1}$ .

## 7.5 Expected Number of Events from MC

### 7.5.1 MC Event Weights

As described in previous sections, there are a series of corrections, SFs, and re-weights for MC samples, for the purpose of correcting their efficiencies and shapes when compared to observed data. Therefore, each MC selected events comes with a series of different event weight scaling factors, some being object-independent, some depending on the kinematics of the final selected objects. This section summarizes all the SFs applied to the event weight after MC event selection. Each uncertainty of these SFs, if any, contributes one term to the systematics of $C_{WW}$ as discussed in Section 6.4.

The MC event weight is the base term of the weight calculation, which is not necessarily an integer (like 0 or 1 for data). For some NLO generators, event weights can be fractional, or even negative, depending on the contribution of that event to the total cross calculation.

*Pile-up* re-weighting is applied as the MC samples were generated with a wide $\langle\mu\rangle$ distribution (see Section 3.1 and Figure 3.2) to encompass that of the data. The re-weighting corrects the MC *pile-up* conditions to what is found in the data taken.

*z-vertex position re-weighting* is applied, which gives event by event weights from the generated $z$-position of the hard interaction to match the $z$-position of the beam spot in data.

Trigger efficiency SF are applied (see Section 3.2.5).

Lepton identification and reconstruction efficiency SFs are applied, which can be decomposed into electron SFs and muon SFs. Electron SFs includes eID efficiency SF and reconstruction efficiency SF (see Section 5.3.4). The muon SF has only one contribution, the muon reconstruction efficiency SF (see Section 5.4.4).

Lepton isolation SFs are applied, which again has two contributions: electron isolation efficiency SF (see Section 5.3.4)) and muon isolation efficiency SF (see Section 5.4.4).

The Drell-Yan MC samples are re-weighted from LO PDF `CTEQ6L1` to the NLO PDF `CT10` in order to better model the lepton $\eta$ distributions at pre-selection level.

After all the re-weighting and corrections, all those SFs are multiplied together with the MC event weight to generate a final weight for the selected event.

### 7.5.2 MC Event Prediction Cut-flow

After applying all the weight corrections, the MC $W^+W^-$ signal cut flows are shown in Table 7.5 for the three di-lepton channels and the combined channel at each step after pre-selection. The MC events are normalized to 20.3 $fb^{-1}$ using the reference pNNLO SM cross section (see Section 6.1). Please note the signal process includes $qq \rightarrow WW$, $gg \rightarrow WW$ and $gg \rightarrow H \rightarrow WW$ processes, which contribute about 93%, 4% and 3% of the total event yields after final selection, respectively. The NLO EW correction is applied in the calculation of the selection efficiency for $qq \rightarrow WW$ events, while the cross section for this process is still taken from **MCFM** calculation in which the EW correction is not applicable. The effect of the NLO EW correction on signal yields is found to be less than one percent. Furthermore, the $WW \rightarrow \tau\tau$ decay channels contribute about 8% of the total signal yields after final selection.

| Cuts | $ee$ | $\mu\mu$ | $e\mu$ | Combined |
|---|---|---|---|---|
| Total | 19156.32 | 19293.62 | 38449.69 | 76899.63 |
| Trigger Match | 3341.61 ± 10.08 | 5491.48 ± 13.36 | 8725.58 ± 16.57 | 17558.67 ± 23.55 |
| $M_{\ell\ell} > 15(10)\ GeV$ | 3317.06 ± 10.05 | 5445.98 ± 13.31 | 8719.01 ± 16.56 | 17482.04 ± 23.51 |
| $\|M_{\ell\ell} - M_Z\| < 15\ GeV$ | 2551.82 ± 8.79 | 4179.35 ± 11.63 | 8719.01 ± 16.56 | 15450.18 ± 22.07 |
| $E_T^{miss,rel} > 45(15)\ GeV$ | 950.67 ± 5.36 | 1634.47 ± 7.27 | 6726.43 ± 14.55 | 9311.56 ± 17.12 |
| $p_T^{miss} > 45(20)\ GeV$ | 736.76 ± 4.73 | 1264.38 ± 6.41 | 6008.53 ± 13.74 | 8009.67 ± 15.88 |
| $\Delta\phi(p_T^{miss}, E_T^{miss}) < 0.3(0.6)$ | 478.57 ± 3.85 | 830.80 ± 5.23 | 4689.69 ± 12.19 | 5999.06 ± 13.81 |
| Jet-Veto | 346.32 ± 3.29 | 612.49 ± 4.51 | 3238.11 ± 10.17 | 4196.92 ± 11.60 |

Table 7.5: $W^+W^-$ MC event selection cut-flow at final selection. The MC $W^+W^-$ signal expectations are normalized to 20.3 $fb^{-1}$, using the reference SM cross section. Only statistical uncertainties are shown.

## 7.6 Fiducial Volume Definition

The fiducial volumes are defined using similar selection cuts as those in reconstruction level, and therefore there are three regions corresponding to the three different channels.Table 7.6 gives the fiducial volume definitions in details.

The fiducial volume is defined at both reconstruction level and truth level. Dressed truth electrons and muons[1] are used to define the fiducial cross section. The truth electrons and muons are required to stem from one of the $W$ bosons produced in the hard scatter. Truth jets are built using the same algorithm as for calorimeter jets, and

[1]For dressed muons and electrons, the truth lepton four-momentum after radiation is used after adding back the four-momenta of all there radiated photons inside a cone of a radius $\Delta R = 0.1$.

| | $e\nu e\nu$ fiducial region | $\mu\nu\mu\nu$ fiducial region | $e\nu\mu\nu$ fiducial region |
|---|---|---|---|
| $p_T^{\ell_1}(p_T^{\ell_2})$ | > 25(20) $GeV$ | > 25(20) $GeV$ | > 25(20) $GeV$ |
| $\lvert\eta^{\ell}\rvert$ | $1.37 < \lvert\eta\rvert$,<br>$1.52 < \lvert\eta\rvert < 2.47$ | $\lvert\eta\rvert < 2.4$ | $1.37 < \lvert\eta^e\rvert$, $1.52 < \lvert\eta^e\rvert < 2.47$<br>and $\lvert\eta^{\mu}\rvert < 2.4$ |
| $M_{\ell\ell}$ | > 15 $GeV$ | > 15 $GeV$ | > 10 $GeV$ |
| $\lvert M_{\ell\ell} - M_Z\rvert$ | > 15 $GeV$ | > 15 $GeV$ | $\geqslant 0$ $GeV$ |
| $N_j$, $j$ is good jets | 0 | 0 | 0 |
| $E_T^{rel}$ | > 45 $GeV$ | > 45 $GeV$ | > 15 $GeV$ |
| $p_T$ | > 45 $GeV$ | > 45 $GeV$ | > 20 $GeV$ |

Table 7.6: Definitions of fiducial volumes for different channels. $p_T^{\ell_1}(p_T^{\ell_2})$ is the transverse momentum for the leading (sub-leading) lepton.

use stable truth particles, including muons, as input. To remove overlapped truth objects, truth jets within $\Delta R = 0.3$ of a truth lepton are removed from the list of valid jets for the jet-veto. For the calculation of the $E_T$ , the 4-vector sum of the neutrinos stemming from the $W$ boson decays is used.

One important note is that the fiducial region is defined in the final states with only leptons from $W$ prompt decay (called prompt leptons), while the selected reconstruction events contain also leptons from $W \to \tau\nu_\tau \to \ell\nu\nu_\tau$ ($\ell \in \{e, \mu\}$). This fact should be kept in mind while comparing the acceptance tables and the cut-flow tables, as it will introduce a subtle variation in calculation of $\mathcal{A}_{WW}$ and $C_{WW}$ (see Section 7.7).

## 7.7 Acceptance and Corrections

As mentioned in Section 6.4, the signal acceptance is expressed in two terms: the fiducial acceptance ($\mathcal{A}_{WW}$) and the reconstruction correction ($C_{WW}$). However, there is a little difference in the actual calculation of $\mathcal{A}_{WW}$ and $C_{WW}$. In this analysis, the $\tau$ contribution in the $W^+W^-$ analysis is considered as a background for the fiducial cross section measurement, thus the $C_{WW}$ and $\mathcal{A}_{WW}$ factors are defined in the following way:

$$
\begin{aligned}
C_{WW} &= \frac{N^{\text{reco,fiducial}}_{WW\to\ell\nu\ell\nu}}{N^{\text{gen,fiducial}}_{WW\to\ell'\nu\ell'\nu}} \\
\mathcal{A}_{WW} &= \frac{N^{\text{gen,fiducial}}_{WW\to\ell'\nu\ell'\nu}}{N^{\text{gen,full}}_{WW\to\ell'\nu\ell'\nu}} \\
\epsilon_{\mathcal{A}} \equiv \mathcal{A}_{WW}\times C_{WW} &= \frac{N^{\text{reco,fiducial}}_{WW\to\ell\nu\ell\nu}}{N^{\text{gen,full}}_{WW\to\ell'\nu\ell'\nu}}
\end{aligned}
\tag{7.3}
$$

where $\ell \in \{e, \mu, \tau\}$ and $\ell' \in \{e, \mu\}$.

With the fiducial volume defined, an overall picture of the signal selection can be seen. Using the full simulated MC samples as well as truth-level information in these samples, the $\mathcal{A}_{WW}$, $C_{WW}$ and $\epsilon_{\mathcal{A}}$ are estimated and shown in Table 7.7. The systematics are presented for reference, with details discussed in Section 9.2.1.

| | $e\nu e\nu$ | $\mu\nu\mu\nu$ | $e\nu\mu\nu$ | Combined |
|---|---|---|---|---|
| $\mathcal{A}_{WW}$ | $0.0855 \pm 0.0003 \pm 0.0038$ | $0.0930 \pm 0.0004 \pm 0.0041$ | $0.2274 \pm 0.0004 \pm 0.0098$ | $0.1583 \pm 0.0002 \pm 0.0069$ |
| $\Delta\mathcal{A}_{WW}/\mathcal{A}_{WW}$ | 4.41% | 4.45% | 4.30% | 4.33% |
| $C_{WW}$ | $0.2913 \pm 0.0023 \pm 0.0174$ | $0.4740 \pm 0.0025 \pm 0.0297$ | $0.5124 \pm 0.0011 \pm 0.0240$ | $0.4769 \pm 0.0010 \pm 0.0231$ |
| $\Delta C_{WW}/C_{WW}$ | 5.96% | 6.26% | 4.69% | 4.85% |
| $\epsilon_{\mathcal{A}}$ | $0.0249 \pm 0.0002 \pm 0.0019$ | $0.0441 \pm 0.0003 \pm 0.0034$ | $0.1165 \pm 0.0003 \pm 0.0075$ | $0.0755 \pm 0.0002 \pm 0.0049$ |
| $\Delta(\epsilon_{\mathcal{A}})/\epsilon_{\mathcal{A}}$ | 7.55% | 7.72% | 6.40% | 6.52% |

Table 7.7: The $WW$ overall acceptance $\epsilon_{\mathcal{A}}$, fiducial volume acceptance $\mathcal{A}_{WW}$, and correction factor $C_{WW}$ as well as their uncertainties. The first and the second errors are statistical and systematic uncertainties, respectively. The systematic uncertainties are also shown in percentage.

## CHAPTER 8

# Background Estimation

Background estimation is one of the most challenging parts of this analysis. Backgrounds from the *W+jets*, *Z+jets*, and *Top* productions are estimated from data and compared with MC simulations, while background from the di-boson productions are estimated using MC simulations.

To estimate the *Z+jets* background, a so-called *ABCD* method (8.1) is used. It partially relies on MC simulated shapes of the $\not{E}_T$ distribution and the relation between $\not{E}_T$ and $\not{p}_T$. The *W+jets* and *multijet* backgrounds are estimated using the so-called *Matrix method* (Section 8.2). For the Top estimate, the method is based on a *transfer factor (TF)* method using a high jet multiplicity region as the top background control region to determine the normalization transfer factor for the signal region (see Section 8.3). The di-boson background is purely estimated from MC (see Section 8.4). Each of the background estimation method mentioned above have been cross checked with other methods independently [53], and the results agree well within the uncertainties. Before getting into technical details for estimating these backgrounds, a summary of the background estimation is given as well as their statistical and systematic uncertainties in Table 8.1, where the background estimation with different methods are compared. The following sections studies of background estimations for this thesis are described.

## 8.1 *Z+jets* and Drell-Yan Contributions

This section describes the estimation of *Z+jets* background using the *ABCD* method, of which I am the main contributor. The results obtained with *ABCD* method was cross checked with other independent methods and achieved agreement within uncertainties (see Table 8.1).

| Process | Method | $ee$ | $\mu\mu$ | $e\mu/\mu e$ |
|---|---|---|---|---|
| $W$+*jets* | Matrix method | 13.9 ± 4.9 ± 14.2 | 6.1 ± 5.0 ± 11.5 | 248.8 ± 15.3 ± 138.7 |
| | Fake-factor method | 7.54 ± 0.72 ± 6.57 | 18.47 ± 2.77 ± 11.98 | 214.46 ± 7.32 ± 140.08 |
| | MC prediction | 21.6 ± 9.7 | 13.6 ± 4.3 | 225.3 ± 24.4 |
| $Z$+*jets* | Simultaneous fit | 54.5 ± 1.2 ± 23.1 | 95.6 ± 1.5 ± 26.5 | 166.1 ± 3.2 ± 26.3 |
| | *ABCD* method | 56.2 ± 3.7 ± 21.6 | 114.5 ± 5.4 ± 31.4 | 166.8 ± 10.7 ± 22.9 |
| | TF method | 58.5 ± 7.0 ± 30.9 | 121.6 ± 10.2 ± 52.3 | 161.5 ± 16.6 ± 26.6 |
| | MC prediction | 55.3 ± 6.3 ± 17.1 | 106.0 ± 7.0 ± 27.4 | 164.6 ± 15.4 ± 18.5 |
| Top | JVSP method | 91.8 ± 7.3 ± 7.9 | 127.2 ± 9.4 ± 10.9 | 608.6 ± 17.5 ± 52.3 |
| | TF method | 97.3 ± 5.1 ± 22.8 | 131.2 ± 6.4 ± 38.6 | 641.4 ± 13.6 ± 145.9 |
| | Simultaneous fit | 93.7 ± 2.5 ± 24.6 | 136.2 ± 2.9 ± 18.7 | 653.4 ± 5.2 ± 122.3 |
| | MC prediction | 96.9 ± 4.8 ± 26.5 | 131.4 ± 6.1 ± 32.8 | 625.9 ± 12.5 ± 129.4 |
| Di-boson | MC prediction | 27.3 ± 1.4 ± 5.3 | 38.4 ± 1.3 ± 5.4 | 149.7 ± 4.0 ± 30.7 |

Table 8.1: Comparison of the background yields obtained with the data-driven methods and MC predictions. The first error is statistical uncertainty, and the second is systematic uncertainty. Besides the methods which will be introduced in the following sections, other independent methods are documented in Reference [53].

### 8.1.1 $Z$+*jets* Estimation with the *ABCD* Method

The background of $WW$ production was dominated by the $Z$+*jets* production which has a cross section of almost 1000 times larger ($\sim nb$). $Z$+*jets* events entered the $WW$ signal region for different reasons depending on channel: for the same-flavor channels ($ee/\mu\mu$), the $Z$+*jets* events entering $WW$ signal region had no high-$p_T$ jet identified, di-lepton mass outside of the $Z$-mass window, and sufficiently large fake $\not{E}_T$ mainly due to the high *pile-up* environment; while for the opposite-flavor channel ($e\mu$), $Z \to \tau\tau$ events with $\tau$ decaying leptonically to $e$ and $\mu$ entered the $WW$ signal region for similar reasons but with real $\not{E}_T$ in the final states.

Since the MC simulation failed to accurately model the fake $\not{E}_T$ due to *pile-up*, a partially data-driven, so-called *ABCD* method, is used for the $Z$+*jets* background estimation. In the *ABCD* method, the data set is split into four regions (A, B, C, and D):

- Region A (Signal Region): $\Delta\phi(\not{p}_T, \not{E}_T) < 0.3(0.6)$ and $\not{E}_T^{rel} > 45(15)$ *GeV* for same-flavor (opposite-flavor) channels

- Region B: $\Delta\phi(\not{p}_T, \not{E}_T) > 0.3(0.6)$ and $\not{E}_T^{rel} > 45(15)$ *GeV* for same-flavor (opposite-flavor) channels

- Region C: $\Delta\phi(\not{p}_T, \not{E}_T) < 0.3(0.6)$ and $\not{E}_T^{rel} < 45(15)$ *GeV* for same-flavor (opposite-flavor) channels

- Region D: $\Delta\phi(\not{p}_T, \not{E}_T) > 0.3(0.6)$ and $\not{E}_T^{rel} < 45(15)\ GeV$ for same-flavor (opposite-flavor) channels

With such definition, region C and D are $Z$+*jets* enriched regions (control regions). The ratio of $Z$+*jets* events in A and B, or C and D, can be defined as TFs. The *ABCD* method is essentially a double TF method: the TF of A and B, is assumed equal to the TF of C and D. If the $Z$+*jets* events in B is accurately estimated, by multiplied with the TF obtained from C and D, the $Z$+*jets* events in signal region A can be estimated.

The $\not{E}_T^{rel}$ and $\Delta\phi(\not{p}_T, \not{E}_T)$ cuts were chosen to define the four regions for the reasons as follows. Firstly, the two cuts had strong discriminating power between signal and $Z$+*jets*. Secondly, the two cuts were within the nominal selection cuts, otherwise the fiducial volume would be different from the signal region A defined in the *ABCD* method. Finally, among all available cut candidates for this method, $\not{E}_T^{rel}$ and $\Delta\phi(\not{p}_T, \not{E}_T)$ had minimal correlation, which was good for the suppression of systematic uncertainty.

As explained in Section 5.6.3, the $\Delta\phi(\not{p}_T, \not{E}_T)$ is small for signal events but large for $Z$+*jets* events. Figure 8.1 shows the two-dimensional normalized distributions of $\not{E}_T^{rel}$ vs $\Delta\phi(\not{p}_T, \not{E}_T)$ in three channels for both $WW$ and $Z$+*jets*, which demonstrates clear distinction between the two processes.

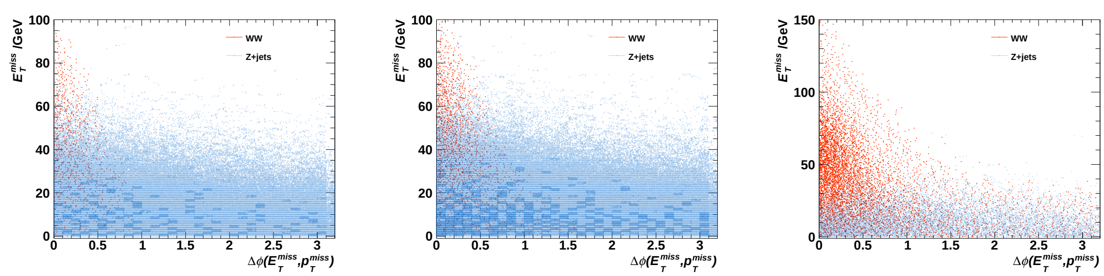


(a) $ee$ channel (b) $\mu\mu$ channel (c) $e\mu$ channel

Figure 8.1: The two-dimensional distribution of $\not{E}_T^{rel}$ vs $\Delta\phi(\not{p}_T, \not{E}_T)$ for signal and $Z$+*jets* MC samples in different channels. All nominal selection cuts are applied except $\not{p}_T$. Yields are normalized to luminosity. A clear distinction of the distribution characteristics for $WW$ and $Z$+*jets* can be seen from the figures.

The number of $Z$+*jets* events in signal region A is calculated using Equation 8.1:

$$N_A = f_{ABCD} \cdot N_B \cdot \frac{N_C}{N_D} \tag{8.1}$$

where

$$N_i = N_i^{\text{data}} - N_i^{\text{Non-Z MC}} \text{ , for } i \in (B, C, D)$$
$$f_{ABCD} = \frac{N_A^{\text{Z MC}}/N_B^{\text{Z MC}}}{N_C^{\text{Z MC}}/N_D^{\text{Z MC}}} = \frac{N_A^{\text{Z MC}} \cdot N_C^{\text{Z MC}}}{N_B^{\text{Z MC}} \cdot N_D^{\text{Z MC}}} \tag{8.2}$$

The $N_i^{\text{data}}$ is the observed number of $Z$+*jets* events from data. To increase the $Z$+*jets* statistics, the nominal cuts were adjusted to suppress other backgrounds but with $Z$+*jets* kept as many as possible. To further eliminate the contamination from non-$Z$ processes, a subtraction of non-$Z$ MC contributions (including signal MC) from $N_i^{\text{data}}$ was applied. The $f_{ABCD}$ is a correction factor. Ideally, if $\not{E}_T^{rel}$ and $\Delta\phi(\not{p}_T, \not{E}_T)$ are completely uncorrelated, $f_{ABCD}$ is unity. However, correlation still exists in reality, as a result of reconstruction limitations of $\not{E}_T$, $\not{p}_T$, and imperfect MC modelling for non-$Z$ processes. Hence, $f_{ABCD}$ was introduced to account for the correlations.

The nominal $f_{ABCD}$ used in the *ABCD* method was derived from $Z$ MC samples. For validation, $f_{ABCD}$ derived using $N_i$ as defined in Equation 8.1 within the $Z$-mass peak (to enrich $Z$+*jets* ) was calculated as well. The $f_{ABCD}$ from both calculations agreed with each other within statistical uncertainty.

If the *ABCD* method is applied in the final phase space, the estimation results suffer from large statistical fluctuations. To cope with that difficulty, an alternative approach is adopted: implementing the *ABCD* method in a larger phase space first, then propagate the results into the final phase space by multiplying a selection efficiency between the two phase spaces. The final selection is re-ordered as following, compared to Section 7.3:

1. $\mathbf{M}_{\ell\ell}$: $M_{\ell\ell} > 15(10)$ *GeV* for same-flavor (opposite-flavor) channels
2. $Z$**-veto**: $|M_{\ell\ell} - M_Z| > 15$ *GeV* for same-flavor channels only.
3. **Jet-veto**: $N_j = 0$ for good jets.
4. $\not{E}_T^{rel}$: $\not{E}_T^{rel} >$ 45(15) *GeV* for same-flavor (opposite-flavor) channels.
5. $\boldsymbol{\Delta}\phi(\not{p}_T, \not{E}_T)$: $|\Delta\phi(\not{p}_T, \not{E}_T)| < 0.3(0.6)$ for same-flavor (opposite-flavor) channels.
6. $\not{p}_T$: $\not{p}_T > 45(20)$ *GeV* for same-flavor (opposite-flavor) channels.

With this selection order, the *ABCD* method was applied at Step 5, where statistical fluctuation is under control. Then the yields were propagated to the final phase space by multiplying the $\not{p}_T$ selection efficiency, $\epsilon_{\not{p}_T}$, which was also derived from $Z$+*jets* MC samples with a fitting method:

1. Fitting ranges of $\epsilon_{\not{p}_T}$ are defined as $[20, 50]$ *GeV* for same-flavor channels, and $[10, 25]$ *GeV* for opposite-flavor channel according to the distributions after $\Delta\phi(\not{p}_T, \not{E}_T)$ cut;

2. Apply different $\not{p}_T$ cuts in step of 0.1 *GeV* in the fitting ranges to acquire multiple $\epsilon_{\not{p}_T}$ as fitting points;

3. Use the fitting points to fit an exponential function ($e^{a+bx}$), then derive the $\epsilon_{\not{p}_T}$ at nominal $\not{p}_T$ points as well as statistical errors.

The $\not{p}_T$ distribution after $\Delta\phi(\not{p}_T, \not{E}_T)$ cut is shown in Figure 8.2, which shows good agreement between data and MC. The fitting plots are shown in Figure 8.3 and the central values of $\epsilon_{\not{p}_T}$ is shown in Table 8.2.

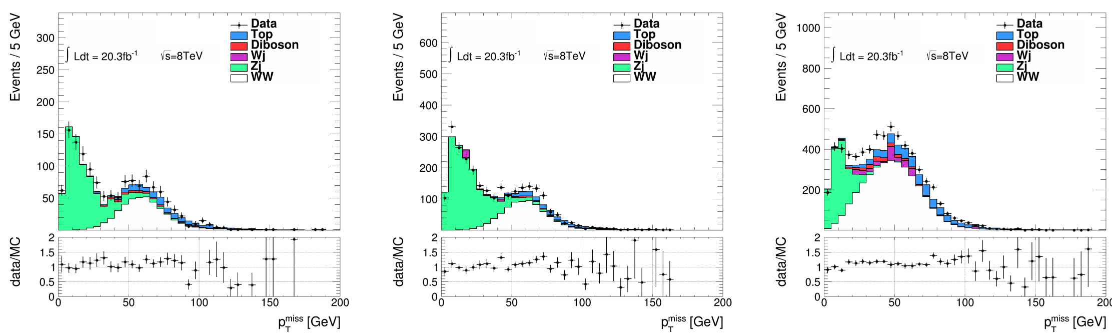


(a) *ee* channel (b) $\mu\mu$ channel (c) $e\mu$ channel

Figure 8.2: The $\not{p}_T$ distribution after $\Delta\phi(\not{p}_T, \not{E}_T)$ cut for signal and $Z$+*jets* MC samples in different channels. The fitting ranges are $[20, 50]$ *GeV* for $ee/\mu\mu$ channels, and $[10, 25]$ *GeV* for $e\mu$ channel.

| | Data | | | Non $Z$+*jets* MC | | | $f_{ABCD}$ | $\epsilon_{\not{p}_T}$ |
|---|---|---|---|---|---|---|---|---|
| | B | C | D | B | C | D | | |
| $ee$ | 3024 ± 54.99 | 40614 ± 201.53 | 232946 ± 482.65 | 234.11 ± 4.10 | 493.05 ± 9.08 | 876.33 ± 35.32 | 1.60 ± 0.10 | 0.073 ± 0.007 |
| $\mu\mu$ | 5581 ± 74.71 | 73276 ± 270.70 | 411025 ± 641.11 | 409.52 ± 19.76 | 802.40 ± 27.09 | 1340.04 ± 34.30 | 1.78 ± 0.08 | 0.070 ± 0.005 |
| $e\mu$ | 4337 ± 65.86 | 3919 ± 62.60 | 7295 ± 85.41 | 1030.00 ± 51.69 | 641.18 ± 45.51 | 871.47 ± 42.07 | 0.77 ± 0.04 | 0.128 ± 0.006 |

Table 8.2: The B/C/D event yields, $f_{ABCD}$ and $\epsilon_{\not{p}_T}$ after $\Delta\phi(\not{p}_T, \not{E}_T)$ cut. Only statistical uncertainties are listed.

The results for the $Z$+*jets* background estimation in signal region are summarized in Table 8.3 with statistical uncertainties. Estimation derived from $Z$+*jets* MC samples are also listed.

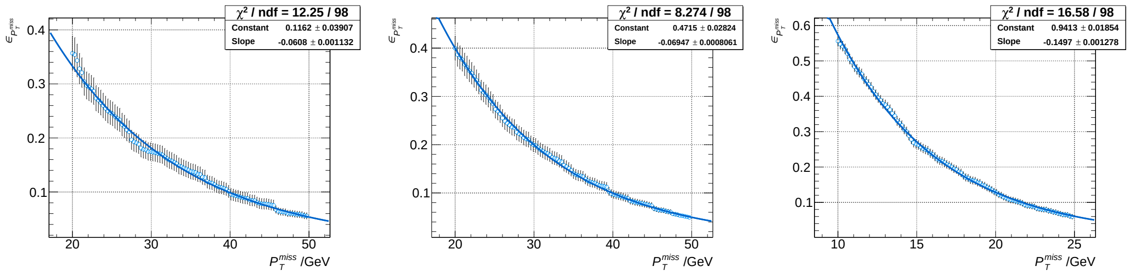


(a) *ee* channel (b) $\mu\mu$ channel (c) $e\mu$ channel

Figure 8.3: The exponential fits of $\epsilon_{\not{p}_T}$ for $Z$+*jets* in different channels. The fitting formula is $e^{a+bx}$, where $a$ and $b$ are fitting parameters. The fitting ranges are $[20, 50]$ $GeV$ for $ee/\mu\mu$ channels, and $[10, 25]$ $GeV$ for $e\mu$ channel, with step of 0.1 $GeV$. The fit was done with $Z$+*jets* MC samples. Fitted parameters were listed at the top right corners of each plot and were used for the calculation of $\epsilon_{\not{p}_T}$ at nominal $\not{p}_T$.

| | $ee$ | $\mu\mu$ | $e\mu$ |
|---|---|---|---|
| ABCD estimation | 56.2 ± 3.7(stat) ± 21.6(syst) | 114.5 ± 5.4(stat) ± 31.4(syst) | 166.8 ± 10.7(stat) ± 22.9(syst) |
| MC prediction | 55.3 ± 6.3(stat) | 106.0 ± 7.0(stat) | 164.6 ± 15.4(stat) |

Table 8.3: $Z$+*jets* background estimation in the signal region for three channels and its comparison to the MC prediction with statistical uncertainties.

### 8.1.2 Systematic Uncertainties

The total statistical and systematic uncertainties of the *ABCD* method is listed in Table 8.1 and Table 8.3. This section analyzes the contributions to the systematics. There are three major sources contributing to the systematic uncertainties: non-$Z$ MC subtraction in $N_i$ (Equation 8.2), the correction factor $f_{ABCD}$ (Equation 8.1), and $\epsilon_{\not{p}_T}$.

The non-$Z$ MC was dominated by $WW$ and $Top$, of which the expected uncertainties were 10% and 10-15%, respectively. So the non-$Z$ MC yields were scaled up and down by a conservative fraction of 15% for non-$Z$ MC subtraction, then propagated to the data-driven result, which is summarized in Table 8.4.

| | non-Z MC Scale Up | non-Z MC Scale Down |
|---|---|---|
| $ee$ | 1.39% | -1.39% |
| $\mu\mu$ | 1.30% | -1.30% |
| $e\mu$ | 5.57% | -5.57% |

Table 8.4: Systematic uncertainties of the *ABCD* method due to non-$Z$ MC subtraction. The up and down scale is taken as ±15% of the total yields of non-$Z$ MC after $\Delta\phi(\not{p}_T, \not{E}_T)$ cut.

For $f_{ABCD}$, the $\not{E}_T^{rel}$ cut was varied by $\pm 5$ *GeV* and the $\Delta\phi(\not{p}_T, \not{E}_T)$ cut was varied by $\pm 0.05$ independently to acquire corresponding uncertainties, denoted by $\delta_{\not{E}_T^{rel}}$ and $\delta_{\Delta\phi(\not{p}_T, \not{E}_T)}$; the total systematic error of $f_{ABCD}$ was calculated by combining statistical error of $f_{ABCD}$ with $\delta_{\not{E}_T^{rel}}$ and $\delta_{\Delta\phi(\not{p}_T, \not{E}_T)}$, which is summarized in Table 8.5.

| | $\delta_{\not{E}_T^{rel}}$ | $\delta_{\Delta\phi(\not{p}_T, \not{E}_T)}$ | Statistics of $f_{ABCD}$ | Total |
|---|---|---|---|---|
| $ee$ | 4.52% | 3.90% | 6.25% | 8.65% |
| $\mu\mu$ | 3.09% | 1.17% | 4.49% | 5.58% |
| $e\mu$ | 5.86% | 1.50% | 5.19% | 7.97% |

Table 8.5: Systematic uncertainties of the *ABCD* method due to $f_{ABCD}$. $\delta_{\not{E}_T^{rel}}$ was estimated by varying $\not{E}_T^{rel}$ cut by $\pm 5$ *GeV*; $\delta_{\Delta\phi(\not{p}_T, \not{E}_T)}$ was estimated by varying $\Delta\phi(\not{p}_T, \not{E}_T)$ cut by $\pm 0.05$.

The $\epsilon_{\not{p}_T}$ was the dominant contribution to the total systematics, which was contributed from 3 sources: its statistic error, the $\not{p}_T$ systematics (denoted by $\delta_{\not{p}_T}$), and the systematics propagated from $\not{E}_T$ (denoted by $\delta_{\not{E}_T}^{\text{propagated}}$), as explained in the following text. $\delta_{\not{p}_T}$ is the combination of different sources of uncertainties provided by the `METUtility` performance package. In addition, since the $\not{E}_T^{rel}$ cut was applied prior to $\not{p}_T$ cut, the systematics of $\not{E}_T$ was effectively propagated to the $\not{p}_T$ cut. The $\not{E}_T$ variation is effectively the variations of four kinds of objects: electrons, muons, soft jets and hard jets. $\delta_{\not{E}_T}^{\text{propagated}}$ then is the combination of the systematics of these objects calculated by Equation 8.3:

$$\delta_{\not{E}_T}^{\text{propagated}} = \sqrt{\sum_{\text{syst}} \left( \frac{|N_{\text{nominal}} - N_{\text{syst+}}| + |N_{\text{nominal}} - N_{\text{syst-}}|}{2} \right)^2} \tag{8.3}$$

where "syst" denotes different sources of the systematics for $\not{E}_T$. Table 8.6 summarizes these sources of $\delta_{\not{p}_T}$ and $\delta_{\not{E}_T}^{\text{propagated}}$ systematics.

The combination of $\delta_{\not{p}_T}$ and $\delta_{\not{E}_T}^{\text{propagated}}$ is denoted by $\delta_{\text{reco}}$ since all these estimation was done on the reconstruction-level $Z$+*jets* MC samples. The total systematics coming from $\epsilon_{\not{p}_T}$ is then summarized in Table 8.7.

| | Systematics Sources | $ee$ | $\mu\mu$ | $e\mu$ |
|---|---|---|---|---|
| $\delta^{\text{propagated}}_{\not{E}_T}$ | $p_T^e$ Resolution Smearing | 4.36% | 0.00% | 0.14% |
| | $e$ R12Stats | 1.23% | 0.00% | 1.26% |
| | $e$ PSStats | 0.48% | 0.00% | 0.21% |
| | Low $p_T^e$ | 0.00% | 0.00% | 0.00% |
| | $e$ Energy Resolution | 1.94% | 0.00% | 0.49% |
| | $p_T^\mu$ in ID | 0.29% | 1.54% | 4.65% |
| | $p_T^\mu$ in MS | 0.29% | 0.76% | 0.40% |
| | $\mu$ Energy Scale | 0.00% | 0.62% | 0.20% |
| | Soft Jet Energy Scale | 26.04% | 17.74% | 2.70% |
| | Soft Jet Energy Resolution | 10.32% | 3.93% | 1.15% |
| | JES Effective NP1 | 1.37% | 2.51% | 0.70% |
| | JES Effective NP2 | 3.01% | 2.98% | 1.32% |
| | JES Effective NP3 | 1.12% | 2.02% | 0.72% |
| | JES Effective NP4 | 0.79% | 0.42% | 0.31% |
| | JES Effective NP5 | 1.25% | 0.45% | 0.26% |
| | JES Effective NP6+RestTerm | 0.69% | 0.48% | 0.21% |
| | JES Eta Intercalibration Modelling | 2.43% | 3.24% | 0.97% |
| | JES Eta Intercalibration StatAndMethod | 1.00% | 0.46% | 0.22% |
| | JES SingleParticle HighPt | 0.00% | 0.00% | 0.00% |
| | JES Relative Non Closure | 0.00% | 0.00% | 0.00% |
| | JES $\langle\mu\rangle$ Offset | 0.71% | 0.97% | 0.39% |
| | JES $N_{PV}$ Offset | 1.93% | 0.66% | 0.75% |
| | JES *Pile-up* Pt | 0.56% | 0.09% | 0.00% |
| | JES *Pile-up* Rho | 2.43% | 2.18% | 0.99% |
| | JES Closeby | 0.00% | 0.00% | 0.00% |
| | JES Flavour Composition | 4.36% | 5.07% | 1.45% |
| | JES Flavour Response | 2.68% | 2.66% | 1.01% |
| | JES B Scale | 0.28% | 0.00% | 0.00% |
| | Hard Jet Resolution | 20.05% | 13.74% | 1.79% |
| $\delta_{\not{p}_T}$ | Soft $\not{p}_T$ Resolution | 1.17% | 3.30% | 6.23% |
| | Soft $\not{p}_T$ Scale | 7.37% | 12.22% | 5.46% |
| $\delta_{\text{reco}}$ | | 36.30% | 26.08% | 10.30% |

Table 8.6: Systematics of the *ABCD* method due to $\delta_{\not{p}_T}$ and $\delta^{\text{propagated}}_{\not{E}_T}$. $\delta^{\text{propagated}}_{\not{E}_T}$ is combined according to Equation 8.3. Here the $\delta^{\text{propagated}}_{\not{E}_T}$ variation propagated to $\epsilon_{\not{p}_T}$, which was the major source of *ABCD* method systematics. $\delta_{\not{p}_T}$ combined from uncertainties provided by `METUtility` performance package was also included. $\delta_{\text{reco}}$ is the combination of $\delta_{\not{p}_T}$ and $\delta^{\text{propagated}}_{\not{E}_T}$.

| | $\delta_{\text{reco}}$ | Statistics | Total |
|---|---|---|---|
| $ee$ | 36.30% | 9.00% | 37.40% |
| $\mu\mu$ | 26.08% | 6.45% | 26.87% |
| $e\mu$ | 10.30% | 4.41% | 11.20% |

Table 8.7: Systematic uncertainties of the *ABCD* method due to $\epsilon_{\not{p}_T}$. $\delta_{\text{reco}}$ is the combination of $\delta_{\not{p}_T}$ and $\delta^{\text{propagated}}_{\not{E}_T}$.

## 8.2 *W+jets* and *Multijet* Contributions

The matrix method is used to estimate the contribution from events with one real and one fake lepton. It was developed and used on previous experiments such as Tevatron and the 7 *TeV WW* production cross section measurement at ATLAS [84] for the simultaneous estimation of *W+jets* and QCD *multijet* backgrounds. It has been validated in this analysis [53] in the same-sign event control region, which is enriched in events of *W+jets*, *multijet*, and di-boson production.

The principle of the matrix method relies on using two orthogonal data sample with different lepton selection criteria, which are the nominal sample selected with tight (nominal) lepton PIDs, and the control sample enriched in jets selected with loose lepton PIDs. By applying the nominal tight PIDs on the control sample, a selection efficiency is obtained, which depends on two parameters: firstly, the composition of the control sample, or how many real and fake leptons consisting of the control sample; secondly, the efficiency of real leptons in the control sample passing the tight PID (lepton efficiency) and the efficiency of fake leptons in the control sample passing the tight PID (fake-rate).

For a di-lepton analysis, this can be expressed as a system of linear equations:

$$\begin{pmatrix} N_{TT} \\ N_{TL} \\ N_{LT} \\ N_{LL} \end{pmatrix} = \begin{pmatrix} r_1 r_2 & r_1 f_2 & f_1 r_2 & f_1 f_2 \\ r_1(1-r_2) & r_1(1-f_2) & f_1(1-r_2) & f_1(1-f_2) \\ (1-r_1)r_2 & (1-r_1)f_2 & (1-f_1)r_2 & (1-f_1)f_2 \\ (1-r_1)(1-r_2) & (1-r_1)(1-f_2) & (1-f_1)(1-r_2) & (1-f_1)(1-f_2) \end{pmatrix} \times \begin{pmatrix} N_{RR} \\ N_{RF} \\ N_{FR} \\ N_{FF} \end{pmatrix} \tag{8.4}$$

with the following definitions:

- $N_{TT}$ is the number of events which have exactly two tight leptons.
- $N_{TL}$ and $N_{LT}$ are the numbers of events which have one tight and one loose lepton (with the first one as the leading one).

- $N_{LL}$ is the number of events which have exactly two loose leptons.
- $N_{RR}$ is the number of events which have exactly two real leptons.
- $N_{RF}$ and $N_{FR}$ are the number of events which have one real and one fake lepton (with the first one as the leading one).
- $N_{FF}$ is the number of events which have exactly two fake leptons.
- $r_1$ ($r_2$) are the leading (sub-leading) lepton efficiencies for the loose real leptons to pass the tight PID.
- $f_1$ ($f_2$) are the leading (sub-leading) fake-rates for loose fake leptons to pass the tight PID.

Note that, $N_{TT}$, $N_{TL}$, $N_{LT}$, and $N_{LL}$ have to pass the full $WW$ selection cuts, only different in the definition of leptons.

The $WW$ signal contains 2 and only 2 tight leptons. With the composition of sample in terms of $N_{RR}$, $N_{FR}$, $N_{RF}$ and $N_{FF}$ defined by Equation 8.4, the contribution from real $WW$ production to the signal region can be expressed as

$$N_{WW} = \sum_{i}^{N_{\text{events}}} N_{RR}^{i} \cdot r_1 r_2 \tag{8.5}$$

where $i$ runs over all selected events in the signal region, while the lepton efficiency ($r$) is double-differentiated in $p_T$ and $\eta$ for the leading and sub-leading leptons. Similarly, the contributions from $W$+*jets* and *multijet* to the signal region are written as Equation 8.6 and Equation 8.7, respectively:

$$\begin{aligned} N_{W+jets} &= \sum_{i}^{N_{\text{events}}} N_{RF}^{i} \cdot r_1 f_2 + N_{FR}^{i} \cdot f_1 r_2 && (8.6) \\ N_{Multijet} &= \sum_{i}^{N_{\text{events}}} N_{FF}^{i} \cdot f_1 f_2 && (8.7) \end{aligned}$$

where the lepton efficiency ($r$) and fake-rate ($f$) are double-differentiated in $p_T$ and $\eta$ as well. This is the advantage of the matrix method: the $W$+*jets* and *multijet* background contributions are estimated at the same time, represented by the single- and di-fake events.

Equations 8.5-8.7 rely on a pre-requisite that $N_{RR}$, $N_{RF}$, $N_{FR}$, and $N_{FF}$ have to be pre-determined for the calculation of $N_{WW}$, $N_{W+jets}$, and $N_{Multijet}$. It is straightforward to obtain them in MC samples, but in a data-driven method, real data is used where an observed lepton is impossible to be known as real or fake. Instead, the number of tight or loose leptons is known. Hence, Equation 8.5 is reversed to determine $N_{RR}$, $N_{RF}$, $N_{FR}$, and $N_{FF}$, as follows:

$$\begin{pmatrix} N_{RR} \\ N_{RF} \\ N_{FR} \\ N_{FF} \end{pmatrix} = \begin{pmatrix} r_1 r_2 & r_1 f_2 & f_1 r_2 & f_1 f_2 \\ r_1(1-r_2) & r_1(1-f_2) & f_1(1-r_2) & f_1(1-f_2) \\ (1-r_1)r_2 & (1-r_1)f_2 & (1-f_1)r_2 & (1-f_1)f_2 \\ (1-r_1)(1-r_2) & (1-r_1)(1-f_2) & (1-f_1)(1-r_2) & (1-f_1)(1-f_2) \end{pmatrix}^{-1} \times \begin{pmatrix} N_{TT} \\ N_{TL} \\ N_{LT} \\ N_{LL} \end{pmatrix} \tag{8.8}$$

In the per-event calculation per Equations 8.5-8.7, only one of the numbers $N_{LL}$, $N_{TL}$, $N_{LT}$ and $N_{TT}$ is non-zero. Lepton efficiencies ($r_1$, $r_2$) and fake-rates ($f_1$, $f_2$) have $p_T$ and $\eta$ dependency. Therefore, $N_{W+jets}$ and $N_{Multijet}$ can be interpreted as weighted event sums, allowing the extraction of the $W$+*jets* and QCD background as a function of any arbitrary variable. Also, for the sake of more careful treatment for the $e\mu$ channel, it is split into $e\mu$ and $\mu e$ according to the leading lepton.

### 8.2.1 Loose Lepton Definition

As the first step of the matrix method, the loose lepton has to be defined by applying a superset of the nominal selection criteria. The looser is the criteria, the better is it to reduce statistical uncertainties of the final $W$+*jets* estimate because of the large difference in loose and tight selection yields. However, in practice, the looseness is limited because available triggers set the loosest criteria that can be applied. The loose criteria for the matrix method are chosen to be:

- Loose electrons: the same as the full electron selection criteria in Table 7.1, except only passing **`MediumLLH`** eID, and without explicit isolation or impact parameter requirements.
- Loose muons: the same as the full muon selection criteria in Table 7.2, without explicit isolation or impact parameter requirements.

**Trigger Bias** Note that, the loose criteria is not independent of the triggers used, because triggers determine a lepton of the event is recorded or not, while the loose criteria is looser than the triggers used in the nominal selection which will cause a bias in the control sample selection. For the likelihood eID, there is no trigger available exactly matching the loose PID; for the $e\mu$ channel, single lepton triggers with explicit track isolation are dropped from the loose selection while they are used in nominal selection. Therefore, some additional triggers are used in the matrix method. However, it is not feasible to use them to select the loose control sample since these trigger are pre-scaled. For each additional trigger, lepton efficiencies and fake-rates are calculated. For un-triggered leptons, special unbiased triggers are used to determine the efficiencies and fake-rates. The triggers used in the analysis as well as the supporting triggers are listed in Table 8.8. Thus, different sets of lepton efficiencies and fake-rates are used for the estimation, depending on whether a lepton fired a single-lepton trigger, a di-lepton trigger or it was not triggered by either.

<table>
<tr><th>Channel</th><th>Nominal Triggers</th><th>Supporting Triggers</th><th>Pre-scale Weight (luminosity weighted)</th></tr>
<tr><td>$ee$</td><td>EF_2e12Tvh_loose1(_L2StarB)</td><td>EF_e15vh_medium1 || EF_e22vh_loose1 || EF_e15vh_loose0 || EF_e60_loose0</td><td>$1.0 \cdot 10^{-3}/3.1 \cdot 10^{-3}/6.4 \cdot 10^{-4}/2.9 \cdot 10^{-2}$</td></tr>
<tr><td>$\mu\mu$</td><td>EF_mu18_tight_mu8_EFFS</td><td>EF_mu15</td><td>$1.1 \cdot 10^{-3}$</td></tr>
<tr><td rowspan="5">$e\mu$</td><td>EF_e12Tvh_medium1_mu8</td><td>EF_e15vh_medium1 || EF_e22vh_loose1 || EF_e15vh_loose0 || EF_e60_loose0, EF_mu15</td><td>$1.0 \cdot 10^{-3}/3.1 \cdot 10^{-3}/6.4 \cdot 10^{-4}/2.9 \cdot 10^{-2}, 1.1 \cdot 10^{-3}$</td></tr>
<tr><td>untriggered $e$</td><td>EF_g20_etcut || EF_g24_etcut</td><td>$1.0 \cdot 10^{-4}/6.3 \cdot 10^{-6}$</td></tr>
<tr><td>untriggered $\mu$</td><td>EF_mu15</td><td>$1.1 \cdot 10^{-3}$</td></tr>
<tr><td>EF_e24vhi_medium1 || EF_e60_medium1</td><td>EF_e24vhi_medium1 || EF_e60_medium1</td><td>1</td></tr>
<tr><td>EF_mu24i_tight || EF_mu36_tight</td><td>EF_mu24i_tight || EF_mu36_tight</td><td>1</td></tr>
</table>

Table 8.8: Supporting triggers to study trigger bias effects and to measure fake-rates. The names of the nominal triggers are shown with the supporting triggers used for studies and the fake-rate calculation. The lumi-weighted pre-scales of the different supporting triggers are also shown.

### 8.2.2 Measurement of Lepton Efficiencies

As seen in Equation 8.6 and 8.7, the lepton efficiencies and fake-rates are the critical part of the matrix method. The lepton efficiencies are determined by MC with data-driven SFs applied for correction (provided by CP groups). Since the $Z$+*jets* events exhibit a lower lepton efficiency than $W$+*jets* events, all MC samples of the nominal analysis are used. In addition, the lepton efficiencies are calculated with loosen $\not{E}_T$ , $\not{p}_T$ and $\Delta\phi(\not{p}_T, \not{E}_T)$ requirements to improve statistic precision for the $Z$+*jets* samples.

The measured lepton efficiencies in signal and background are weighted averaged, accounted for the uncertainties of the SFs. For all triggers used in the nominal analysis, the measurement of the lepton efficiencies is performed differentially with 7 bins in $p_T$ and 4 bins in $\eta$. The precise double-differential lepton efficiencies calculated for the $e\mu$ trigger as an example are shown in Figure 8.4.

### 8.2.3 Measurement of Fake-rates

For the measurement of fake-rates, a clean $W$+*jets* MC sample is in need, yet not existing. Further, it is almost impossible to tag $W$+*jets* events with one additional

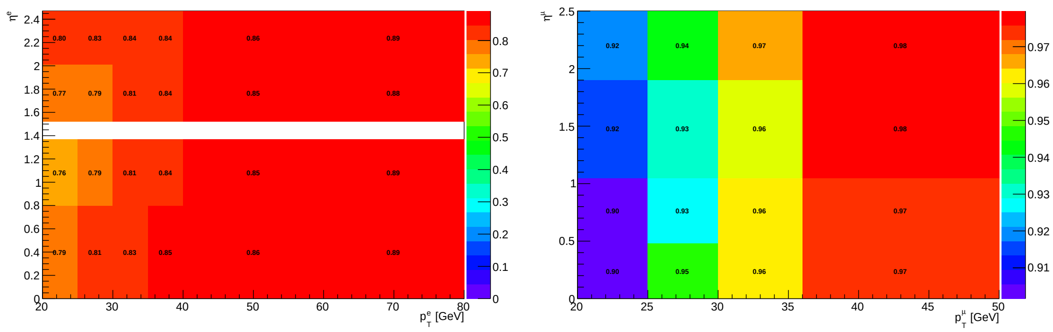

Figure 8.4: Double differential lepton efficiencies used in the matrix method for the $e\mu$-trigger electrons (left) and muons (right).

fake lepton. Hence, the fake-rates are measured on di-jet events (enriched in fake leptons) instead of MC. Di-jet events are selected from real data by the following criteria to suppress contributions from real leptons:

- The same data quality requirement as that in nominal analysis
- Loose lepton selection according to the criteria listed in Section 8.2.1.
- $Z$-veto: events with more than one loose lepton are rejected.
- $W$-veto: events with $m_T > 40\ GeV$ or $\not{E}_T > 25\ GeV$ are rejected.
- Exactly one jet in the detector.
- Azimuth angle between fake candidate and jet $\Delta\phi > 2$

To avoid trigger bias, a set of supporting single-lepton triggers are used. The requirement of exactly one jet is for that the fake leptons (from jets) are not identified as jets due to object overlap removal (see Section 7.1). Still highly contaminated with real leptons from $W \to \ell\nu$ and $Z \to \ell\ell$ decays, the selected sample further subtracts contributions from real leptons using MC. For the input to the matrix method, the fake-rate measurement is binned in 7(5) bins in $p_T$ for electrons(muons) respectively and 2 bins in $\eta$ (barrel and end-cap). The resulting fake-rates for the different triggers are shown in Figure 8.5.

A systematic uncertainty is assigned for the difference of kinematics between the di-jet sample selection and the nominal $WW$ selection, by removing the $\not{E}_T$ cut or loosening the $m_T$ cut. The resulting differences of fake-rates from the nominal setting is used as the kinematic systematic uncertainties. As the *pile-up* conditions in the

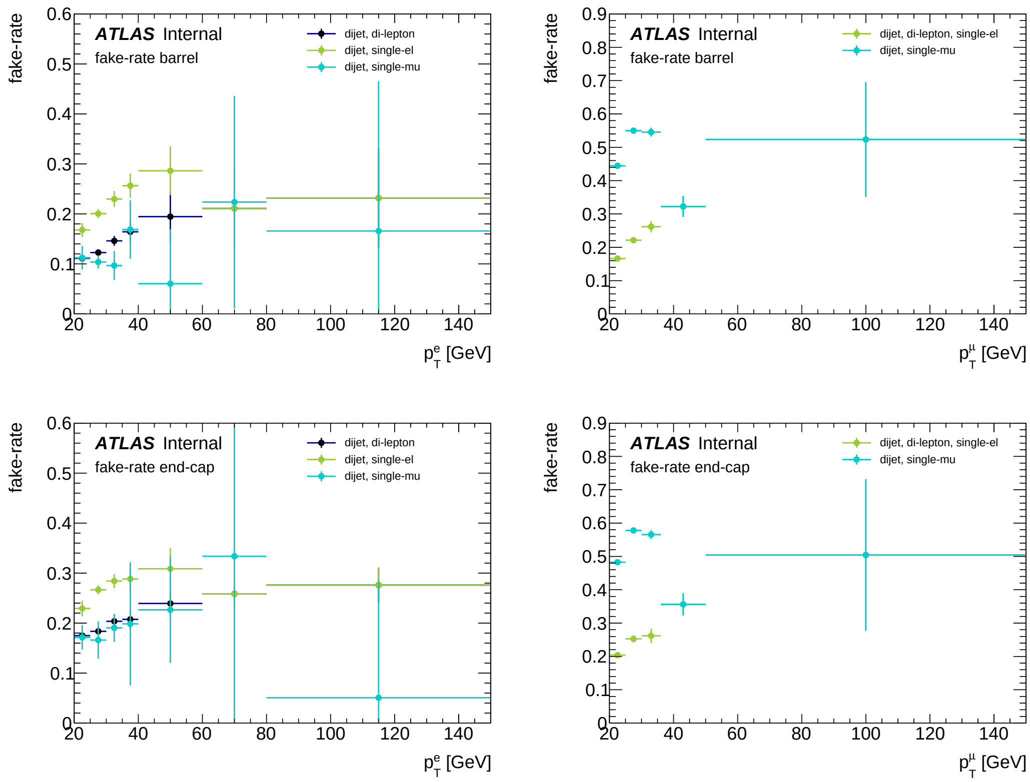


Figure 8.5: $p_T$ -binned fake-rates measured in data used in the matrix method for electrons (left) and muons (right) in barrel (top) and end-cap (bottom) regions. The fake-rates are measured with a set of supporting triggers, with labels indicating for which analysis triggers they are used. Systematic uncertainties are shown not including the sample dependence uncertainty (shown in Figure 8.6).

di-jet sample are very different from the nominal analysis, fake-rats only measured on events with $\langle\mu\rangle > 20$ or $\langle\mu\rangle < 20$ are added as a systematic uncertainty as well.

The most important systematic uncertainty deals with an implicit assumption in the matrix method: it assumes that the fake-rates in the two event types (measured from *W*+*jets* or *multijet*) are identical, or that it is appropriate to average the two fake-rates by their contribution in data. This assumption is not true since the di-jet and *W*+*jets* events have different heavy flavor compositions, hence this systematic uncertainty is assessed by comparing the measured fake-rates on di-jet and *W*+*jets* MC samples (called sample dependence uncertainty). The sample dependence uncertainty is shown as a function of $p_T$ in Figure 8.6. Further study of sample dependence and fake-rate measurements are detailed in [53].

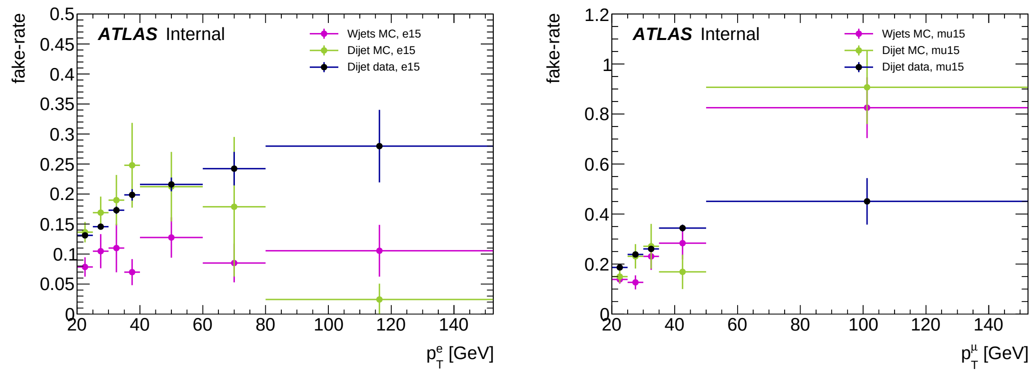


Figure 8.6: Fake-rates measured on a $W$+*jets* and di-jet MC samples for electrons (left) and muons(right) shown for two different triggers. The difference is assigned as a systematic uncertainty on the fake-rates measured on data. The integral over the full $p_T$ range is used in order to average out statistical fluctuations.

### 8.2.4 Results from the Matrix Method

The matrix method is not limited to the $W$+*jets* estimation. There are two non-negligible processes contributing in the $WW$ signal region, $W$+*jets* and $W\gamma$ . However, the matrix method can only estimate $W$+*jets* contributions correctly since the fake-rates are measured on jets, not photons. On the other hand, photons faking an electron are well modelled in MC, thus a data-driven estimation is not needed. Nevertheless, the $W$+*jets* estimate is contaminated by $W\gamma$ events, so they are subtracted by applying the matrix-method to $W\gamma$ MC.

The resulting $W$+*jets* data-driven estimate with uncertainties is shown in Table 8.9. The $W$+*jets* and QCD *Multijet* results are estimated to be: 13.9 ± 4.9(*stat*) ± 14.2(*syst*) in the $ee$ channel, 6.1 ± 5.0(*stat*) ± 11.5(*syst*) in the $\mu\mu$ channel and 248.8 ± 15.3(*stat*) ± 138.7(*syst*) in the combined $e\mu + \mu e$ channel. The dominant systematic source is the sample dependence.

## 8.3 *Top* Contributions

The decay products from both *Top*-pair ($t\bar{t} \rightarrow WbWb$) and single *Top* ($tW \rightarrow WbW$) processes contain $W^+W^-$ , which are characteristic by hadronic jet activities in final states. The jet-veto cut removes most of the *Top* background from the $W^+W^-$ signal region. However, *Top* events containing jets with $E_T^{jet} < 25\ GeV$ may still contaminate the $W^+W^-$ signal. The *Top* background is estimated from data in high

| Channel | Data-driven $W$+*jets* and QCD (± stats) | | | | | | | $W$+*jets* MC Prediction (± stats) |
|---|---|---|---|---|---|---|---|---|
| | Estimate | $r$(up) | $r$(down) | $f$(up) | $f$(down) | $f_{\text{sample}}$(up) | $f_{\text{sample}}$(down) | |
| ee | 13.93 ± 4.87 | 3.17 | -3.28 | 3.36 | -2.87 | 17.67 | -7.07 | 21.55 ± 9.66 |
| $\mu\mu$ | 6.07 ± 5.03 | 9.94 | -10.29 | -6.54 | 1.40 | -3.37 | -1.84 | 13.61 ± 4.30 |
| $e\mu$ | 150.14 ± 11.76 | 17.87 | -18.46 | 2.98 | -27.87 | 73.74 | -69.68 | 127.60 ± 17.44 |
| $\mu e$ | 98.69 ± 9.73 | 19.41 | -20.05 | 6.15 | -12.52 | 68.95 | -52.10 | 97.73 ± 17.02 |
| $e\mu + \mu e$ | 248.84 ± 15.26 | 37.28 | -38.50 | 9.14 | -40.39 | 142.69 | -121.79 | 225.32 ± 24.37 |
| | Data-driven QCD (± stats) | | | | | | | |
| ee | 0.20 ± 0.41 | 0.05 | -0.04 | 0.35 | -0.18 | | | |
| $\mu\mu$ | 1.87 ± 1.36 | 0.03 | 0.02 | 5.27 | -1.31 | | | |
| $e\mu$ | 13.89 ± 1.67 | 0.56 | -0.52 | 19.19 | -3.32 | | | |
| $\mu e$ | 8.31 ± 1.38 | 0.68 | -0.63 | 3.23 | -1.84 | | | |
| $e\mu + \mu e$ | 22.20 ± 2.17 | 1.24 | -1.15 | 22.42 | -5.16 | | | |

Table 8.9: Data-driven $W$+*jets* estimate with statistical and systematic uncertainties. The top part of the table shows the combined $W$+*jets* + QCD (*Multijets*) estimate; the bottom part shows only the QCD part. The symbols $r$(up) and $r$(down) indicate the up and down variations of the lepton efficiencies, while $f$(up) and $f$(down) indicate the up and down variations of the fake-rates (without the sample dependence). $f_{\text{sample}}$(up) and $f_{\text{sample}}$(down) indicate the up and down variations of the fake-rates by the sample dependence uncertainty.

jet multiplicity ($N_j$)control regions where a normalization scale factor (transfer factor) is determined then applied in the $W^+W^-$ signal region (in the 0-jet bin) to estimate the *Top* contamination in the selected signal sample.

This method is based on the consideration that *Top* events are dominated in high jet multiplicity region as shown in Figure 7.5. In order to estimate the *Top* background in the signal region (0-jet bin), events with $N_j \geqslant 3$ are used as the *Top* background control sample, and all the observed data events in the control region are assumed to be *Top* events since other background contamination in this region is very small. The transfer factor from the control region can be determined as

$$SF^{Top}_{N_j \geqslant 3}(\text{normalization}) = \frac{N^{Top,\text{data}}_{N_j \geqslant 3}}{N^{Top,\text{MC}}_{N_j \geqslant 3}} \tag{8.9}$$

With total observed data events and expected *Top* events in the control region, the transfer factor was determined to be $SF = 1.03$. The estimated *Top* events was transferred to the signal region based on the following equation:

$$\begin{aligned} N^{estimated}_{Top}(N_j = 0) &= N^{Top,\text{MC}}_{N_j=0} \times SF^{Top}_{N_j \geqslant 3} \\ &= N^{Top,\text{data}}_{N_j \geqslant 3} \times \frac{N^{Top,\text{MC}}_{N_j=0}}{N^{Top,\text{MC}}_{N_j \geqslant 3}} \end{aligned} \tag{8.10}$$

The estimated *Top* background in signal region are 97.3 ± 5.1(*stat*) ± 22.8(*syst*) for *ee*, 131.2 ± 6.4(*stat*) ± 38.6(*syst*) for $\mu\mu$, and 641.4 ± 13.6(*stat*) ± 145.9(*syst*) for $e\mu$ channel. The systematic uncertainties were determined by variations on jet-related terms, where the dominant part are JES and JER in MC solutions as well as statistical uncertainties in the control regions for three different di-lepton channels.

The estimation using this simple method has been cross checked using the so-called the *jet-veto survival probability (JVSP)* using b-tagging [53], and with MC simulations. The results obtained from different methods are consistent within the uncertainties.

## 8.4 Di-boson Contributions

The di-boson contribution from $WZ$, $ZZ$, $W\gamma$ and $W\gamma^*$ processes are estimated on MC samples normalized to the SM calculated cross sections (to NLO QCD) and the integrated luminosity of 20.3 $fb^{-1}$ . The $Z\gamma$ process is not included here since it is already included in the $Z$+*jets* data-driven estimation. The MC programs used for the di-boson production are listed in Table 6.10.

Table 8.10 summarizes the di-boson background yields as well as statistical uncertainties. Systematic uncertainties are listed in Table 8.11, which shows that the theoretical modeling uncertainties are large due to the jet-veto uncertainties and from the higher-order corrections for the $W\gamma^*$ process.

| Di-boson Background | $ee$ | $\mu\mu$ | $e\mu$ | Combined |
|---|---|---|---|---|
| $WZ$ | 7.72±0.68 | 19.35±1.00 | 62.86 ± 1.75 | 89.92 ± 2.12 |
| $ZZ$ | 10.61±0.43 | 16.06±0.54 | 2.76 ± 0.14 | 29.43 ± 0.70 |
| $W\gamma$ | 3.67±0.81 | 0.00±0.00 | 41.08 ± 2.72 | 44.75 ± 2.84 |
| $W\gamma^*$ | 5.35±0.83 | 2.96±0.60 | 42.98 ± 2.31 | 51.28 ± 2.53 |
| Total Background | 27.34±1.41 | 38.36±1.28 | 149.68±3.98 | 215.39 ± 4.41 |

Table 8.10: Other di-boson background yields and their statistical uncertainties as determined from MC for 20.3 $fb^{-1}$ . The systematic uncertainties for total di-boson backgrounds are calculated according to Table 8.11.

| Sources | $ee$ | $\mu\mu$ | $e\mu$ | Combined |
|---|---|---|---|---|
| Luminosity | 2.8% | 2.8% | 2.8% | 2.8% |
| *Pile-up* | 1.57% | 0.28% | 0.92% | 0.88% |
| Trigger Efficiency SF (muons) | 0% | 2.84% | 0.44% | 0.79% |
| Trigger Efficiency SF (electrons) | 2.75% | 0% | 0.44% | 0.67% |
| Muon MS Resolution | 0.55% | 3.12% | 2.14% | 2.09% |
| Muon ID Resolution | 0.93% | 2.29% | 0.38% | 0.53% |
| Muon Scale | 0% | 0.65% | 0.06% | 0.16% |
| Muon Efficiency SF | 0% | 0.80% | 0.38% | 0.40% |
| Muon Isolation SF | 0% | 1.12% | 0.59% | 0.60% |
| Electron Resolution | 0.88% | 0% | 0.11% | 0.07% |
| Electron Scale | 0.55% | 0% | 1.10% | 0.82% |
| Electron Efficiency SF | 2.30% | 0% | 1.33% | 1.24% |
| Electron Isolation SF | 0.46% | 0% | 0.27% | 0.25% |
| Jet Vertex Fraction | 0.40% | 0.41% | 0.23% | 0.29% |
| Jet Energy Resolution | 0.58% | 2.32% | 0.31% | 0.26% |
| Jet Energy Scale | 5.59% | 5.25% | 6.74% | 6.33% |
| $E_T^{rel}$ Reso Soft Terms | 1.10% | 0.42% | 0.48% | 0.39% |
| $E_T^{rel}$ Scale Soft Terms | 1.98% | 2.19% | 1.00% | 1.33% |
| $p_T$ Reso Soft Terms | 0.51% | 0.79% | 0.45% | 0.41% |
| $p_T$ Scale Soft Terms | 0.34% | 1.10% | 0.08% | 0.18% |
| Theory | 16% | 11% | 18% | 16% |
| Total | 17.86% | 13.94% | 19.71% | 17.76% |

Table 8.11: Systematic uncertainties for the combined di-boson background processes ($WZ$, $ZZ$, $W\gamma$ and $W\gamma^*$). The total systematic uncertainty includes theoretical uncertainty for various di-boson processes.

CHAPTER 9

# Systematic Uncertainties on $WW$ Signal Acceptance

This chapter summarizes the systematic uncertainties on the $W^{+}W^{-}$ signal acceptance. Sources of experimental and theoretical uncertainties as well as their relative uncertainties for signal acceptance are listed in Table 9.1. The following sections will briefly explains the compositions of these systematic terms.

Theses uncertainties are studied in details for all three different final states. The combinations of the uncertainties have taken into account of the un-correlated and correlated uncertainties from different final states. The statistical uncertainty is lower than 0.01% and hence uncertainties are shown in two-digit precision. These uncertainties will be used to calculate the uncertainties for cross section measurements as well as to probe the aTGCs. This chapter will first present the study on experimental uncertainties and then describe the theoretical uncertainties.

## 9.1 Experimental Systematics

Experimental uncertainties are dominated by object reconstruction uncertainties and grouped under the $C_{WW}$ uncertainties. This section describes the sources of them.

### 9.1.1 Lepton Detection Systematics

Lepton systematic uncertainties were handled independently for electrons and muons. Electron and muon trigger SFs are provided by the performance groups of the ATLAS Collaboration. The systematics on the electron object selection accounts for the following systematic effects:

- Energy scale and resolution smearing uncertainties

| Sources | $e^+e^-\not{E}_T$ | $\mu^+\mu^-\not{E}_T$ | $e^\pm\mu^\mp\not{E}_T$ | Combined |
|---|---|---|---|---|
| $\mathcal{A}_{WW}$ uncertainties | | | | |
| PDF | 0.94% | 0.93% | 0.81% | 0.82% |
| Scale | 0.2% | 0.2% | 0.2% | 0.2% |
| PS + Generator | 2.61% | 2.67% | 2.46% | 2.50% |
| EW Correction | 0.41% | 0.43% | 0.46% | 0.45% |
| Jet-Veto | 3.4% | 3.4% | 3.4% | 3.4% |
| $\Delta\mathcal{A}_{WW}/\mathcal{A}_{WW}$ | 4.41% | 4.45% | 4.30% | 4.33% |
| $C_{WW}$ uncertainties | | | | |
| *Pile-up* | 1.87% | 1.97% | 1.30% | 1.44% |
| $e$-trigger Efficiency SF | 2.52% | 0% | 0.30% | 0.44% |
| $\mu$-trigger Efficiency SF | 0% | 2.84% | 0.27% | 0.62% |
| $\mu$ MS Resolution | 0% | 0.05% | 0.01% | 0.01% |
| $\mu$ ID Resolution | 0% | 1.53% | 0.54% | 0.63% |
| $\mu$ Scale | 0% | 0.35% | 0.10% | 0.12% |
| $\mu$ Efficiency SF | 0% | 0.77% | 0.39% | 0.41% |
| $\mu$ Isolation SF | 0% | 1.13% | 0.56% | 0.60% |
| $e$ Resolution | 0.18% | 0% | 0.03% | 0.02% |
| $e$ Scale | 1.40% | 0% | 0.37% | 0.40% |
| $e$ Efficiency SF | 2.00% | 0% | 0.93% | 0.88% |
| $e$ Isolation SF | 0.44% | 0% | 0.21% | 0.20% |
| Jet Vertex Fraction | 0.24% | 0.21% | 0.21% | 0.21% |
| Jet Energy Resolution | 1.25% | 1.33% | 1.32% | 1.32% |
| Jet Energy Scale | 3.56% | 4.11% | 3.85% | 3.86% |
| $\not{E}_T$ Reso Soft Terms | 0.31% | 0.50% | 0.29% | 0.32% |
| $\not{E}_T$ Scale Soft Terms | 1.91% | 1.71% | 1.07% | 1.33% |
| $p_T$ Reso Soft Terms | 0.16% | 0.09% | 0.11% | 0.10% |
| $p_T$ Scale Soft Terms | 0.36% | 0.29% | 0.22% | 0.24% |
| Residual Theory | 1.15% | 1.01% | 0.70% | 0.61% |
| $\Delta C_{WW}/C_{WW}$ | 5.96% | 6.26% | 4.69% | 4.85% |
| $\mathcal{A}_{WW}C_{WW}$ uncertainties | | | | |
| PDF | 1.25% | 0.98% | 0.85% | 0.90% |
| Scale | 0.7% | 0.7% | 0.7% | 0.7% |
| PS + Generator | 3.01% | 2.87% | 2.52% | 2.50% |
| EW Correction | 0.34% | 0.40% | 0.47% | 0.45% |
| Jet-Veto | 3.4% | 3.4% | 3.4% | 3.4% |
| $\Delta C_{WW}\mathcal{A}_{WW}/C_{WW}\mathcal{A}_{WW}$ | 7.55% | 7.72% | 6.40% | 6.52% |
| Luminosity | 2.8% | 2.8% | 2.8% | 2.8% |
| $\sigma(WW)$ theoretic uncertainty | 4.60% | 4.60% | 4.60% | 4.60% |
| Full $W^+W^-$ signal estimation uncertainty | 9.64% | 9.78% | 8.77% | 8.86% |

Table 9.1: Systematic sources and associated relative uncertainties for $W^+W^-$ signal acceptance estimations for $ee$, $e\mu$, $\mu\mu$ and inclusive channels. The uncertainties for $\mathcal{A}_{WW}$ and $C_{WW}$ are shown in upper and middle parts. The theoretical uncertainty specific for $\mathcal{A}_{WW} \times C_{WW}$ are shown at the bottom part, and to derive the total uncertainties on $\mathcal{A}_{WW} \times C_{WW}$ the reconstruction uncertainties on $C_{WW}$ haven to be added in quadrature. The overall $W^+W^-$ signal estimation uncertainties include $\mathcal{A}_{WW} \times C_{WW}$ uncertainties, luminosity (2.8%) and theoretical cross section (4.6%) uncertainties (use pNNLO results, discussed in section 6.2). If a definitive 0% effect is implied, there is no effect expected in the given channel and it has been measured to be exactly zero.

- Particle identification via track quality and identification uncertainties
- Reconstruction efficiency uncertainties
- Isolation efficiency uncertainties

while the systematics on the muon object selection considers:

- Momentum scale and resolution smearing uncertainties
- Reconstruction efficiency uncertainties
- ID track uncertainties of CB muons
- MS track uncertainties of CB muons
- Isolation efficiency uncertainties

The systematic for each individual effect is assumed to be independent from each other. The full systematic uncertainty was then estimated by recomputing the whole analysis with each systematic term varied by $\pm1\sigma$ from the central correction value. In this way, the $\not{E}_T$ is rebuilt each time, hence all object corrections to $\not{E}_T$ are forwarded and evaluated correctly.

The electron scale systematics components are listed as an example in Table 9.2.

| Sources | $e^+e^-\not{E}_T$ | $\mu^+\mu^-\not{E}_T$ | $e^\pm\mu^\mp\not{E}_T$ | Combined |
|---|---|---|---|---|
| Electron Scale ZeeAll | 1.40% | 0% | 0.36% | 0.39% |
| Electron Scale R12Stat | 0.06% | 0% | 0.09% | 0.07% |
| Electron Scale PSStat | 0.06% | 0% | 0.03% | 0.02% |
| Electron Scale Low $p_T$ | 0.02% | 0% | 0.01% | 0.01% |
| Electron Scale Total | 1.41% | 0% | 0.37% | 0.40% |

Table 9.2: The sources of Electron scale uncertainties. There is no effect of electron scale on the $\mu\mu$ channel.

### 9.1.2 Jet Measurement Systematics

The JES and JER uncertainty estimation is based on the recommendations of the combined performance group. JES uncertainties are separated into components, as summarized in Table 9.3. The JES uncertainty estimation used similar strategy as the lepton scale systematics estimation, i.e. varying the nominal values of the terms by $\pm1\sigma$; however, the JER used different implementation: the nominal reconstructed MC jets are not smeared in the analysis, following the standard procedure of the *Standard Model Electroweak Group*. The `ApplyJetResolutionSmearing` package (provided by the combined performance group) provides the uncertainties on JER measured in data and the corresponding uncertainties.

| Sources | $e^+e^-\not{E}_T$ | $\mu^+\mu^-\not{E}_T$ | $e^\pm\mu^\mp\not{E}_T$ | Combined |
|---|---|---|---|---|
| JES Effective NP1 | 0.47% | 0.57% | 0.35% | 0.39% |
| JES Effective NP2 | 0.68% | 0.94% | 0.57% | 0.63% |
| JES Effective NP3 | 0.31% | 0.40% | 0.21% | 0.24% |
| JES Effective NP4 | 0.08% | 0.13% | 0.06% | 0.07% |
| JES Effective NP5 | 0.09% | 0.14% | 0.05% | 0.07% |
| JES Effective NP6+RestTerm | 0.07% | 0.10% | 0.05% | 0.06% |
| JES Eta Intercalibration Modelling | 0.22% | 0.23% | 0.14% | 0.16% |
| JES Eta Intercalibration StatAndMethod | 0.65% | 0.80% | 0.57% | 0.61% |
| JES SingleParticle HighPt | 0% | 0% | 0% | 0% |
| JES Relative Non Closure | 0% | 0% | 0% | 0% |
| JES $N_{PV}$ Offset | 0.23% | 0.37% | 0.22% | 0.24% |
| JES $\langle\mu\rangle$ Offset | 0.07% | 0.09% | 0.06% | 0.07% |
| JES *Pile-up* Pt | 0.02% | 0.01% | 0.02% | 0.02% |
| JES *Pile-up* Rho | 0.49% | 0.69% | 0.37% | 0.42% |
| JES Closeby | 0% | 0% | 0% | 0% |
| JES Flavour Composition | 0.55% | 0.80% | 0.46% | 0.51% |
| JES Flavour Response | 0.92% | 1.25% | 0.80% | 0.87% |
| JES B Scale | 0% | 0.01% | 0% | 0% |
| JES Baseline | 1.21% | 1.52% | 1.02% | 1.10% |
| JES Total | 1.65% | 2.34% | 1.56% | 1.67% |

Table 9.3: Jet energy scale uncertainty components for signal samples. The entries "JES Baseline" and "JES Total" refer to two different sets of systematic uncertainties where "JES Baseline" is included in "JES Total". "JES Baseline" corresponds to the quadratic sum of uncertainties from in-situ and $\eta$ inter-calibration (first 11 entries). "JESTotal" includes the baseline uncertainties and in addition uncertainties due to pileup, flavour and event topology. Refer to Reference [65] for the explanation of each uncertainty term.

### 9.1.3 $\not{E}_T$ Determination Systematics

The $\not{E}_T$ object in this analysis is reconstructed by the `METRefFinal` algorithm (see Section 5.6.1). In the reconstruction process, bare calorimeter cell energy deposits are associated with high-$p_T$ objects such as electrons, photons, muons and jets, then replaced by the $E_T$ of the high-$p_T$ objects, which have more accurate calibrations. Therefore, the scale and resolution uncertainties on those objects have a 100%

correlation with the $\not{E}_T$ object uncertainties. The $\not{E}_T$ uncertainties are determined by handling the associated object uncertainties as well as $\not{E}_T$ soft scale and resolution systematic terms, which are denoted in Table 9.1.

### 9.1.4 $\not{p}_T$ Determination Systematics

Similar to the reconstruction of the $\not{E}_T$ , the $\not{p}_T$ is fully correlated with the momentum of the selected leptons as well as the tracks not associated with the leptons (soft tracks). Its lepton related uncertainty is therefore correctly forwarded and evaluated when recomputing the whole analysis during the study of lepton momentum scale and resolution systematics. Its soft track related uncertainty is evaluated with a data-driven method, based on $Z \to \mu\mu$ data in 0-jet bin, which is performed by the *JET/$\not{E}_T$ Group* and described below.

The $\not{p}_T$ is decomposed to two components: the total vectorial $p_T$ sum of the hard interaction leptons (including neutrinos) system ($p_T^{\text{lep}}$) and the residual $p_T$ of the soft tracks ($p_T^{\text{soft}}$) after subtracting $p_T^{\text{lep}}$ from $\not{p}_T$ . Then, the $p_T^{\text{soft}}$ is further decomposed along the transverse and longitudinal direction defined by the $p_T^{\text{lep}}$ into $p_T^{\text{soft, perp}}$ and $p_T^{\text{soft,para}}$, respectively. The scale is defined as the mean value of $p_T^{\text{soft,para}}$, or $\overline{p_T^{\text{soft,para}}}$. The resolution are then derived on both $\overline{p_T^{\text{soft,para}}}$ and $\left(p_T^{\text{soft}} - \overline{p_T^{\text{soft,para}}}\right)$. The scale and resolution systematic uncertainties of the $\not{p}_T$ from soft tracks are then defined to be the scale shift and resolution ratio between data and MC on the $Z \to \mu\mu$ sample.

## 9.2 Theoretical Systematics

The theoretical systematic uncertainties for this analysis are considered in this section. The systematics on signal acceptance are important in the cross section measurement, while the systematics on both the signal shape and fiducial acceptance are important in the aTGCs studies.

### 9.2.1 Total Theoretical Uncertainties on $\mathcal{A}_{WW}$, $C_{WW}$ and $\mathcal{A}_{WW} \times C_{WW}$

The signal selection efficiency (acceptance) is crucial for the theoretical calculation precision and MC modelling. The uncertainties are for the fiducial acceptance $\mathcal{A}_{WW}$, the reconstruction correction $C_{WW}$ which is used in the extraction of the fiducial cross sections, and the combined signal efficiency $\mathcal{A}_{WW} \times C_{WW}$ which is used in the extraction of total cross sections. While the $C_{WW}$ is expected to slightly dependent on theoretical calculation since the fiducial volume is defined at the reconstruction level (see Section 7.6), its uncertainty is still considered to address the residual theoretical dependence as well as the uncertainty of $\tau$ contribution which is only evaluated in the numerator of $C_{WW}$ calculation (see Section 7.7). The acceptance uncertainties are induced by the uncertainties of PDFs, QCD renormalization and factorization scales, generators and parton showerers, and the NLO EW correction.

Because the jet-veto cut (see Section 7.3) introduces another scale at jet $p_T$ threshold where large logarithmic terms are involved in the calculation, the jet-veto efficiency subjects to large theoretical uncertainty, which is usually derived by varying QCD scales but found to be failed in this case. The detailed discussion of the jet-veto uncertainty will be presented in Section 9.2.1.5.

The summary of the theoretical uncertainties of $\mathcal{A}_{WW}$, $C_{WW}$, and $\mathcal{A}_{WW} \times C_{WW}$ is presented in Table 9.4. The following sections provides details on each row of the contributing sources.

| | $\mathcal{A}_{WW}$ | | | | $C_{WW}$ | | | | $\mathcal{A}_{WW} \times C_{WW}$ | | | |
|---|---|---|---|---|---|---|---|---|---|---|---|---|
| | $ee$ | $\mu\mu$ | $e\mu$ | incl. | $ee$ | $\mu\mu$ | $e\mu$ | incl. | $ee$ | $\mu\mu$ | $e\mu$ | incl. |
| PDF | 0.94% | 0.93% | 0.81% | 0.82% | 0.34% | 0.13% | 0.10% | 0.10% | 1.25% | 0.98% | 0.85% | 0.90% |
| Scale | 0.2% | 0.2% | 0.2% | 0.2% | 0.6% | 0.6% | 0.6% | 0.6% | 0.7% | 0.7% | 0.7% | 0.7% |
| *GEN+PS* | 2.61% | 2.67% | 2.46% | 2.50% | 0.92% | 0.80% | 0.35% | 0.00% | 3.01% | 2.87% | 2.52% | 2.50% |
| EWCorr | 0.41% | 0.43% | 0.46% | 0.45% | 0.06% | 0.04% | 0.01% | 0.00% | 0.34% | 0.40% | 0.47% | 0.45% |
| Jet-Veto | 3.4% | 3.4% | 3.4% | 3.4% | | | | | 3.4% | 3.4% | 3.4% | 3.4% |
| Total | 4.41% | 4.45% | 4.30% | 4.33% | 1.15% | 1.01% | 0.70% | 0.61% | 4.77% | 4.63% | 4.40% | 4.40% |

Table 9.4: Fractional theoretical uncertainties on signal acceptance for $WW$ signal events. The total uncertainties are calculated as the quadratic sum of the uncertainties from each sources.

#### 9.2.1.1 PDFs Uncertainty

Following the recommendation of *PDF4LHC Working Group* [85], 3 common PDF sets are considered here: `NNPDF2.3` [22], `MSTW2008NLO` [21], and `CT10` [20].

As the first step, The internal PDF error bands are evaluated, where there are 100 sets for `NNPDF`, 40 sets for `MSTW` and 52 sets for `CT10`. The calculation of the signal acceptance uses default signal MC samples and the default `CT10` sets in the MC samples are replaced by the **`LHAPDF`** library [23]. For `CT10` and `MSTW`, the internal uncertainty is obtained by the formulas:

$$\sigma^{+} = \sqrt{\sum_{i=0}^{N} \frac{[max(A_{i+} - A_0, A_{i-} - A_0, 0)]^2}{A_0}} \tag{9.1}$$

$$\sigma^{-} = \sqrt{\sum_{i=0}^{N} \frac{[max(A_0 - A_{i+}, A_0 - A_{i-}, 0)]^2}{A_0}} \tag{9.2}$$

where $A_0$ is the $WW$ acceptance evaluated at the central value of PDFs, while $A_{i\pm}$ are the $WW$ acceptances with one sigma up or down variation of the $i$-th eigen error set. The `MSTW` error sets are provided at 68% CL, but the `CT10` are provided at 90% CL, which is then divided by 1.64 to match to `MSTW`. The `NNPDF` internal uncertainty was evaluated another way as the standard deviation of the $WW$ acceptances calculated on the 100 error sets. All the PDFs internal uncertainties are symmetrized by taking the largest deviations from the up and down variations.

In the final step, the PDFs uncertainty is calculated as the envelope of the three PDFs bands, which is summarized in Table 9.5.

| PDFs Uncertainty | $\mathcal{A}_{WW}$ | | | | $C_{WW}$ | | | | $\mathcal{A}_{WW} \times C_{WW}$ | | | |
|---|---|---|---|---|---|---|---|---|---|---|---|---|
| | $ee$ | $\mu\mu$ | $e\mu$ | incl. | $ee$ | $\mu\mu$ | $e\mu$ | incl. | $ee$ | $\mu\mu$ | $e\mu$ | incl. |
| $qq$ | | | | | | | | | | | | |
| `CT10` | 0.45% | 0.46% | 0.49% | 0.48% | 0.20% | 0.08% | 0.07% | 0.08% | 0.56% | 0.45% | 0.52% | 0.51% |
| `MSTW` | 0.88% | 0.87% | 0.72% | 0.76% | 0.34% | 0.12% | 0.10% | 0.11% | 1.19% | 0.94% | 0.80% | 0.85% |
| `NNPDF` | 0.48% | 0.58% | 0.75% | 0.68% | 0.30% | 0.08% | 0.06% | 0.07% | 0.34% | 0.54% | 0.73% | 0.67% |
| Final | 0.88% | 0.87% | 0.75% | 0.76% | 0.34% | 0.12% | 0.10% | 0.11% | 1.19% | 0.94% | 0.80% | 0.85% |
| $gg$ | | | | | | | | | | | | |
| `CT10` | 1.06% | 1.06% | 1.06% | 1.06% | 0.28% | 0.17% | 0.03% | 0.03% | 1.30% | 0.98% | 1.04% | 1.05% |
| `MSTW` | 0.75% | 0.77% | 0.74% | 0.75% | 0.17% | 0.11% | 0.02% | 0.01% | 0.84% | 0.68% | 0.74% | 0.74% |
| `NNPDF` | 1.68% | 1.69% | 1.68% | 1.68% | 0.34% | 0.19% | 0.03% | 0.03% | 1.99% | 1.55% | 1.65% | 1.66% |
| Final | 1.68% | 1.69% | 1.68% | 1.68% | 0.34% | 0.19% | 0.03% | 0.03% | 1.99% | 1.55% | 1.65% | 1.66% |
| Total | 0.94% | 0.93% | 0.81% | 0.82% | 0.34% | 0.13% | 0.10% | 0.10% | 1.25% | 0.98% | 0.85% | 0.90% |

Table 9.5: Fractional PDFs uncertainties on signal acceptances for $WW$ signal events: from $q\bar{q} \to WW$ process ($qq$) on the top and from $gg \to H \to WW$ ($gg$) process at the bottom. The final uncertainties for each processes is calculated as the envelope of `CT10`, `MSTW` and `NNPDF`. The total PDFs uncertainties for signal acceptance at the bottom row are combined from the $qq$ and $gg$ processes assuming 100% correlation. The "inclusive" column represents the PDFs uncertainty for the combined channel where three channels are merged for calculation. The $\mathcal{A}_{WW} \times C_{WW}$ uncertainty is explicitly calculated with MC samples.

#### 9.2.1.2 QCD Scale Uncertainty

The QCD scale uncertainty on $WW$ acceptance is evaluated by independently varying renormalization ($\mu_r$) and factorization ($\mu_f$) scales by a factor of 2 or $\frac{1}{2}$, in a total of 9 variation scenarios including the nominal one ($\mu_r = \mu_f = M_{WW}$). The scale uncertainty study for $qq \to WW$ process is done at truth level, where $\mathcal{A}_{WW}$ is checked with privately generated (Powheg + Pythia with official configuration) MC samples on all scale variations, while $C_{WW}$ is checked with fast simulation samples on only two scale variations: $\mu_r = \mu_f = 2M_{WW}$ and $\mu_r = \mu_f = 0.5M_{WW}$. The calculation is done on samples of $qq \to W^+W^- \to e\nu\mu\nu$ process, while the results are applied for all di-lepton channels. Note that, the evaluation of QCD scale uncertainty here does not include the jet-veto cut, which is dedicated in another study (see Section 9.2.1.5).

The $\mathcal{A}_{WW}$ uncertainty is defined as the envelope of the acceptances of all the scale variations. The $C_{WW}$ uncertainty is found to be ~ 0.6% for $qq \to WW$ process, but is assumed for initial states for simplicity.

The $\mathcal{A}_{WW}$ uncertainty for $gg \to H \to WW$ is studied in a similar way in Reference [86] and the results are quoted here. As for the non-resonant $gg \to WW$ process, `MCFM` [27] is used for the calculation instead of Powheg + Pythia.

The summary of scale uncertainties for $WW$ signal acceptance is provided in Table 9.6.

| Scale Uncertainty | $\mathcal{A}_{WW}$ | $C_{WW}$ | $\mathcal{A}_{WW} \times C_{WW}$ |
|---|---|---|---|
| $qq$ | 0.2% | 0.6% | 0.7% |
| $ggH$ | 1.4% | 0.6% | 1.5% |
| $gg$ | 0.3% | 0.6% | 0.7% |
| Total | 0.2% | 0.6% | 0.7% |

Table 9.6: Fractional scale uncertainties on signal acceptances for $WW$ signal events from different initial states. The total scale uncertainties are combined from individual processes assuming 100% correlation. The $\mathcal{A}_{WW} \times C_{WW}$ uncertainties are simply calculated as the quadratic sum from the uncertainties of $\mathcal{A}_{WW}$ and $C_{WW}$ .

#### 9.2.1.3 Generator and Parton Showering Uncertainties

For simplicity, the combination of generator and parton showering uncertainties on acceptances denoted as the *GEN+PS* uncertainty.

For $qq \to WW$ process, the generator uncertainty for $\mathcal{A}_{WW}$ is the truth-level difference between the Powheg + Herwig/Jimmy and **MC@NLO**+Herwig/Jimmy private MC samples, while the parton showering uncertainty for $\mathcal{A}_{WW}$ is the truth-level difference between the Powheg + Pythia and Powheg + Herwig/Jimmy private MC samples. Then the *GEN+PS* uncertainty is the quadratic sum of the individual generator and parton showering uncertainties. For $C_{WW}$, the *GEN+PS* uncertainty is evaluated in whole as the difference between the Powheg + Pythia and **MC@NLO**+Herwig/Jimmy official samples (full simulation). Note that, by evaluating the *GEN+PS* uncertainty for $\mathcal{A}_{WW}$ in whole on the Powheg + Pythia and **MC@NLO**+Herwig/Jimmy official samples, the results are found to be comparable to the combination of individually derived uncertainties of generator and parton showering, given that there is $\sim 1\%$ statistical uncertainty in the comparison. Also note that, for similar reasons, the *GEN+PS* uncertainties here are evaluated without the jet-veto cuts.

For the non-resonant $gg \to WW$ process, the generator uncertainty for $\mathcal{A}_{WW}$ is the truth-level difference between the **gg2WW**+Herwig/Jimmy official sample and the **MCFM**+Herwig/Jimmy private sample, while the parton showering uncertainty for $\mathcal{A}_{WW}$ is the difference between **MCFM**+Pythia and **MCFM**+Herwig/Jimmy private samples. The *GEN+PS* uncertainty is then combined similarly to the $qq$ case. For $C_{WW}$, since there is no fully simulated MC samples available for the *GEN+PS* uncertainty study, this uncertainty is quoted from the $qq$ results. This is also the case for the $C_{WW}$ *GEN+PS* uncertainty for $gg \to H \to WW$.

For the $gg \to H \to WW$ process, results are taken from [86] as well, considering that the chosen official sample is the same and the phase spaces are similar as well.

Finally, the *GEN+PS* uncertainties for $\mathcal{A}_{WW} \times C_{WW}$ are calculated by adding those for $\mathcal{A}_{WW}$ and $C_{WW}$ in quadrature. The total *GEN+PS* uncertainties for $\mathcal{A}_{WW}$, $C_{WW}$, and $\mathcal{A}_{WW} \times C_{WW}$ are combined from all 3 processes with 100% correlation. Table 9.7 gives a summary on the *GEN+PS* uncertainties for each process and the total one as well.

#### 9.2.1.4 Uncertainties due to NLO Electroweak Correction

The NLO EW contribution of $\mathcal{O}(\alpha^3_{\mathrm{EW}})$ on di-boson production is described in [76, 77, 87, 88]. An event-wise EW k-factor ($k_{\mathrm{EW}}$) binned in the Mandelstam variables $s$ and $t$ is calculated from the kinematics of the initial state quarks at MC generator level. $k_{\mathrm{EW}}$ is only applied when the bosons are on-shell since the calculation uses narrow width approximation. There is no EW correction applied ($k_{\mathrm{EW}} = 1$) for events when $\sqrt{s} > 2M_W$, which assumes that the EW correction is valid if the corrections from QCD are small [89]. $k_{\mathrm{EW}}$ is applied to $qq$ induced process only.

Hence, the systematic uncertainty is evaluated when at least one of the bosons are

| *GEN+PS* Uncertainty | $\mathcal{A}_{WW}$ | | | | $C_{WW}$ | | | | $\mathcal{A}_{WW} \times C_{WW}$ | | | |
|---|---|---|---|---|---|---|---|---|---|---|---|---|
| | *ee* | *μμ* | *eμ* | incl. | *ee* | *μμ* | *eμ* | incl. | *ee* | *μμ* | *eμ* | incl. |
| *qq* | | | | | | | | | | | | |
| Parton Shower | 0.30% | 0.30% | 0.30% | 0.30% | | | | | | | | |
| Generator | 1.25% | 1.25% | 1.25% | 1.25% | | | | | | | | |
| *GEN+PS* | 1.29% | 1.29% | 1.29% | 1.29% | 0.92% | 0.80% | 0.35% | 0.00% | 1.58% | 1.51% | 1.33% | 1.29% |
| *gg* | | | | | | | | | | | | |
| Parton Shower | 27.87% | 28.23% | 26.96% | 27.36% | | | | | | | | |
| Generator | 3.46% | 6.07% | 15.78% | 12.10% | | | | | | | | |
| *GEN+PS* | 28.08% | 28.88% | 31.24% | 29.92% | 0.92% | 0.80% | 0.35% | 0.00% | 28.10% | 28.89% | 31.24% | 29.92% |
| *ggH* | | | | | | | | | | | | |
| *GEN+PS* | 6.87% | 6.87% | 6.87% | 6.87% | 0.92% | 0.80% | 0.35% | 0.00% | 6.93% | 6.92% | 6.88% | 6.87% |
| Total | 2.61% | 2.67% | 2.46% | 2.50% | 0.92% | 0.80% | 0.35% | 0.00% | 3.01% | 2.87% | 2.52% | 2.50% |

Table 9.7: Fractional Parton Shower and Generator uncertainties on signal acceptance for $WW$ signal events: from $q\bar{q}$ initial state ($qq$) on the top, non-resonant $gg \rightarrow WW$ ($qq$) process in the middle, and $gg \rightarrow H \rightarrow WW$ ($ggH$) process at the bottom. The *GEN+PS* uncertainties for each processes is calculated as the quadratic sum of the Parton Shower and the Generator uncertainties. The *GEN+PS* uncertainties for $\mathcal{A}_{WW} \times C_{WW}$ are calculated as the quadratic sum of those for $\mathcal{A}_{WW}$ and $C_{WW}$ . The total uncertainties for signal acceptance at the bottom row are combined from the $qq$ and $gg$ processes assuming 100% correlation. There is an accidental agreement in the combined channel for $C_{WW}$, therefore the uncertainty is shown as zero.

off-shell (defined as $|m - M_W| > 25\ GeV$), while no systematic term is derived where no correction is applied for the events. Nevertheless, a systematic term for the size of the correction is assigned for events with a large QCD effect, which only affects $1 \sim 2\%$ of the events after final selection. The uncertainty for $gg$ induced process is set to be 0 and therefore its combined uncertainty is less than the $qq$ uncertainty alone.

This uncertainty evaluation is implemented on the official $qq \rightarrow WW$ samples with the `EWCorrector` tool provided by the performance group. Table 9.8 presents the summary of the uncertainties due to the NLO EW correction.

| EWK Uncertainty | $\mathcal{A}_{WW}$ | | | | $C_{WW}$ | | | | $\mathcal{A}_{WW} \times C_{WW}$ | | | |
|---|---|---|---|---|---|---|---|---|---|---|---|---|
| | *ee* | *μμ* | *eμ* | incl. | *ee* | *μμ* | *eμ* | incl. | *ee* | *μμ* | *eμ* | incl. |
| *qq* | 0.44% | 0.47% | 0.49% | 0.48% | 0.07% | 0.04% | 0.01% | 0.00% | 0.37% | 0.43% | 0.50% | 0.48% |
| Total | 0.41% | 0.43% | 0.46% | 0.45% | 0.06% | 0.04% | 0.01% | 0.00% | 0.34% | 0.40% | 0.47% | 0.45% |

Table 9.8: Fractional EW correction uncertainties on signal acceptance for $WW$ signal events from $q\bar{q}$ initial state ($qq$). The total uncertainties for signal acceptance at the bottom row are scaled by the fraction of $qq$ yields over total signal prediction.

#### 9.2.1.5 Jet-veto Uncertainty

It has been shown [90] that in a jet-binned analysis, accidental cancellations with log terms introduced by restricting QCD radiation can cause the scale uncertainty to be underestimated with the same evaluation method as in Section 9.2.1.2. Proposed by Stewart and Tackmann [90], a more reliable estimate of the scale uncertainty of jet-veto acceptance is implemented, named the *S-T Method*. It assumes there is no correlation between the uncertainties of inclusive and jet-binned cross sections, of which the perturbative series have different structures. The *S-T Method* defines the jet-veto acceptance uncertainty to be:

$$\frac{\delta\epsilon}{\epsilon} = \left(\frac{1-\epsilon}{\epsilon}\right)\sqrt{\left(\frac{\delta\sigma_{\geqslant 0\text{ jet}}}{\sigma_{\geqslant 0\text{ jet}}}\right)^2 + \left(\frac{\delta\sigma_{\geqslant 1\text{ jet}}}{\sigma_{\geqslant 1\text{ jet}}}\right)^2} \tag{9.3}$$

where $\epsilon$ is the jet-veto acceptance, $\sigma_{\geqslant i\text{ jet}}$ is the fiducial cross section in jet bins, and the $\delta\sigma_{\geqslant i}$ jet is the uncertainty of $\sigma_{\geqslant i\text{ jet}}$ due to scale variations. The 9 scale variation scenarios are the same as described in Section 9.2.1.2.

For cross checks, the *S-T Method* is applied on 3 theoretical scenarios: the pure NLO calculation using **MCFM**, the NNLO prediction provided by the author of [73], and the NLO+NLL calculation using Powheg . In all 3 scenarios no selection cut is applied since it is non-trivial to apply them in the fix-order calculations. The truth jet is reconstructed with the anti-$k_T$ algorithm [66] with $R = 0.4$, and is required to have $p_T > 25\ GeV$ and $|\eta| < 4.5$ as well as electron overlap removal in a cone of $R = 0.3$.

In the NLO+NLL case, private truth samples of $qq \to WW \to e\nu\mu\nu$ process is used. The LO $gg$ contribution is not included in the NLO+NLL and NLO calculations, but is contained in the NNLO calculation by default, which results in slightly larger $\epsilon$ compared to the cases of NLO+NLL and NLO. The calculation of the nominal NNLO $\epsilon$ therefore subtracts the LO $gg$ contribution, which is $\sim 1.45\ pb$ in total phase space; but for simplicity, the calculation of NNLO $\delta\epsilon$ includes the $gg$ contribution, which is verified to be of no effect on the results.

Furthermore, the NLO and NLO+NLL cases evaluate all 9 scale variations with the central scales to be $\mu_r = \mu_f = M_{WW}$, while the NNLO calculation use the central scales of $\mu_r = \mu_f = 0.5M_{WW}$ but excludes 2 extreme variations of $\mu_r, \mu_f = 2, 0.5$ and $\mu_r, \mu_f = 0.5, 2$.

The cross sections with different scale variations, as well as the jet-veto acceptance and associated uncertainties using the *S-T Method* are listed in Table 9.9. Results of all 3 theoretical scenarios are also included.

This analysis derives the jet-veto acceptance for $qq \to WW$ process with default Powheg + Pythia MC samples, which is found to be close to the NNLO calculation as shown in Table 9.9. The final uncertainty for jet-veto acceptance with *S-T Method*

| Scale Variations | NLO+NLL | | | NLO | | | NNLO | | |
|---|---|---|---|---|---|---|---|---|---|
| | $\sigma_{incl}$ | $\sigma_{0j}$ | $\sigma_{\geqslant 1j}$ | $\sigma_{incl}$ | $\sigma_{0j}$ | $\sigma_{\geqslant 1j}$ | $\sigma_{incl}$ | $\sigma_{0j}$ | $\sigma_{\geqslant 1j}$ |
| $\mu_r, \mu_f = 1, 1$ | 51.44 | 34.99 | 16.45 | 52.29 | 39.24 | 13.05 | 59.13 | 40.38 | 18.75 |
| $\mu_r, \mu_f = 1, 2$ | 51.75 | 35.30 | 16.45 | 52.64 | 39.95 | 12.69 | 59.12 | 40.43 | 18.68 |
| $\mu_r, \mu_f = 2, 2$ | 50.70 | 34.69 | 16.02 | 51.58 | 39.94 | 11.64 | 58.08 | 40.40 | 17.68 |
| $\mu_r, \mu_f = 2, 1$ | 50.39 | 34.38 | 16.01 | 51.23 | 39.26 | 11.97 | 58.04 | 40.25 | 17.79 |
| $\mu_r, \mu_f = 1, 0.5$ | 51.15 | 34.68 | 16.46 | 51.96 | 38.60 | 13.37 | 59.16 | 40.25 | 18.91 |
| $\mu_r, \mu_f = 0.5, 0.5$ | 52.45 | 35.43 | 17.01 | 53.29 | 38.60 | 14.69 | 60.38 | 40.53 | 19.85 |
| $\mu_r, \mu_f = 0.5, 1$ | 52.70 | 35.72 | 16.98 | 53.59 | 39.25 | 14.34 | 60.27 | 40.55 | 19.72 |
| $\mu_r, \mu_f = 0.5, 2$ | 53.00 | 36.03 | 16.97 | 53.90 | 39.95 | 13.95 | | | |
| $\mu_r, \mu_f = 2, 0.5$ | 50.07 | 34.06 | 16.00 | 50.86 | 38.60 | 12.26 | | | |
| Scale Uncertainty | 3.03% | | 3.40% | 3.07% | | 12.58% | 2.12% | | 5.88% |
| Jet-veto Acceptance | | 68.02% | | | 75.04% | | | 67.49% | |
| S-T Uncertainty | | 2.14% | | | 4.31% | | | 2.90% | |

Table 9.9: The inclusive and jet-binned cross sections with different scale variations for $qq \to WW$ process and the jet-veto acceptance calculated with default QCD scales as well as the corresponding fractional jet-veto uncertainties evaluated with *S-T Method*. The relevant numbers are derived from Powheg + Pythia MC (NLO+NLL), MCFM (NLO) and NNLO calculations. The extreme scale variations are not available for NNLO calculation so these are left blank in the table. The LO non-resonant $gg$ contribution is included in the NNLO cross sections, while the cross sections from NLO+NLL and NLO are derived for $qq \to WW$ only. The LO $gg$ contribution of about 1.45 $pb$ is removed while calculating the nominal jet-veto acceptance for NNLO case.

| Jet-Veto Uncertainty | $\mathcal{A}_{WW}$ | $C_{WW}$ | $\mathcal{A}_{WW} \times C_{WW}$ |
|---|---|---|---|
| $qq$ | 2.9% | | 2.9% |
| $ggH$+$gg$ | 11% | | 11% |
| Total | 3.4% | | 3.4% |

Table 9.10: Fractional jet-veto uncertainties on signal acceptance for $WW$ signal events from $q\bar{q}$ initial state ($qq$) and $gg$-induced ($ggH$+$gg$) processes. The total jet-veto uncertainties for signal acceptance at the bottom row are combined from the individual processes assuming 100% correlation. The theoretical jet-veto uncertainty on $C_{WW}$ is neglected, therefore uncertainties for $\mathcal{A}_{WW}$ and $\mathcal{A}_{WW} \times C_{WW}$ are the same.

is chosen to be the results of the NNLO calculation. This result is also checked with another more conservative method (*JVE Method*) which is provided in [17].

As for the $gg$ induced process, the final jet-veto uncertainty is quoted from [86] except that the quoted uncertainty is the envelope of the *S-T* and *JVE* methods. This uncertainty is $\sim$ 11% and is included in Table 9.10. The $gg$ and $qq$ processes are treated as fully correlated for the combination of the total uncertainty, which is also presented in the same table.

### 9.2.2 Fiducial Cross-section Uncertainties

As mentioned in Section 6.1, the NNLO cross section is available at total phase space, but the acceptance calculation can be only done at NLO precision. Hence the theoretical fiducial cross section $\sigma^{\text{fiducial}}$ is defined as the product of pNNLO cross section at total phase space (Table 6.1), the $W$ decay BR ($Br_{W\to\ell\nu} = 0.108$, $\ell \in \{e, \mu\}$), and the $\mathcal{A}_{WW}$. Hence the contributing terms to the uncertainty of $\sigma^{\text{fiducial}}$ are the pNNLO cross section (quoted from Table 6.1) and the $\mathcal{A}_{WW}$ (quoted from Table 9.4). The systematic uncertainties are symmetrized by averaging the up and down errors for simplicity. Table 9.11 presents the theoretical $\sigma^{\text{fiducial}}$ and its uncertainties.

| | Fiducial $\sigma$ | Scale | PDFs | *GEN+PS* | EWCorr | Jet-Veto | Total Uncertainty |
|---|---|---|---|---|---|---|---|
| $\sigma_{ee}$ $[fb]$ | 58.54 | ±2.84 | ±1.45 | ±1.53 | ±0.24 | ±1.99 | ±4.07 |
| $\Delta_{\sigma_{ee}}/\sigma_{ee}$ | | ±4.86% | ±2.48% | ±2.61% | ±0.41% | ±3.4% | ±6.95% |
| $\sigma_{\mu\mu}$ $[fb]$ | 63.67 | ±3.09 | ±1.58 | ±1.70 | ±0.27 | ±2.16 | ±4.44 |
| $\Delta_{\sigma_{\mu\mu}}/\sigma_{\mu\mu}$ | | ±4.86% | ±2.48% | ±2.67% | ±0.43% | ±3.4% | ±6.97% |
| $\sigma_{e\mu}$ $[fb]$ | 311.39 | ±15.13 | ±7.59 | ±7.66 | ±1.43 | ±10.59 | ±21.43 |
| $\Delta_{\sigma_{e\mu}}/\sigma_{e\mu}$ | | ±4.86% | ±2.44% | ±2.46% | ±0.46% | ±3.4% | ±6.88% |

Table 9.11: The theoretical fiducial cross sections for $ee$, $\mu\mu$ and $e\mu$ channels, as well as associated uncertainties. The fiducial cross sections are calculated as the product of pNNLO total cross section, BR and the $\mathcal{A}_{WW}$. The $\mathcal{A}_{WW}$ uncertainties are taken from the Table 9.4 in Section 9.2.1, while the total cross section uncertainties are taken from Table 6.1.

The uncertainties (from PDFs and scale) of the total cross section and those of the $\mathcal{A}_{WW}$ are combined independently for the uncertainties of the fiducial cross section, since the total cross section account for the overall normalization while the $\mathcal{A}_{WW}$ represent the relative difference between the fiducial volume and the total phase space. Finally, the fiducial acceptance uncertainties are usually much smaller than the total cross section uncertainties because the uncertainties of PDFs and scales are relatively flat in the fiducial volume (see Section 9.2.3).

### 9.2.3 Kinematic Distribution Shape Uncertainties

When comparing the kinematic distributions of data and MC, the theoretical uncertainties are assumed to be flat in the considered distributions. It is crucial to assign theoretical uncertainties during the comparison for the aTGCs study. This section investigates the "flatness" of the theoretical uncertainties, and cases show that there are indeed shape dependence where new uncertainties are assigned.

For $qq \to WW$ process, the shape uncertainty study is performed in the $e\mu$ fiducial region with private Powheg + Pythia MC samples. Corresponding to the aTGCs studies, 6 kinematic variables are chosen: $p_T$, $p_T^{\ell\ell}$, $M_{\ell\ell}$, $\Delta\phi_{\ell\ell}$, $|y_{\ell\ell}|$ (rapidity), and $|\cos\theta^*|$.

In Figure 9.1, the PDFs uncertainties are shown to be flat in most distributions. For simplicity, an uncertainty of 3% can be assigned to the MC distributions in the fiducial region, which is compatible with Table 9.11. One exception is observed for the high-$p_T$ region, where the PDFs uncertainty goes up to 5%-10%. This should be considered especially in the aTGCs study which relies on the high-$p_T$ spectra.

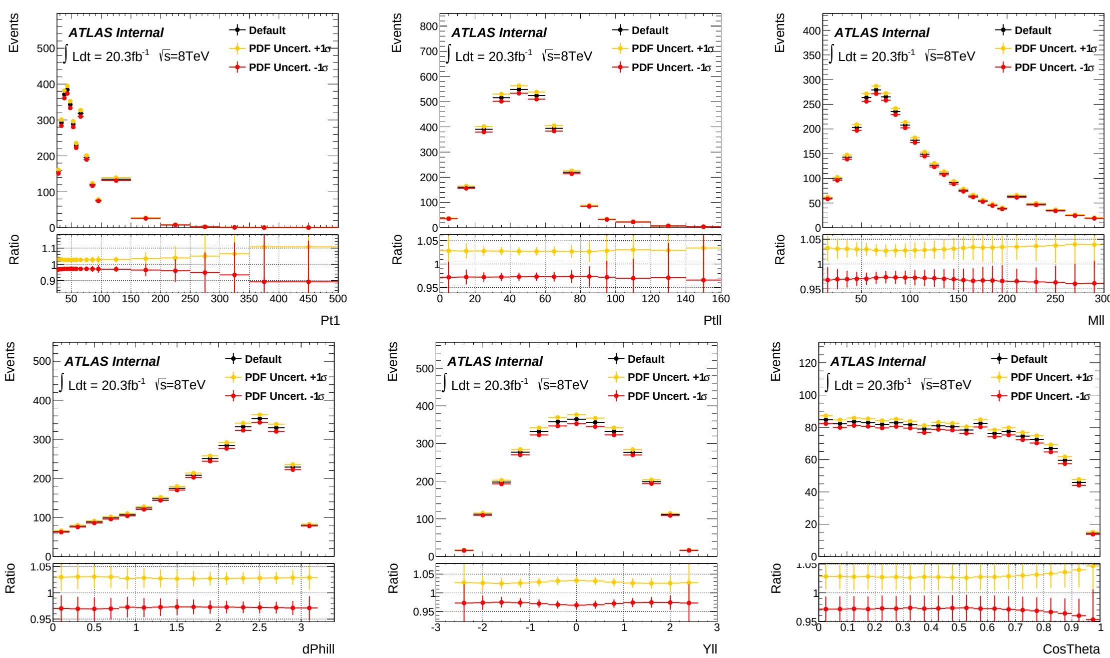


Figure 9.1: The PDFs uncertainties of $qq \to WW$ signal events in fiducial region for leading lepton $p_T$, $p_T^{\ell\ell}$, $M_{\ell\ell}$, $\Delta\phi_{\ell\ell}$, $|y_{\ell\ell}|$ and $|\cos\theta^*|$.

In Figure 9.2, the QCD scales uncertainties are presented. The jet-veto cut is not considered here, hence the flatness only shows the 9 scale variations. The actual uncertainty for data and MC comparisons comes from Table 9.11, which is $\sim 5\%$ as the quadratic sum of the scale and jet-veto uncertainties.

Figure 9.3 summarizes all the comparisons of *GEN+PS* uncertainties. The *GEN+PS* uncertainties in fiducial region are evaluated similarly as in Section 9.2.1.3 on private MC samples generated with Powheg + Pythia, Powheg + Herwig/Jimmy, and **MC@NLO** + Herwig/Jimmy. The private samples are proved to be consistent with the

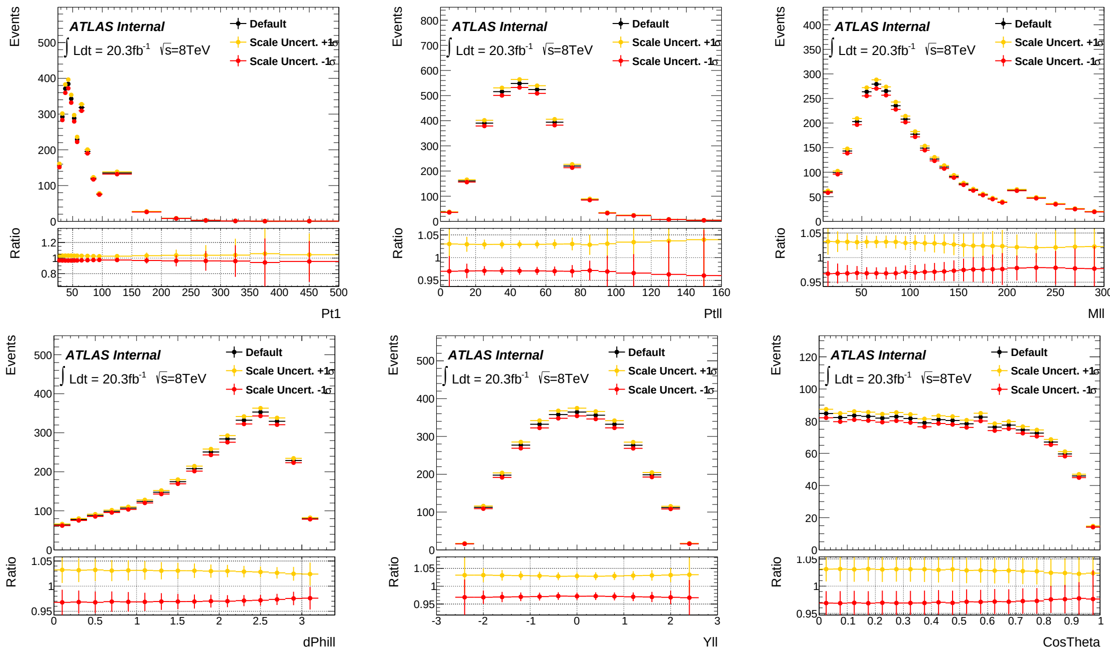


Figure 9.2: The QCD scale uncertainties of $qq \rightarrow WW$ signal events in fiducial region for leading lepton $p_T$, $p_T^{\ell\ell}$, $M_{\ell\ell}$, $\Delta\phi_{\ell\ell}$, $|y_{\ell\ell}|$ and $|\cos\theta^*|$.

official samples. Some samples contains about 10 million events to cope with the problem of insufficient tail statistics of kinematic distributions. For angular kinematic variables, the *GEN+PS* uncertainties are flat and consistent with the inclusive numbers in Table 9.11, which is ~ 3%. As for remaining kinematic variables, the *GEN+PS* uncertainties are found to be shape-dependent. E.g., the parton-shower difference between Pythia and Herwig/Jimmy is ~ 5% at low $p_T$ and ~ 0% at high $p_T$, while the generator difference between **MC@NLO** and Powheg is ~ 5% at low $p_T$ and up to 20% at high $p_T$, which is the most sensitive region for aTGCs study.

There is another non-negligible source, the LO non-resonant $gg \rightarrow WW$ process, to be considered for the *GEN+PS* shape uncertainties, which are shown in Figure 9.4. Both official and private samples are used in the comparisons, the latter of which are generated with **gg2VV** + Pythia, **MCFM** + Pythia, and **MCFM** + Herwig/Jimmy. A flat 40% uncertainties are observed for the angular variables and in the low-$p_T$ region, which is consistent with the number in Tables 9.7. The *GEN+PS* uncertainties increase up to 80% in the high-$p_T$ region, where a shape dependent uncertainty should be considered.

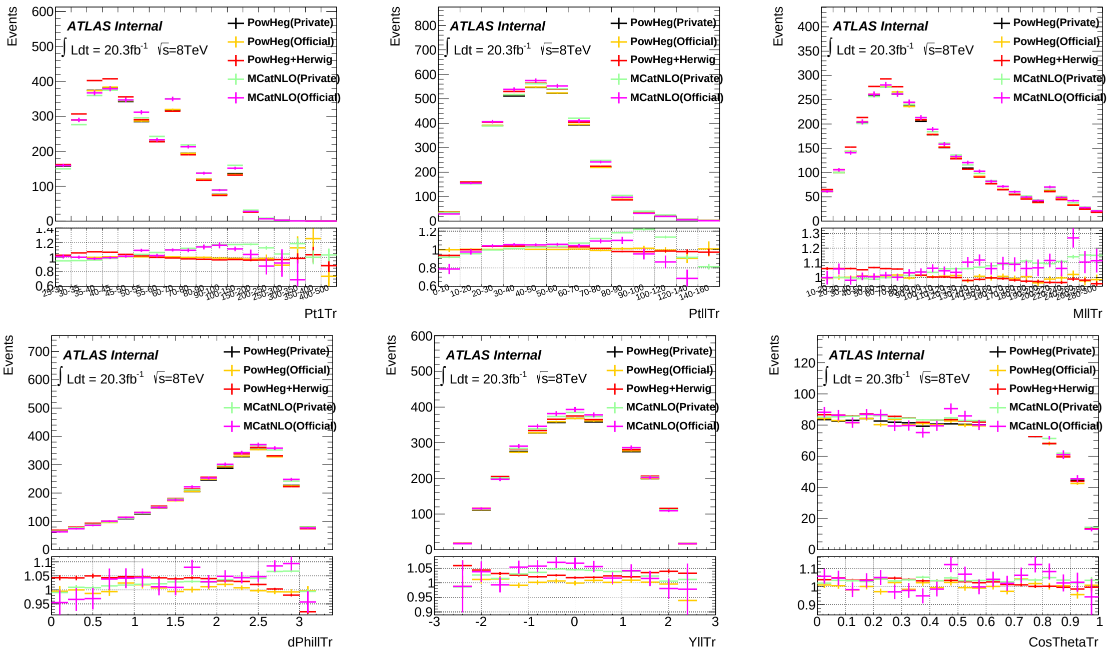


Figure 9.3: The comparison of different *GEN+PS* for $qq \to WW$ signal events in fiducial region for leading lepton $p_T$, $p_T^{\ell\ell}$, $M_{\ell\ell}$, $\Delta\phi_{\ell\ell}$, $|y_{\ell\ell}|$ and $|\cos\theta^*|$.

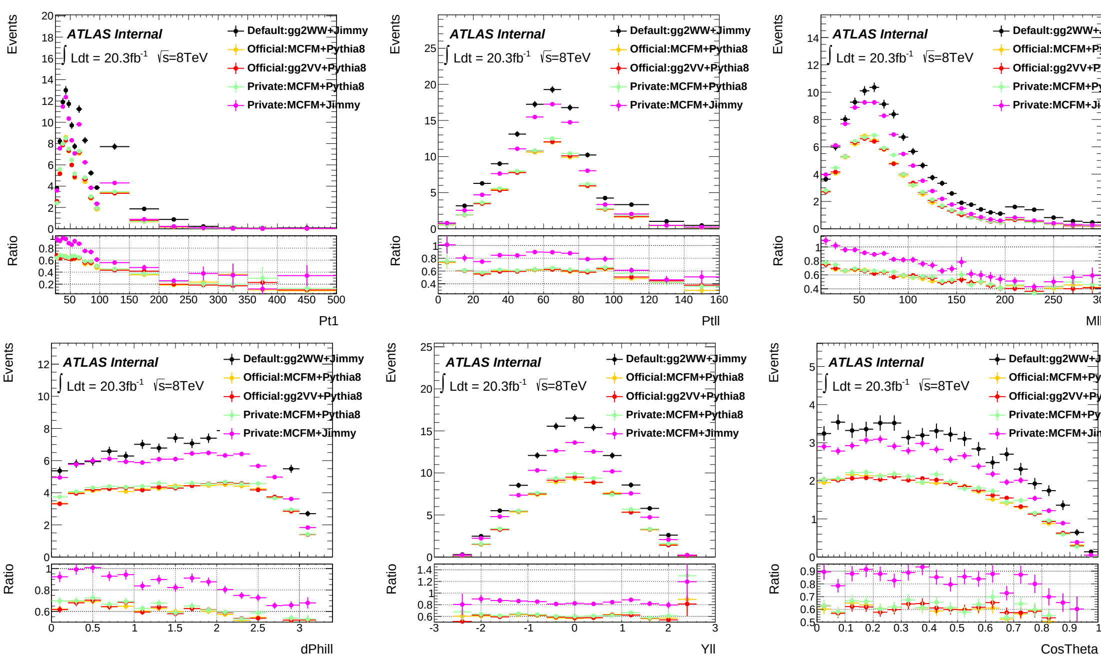


Figure 9.4: The comparison of different *GEN+PS* for non-resonant $gg \to WW$ signal events in fiducial region for leading lepton $p_T$, $p_T^{\ell\ell}$, $M_{\ell\ell}$, $\Delta\phi_{\ell\ell}$, $|y_{\ell\ell}|$ and $|\cos\theta^*|$.

CHAPTER 10

# Cross Section Measurement

This chapter summarizes the observed $W^+W^-$ candidates as well as the signal and background estimates from which the $W^+W^-$ production cross section is extracted. The $W^+W^-$ detection significance is also calculated.

## 10.1 Observation Compared with Predictions

Table 10.1 summarizes the observed and expected signal and background event yields after all *WW* selection cuts are applied for all three di-lepton channels. The associated statistical and systematic uncertainties are also listed. The *Z+jets*, *W+jets* & *multijet*, and *Top* background processes are estimated using data-driven methods as described in the respective Sections 8.1, 8.2 and 8.3, while the di-boson background is estimated using MC, as described in Section 8.4.

| Final State | $e^+e^-\not{E}_T$ | $\mu^+\mu^-\not{E}_T$ | $e^\pm\mu^\mp\not{E}_T$ |
|---|---|---|---|
| Observed Events | 594 | 975 | 5067 |
| Total expected events (S+B) | 507.3 ± 9.4 ± 73.4 | 817.2 ± 11.6 ± 105.1 | 4419.7 ± 25.9 ± 522.2 |
| MC *WW* signal | 346.3 ± 3.3 ± 33.4 | 612.5 ± 4.5 ± 59.9 | 3238.1 ± 10.2 ± 284.0 |
| Top(data-driven) | 91.8 ± 7.3 ± 7.9 | 127.2 ± 9.4 ± 10.9 | 608.6 ± 17.5 ± 52.3 |
| *W+jets* (data-driven) | 13.9 ± 4.9 ± 14.2 | 6.1 ± 5.0 ± 11.5 | 248.8 ± 15.3 ± 138.7 |
| *Z+jets* (data-driven) | 28.0 ± 0.5 ± 13.0 | 33.0 ± 0.5 ± 17.4 | 174.5 ± 3.4 ± 17.7 |
| Other di-bosons (MC) | 27.3 ± 1.4 ± 4.9 | 38.4 ± 1.3 ± 5.4 | 149.7 ± 4.0 ± 29.5 |
| Total background | 161.0 ± 8.8 ± 40.0 | 204.7 ± 10.7 ± 45.2 | 1181.6 ± 23.8 ± 238.2 |

Table 10.1: Summary of observed events and expected signal and background contributions in 3 di-lepton channels. The first error is statistical, the second error is systematic. The systematic uncertainties for total background and total expectation are calculated assuming full correlation among processes.

## 10.2 Cross Section Extraction

### 10.2.1 Cross Section Definition

The extraction of fiducial and total cross section has been defined in Section 6.4. To account for the inconsistency between the final state particles, for a given channel $WW \to \ell_1\nu\ell_2\nu$ where $\ell_1, \ell_2 \in \{e, \mu\}$, the fiducial cross section is defined to be:

$$\sigma^{\text{fiducial}}_{WW\to\ell_1\nu\ell_2\nu} = \frac{N^{\text{obs}}_{\ell_1\nu\ell_2\nu} - N^{\text{bkg}}_{\ell_1\nu\ell_2\nu}}{\mathcal{L} \times C_{WW\to\ell_1\nu\ell_2\nu}} \times \left(1 - \frac{N^{\text{MC}}_{\tau}}{N^{\text{MC}}_{WW\to\ell\nu\ell\nu}}\right) \tag{10.1}$$

where $N^{\text{obs}}_{\ell_1\nu\ell_2\nu}$ and $N^{\text{bkg}}_{\ell_1\nu\ell_2\nu}$ are the numbers of observed and expected background event yields, respectively; $\mathcal{L}$ is the integrated luminosity; $C_{WW\to\ell_1\nu\ell_2\nu}$ is the reconstruction correction factor; $N^{\text{MC}}_{\tau}$ is the MC signal event yields with at least one $W$ decaying to a $\tau$; and $N^{\text{MC}}_{WW\to\ell\nu\ell\nu}$ is the MC signal event yields with all leptonic final states ($\ell \in \{e, \mu, \tau\}$).

In addition, the total cross section in each channel is defined to be:

$$\sigma^{\text{total}}_{WW} = \frac{N^{\text{obs}}_{\ell_1\nu\ell_2\nu} - N^{\text{bkg}}_{\ell_1\nu\ell_2\nu}}{\mathcal{L} \times Br_{WW\to\ell_1\nu\ell_2\nu} \times \mathcal{A}_{WW\to\ell_1\nu\ell_2\nu} \times C_{WW\to\ell_1\nu\ell_2\nu}} \times \left(1 - \frac{N^{\text{MC}}_{\tau}}{N^{\text{MC}}_{WW\to\ell\nu\ell\nu}}\right) \tag{10.2}$$

where $\mathcal{A}_{WW\to\ell_1\nu\ell_2\nu}$ is the acceptance correction factor, and $Br_{WW\to\ell_1\nu\ell_2\nu}$ is the branching ratio for $\ell_1, \ell_2 \in \{e, \mu\}$.

However, Equations 10.1 and 10.2 are not used for the direct extraction of the cross sections in practice. Instead, a maximum log-likelihood method is used, which makes use of the Poisson statistics of the samples and readily includes the $WW \to \tau + X$ contributions as described below.

### 10.2.2 Maximum Log-likelihood Method

In order to compute the cross sections, a maximum log-likelihood fitting method is used to estimate the observed and expected event yields, including signal and backgrounds. The number of expected events in the $i$-th channel, $N^i_{\text{exp}}$ ($i \in \{ee, \mu\mu, e\mu\}$) is written as:

$$N^i_{\text{exp}} = N^i_s + N^i_b. \tag{10.3}$$

where $N^i_b$ is the background yields predicted with MC simulation or data-driven methods, and $N^i_s$ is the expected signal yields. $N^i_s$ relates to the total cross section

$\sigma_{WW}^{\text{total}}$ (or $\sigma$ for short if no ambiguity in the context) by:

$$N_s^i(\sigma) = \sigma \times Br \times \mathcal{L} \times \mathcal{A}_{WW} \times C_{WW} \tag{10.4}$$

To extract the fiducial cross section, $N_s^i(\sigma_{WW}^{\text{fiducial}})$ is evaluated instead of $N_s^i(\sigma_{WW}^{\text{total}})$. The formula is the same as Equation 10.4 but with the $\mathcal{A}_{WW}$ and $Br$ taken away.

Moreover, to account for the systematic uncertainties of the signal and backgrounds, $N_s^i$ and $N_b^i$ have to be corrected by:

$$\begin{aligned} N_s^i(\sigma, \{x_k\}) &= \sigma \times Br \times \mathcal{L} \times \mathcal{A}_{WW} \times C_{WW} \times \left(1 + \sum_{k=1}^{n} x_k S_k^i\right) \\ N_b^i(\{x_k\}) &= N_b^i \left(1 + \sum_{k=1}^{n} x_k B_k^i\right) \\ N_{\text{exp}}^i(\sigma, \{x_k\}) &= N_s^i(\sigma, \{x_k\}) + N_b^i(\{x_k\}) \end{aligned} \tag{10.5}$$

where $S_k^i$ is the $k$-th *signal* systematic term in the $i$-th channel; $B_k^i$ is the $k$-th *background* systematic term in the $i$-th channel; and $n$ is the total number of systematic sources. The uncertainty of each systematic terms is typically assumed to be a standard normal distribution, $x_k \sim N(0,1)$. In some cases, distributions other than $N(0,1)$, e.g. Gamma or Log-Normal distributions, can be considered. The $\{x_k\}$ (called nuisance parameters, describing the uncertainties of the measurement) in $N_s^i(\sigma, \{x_k\})$ and $N_b^i(\{x_k\})$ indicates that the expected numbers of signal and backgrounds in each channel are dependent on all the systematic terms, or a subset of them.

Considering the nature of event selection, after full analysis selection, the probability of observing $N_{\text{obs}}$ events under the expectation of $N_{\text{exp}}$ events is a Poisson distribution:

$$P\left(N_{\text{obs}}; N_{\text{exp}}\right) = \frac{{N_{\text{exp}}}^{N_{\text{obs}}} e^{-N_{\text{exp}}}}{(N_{\text{obs}})!} \tag{10.6}$$

Therefore, a negative log-likelihood function corresponding to the cross section can be defined as:

$$-\ln L(\sigma, \{x_k\}) = -\sum_{i=1}^{3} \ln\left(\frac{e^{-(N_s^i(\sigma,\{x_k\}) + N_b^i(\{x_k\}))} \times (N_s^i(\sigma, \{x_k\}) + N_b^i(\{x_k\}))^{N_{\text{obs}}^i}}{\left(N_{\text{obs}}^i\right)!}\right) + \sum_{k=1}^{n} \frac{x_k^2}{2} \tag{10.7}$$

Here, the expression inside the natural logarithm is the $P(N_{\text{obs}}; N_{\text{exp}})$ for the $i$-th channel. The last term in Equation 10.7 is the term accounting for the Gaussian constraints on the $x_k$, previously defined in equations 10.5. It can be modified if

Gamma or Log-Normal distributions are chosen for the nuisance parameters. Each independent systematic source $k$ is assigned with a $x_k$. The same $x_k$ is used across all channels, in both signal and backgrounds, since the systematics are considered fully correlated over all channels and between signal and backgrounds.

The minimization and uncertainty determination of $-\ln L(\sigma, \{x_k\})$ is performed using the **`Minuit`** package [91]. In the single channel calculation for cross sections (either $\sigma_{WW}^{\text{total}}$ or $\sigma_{WW}^{\text{fiducial}}$), Equation 10.7 is only used for channel $i$ rather than the product of all channels.

### 10.2.3 Cross Section Results

Tables 10.2 and 10.3 summarize respectively the final results for $\sigma_{WW}^{\text{fiducial}}$ and $\sigma_{WW}^{\text{total}}$ for each channel. The combined measurement of 3 channels is also provided for the total cross section.

| Channel | Fiducial Cross Section [$fb$] |
|---|---|
| $ee$ | $73.3^{+4.2}_{-4.1}(\text{stat})\ ^{+0.8}_{-0.8}(\text{theo})\ ^{+6.4}_{-5.5}(\text{reco})\ ^{+2.2}_{-2.1}(\text{lumi})$ |
| $\mu\mu$ | $80.1^{+3.3}_{-3.2}(\text{stat})\ ^{+0.8}_{-0.8}(\text{theo})\ ^{+6.4}_{-5.5}(\text{reco})\ ^{+2.4}_{-2.3}(\text{lumi})$ |
| $e\mu$ | $373.8^{+6.9}_{-6.8}(\text{stat})\ ^{+2.6}_{-2.6}(\text{theo})\ ^{+24.9}_{-22.4}(\text{reco})\ ^{+11.2}_{-10.5}(\text{lumi})$ |

Table 10.2: Measured fiducial cross sections for each channel.

| Channel | Total Cross Section [$pb$] |
|---|---|
| $ee$ | $73.5^{+4.2}_{-4.1}(\text{stat})\ ^{+7.5}_{-6.4}(\text{syst})\ ^{+2.3}_{-2.1}(\text{lumi})$ |
| $\mu\mu$ | $73.9^{+3.0}_{-3.0}(\text{stat})\ ^{+7.1}_{-5.9}(\text{syst})\ ^{+2.2}_{-2.1}(\text{lumi})$ |
| $e\mu$ | $70.5^{+1.3}_{-1.3}(\text{stat})\ ^{+5.8}_{-5.1}(\text{syst})\ ^{+2.1}_{-2.0}(\text{lumi})$ |
| Combined | $71.0^{+1.1}_{-1.1}(\text{stat})\ ^{+5.7}_{-5.0}(\text{syst})\ ^{+2.1}_{-2.0}(\text{lumi})$ |
| | $\sigma^{total}$ with separate experimental and theoretical uncertainties |
| $ee$ | $73.5^{+4.2}_{-4.1}(\text{stat})\ ^{+3.6}_{-3.4}(\text{theo})\ ^{+6.6}_{-5.4}(\text{reco})\ ^{+2.3}_{-2.1}(\text{lumi})$ |
| $\mu\mu$ | $73.9^{+3.0}_{-3.0}(\text{stat})\ ^{+3.5}_{-3.3}(\text{theo})\ ^{+6.1}_{-4.9}(\text{reco})\ ^{+2.2}_{-2.1}(\text{lumi})$ |
| $e\mu$ | $70.5^{+1.3}_{-1.3}(\text{stat})\ ^{+3.2}_{-3.0}(\text{theo})\ ^{+4.9}_{-4.1}(\text{reco})\ ^{+2.1}_{-2.0}(\text{lumi})$ |
| Combined | $71.0^{+1.1}_{-1.1}(\text{stat})\ ^{+3.2}_{-3.1}(\text{theo})\ ^{+4.8}_{-3.9}(\text{reco})\ ^{+2.1}_{-2.0}(\text{lumi})$ |

Table 10.3: Measured total cross sections for each channel as well as the combination.

From Table 10.3, one can easily tell that the combined measurement is driven by the result of the $e\mu$ channel, which is reasonable since the $e\mu$ channel dominates the final yield statistics in this analysis. The low contribution of the *ee* and $\mu\mu$ channels as well as their higher uncertainties are due to the suppression of backgrounds, especially the $Z$+*jets* where a very high $\not{E}_T$ cut is applied. However, the $p$-value of the combined fit (0.72) indicates that the measurements of different channels are compatible and a good understanding of the entire data set is achieved.

In Tables 10.2 and 10.3, the luminosity uncertainty is excluded from the systematic uncertainty, therefore listed separately. The correlations of the systematic uncertainties between the channels are summarized as follows:

- The object systematics are considered fully correlated when the objects (leptons, jets, $\not{E}_T$ , $\not{p}_T$) are used on more than one channels.
- The systematic uncertainties of the data-driven background sources are considered fully correlated between channels, while the statistical uncertainties of the backgrounds are considered uncorrelated.
- An exception is made for the case of the $W$+*jets* background:
  - The lepton efficiency uncertainty is considered uncorrelated between channels since it is dominated by the MC statistical uncertainty
  - The fake-rate and sample-dependence uncertainties are considered fully correlated between channels.

For uncertainty determination, the nuisance parameters in Equation 10.7 automatically takes them into account and correctly propagate them to the final uncertainty, which is described as follows.

For statistical uncertainty, all the nuisance parameters are fixed to the central values obtained from the nominal fit, then a new fit is performed. The returned uncertainty of the new fit is the statistical uncertainty of the cross section.

For the luminosity uncertainty, all the nuisance parameters except the luminosity are fixed to the central values obtained from the nominal fit, then 2 new fits are performed with the luminosity set to be $\pm 1\sigma$. The luminosity uncertainty is taken as the difference of the newly fitted cross sections from the results obtained from the nominal fit.

For systematics of the cross section, the total uncertainties is the quadratic sum of all the decomposed uncertainties. The individual systematic uncertainties from each source for each channel are derived with the same way as the luminosity uncertainty, which are listed in Tables 10.4 and 10.5 for fiducial and total cross sections, respectively.

## 10.3 Comparison with the SM Prediction

The measured combined total cross section is $71.0^{+1.1}_{-1.1}(\text{stat})^{+5.7}_{-5.0}(\text{syst})^{+2.1}_{-2.0}(\text{lumi})$ $pb$, comparing to the theoretical Standard Model partial NNLO prediction of $58.7^{+3.0}_{-2.7}$ $pb$ and full NNLO prediction of $63.2^{+2.0}_{-1.8}$ $pb$ (see Table 6.1). The $WW$ total cross section measurement is $+1.7\sigma$ and $+1.1\sigma$ away from the partial NNLO and full NNLO SM prediction quoted here, respectively, indicating the full NNLO correction on the $W^+W^-$ production cross-section calculation is important. Further note here that the gluon-induced signal cross section calculation is only performed at LO approximation.

Table 10.6 compares the measured fiducial cross sections with the theoretical fiducial predictions quoted from different sources [73, 74, 92, 93], where in [73, 74] (see Table 6.1) the fiducial cross section $\sigma^{\text{fiducial}}_{\text{NNLO}}$ is derived by $\sigma^{\text{total}}_{\text{NNLO}} \times \mathcal{A}_{WW} \times Br$ with $Br = 0.108$. The $p_T$ resummation effects in $\mathcal{A}_{WW}$ calculation is accounted for in the extraction of fiducial cross section, $\sigma^{\text{fiducial}}_{\text{NNLO,Resum}}$, in [93] using the same method. The partial NNLO results used in the data/MC comparison plots are quoted as well (see Table 6.1). In the error propagation, the $\mathcal{A}_{WW}$ uncertainties are taken from Table 9.4, while the total cross section uncertainties are taken from Table 6.1.

The nominal cross section is calculated with `CT10` PDFs. On Table 6.4, 4 PDFs results are shown with various difference from the `CT10` results, ranging from +0.6% to +5.3%. Not only the central values, but also the errors on PDFs sets affect the theoretical predictions, e.g. the +5.3% higher cross section for the `ATLAS-epWZ` PDFs exceeds the PDFs uncertainty band which is of the level of 2%.

A detailed discussion on possible additional signal contributions can be found in Section 6.1. Figure 10.1 shows the comparison of the measured cross section with the theoretical full NNLO prediction of the $WW$ production.

| Source | $ee$ | $\mu\mu$ | $e\mu$ |
|---|---|---|---|
| *Pile-up* [$fb$] | $^{+2.00}_{-1.94}$ | $^{+2.03}_{-1.94}$ | $^{+1.35}_{-1.32}$ |
| $e$-trigger Efficiency [$fb$] | $^{+2.76}_{-2.63}$ | $^{+0.00}_{-0.00}$ | $^{+0.32}_{-0.31}$ |
| $\mu$-trigger Efficiency [$fb$] | $^{+0.00}_{-0.00}$ | $^{+3.07}_{-2.90}$ | $^{+0.29}_{-0.28}$ |
| $e$ Scale [$fb$] | $^{+1.45}_{-1.42}$ | $^{+0.00}_{-0.00}$ | $^{+0.42}_{-0.41}$ |
| $e$ Resolution [$fb$] | $^{+0.23}_{-0.24}$ | $^{+0.00}_{-0.00}$ | $^{+0.04}_{-0.03}$ |
| $\mu$ Scale [$fb$] | $^{+0.00}_{-0.00}$ | $^{+0.39}_{-0.37}$ | $^{+0.11}_{-0.10}$ |
| $\mu$ ID Resolution [$fb$] | $^{+0.06}_{-0.06}$ | $^{+1.67}_{-1.61}$ | $^{+0.56}_{-0.55}$ |
| $\mu$ MS Resolution [$fb$] | $^{+0.03}_{-0.04}$ | $^{+0.21}_{-0.20}$ | $^{+0.10}_{-0.09}$ |
| $e$ ID & Recon Efficiency [$fb$] | $^{+2.19}_{-2.11}$ | $^{+0.00}_{-0.00}$ | $^{+0.99}_{-0.97}$ |
| $\mu$ ID & Recon Efficiency [$fb$] | $^{+0.00}_{-0.00}$ | $^{+0.82}_{-0.80}$ | $^{+0.41}_{-0.40}$ |
| $e$ Isolation [$fb$] | $^{+0.47}_{-0.47}$ | $^{+0.00}_{-0.00}$ | $^{+0.22}_{-0.22}$ |
| $\mu$ Isolation [$fb$] | $^{+0.00}_{-0.00}$ | $^{+1.21}_{-1.17}$ | $^{+0.59}_{-0.58}$ |
| $\not{E}_T$ Reso Soft Terms [$fb$] | $^{+0.38}_{-0.38}$ | $^{+0.53}_{-0.51}$ | $^{+0.31}_{-0.30}$ |
| $\not{E}_T$ Scale Soft Terms [$fb$] | $^{+2.07}_{-2.00}$ | $^{+1.85}_{-1.78}$ | $^{+1.12}_{-1.10}$ |
| $p_T$ Reso Soft Terms [$fb$] | $^{+0.19}_{-0.19}$ | $^{+0.14}_{-0.12}$ | $^{+0.13}_{-0.12}$ |
| $p_T$ Scale Soft Terms [$fb$] | $^{+0.38}_{-0.38}$ | $^{+0.35}_{-0.34}$ | $^{+0.23}_{-0.22}$ |
| JES [$fb$] | $^{+4.02}_{-3.75}$ | $^{+4.54}_{-4.21}$ | $^{+4.25}_{-3.92}$ |
| JER [$fb$] | $^{+1.30}_{-1.27}$ | $^{+1.47}_{-1.42}$ | $^{+1.34}_{-1.32}$ |
| JVF [$fb$] | $^{+0.26}_{-0.27}$ | $^{+0.24}_{-0.22}$ | $^{+0.22}_{-0.22}$ |
| Di-boson Cross section [$fb$] | $^{+1.01}_{-1.01}$ | $^{+0.56}_{-0.54}$ | $^{+0.69}_{-0.69}$ |
| $C_{WW}$ PDFs [$fb$] | $^{+0.34}_{-0.34}$ | $^{+0.14}_{-0.12}$ | $^{+0.10}_{-0.10}$ |
| $C_{WW}$ Scale [$fb$] | $^{+0.60}_{-0.60}$ | $^{+0.61}_{-0.59}$ | $^{+0.60}_{-0.59}$ |
| $C_{WW}$ GEN+PS [$fb$] | $^{+0.93}_{-0.91}$ | $^{+0.81}_{-0.79}$ | $^{+0.35}_{-0.35}$ |
| $C_{WW}$ EWK [$fb$] | $^{+0.06}_{-0.06}$ | $^{+0.05}_{-0.03}$ | $^{+0.01}_{-0.01}$ |
| *Top* [$fb$] | $^{+1.82}_{-1.82}$ | $^{+1.42}_{-1.41}$ | $^{+1.34}_{-1.35}$ |
| $W$+*jets* & *multijet* Lepton Efficiency [$fb$] | $^{+0.74}_{-0.75}$ | $^{+1.32}_{-1.31}$ | $^{+0.97}_{-0.98}$ |
| $W$+*jets* & *multijet* Fake-rate [$fb$] | $^{+0.72}_{-0.72}$ | $^{+0.52}_{-0.51}$ | $^{+0.64}_{-0.64}$ |
| $W$+*jets* & *multijet* Sample Dependence [$fb$] | $^{+2.86}_{-2.85}$ | $^{+0.35}_{-0.33}$ | $^{+3.41}_{-3.40}$ |
| $Z$+*jets* [$fb$] | $^{+3.01}_{-3.00}$ | $^{+2.26}_{-2.26}$ | $^{+0.46}_{-0.45}$ |
| Bkg stat. (Data-Driven) [$fb$] | $^{+2.03}_{-2.03}$ | $^{+1.39}_{-1.38}$ | $^{+0.61}_{-0.60}$ |
| Bkg stat. (MC) [$fb$] | $^{+0.32}_{-0.33}$ | $^{+0.18}_{-0.16}$ | $^{+0.11}_{-0.10}$ |
| Total (no $\delta_{\mathcal{L}}$) [$fb$] | $^{+8.83}_{-7.68}$ | $^{+8.01}_{-6.92}$ | $^{+6.69}_{-6.02}$ |

Table 10.4: Relative systematic uncertainties on the fiducial cross section.

| Source | $ee$ | $\mu\mu$ | $e\mu$ | Combined |
|---|---|---|---|---|
| *Pile-up* [$fb$] | $^{+2.00}_{-1.94}$ | $^{+2.03}_{-1.94}$ | $^{+1.35}_{-1.32}$ | $^{+1.48}_{-1.44}$ |
| $e$-trigger Efficiency [$fb$] | $^{+2.76}_{-2.63}$ | $^{+0.00}_{-0.00}$ | $^{+0.32}_{-0.31}$ | $^{+0.43}_{-0.42}$ |
| $\mu$-trigger Efficiency [$fb$] | $^{+0.00}_{-0.00}$ | $^{+3.07}_{-2.90}$ | $^{+0.29}_{-0.28}$ | $^{+0.61}_{-0.60}$ |
| $e$ Scale [$fb$] | $^{+1.45}_{-1.42}$ | $^{+0.00}_{-0.00}$ | $^{+0.42}_{-0.41}$ | $^{+0.43}_{-0.42}$ |
| $e$ Resolution [$fb$] | $^{+0.23}_{-0.24}$ | $^{+0.00}_{-0.00}$ | $^{+0.04}_{-0.03}$ | $^{+0.05}_{-0.04}$ |
| $\mu$ Scale [$fb$] | $^{+0.00}_{-0.00}$ | $^{+0.39}_{-0.37}$ | $^{+0.10}_{-0.10}$ | $^{+0.14}_{-0.13}$ |
| $\mu$ ID Resolution [$fb$] | $^{+0.06}_{-0.06}$ | $^{+1.67}_{-1.62}$ | $^{+0.56}_{-0.55}$ | $^{+0.67}_{-0.66}$ |
| $\mu$ MS Resolution [$fb$] | $^{+0.03}_{-0.04}$ | $^{+0.21}_{-0.20}$ | $^{+0.09}_{-0.09}$ | $^{+0.11}_{-0.10}$ |
| $e$ ID & Recon Efficiency [$fb$] | $^{+2.19}_{-2.11}$ | $^{+0.00}_{-0.00}$ | $^{+0.99}_{-0.97}$ | $^{+0.91}_{-0.89}$ |
| $\mu$ ID & Recon Efficiency [$fb$] | $^{+0.00}_{-0.00}$ | $^{+0.82}_{-0.80}$ | $^{+0.41}_{-0.40}$ | $^{+0.43}_{-0.42}$ |
| $e$ Isolation [$fb$] | $^{+0.47}_{-0.47}$ | $^{+0.00}_{-0.00}$ | $^{+0.22}_{-0.22}$ | $^{+0.21}_{-0.20}$ |
| $\mu$ Isolation [$fb$] | $^{+0.00}_{-0.00}$ | $^{+1.20}_{-1.17}$ | $^{+0.59}_{-0.58}$ | $^{+0.62}_{-0.61}$ |
| $\not{E}_T$ Reso Soft Terms [$fb$] | $^{+0.38}_{-0.38}$ | $^{+0.53}_{-0.51}$ | $^{+0.31}_{-0.31}$ | $^{+0.35}_{-0.34}$ |
| $\not{E}_T$ Scale Soft Terms [$fb$] | $^{+2.07}_{-2.00}$ | $^{+1.85}_{-1.79}$ | $^{+1.12}_{-1.10}$ | $^{+1.28}_{-1.24}$ |
| $p_T$ Reso Soft Terms [$fb$] | $^{+0.19}_{-0.19}$ | $^{+0.14}_{-0.12}$ | $^{+0.13}_{-0.13}$ | $^{+0.13}_{-0.13}$ |
| $p_T$ Scale Soft Terms [$fb$] | $^{+0.38}_{-0.38}$ | $^{+0.35}_{-0.34}$ | $^{+0.23}_{-0.22}$ | $^{+0.25}_{-0.25}$ |
| JES [$fb$] | $^{+4.01}_{-3.75}$ | $^{+4.54}_{-4.21}$ | $^{+4.23}_{-3.94}$ | $^{+4.23}_{-3.93}$ |
| JER [$fb$] | $^{+1.30}_{-1.27}$ | $^{+1.47}_{-1.42}$ | $^{+1.35}_{-1.31}$ | $^{+1.35}_{-1.32}$ |
| JVF [$fb$] | $^{+0.26}_{-0.27}$ | $^{+0.24}_{-0.22}$ | $^{+0.22}_{-0.22}$ | $^{+0.23}_{-0.22}$ |
| Di-boson Cross section [$fb$] | $^{+1.01}_{-1.01}$ | $^{+0.55}_{-0.54}$ | $^{+0.70}_{-0.69}$ | $^{+0.69}_{-0.69}$ |
| $\epsilon_{\mathcal{A}}$ PDFs [$fb$] | $^{+1.26}_{-1.24}$ | $^{+1.00}_{-0.96}$ | $^{+0.86}_{-0.84}$ | $^{+0.90}_{-0.88}$ |
| $\epsilon_{\mathcal{A}}$ Scale [$fb$] | $^{+0.70}_{-0.70}$ | $^{+0.71}_{-0.69}$ | $^{+0.71}_{-0.69}$ | $^{+0.70}_{-0.69}$ |
| $\epsilon_{\mathcal{A}}$ GEN+PS [$fb$] | $^{+3.10}_{-2.93}$ | $^{+2.95}_{-2.79}$ | $^{+2.58}_{-2.46}$ | $^{+2.65}_{-2.52}$ |
| $\epsilon_{\mathcal{A}}$ EWK [$fb$] | $^{+0.34}_{-0.34}$ | $^{+0.41}_{-0.39}$ | $^{+0.47}_{-0.47}$ | $^{+0.45}_{-0.44}$ |
| $\epsilon_{\mathcal{A}}$ Jet-veto [$fb$] | $^{+3.51}_{-3.30}$ | $^{+3.51}_{-3.29}$ | $^{+3.51}_{-3.29}$ | $^{+3.49}_{-3.27}$ |
| *Top* [$fb$] | $^{+1.82}_{-1.83}$ | $^{+1.42}_{-1.41}$ | $^{+1.35}_{-1.35}$ | $^{+1.39}_{-1.38}$ |
| $W{+}jets$ & $multijet$ Efficiency [$fb$] | $^{+0.74}_{-0.75}$ | $^{+1.32}_{-1.31}$ | $^{+0.98}_{-0.97}$ | $^{+0.76}_{-0.76}$ |
| $W{+}jets$ & $multijet$ Fake-rate [$fb$] | $^{+0.72}_{-0.72}$ | $^{+0.52}_{-0.51}$ | $^{+0.64}_{-0.64}$ | $^{+0.62}_{-0.62}$ |
| $W{+}jets$ & $multijet$ Sample Dependence [$fb$] | $^{+2.85}_{-2.86}$ | $^{+0.34}_{-0.33}$ | $^{+3.40}_{-3.41}$ | $^{+2.60}_{-2.58}$ |
| $Z{+}jets$ [$fb$] | $^{+3.00}_{-3.01}$ | $^{+2.26}_{-2.26}$ | $^{+0.46}_{-0.45}$ | $^{+0.86}_{-0.85}$ |
| Bkg stat. (Data-Driven) [$fb$] | $^{+2.03}_{-2.04}$ | $^{+1.39}_{-1.38}$ | $^{+0.61}_{-0.60}$ | $^{+0.53}_{-0.51}$ |
| Bkg stat. (MC) [$fb$] | $^{+0.32}_{-0.32}$ | $^{+0.18}_{-0.16}$ | $^{+0.10}_{-0.10}$ | $^{+0.09}_{-0.08}$ |
| Total (no $\delta_{\mathcal{L}}$) [$fb$] | $^{+10.27}_{-8.71}$ | $^{+9.52}_{-7.99}$ | $^{+8.25}_{-7.18}$ | $^{+8.06}_{-6.98}$ |

Table 10.5: Relative systematic uncertainties on the total cross section.

| Channel | Cross Section [$fb$] |
|---|---|
| $ee$ | $73.3^{+4.2}_{-4.1}$(stat) $^{+6.5}_{-5.6}$(syst) $^{+2.2}_{-2.1}$(lumi) |
| $\sigma^{\text{fiducial}}$ [$fb$] [92] | $69.0 \pm 2.7$ |
| $\sigma^{\text{fiducial}}_{\text{NNLO}}$ [$fb$] [73, 74] | $63.0 \pm 3.4$ |
| $\sigma^{\text{fiducial}}_{\text{NNLO,Resum}}$ [$fb$] [93] | $65.5 \pm 3.6$ |
| $\sigma^{\text{fiducial}}_{\text{pNNLO}}$ [$fb$] | 58.54 ±2.84 |
| $\mu\mu$ | $80.1^{+3.3}_{-3.2}$(stat) $^{+6.4}_{-5.5}$(syst) $^{+2.4}_{-2.3}$(lumi) |
| $\sigma^{\text{fiducial}}$ [$fb$] [92] | $69.0 \pm 2.7$ |
| $\sigma^{\text{fiducial}}_{\text{NNLO}}$ [$fb$] [73, 74] | 68.6 ±3.7 |
| $\sigma^{\text{fiducial}}_{\text{NNLO,Resum}}$ [$fb$] [93] | $71.2 \pm 4.0$ |
| $\sigma^{\text{fiducial}}_{\text{pNNLO}}$ [$fb$] | 63.67 ±3.09 |
| $e\mu$ | $373.8^{+6.9}_{-6.8}$(stat) $^{+25.0}_{-22.5}$(syst) $^{+11.2}_{-10.5}$(lumi) |
| $\sigma^{\text{fiducial}}$ [$fb$] [92] | $357.9 \pm 14.4$ |
| $\sigma^{\text{fiducial}}_{\text{NNLO}}$ [$fb$] [73, 74] | $335.3 \pm 17.7$ |
| $\sigma^{\text{fiducial}}_{\text{NNLO,Resum}}$ [$fb$] [93] | 348.7 ±19.1 |
| $\sigma^{\text{fiducial}}_{\text{pNNLO}}$[$fb$] | 311.39 ±15.13 |

Table 10.6: Measured fiducial cross sections for each channel compared with the theoretical predictions: the fiducial predictions quoted in [92]; the fiducial cross section derived from the full NNLO total cross section [73, 74]; the fiducial cross section derived from an alternative calculation including resummation effects [93], where the $\mathcal{A}_{WW}$ is obtained using re-weighted distributions to mimic the $WW$ $p_T$ resummation effect. The partial NNLO fiducial cross sections used in the data/MC comparison plots are quoted as well. The $\mathcal{A}_{WW}$ uncertainties are taken from Table 9.4, while the total cross section uncertainties are taken from Table 6.1.

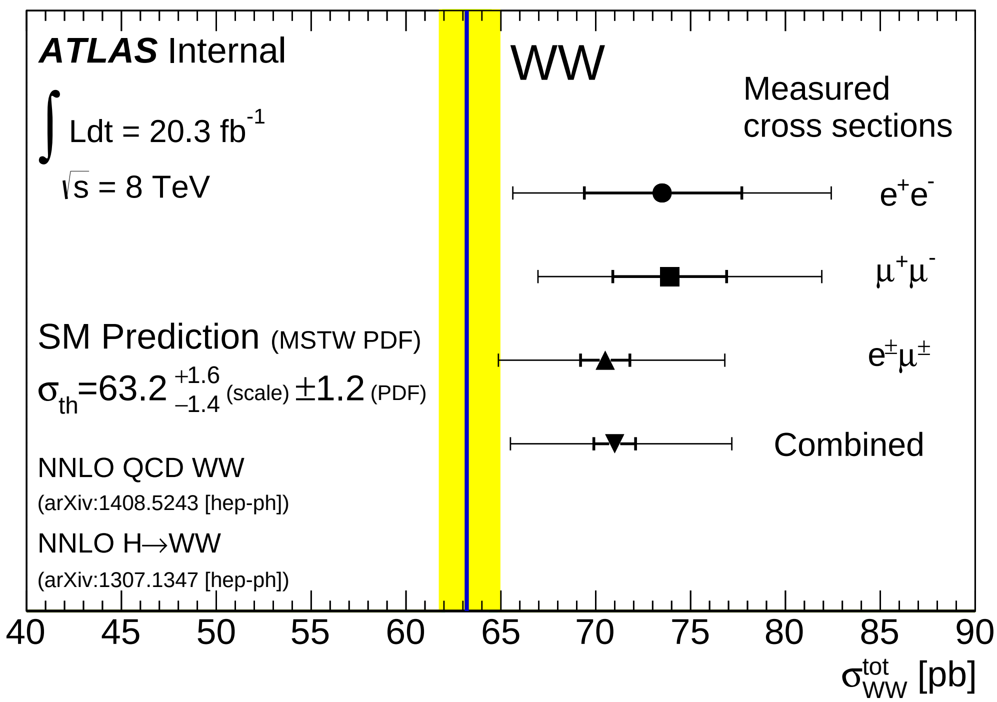


Figure 10.1: Comparison of the measured cross section from different di-lepton channels with the theoretical calculations of the $W^+W^-$ production cross section at $\sqrt{s} = 8\ TeV$. The $W^+W^-$ production originating from $q\bar{q}$ and from the Higgs decays are calculated with NNLO QCD and NLO EW corrections, while the continuum $W^+W^-$ production from the gluon fusion process is only calculated at LO QCD.

CHAPTER 11

# Probing Anomalous Triple-Gauge-Boson Couplings

The $W^+W^-$ production with $\ell^+\ell^- + \not{E}_T$ final state is sensitive to physics beyond the Standard Model, which will introduce new production diagrams altering total or differential cross section. Examples of new physics include theories which involves new particles decaying to vector bosons [94], or involves new particles directly decaying to the $\ell^+\ell^- + \not{E}_T$ final state [95, 96]. In this thesis the measured leading lepton transverse momentum, $p_T^{\ell_1}$, will be used to probe the anomalous triple-gauge-boson couplings (aTGCs), comparing theoretical models in anomalous coupling phase space with different assumption scenarios. This chapter describes the theoretical models, followed by experimental techniques to constraint the aTGCs.

## 11.1 Effective Field Theory

Physics beyond the SM can be parameterized in terms of aTGCs, depending on theories. A general form of Lagrangian parameterized in TGC terms is written as Equation 2.36 (see Section 2.2.1). In the SM, only three of these coupling parameters are non-zero: $g_1^Z = 1$, $\kappa^Z = 1$, and $\kappa^\gamma = 1$. EM gauge invariance requires that $g_1^\gamma = 1$. These couplings are often expressed as deviations from the Standard Model:

$$\Delta g_1^Z = 1 - g_1^Z; \qquad \Delta\kappa^Z = 1 - \kappa^Z; \qquad \Delta\kappa^\gamma = 1 - \kappa^\gamma \tag{11.1}$$

To conserve unitarity, dipole form factors are introduced (see Section 2.2.1).

$$\Delta g_1^V \rightarrow \frac{\Delta g_1^Z}{\left(1 + \frac{s}{\Lambda^2}\right)^2} \qquad \Delta\kappa^V \rightarrow \frac{\Delta\kappa^V}{\left(1 + \frac{s}{\Lambda^2}\right)^2} \qquad \lambda^V \rightarrow \frac{\lambda^V}{\left(1 + \frac{s}{\Lambda^2}\right)^2} \tag{11.2}$$

where $s$ is the invariant mass of the vector boson pair; the form factor, $\Lambda$, is the mass scale at which new physics appears, typically taken to be in multi-$TeV$ range at the LHC.

Unitarity limits for different form factors are derived in [97]. The limits for dipole form factors are

$$
\begin{aligned}
|\Delta g_1^Z| &\leq \frac{3.36\ TeV^2}{\Lambda^2} \\
|\Delta \kappa^Z| &\leq \frac{3.32\ TeV^2}{\Lambda^2} \\
|\lambda^Z| &\leq \frac{2.08\ TeV^2}{\Lambda^2} \\
|\Delta \kappa^\gamma| &\leq \frac{7.24\ TeV^2}{\Lambda^2} \\
|\lambda^\gamma| &\leq \frac{3.84\ TeV^2}{\Lambda^2}
\end{aligned}
$$

Nevertheless, there are critiques against this framework, one of which is that the aTGCs are promoted from simple constants to arbitrary form factors [98]. Moreover, the Lagrangian in Equation 2.36 does not respect $SU(2) \otimes U(1)$ gauge invariance. Therefore, an EFT approach is proposed to remove these two complications [98]. In the EFT, the effective Lagrangian is an expansion in operators which are $SU(2) \otimes U(1)$ gauge invariant and conserve charge ($C$) and parity ($P$). The strength of the coupling between new physics and the SM are parameterized by dimensionless coefficients, $c_i$.

$$
\mathcal{L} = \mathcal{L}_{\mathrm{SM}} + \sum_i \frac{c_i}{\Lambda^2} \mathcal{O}_i \tag{11.3}
$$

There are 3 dimension-6 operators, $\mathcal{O}_i$, that lead to aTGCs.

$$
\begin{aligned}
\mathcal{O}_{WWW} &= Tr[W_{\mu\nu} W^{\nu\rho} W_\rho^\mu] \\
\mathcal{O}_W &= \left(D_\mu \phi^0\right)^\dagger W^{\mu\nu} \left(D_\nu \phi^0\right) \\
\mathcal{O}_B &= \left(D_\mu \phi^0\right) B^{\mu\nu} \left(D_\nu \phi^0\right)
\end{aligned} \tag{11.4}
$$

where $\phi^0$ is the Higgs doublet field and

$$
\begin{aligned}
D_\mu &= \partial_\mu + \frac{i}{2} g \tau^I W_\mu^I + \frac{i}{2} g' B_\mu^I \\
W_{\mu\nu} &= \frac{i}{2} g \tau^I \left(\partial_\mu W_\nu^I - \partial_\nu W_\mu^I + g \epsilon_{IJK} W_\mu^J W_\nu^K\right) \\
B_{\mu\nu} &= \frac{i}{2} g' \left(\partial_\mu B_\nu - \partial_\nu B_\mu\right)
\end{aligned} \tag{11.5}
$$

The aTGCs constants can be calculated in terms of the constants in the EFT:

$$\begin{aligned}
\Delta g_1^Z &= c_W \frac{m_Z^2}{2\Lambda^2} \\
\Delta\kappa^Z &= [c_W - \tan^2\theta_W c_B] \frac{m_W^2}{2\Lambda^2} \\
\Delta\kappa^\gamma &= (c_B + c_W) \frac{m_W^2}{2\Lambda^2} \\
\lambda^\gamma = \lambda^Z &= \frac{3m_W^2 g^2}{2\Lambda^2} c_{WWW} \qquad (11.6) \\
& \qquad (11.7)
\end{aligned}$$

Or vice versa:

$$\begin{aligned}
\frac{c_W}{\Lambda^2} &= \frac{2}{m_Z^2}\Delta g_1^Z \\
\frac{c_B}{\Lambda^2} &= \frac{2}{m_Z^2}(\Delta\kappa^\gamma - \Delta\kappa^Z) \\
\frac{c_{WWW}}{\Lambda^2} &= \frac{2}{3g^2 m_W^2}\lambda \qquad (11.8)
\end{aligned}$$

In contrast to the aTGCs framework, the free parameters of an EFT are $\frac{c_{WWW}}{\Lambda^2}$, $\frac{c_W}{\Lambda^2}$, $\frac{c_B}{\Lambda^2}$, which restores unitarity without introducing arbitrary form factors.

## 11.2 Additional Constraints on $WWZ$ and $WW\gamma$ Couplings Parameters

We discuss different TGC parameter constraint scenarios used in previous experiments and in this analysis: *LEP*, *HISZ*, and *Equal Couplings*.

***LEP* Constraint** According to Equation 11.6, by requiring $SU(2) \otimes U(1)$ gauge invariance, the *LEP* constraint [99] is defined, which reduces the number of free aTGC parameters to three.

$$\begin{aligned}
\Delta g_1^Z &= \Delta\kappa^Z + \tan^2\theta_W \Delta\kappa^\gamma \\
\lambda^\gamma &= \lambda^Z \qquad (11.9)
\end{aligned}$$

***HISZ* Constraint** In addition to require $SU(2) \otimes U(1)$ gauge invariance, the choice of setting $c_W = c_B$ leads to the so-called Hagiwara-Ishihara-Szalapski-Zeppenfeld [100], or *HISZ* constraint, which reduces the number of free aTGC parameters to two.

$$\begin{aligned}
\Delta g_1^Z &= \frac{\Delta\kappa^Z}{\cos^2\theta_W - \sin^2\theta_W} \\
\Delta\kappa^\gamma &= 2\Delta\kappa^Z \frac{\cos^2\theta_W}{\cos^2\theta_W - \sin^2\theta_W} \\
\lambda^\gamma &= \lambda^Z
\end{aligned} \tag{11.10}$$

***Equal Couplings* Constraint** By assuming that the couplings for the $WWZ$ and $WW\gamma$ vertex are equal, the *Equal Couplings* constraint is defined, which reduces leaves the number of free aTGC parameters to two.

$$\begin{aligned}
g_1^Z &= g_1^\gamma = 1 \\
\Delta\kappa^\gamma &= \Delta\kappa^Z \\
\lambda^\gamma &= \lambda^Z
\end{aligned} \tag{11.11}$$

## 11.3 Limit Setting Methodology

This section gives a brief description of the parameterization and derivation of the limits on aTGCs. The limits are calculated using **`TGClim`** program, a package originally developed by the *ATLAS SM Physics Group*.

### 11.3.1 Maximum Likelihood

The same principle of likelihood fitting method prevails here as described in Section 10.2.2. Similar to Equation 10.6, instead of cross section $\sigma$, the number of SM+aTGCs signal events $N_{\text{sig}}$ is parameterized to depend on $n$ aTGC parameters, $\boldsymbol{\mu} = \{1, \mu_1, \ldots, \mu_n\}$. The Poisson probability of observing $N_{\text{data}}$ events is

$$p(N_{\text{data}}, N_{\text{sig}}(\boldsymbol{\mu}) + N_{\text{bkg}}) = \frac{(N_{\text{sig}}(\boldsymbol{\mu}) + N_{\text{bkg}})^{N_{\text{data}}} e^{-(N_{\text{sig}}(\boldsymbol{\mu}) + N_{\text{bkg}})}}{N_{\text{data}}!} \tag{11.12}$$

where $N_{\text{sig}}$ is the expected number of signal events which depends on $\boldsymbol{\mu}$; $N_{\text{bkg}}$ is the expected number of background events; and $N_{\text{data}}$ is the number of observed data events.

In the aTGCs study, the signal only refers to the $qq \to WW$ process. The gluon fusion processes are treated as background. The number of signal events scales with terms up to quadratic dependence of the $n$ aTGC parameters. Define the coefficients $F^{ij}$ such that

$$N_{\text{sig}}(\boldsymbol{\mu}) = \sum_{i,j} F^{ij}\mu_i\mu_j, \qquad i, j \in \{1, \ldots, n\} \tag{11.13}$$

In this study, the $p_T^{\ell_1}$ is chosen to be the probing variable, which is binned with an index $i = \{0, \ldots, m\}$ where $m$ is the total number of bins. To account for the binned statistical or systematic uncertainties associated with $N_{\text{sig}}$ and $N_{\text{bkg}}$, nuisance parameters, $\boldsymbol{\theta} = \{\theta_1, \ldots, \theta_{2m}\}$, are introduced. Remember that, $\boldsymbol{\mu}$ are the parameters of interest (aTGCs), while $\boldsymbol{\theta}$ are with limited accuracy and are allowed to be set at any values other than their nominal fitted values.

$$N^i_{\text{total}}(\boldsymbol{\mu}, \boldsymbol{\theta}) = N^i_{\text{sig}}(\boldsymbol{\mu})(1 + \theta_i) + N^i_{\text{bkg}}(1 + \theta_{i+m}) \tag{11.14}$$

The covariance matrix, $C$, is given by

$$C_{ij} = \sum_k \rho\sigma_{ik}\sigma_{jk} \tag{11.15}$$

where $\sigma_{ik}$ and $\sigma_{(i+m)k}$ are the the fractional systematic uncertainties on $N^i_{\text{sig}}$ and $N^i_{\text{bkg}}$ in the $i$-th bin due to the $k$-th source. $\rho = 1$ or $\rho = 0$ represent full or no correlation.

Based on Equations 11.12, 11.14 and 11.15, the likelihood with nuisance parameters is defined as

$$\mathcal{L}(N_{\text{data}}, \boldsymbol{\mu}, \boldsymbol{\theta}) = \prod_{i=1}^{m} p\left(N^i_{\text{data}}, N^i_{\text{total}}(\boldsymbol{\mu}, \boldsymbol{\theta})\right) \frac{1}{(2\pi)^m} e^{-\frac{1}{2}(\boldsymbol{\theta}\cdot C^{-1}\cdot\boldsymbol{\theta})} \tag{11.16}$$

The systematic uncertainties on signal and background are considered as nuisance parameters, which are generally categorized into 2 types:

1. Flat: For each systematic source, all bins are varied coherently up or down, or in other words, the overall normalization but not the shape of the distribution is varied. Examples include cross section and luminosity uncertainties.

2. Shape: For each systematic source, bin migrations, or bin-by-bin correlations are presented. In other words, the shape of the distribution is varied. Examples include lepton energy scale and resolution uncertainties.

### 11.3.2 Delta Log Likelihood Limits and Frequentist Limits

**dLogL** Since the likelihood as defined in Equation 11.16 is Gaussian, the log of it is parabolic.

$$-\ln \mathcal{L}(N_{\text{data}}, \boldsymbol{\mu}, \boldsymbol{\theta}) = -\ln \mathcal{L}_{\max} + s^2/2 \tag{11.17}$$

where $\ln \mathcal{L}_{\max}$ is the maximum(minimum) likelihood and $s$ is the standard deviation. With Equation 11.17, limits on aTGC parameters can be derived based on the maximum likelihood method (MLM). The 1-dimensional (1-D) 95% CL limit for an aTGC parameter is evaluated with all others set to zero, by generating a series of values which results in deviation from the minimum of Equation 11.17 within ±1.92, and the boundary of that series is defined as the 1-D limit of that aTGC parameter. Similar approach is used for the 2-dimensional (2-D) limit evaluation for two of the aTGC parameters, where a set of values for the two parameters is used and the deviation is required to be within ±2.99 with respect to the minimum. The MLM is used in the optimization studies described in Section 11.3.3 for its low computation overhead compared to the frequentist approach used in the evaluation of final results.

**Frequentist Limits** The evaluation of the final results uses the standard frequentist approach [101, 102]. For an aTGC parameter $\alpha$, a large number of pseudo experiments is generated using different test values of $\alpha$. The test statistic $q(\alpha)$ is defined to be

$$q(\alpha) = -ln\frac{L(n|\alpha, \hat{\hat{\beta}})}{L(n|\hat{\alpha}, \hat{\beta})} \tag{11.18}$$

where $n$ is the number of events; $\beta$ is the nuisance parameter; $\hat{\hat{\beta}}$ is the MLM estimator of $\beta$ that maximizes the numerator for a fixed $\alpha$; $\hat{\alpha}$ and $\hat{\beta}$ are the MLM estimators of $\alpha$ and $\beta$ which maximize the denominator. For the denominator $L(n|\hat{\alpha}, \hat{\beta})$, the minimization is done with $\alpha$ and $\beta$ as free parameters; while for the numerator $L(n|\alpha, \hat{\hat{\beta}})$, the minimization is done with $\alpha$ free and $\beta$ minimized. Pseudo experiments are generated by sampling $n$ events on a Poisson distribution, in which the mean is the expected number of events evaluated with a fixed $\alpha$ and a fluctuating $\beta$ (within Gaussian constraints). The $p$-value for each fixed value of $\alpha$ is calculated as:

$$p = \frac{N_{\text{pe}}(q_{\text{pe}}(\alpha) < q_{\text{obs}}(\alpha))}{N_{\text{pe}}} \tag{11.19}$$

where $N_{\text{pe}}$ is the number of pseudo experiments; $q_{\text{pe}}$ is the test statistic of the pseudo experiments; $q_{\text{obs}}$ is the observed value of the test statistic, which is evaluated by setting $n = n_{\text{obs}}$ with $n_{\text{obs}}$ being the observed data.

### 11.3.3 Optimization

**Bin Optimization** The aTGCs effect is sensitive at the high-$p_T$ region while most of the events fall in the low-$p_T$ region. To effectively extract stringent limits of aTGC parameters, the $p_T^{\ell_1}$ distribution is binned such that it exploits the changes in the high-$p_T$ tails while keep sufficient statistics in each bin. The optimization of binning is done by calculating expected limits of aTGC parameters with various bin boundaries, with the procedure described below. At first, only a single bin of $p_T^{\ell_1}$ ([25,1000] $GeV$) is used for the calculation of expected limits of each aTGC parameter for each constraint scenario. Then the bin is split into two bins for the calculation and the bin boundary is fixed when the most stringent limits are achieved for all scenarios. The process is repeated iteratively to add more bins until the derived limits differ by less than 1% from the last iteration. The optimum binning achieved for $p_T^{\ell_1}$ is [25, 75, 150, 250, 350, 1000] $GeV$.

**Variable Choice Optimization** There are multiple choices of dynamic variables for the probing of aTGCs limits: the di-lepton $p_T$ ($p_T^{\ell\ell}$), the transverse mass of the $\ell\ell + \not{E}_T$ system ($m_T$), the di-lepton mass ($M_{\ell\ell}$) and the leading lepton $p_T$ ($p_T^{\ell_1}$). To choose the optimum variable, the bin optimization is done independently for each variable in coarser step sizes until the limit difference between iteration is less than the limit difference between variables. As a result, the most stringent limits are found with $p_T^{\ell_1}$.

**Channel Optimization** As shown in Section 10.2.3, the combined cross section result is dominated by the results in the $e\mu$ channel. The aTGCs limit setting also uses the $e\mu$ channel only, for the following reasons: firstly, it is quite challenging to obtain the binned systematic uncertainties for the data-driven backgrounds in the same-flavor channel; secondly, the same-flavor channels have lower event yields and higher statistic fluctuations. Even though, to compensate the loss from using only the $e\mu$ channel, the expected and observed limits were computed for all 3 channels, which shows that the results improves by 8-15% if all channels are included.

**Removal of Low $p_T$ Bins** The $p$-values of the fitting for 95% CL limit setting for the aTGC parameters with $p_T^{\ell_1}$ binning of [25,75,150,250,350,1000] *GeV* are at the level of 0.1%, for the cause of the excess in data at the low-$p_T$ region which results to a poor fit. One approach to improve the fit quality is to remove the first two low $p_T$ bins for the fits. It would not significantly decrease the sensitivity of aTGCs since the effect lies mostly in the high-$p_T$ tail of the distribution. The expected limits fitted with 5-bin and 3-bin settings shows a difference of 7-12%. The $p$-values for the 3-bin fits are at the level of 2-3%, which is a great improvement.

## 11.4 Limit Setting Procedures

From Equation 11.16, 11.17 and 11.18, one can see that to find the aTGCs limits by maximizing the likelihood, a lot of $\boldsymbol{\mu}$ trial values have to be used to generate the expected number of events ($N^i_{\text{total}}(\boldsymbol{\mu}, \boldsymbol{\theta})$ in Equation 11.16). Powheg , **MC@NLO**, and **BHO** are all NLO generators capable of producing di-boson events with aTGCs. However, if the directly generated MC samples with aTGCs are used alone, huge amount of them are required. To reduce computation cost of generating so many events with different aTGC parameters, a re-weighting procedure is in need. It is used to scale the sample produced with fixed values of a particular set of aTGC parameters to another sample with different aTGCs values.

The disadvantage of **BHO** or Powheg is that they do not provide anomalous coupling weights inherently, while **MC@NLO** provides event-by-event weights for easy calculation with alternate aTGC parameter values, as described in Section 11.4.2. Since these weights are given event-wise, kinematic dependencies are automatically considered.

An alternative re-weighting method (Section 11.4.3) using the **BHO** generator was used in the 7 *TeV WW* analysis[1], which developed a 3D re-weighting method.

### 11.4.1 MC Samples and Generator Comparisons

The official MC samples generated with different aTGC parameters as well as full detector simulation and object reconstruction are listed in Table 11.1. It is important to compare Powheg with **MC@NLO** since it is the official $W^+W^-$ signal sample in this analysis.

Figure 11.1 shows the reconstruction-level comparisons of some kinematic distributions using Powheg + Pythia and **MC@NLO**+Herwig/Jimmy with SM settings

| Generator | Couplings | Dataset ID |
|---|---|---|
| Powheg + Pythia | SM | 126928-126936 |
| **MC@NLO**+Herwig/Jimmy | SM | 129933-129941 |
| **MC@NLO**+Herwig/Jimmy | $\Delta g_1^Z = 0.6, \Delta\kappa^Z = 0.2, \lambda^Z = 0.2$ | 129942-129950 |
| **MC@NLO**+Herwig/Jimmy | $\Delta g_1^Z = 0.6$ | 129951-129959 |

Table 11.1: Officially produced MC samples for $WW \to \ell\nu\ell\nu$ process with SM or aTGC parameters. For the case of non-SM, the non-zero coupling parameters are listed.

after full selection in the $e\mu$ channel. The agreement is reasonable and generator uncertainties are assigned for the difference. Note that the large discrepancy in the high energy tails are due to statistical fluctuations.

Figure 11.2 presents the generator-level comparisons of the $p_T^{\ell_1}$ using **BHO**, Powheg+Pythia and **MC@NLO**+Herwig/Jimmy with various aTGCs settings after full selection (to the best knowledge of reconstruction-level cuts) in the $e\mu$ channel. These samples are privately generated with SM and various aTGCs settings without detector simulation or object reconstruction due to unavailability, but with very high statistics for high precision comparisons. No available parton shower was used for **BHO**. The agreement is reasonable, with a 20% difference in the high energy tails which is covered by the generator and parton shower uncertainties.

### 11.4.2 Re-weighting with MC@NLO

The re-weighting method with the **MC@NLO** generator is detailed in this section. The number of signal events $N_{\text{sig}}$ scales with the cross section as well as the squared amplitude:

$$N_{\text{sig}} \propto \sigma \propto \mathcal{A}^2 \tag{11.20}$$

in which the amplitude $\mathcal{A}$ expands as

$$\mathcal{A} = \mathcal{A}_{\text{SM}} + \mu_1 \mathcal{A}_{\mu_1} + \ldots + \mu_n \mathcal{A}_{\mu_n} \tag{11.21}$$

where $\boldsymbol{\mu} = \{\mu_1, \ldots, \mu_n\}$ are the $n$ aTGC parameters, with $\mu_0 = 1$ since the first term represents the SM only. **MC@NLO** internally integrates 6 aTGC parameters: $\boldsymbol{\mu} = \{1, \Delta g_1^Z, \Delta\kappa^Z, \lambda^Z, \Delta g_1^\gamma, \Delta\kappa^\gamma, \lambda^\gamma\}$. The independent parameters are up to 6, but additional constraints will lower this number. The generator calculates event weights

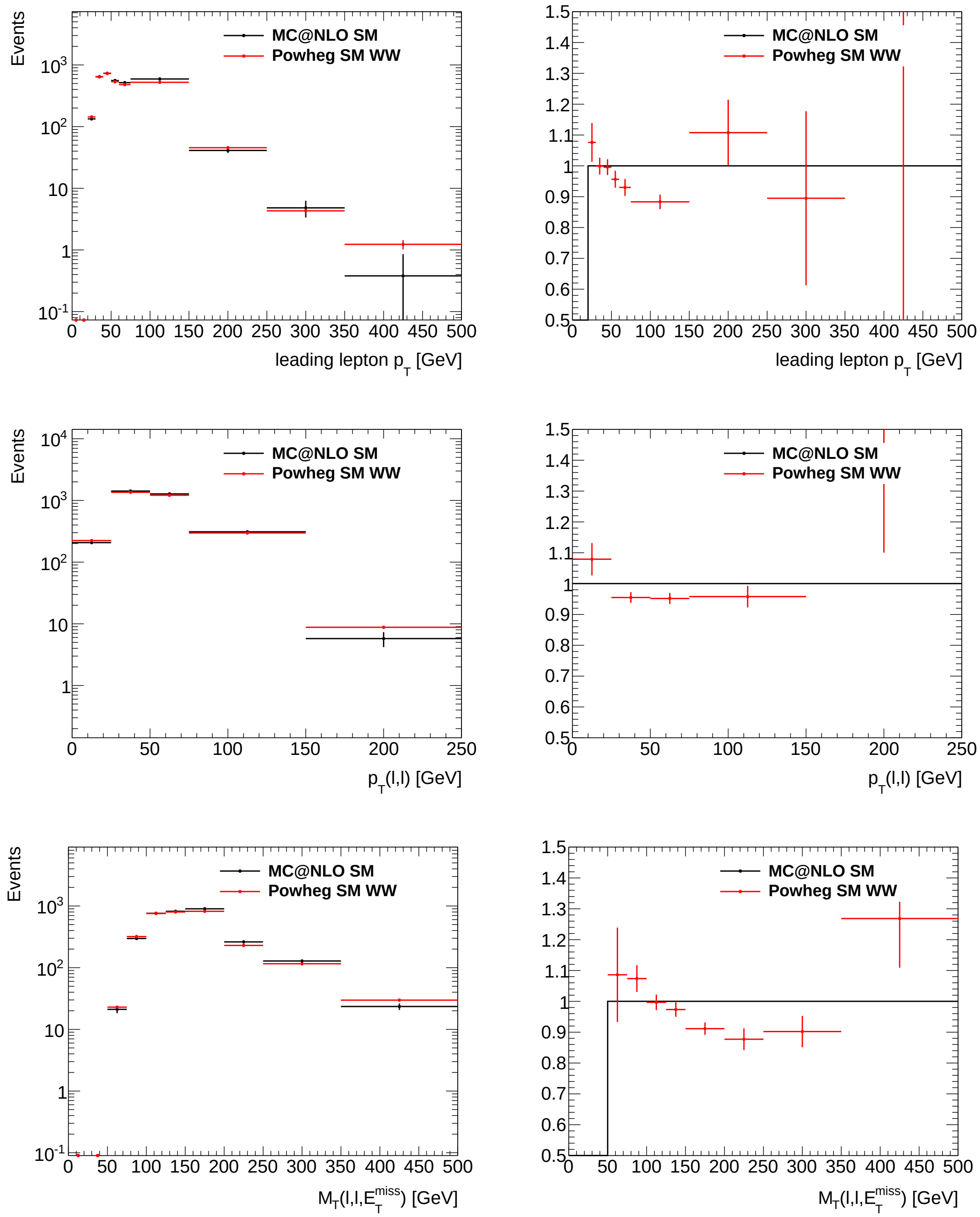


Figure 11.1: Comparison of reconstruction level SM $W^{+}W^{-}$ kinematic distributions after all final selection cuts (in the $e\mu$ channel) from using Powheg + Pythia (red) and **MC@NLO**+Herwig/Jimmy (black). Events are normalized to 20.3 $fb^{-1}$ . The left column shows the event yields and the right column shows the ratio of the two generators.

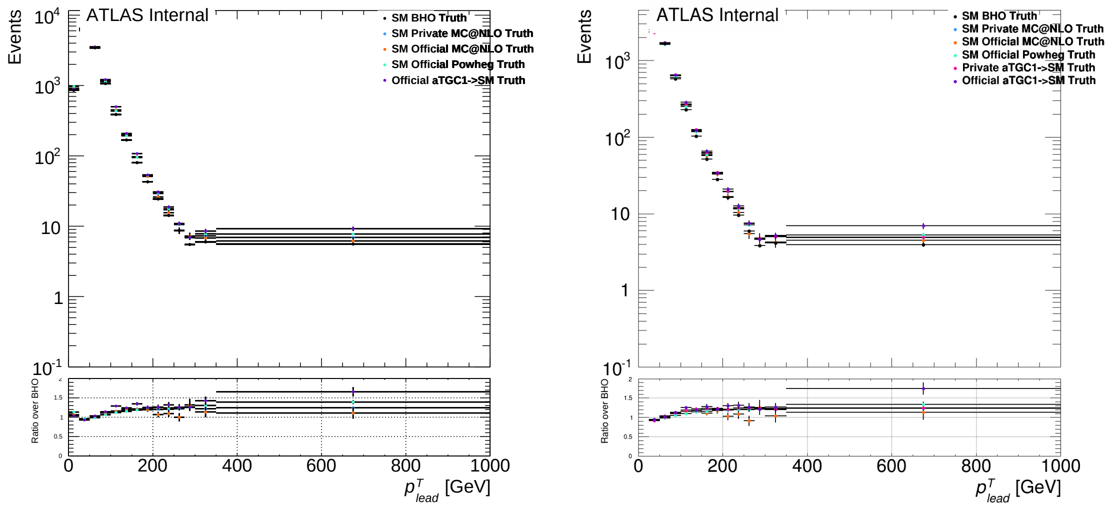


Figure 11.2: $p_T^{\ell_1}$ distributions of different samples: the **BHO** SM sample, the high-statistics private **MC@NLO** SM sample, the official **MC@NLO** SM sample, the official POWHEG SM sample, the SM sample re-weighted from high-statistics private aTGCs sample, and the SM sample re-weighted from official aTGCs sample. The "aTGC1" refers to the aTGC parameter setting of line 3 in Table 11.1. The left plot is in full volume, and the right plot is in fiducial volume. Note that the SM sample re-weighted from high-statistics private aTGCs sample is only available in fiducial region, so is the comparison. The ratios are derived by dividing the distributions by **BHO** sample. The plots only compares the case of infinite form factor and *No Constraint* scenario.

inherently by:

$$\begin{aligned} w_{\text{Total}} = w_0 &+ (\Delta g_1^Z)^2 w_1 + (\Delta\kappa^Z)^2 w_2 + (\lambda^Z)^2 w_3 \\ &+ (\Delta g_1^\gamma)^2 w_4 + (\Delta\kappa^\gamma)^2 w_5 + (\lambda^\gamma)^2 w_6 \\ &+ 2\Delta g_1^Z w_7 + \ldots + 2\lambda^\gamma w_{12} \\ &+ 2\Delta g_1^Z \Delta\kappa^Z w_{13} + \ldots + 2\Delta\kappa^\gamma \lambda^\gamma w_{27} \end{aligned} \tag{11.22}$$

The aTGCs event weights, $a_i \equiv \dfrac{w_i}{w_{\text{Total}}}$, are stored in the `D3PD` vectorial branch `mcevt_weight`:

$$\texttt{mcevt\_weight} = \{\texttt{mc\_weight}, a_0, \ldots, a_{27}\} \tag{11.23}$$

where `mc_weight` is the generator weight, which is either 1 or -1 for **MC@NLO**. The weights stored in `mcevt_weight` will be used to re-weight the event to a new set of aTGCs on an event-by-event base:

$$w(\Delta g^Z_{1,\mathrm{new}}, \ldots, \lambda^\gamma_{\mathrm{new}}) = a_0 + a_1(\Delta g^Z_{1,\mathrm{new}})^2 + \ldots + 2a_{27}\Delta\kappa^\gamma_{\mathrm{new}}\lambda^\gamma_{\mathrm{new}} \tag{11.24}$$

Comparing to Equation 11.13, one can find that it is straightforward to match the coefficients $F^{ij}$ with the **MC@NLO** aTGC weights in Equation 11.22.

To validate the **MC@NLO** re-weighting, two samples are compared: a directly generated sample with one set of aTGCs $\boldsymbol{\mu}_1$, and a sample generated with $\boldsymbol{\mu}_2$ then re-weighted to $\boldsymbol{\mu}_1$. The results shows that the discrepancy between the two compared samples is within the generator uncertainty.

Table 11.2 lists the normalized signal parameterization as in Equation 11.22 after applying EW corrections for the *No Constraint* scenario.

Table 11.3 lists the signal event yields in each $p_T^{\ell_1}$ bin and associated statistical uncertainties. Note that $gg \to WW$ is listed as background. The binned flat and shape systematic uncertainties (see Section 11.3.1) of signal (both $qq \to WW$ and $gg \to WW$) are listed in Table 11.5, in which the signs of the uncertainties are kept to conserve bin-by-bin correlations. Similarly, the binned shape systematics of di-boson and data-driven ($Z$+*jets*, $W$+*jets*, and *Top*) backgrounds are listed in Tables 11.6 and 11.4, respectively.

### 11.4.3 Re-weighting with BHO

The alternative re-weighting method with the **BHO** generator is detailed in this section.

#### 11.4.3.1 3-D Re-weighting Parameterization

According to Equation 11.22, the event weights of a set of aTGC parameters could be scaled from SM weights by:

$$\begin{aligned}
w_{\mathrm{aTGCs}} &= w_{\mathrm{SM}} \cdot R(\Delta g^Z_1, \ldots, \lambda^\gamma) && (11.25a)\\
&= w_{\mathrm{SM}} \cdot (a_0 + a_1(\Delta g^Z_1)^2 + \ldots + 2a_{27}\Delta\kappa^\gamma\lambda^\gamma) && (11.25b)\\
&= w_0 + w_1(\Delta g^Z_1)^2 + \ldots + 2w_{27}\Delta\kappa^\gamma\lambda^\gamma && (11.25c)
\end{aligned}$$

where $R(\Delta g^Z_1, \ldots, \lambda^\gamma)$ is the ratio function depending on aTGC parameters. However, there is neither available parton showerer interfaced with the **BHO** generator, nor available inherently stored generator aTGC weights. Therefor, $R(\Delta g^Z_1, \ldots, \lambda^\gamma)$ could not be obtained event-wise. Alternatively, $R$ could be re-written as a function

| $p_T^{\ell_1}$ (*GeV*) | 25-75 | 75-150 | 150-250 | 250-350 | 350-1000 |
|---|---|---|---|---|---|
| w0 | 2538.3511 | 580.6191 | 51.445 | 5.6007 | 1.1535 |
| w1 | 403.8496 | 446.2231 | 169.6013 | 52.5405 | 28.4782 |
| w2 | 1090.4524 | 2810.4971 | 2844.4399 | 1879.9718 | 2435.0181 |
| w3 | 1867.9723 | 5260.8721 | 5535.0732 | 3709.8433 | 4842.2754 |
| w4 | 55.0165 | 70.5879 | 31.0981 | 11.1002 | 6.423 |
| w5 | 159.5249 | 481.7927 | 536.6505 | 403.4465 | 551.4489 |
| w6 | 275.0844 | 906.0109 | 1045.1257 | 796.311 | 1096.6353 |
| w7 | -21.5405 | -79.6714 | -12.7283 | -1.8791 | -0.5073 |
| w8 | -61.6708 | -187.1691 | -66.8313 | -20.5484 | -11.817 |
| w9 | 12.1891 | -59.2387 | -5.4303 | -0.2373 | 0.3681 |
| w10 | -18.0217 | -32.6403 | -5.695 | -0.9255 | -0.2612 |
| w11 | -35.2449 | -80.0386 | -31.278 | -10.5907 | -6.3282 |
| w12 | -9.2589 | -28.9713 | -3.8634 | -0.465 | 0.0179 |
| w13 | 441.3488 | 578.8314 | 255.0313 | 84.5859 | 48.5844 |
| w14 | 569.7651 | 797.5406 | 356.2559 | 119.0714 | 69.4078 |
| w15 | 59.1645 | 70.7196 | 28.6899 | 9.3102 | 5.1566 |
| w16 | 65.117 | 92.0646 | 43.1749 | 14.9939 | 8.7882 |
| w17 | 83.7941 | 126.7233 | 60.3253 | 21.1098 | 12.5492 |
| w18 | 312.9323 | 360.1221 | 153.8068 | 50.1005 | 27.7609 |
| w19 | 65.117 | 92.0646 | 43.1749 | 14.9939 | 8.7882 |
| w20 | 166.0535 | 460.094 | 486.35 | 334.8567 | 441.7253 |
| w21 | 46.4399 | 57.406 | 26.0246 | 8.878 | 5.0271 |
| w22 | 83.7941 | 126.7233 | 60.3253 | 21.1098 | 12.5492 |
| w23 | 46.4399 | 57.406 | 26.0246 | 8.878 | 5.0271 |
| w24 | 285.6671 | 862.782 | 946.6754 | 660.8354 | 878.4234 |
| w25 | 60.8929 | 92.2435 | 46.9195 | 17.9032 | 10.9199 |
| w26 | 77.8205 | 126.9126 | 65.6638 | 25.2243 | 15.5773 |
| w27 | 43.9654 | 57.5744 | 28.1752 | 10.5821 | 6.2625 |

Table 11.2: Signal aTGC parameterization for the *No Constraint* scenario using 28 **MC@NLO** generator weights (see Equation 11.22). The parameterization is given in bins of $p_T^{\ell_1}$ in *GeV* in the $e\mu$ channel only. EW corrections are applied.

differentially depending on a set of kinematic variables $\boldsymbol{x}$ which is sensitive to aTGCs:

$$R(\boldsymbol{x}; \Delta g_1^Z, \ldots, \lambda^\gamma) \tag{11.26}$$

The choice of $\boldsymbol{x}$ subjects to the fiducial volume definition as well as minimum mutual correlation. In this analysis, $\boldsymbol{x}$ is chosen to consist of three components: the transverse momenta of positive and negative leptons, and the relative transverse missing energy:

$$\boldsymbol{x} = (p_T^{\ell+}, p_T^{\ell-}, \not{E}_T^{rel}) \tag{11.27}$$

| Number of events | 25-75 | 75-150 | 150-250 | 250-350 | 350-1000 |
|---|---|---|---|---|---|
| Observed | 4053 | 936 | 75 | 2 | 1 |
| Signal | 2538.35 | 580.62 | 51.45 | 5.60 | 1.15 |
| *W+jets* | 219.05 | 26.16 | 3.23 | 0.13 | 0.27 |
| *Z+jets* | 166.22 | 9.60 | 1.30 | 0 | 0 |
| Di-boson | 129.93 | 19.26 | 1.07 | 0.41 | 0.03 |
| Top | 334.78 | 238.21 | 31.05 | 3.06 | $-0.01 \rightarrow 0$ |
| $gg \rightarrow WW$ | 174.04 | 24.28 | 3.25 | 0.34 | 0.30 |
| Statistical uncertainty | 25-75 | 75-150 | 150-250 | 250-350 | 350-1000 |
| Signal | 1.51% | 2.59% | 5.05% | 6.43% | 7.06% |
| *W+jets* | 6.22% | 25.05% | 64.24% | 265.62% | 119.16% |
| Di-boson | 2.80% | 7.61% | 21.90% | 48.35% | 89.13% |
| Top | 3.98% | 4.44% | 11.91% | 44.63% | 505.05% |
| gg | 0.96% | 2.79% | 7.66% | 22.11% | 25.76% |

Table 11.3: Number of events (top) and statistical uncertainties (bottom) in signal and backgrounds (using data-driven estimates for *W+jets* and *Top*) in each $p_T^{\ell_1}$ bin in the $e\mu$ channel. Signal events are given under SM expectations with EW corrections applied to the SM-only term. The *Top* background yield is negative in the last bin because **`MC@NLO`** allows negative generator weights. This yield is set to zero for limit setting, as it is nonphysical.

| Shape systematic uncertainties | 25-75 | 75-150 | 150-250 | 250-350 | 350-1000 |
|---|---|---|---|---|---|
| *W+jets* Efficiency | 12.67% | 33.55% | 21.71% | 26.69% | 2.52% |
| *W+jets* Fake rate | 8.31% | -45.74% | 82.28% | 61.04% | 65.50% |
| *W+jets* Sample dependence | 47.22% | 133.03% | 122.52% | 99.81% | 134.92% |
| *Top* Shape | 10.36% | 11.37% | 8.76% | 0.00% | 0.00% |
| *Top* Normalization | 8.6% | 8.6% | 8.6% | 8.6% | 8.6% |
| *Z+jets* (Stat+Syst) | 14.16% | 76.90% | 28.40% | 0.00% | 0.00% |

Table 11.4: Systematic uncertainties on data-driven backgrounds in $p_T^{\ell_1}$ ($GeV$) bins for the $e\mu$ channel. The sign is kept to conserve bin-by-bin correlations.

Each kinematic variable is divided into 15 bins (0 to 300 $GeV$ in step of 25 $GeV$, 300 - 350 $GeV$, 350 - 1000 $GeV$, and above 1000 $GeV$). $R$ is determined in each cell of the binned 3-D space of $\boldsymbol{x}$ at ME-level due to the limitation of the **`BHO`**.

With the EM gauge invariance requirement $\Delta g_1^{\gamma} = 0$, $R$ is expressed for the following scenarios as:

| Source | 25-75 | 75-150 | 150-250 | 250-350 | 350-1000 |
|---|---|---|---|---|---|
| *Pile-up* | 1.77% | 1.40% | 1.64% | -0.93% | 2.59% |
| $\mu$-trigger Efficiency SF | -0.25% | -0.09% | -0.06% | -0.06% | -0.03% |
| $e$-trigger Efficiency SF | -0.26% | -0.20% | -0.26% | -0.27% | -0.28% |
| $\mu$ MS Resolution | -0.02% | 0.12% | 0.16% | 1.86% | 0.22% |
| $\mu$ ID Resolution | -0.51% | -0.92% | -1.20% | -0.92% | -2.51% |
| $\mu$ Scale | 0.05% | 0.04% | 0.35% | 0.00% | 0.00% |
| $\mu$ Isolation SF | -0.57% | -0.52% | -0.51% | -0.51% | -0.51% |
| $\mu$ Efficiency SF | -0.43% | -0.46% | -0.50% | -0.56% | -0.60% |
| $e$ Resolution | -0.02% | -0.10% | 0.14% | -2.37% | 0.00% |
| $e$ Scale ZeeAll | -0.24% | -0.89% | -1.10% | 0.04% | 0.00% |
| $e$ Scale R12Stat | -0.25% | 0.55% | 1.21% | 1.20% | 0.39% |
| $e$ Scale PSStat | -0.07% | 0.11% | 0.22% | 0.00% | 0.00% |
| $e$ Scale LowPt | -0.01% | 0.00% | 0.00% | 0.00% | 0.00% |
| $e$ Efficiency: eID | -0.85% | -0.97% | -1.05% | -1.04% | -0.97% |
| $e$ Efficiency: Track | -0.26% | -0.40% | -0.46% | -0.44% | -0.42% |
| $e$ Isolation SF | -0.22% | -0.19% | -0.18% | -0.18% | -0.17% |
| $\not{E}_T$ Reso Soft Terms | -0.28% | -0.25% | -0.18% | 1.18% | -4.32% |
| $\not{E}_T$ Scale Soft Terms | -2.41% | -2.07% | -0.94% | 0.41% | 2.13% |
| $p_T$ Reso Soft Terms | -0.03% | -0.13% | 0.18% | -0.97% | 0.00% |
| $p_T$ Scale Soft Terms | -0.33% | -0.36% | -0.04% | 0.00% | 0.00% |
| JVF | 0.22% | 0.23% | 0.25% | 0.16% | 0.00% |
| JER | -1.37% | -1.14% | -0.40% | -1.48% | 0.59% |
| JES Effective NP1 | -0.77% | -0.96% | -0.84% | -2.77% | -1.22% |
| JES Effective NP2 | 1.37% | 1.50% | 2.04% | 1.91% | 3.05% |
| JES Effective NP3 | -0.59% | -0.70% | -0.58% | -1.08% | 0.00% |
| JES Effective NP4 | -0.23% | -0.26% | -0.15% | -0.49% | 0.00% |
| JES Effective NP5 | -0.27% | -0.34% | -0.25% | -0.49% | 0.00% |
| JES Effective NP6+RestTerm | -0.11% | -0.14% | -0.12% | -0.49% | 0.00% |
| JES Eta Intercalibration Modelling | 1.56% | 1.71% | 2.15% | 1.49% | 3.59% |
| JES Eta Intercalibration StatAndMethod | -0.39% | -0.49% | -0.36% | -0.64% | 0.00% |
| JES SingleParticle HighPt | 0.00% | 0.00% | 0.00% | 0.00% | 0.00% |
| JES Relative Non Closure | 0.00% | 0.00% | 0.00% | 0.00% | 0.00% |
| JES $N_{PV}$ Offset | -0.51% | -0.83% | -0.65% | -2.27% | 0.00% |
| JES $\langle\mu\rangle$ Offset | -0.24% | -0.38% | -0.39% | -0.94% | 0.00% |
| JES *Pile-up* Pt | -0.01% | -0.01% | 0.00% | 0.00% | 0.00% |
| JES *Pile-up* Rho | -1.05% | -1.24% | -1.18% | -2.77% | -1.22% |
| JES Closeby | 0.00% | 0.00% | 0.00% | 0.00% | 0.00% |
| JES Flavour Composition | 1.81% | 2.07% | 2.53% | 1.91% | 3.05% |
| JES Flavour Response | 1.07% | 1.14% | 1.38% | 1.07% | 3.05% |
| JES B Scale | -0.01% | -0.01% | 0.00% | 0.00% | 0.00% |
| EW Corr Err(qq only) | -0.01% | -0.41% | -1.67% | -3.95% | -7.08% |
| PDF (qq only) | 3% | 3% | 3% | 5% | 10% |
| PDF (gg only) | 10% | 10% | 10% | 10% | 10% |
| Scale (qq only) | 5% | 5% | 5% | 5% | 5% |
| Scale (gg only) | 20% | 20% | 20% | 20% | 20% |
| Parton Shower (qq only) | 5% | 5% | 0% | 0% | 0% |
| Generator (qq only) | 5% | 15% | 20% | 20% | 20% |
| Parton Shower+Generator (gg only) | 40% | 50% | 50% | 80% | 80% |

Table 11.5: Systematic uncertainties on $WW$ signal ($qq \to WW$) and $WW$ background ($gg \to WW$) events in $p_T^{\ell_1}$ ($GeV$) bins for the $e\mu$ channel. The sign is kept to conserve bin-by-bin correlations.

| Source | 25-75 | 75-150 | 150-250 | 250-350 | 350-1000 |
|---|---|---|---|---|---|
| *Pile-up* | 0.20% | 2.38% | -4.12% | 1.03% | -1.79% |
| $\mu$-trigger Efficiency SF | 0.45% | 0.12% | 0.05% | 0.02% | 0.03% |
| $e$-trigger Efficiency SF | 0.36% | 0.27% | 0.32% | 0.14% | 0.10% |
| $\mu$ MS Resolution | -1.07% | 0.75% | 0.96% | 0.00% | 0.00% |
| $\mu$ ID Resolution | -0.41% | 0.40% | -2.15% | 42.77% | 0.00% |
| $\mu$ Scale | 0.21% | 0.05% | 0.00% | 0.00% | 0.00% |
| $\mu$ Isolation SF | 0.60% | 0.53% | 0.51% | 0.50% | 0.50% |
| $\mu$ Efficiency SF | 0.42% | 0.45% | 0.51% | 0.52% | 0.41% |
| $e$ Resolution | -0.17% | 0.04% | -1.87% | 56.13% | 0.00% |
| $e$ Scale ZeeAll | 0.47% | -0.22% | 2.69% | 0.00% | 0.00% |
| $e$ Scale R12Stat | 0.65% | -2.69% | 1.15% | 0.00% | -88.37% |
| $e$ Scale PSStat | 0.03% | -0.38% | 0.00% | 0.00% | 0.00% |
| $e$ Scale LowPt | 0.08% | 0.00% | 0.00% | 0.00% | 0.00% |
| $e$ Efficiency: eID | 1.27% | 1.33% | 1.27% | 0.94% | 1.00% |
| $e$ Efficiency: Track | 0.34% | 0.55% | 0.53% | 0.38% | 0.46% |
| $e$ Isolation SF | 0.27% | 0.23% | 0.22% | 0.14% | 0.14% |
| $\not{E}_T$ Reso Soft Terms | 0.09% | 1.73% | 8.03% | -0.73% | 0.00% |
| $\not{E}_T$ Scale Soft Terms | 3.08% | 0.88% | 16.13% | 0.00% | 0.00% |
| $p_T$ Reso Soft Terms | 0.64% | -0.24% | 1.86% | 49.14% | 0.00% |
| $p_T$ Scale Soft Terms | 0.04% | 0.16% | 0.00% | 0.00% | 0.00% |
| JVF | 0.15% | 1.02% | 0.00% | 0.00% | 0.00% |
| JER | 0.52% | 2.31% | 32.08% | -14.21% | 0.00% |
| JES Effective NP1 | 1.10% | 1.35% | 5.22% | 0.23% | 0.00% |
| JES Effective NP2 | 1.84% | 2.01% | 17.31% | 0.23% | 0.00% |
| JES Effective NP3 | 0.74% | 1.20% | 5.55% | 0.23% | 0.00% |
| JES Effective NP4 | 0.43% | 0.34% | 5.55% | 0.00% | 0.00% |
| JES Effective NP5 | 0.43% | 1.10% | 5.55% | 0.00% | 0.00% |
| JES Effective NP6+RestTerm | 0.36% | 0.02% | 5.55% | 0.00% | 0.00% |
| JES Eta Intercalibration Modelling | 2.54% | 2.70% | 15.14% | 0.23% | 0.00% |
| JES Eta Intercalibration StatAndMethod | 0.68% | 0.36% | 5.55% | 0.23% | 0.00% |
| JES SingleParticle HighPt | 0.00% | 0.00% | 0.00% | 0.00% | 0.00% |
| JES Relative Non Closure | 0.00% | 0.00% | 0.00% | 0.00% | 0.00% |
| JES $N_{PV}$ Offset | 0.88% | 2.01% | 11.76% | 0.23% | 0.00% |
| JES $\langle\mu\rangle$ Offset | 0.30% | 0.87% | 0.00% | 0.23% | 0.00% |
| JES *Pile-up* Pt | 0.00% | 0.00% | 0.00% | 0.00% | 0.00% |
| JES *Pile-up* Rho | 1.42% | 1.80% | 17.31% | 0.23% | 0.00% |
| JES Closeby | 0.00% | 0.00% | 0.00% | 0.00% | 0.00% |
| JES Flavour Composition | 2.34% | 2.81% | 31.38% | 0.23% | 0.00% |
| JES Flavour Response | 1.45% | 1.54% | 17.31% | 0.23% | 0.00% |
| JES B Scale | 0.00% | 0.00% | 0.00% | 0.00% | 0.00% |

Table 11.6: Systematic uncertainties on di-boson background events in $p_T^{\ell_1}$ $(GeV)$ bins for the $e\mu$ channel. The sign is kept to conserve bin-by-bin correlations.

***No Constraint*** **scenario:**

$$
\begin{aligned}
R(\boldsymbol{x};\Delta\kappa^Z,\lambda^Z,\Delta g_1^Z,\Delta\kappa^\gamma,\lambda^\gamma) = 1 &+ A_0(\boldsymbol{x})\Delta\kappa^Z + B_0(\boldsymbol{x})(\Delta\kappa^Z)^2 + C_0(\boldsymbol{x})\lambda^Z + D_0(\boldsymbol{x})(\lambda^Z)^2 \\
&+ E_0(\boldsymbol{x})\Delta g_1^Z + F_0(\boldsymbol{x})(\Delta g_1^Z)^2 + G_0(\boldsymbol{x})\Delta\kappa^\gamma + H_0(\boldsymbol{x})(\Delta\kappa^\gamma)^2 \\
&+ I_0(\boldsymbol{x})\lambda^\gamma + J_0(\boldsymbol{x})(\lambda^\gamma)^2 \\
&+ K_0(\boldsymbol{x})\Delta\kappa^Z\lambda^Z + L_0(\boldsymbol{x})\Delta\kappa^Z\Delta g_1^Z + M_0(\boldsymbol{x})\Delta\kappa^Z\Delta\kappa^\gamma \\
&+ N_0(\boldsymbol{x})\Delta\kappa^Z\lambda^\gamma + O_0(\boldsymbol{x})\lambda^Z\Delta g_1^Z + P_0(\boldsymbol{x})\lambda^Z\Delta\kappa^\gamma \\
&+ Q_0(\boldsymbol{x})\lambda^Z\lambda^\gamma + R_0(\boldsymbol{x})\Delta g_1^Z\Delta\kappa^\gamma + S_0(\boldsymbol{x})\Delta g_1^Z\lambda^\gamma + T_0(\boldsymbol{x})\Delta\kappa^\gamma\lambda^\gamma
\end{aligned} \tag{11.28}
$$

***LEP*** **scenario:**

$$
\begin{aligned}
R(\boldsymbol{x};\Delta\kappa^Z,\lambda,\Delta g_1^Z) = 1 &+ A_1(\boldsymbol{x})\Delta\kappa^Z + B_1(\boldsymbol{x})(\Delta\kappa^Z)^2 + C_1(\boldsymbol{x})\lambda \\
&+ D_1(\boldsymbol{x})(\lambda)^2 + E_1(\boldsymbol{x})\Delta g_1^Z + F_1(\boldsymbol{x})(\Delta g_1^Z)^2 \\
&+ G_1(\boldsymbol{x})\Delta\kappa^Z\lambda + H_1(\boldsymbol{x})\Delta\kappa^Z\Delta g_1^Z + I_1(\boldsymbol{x})\lambda\Delta g_1^Z
\end{aligned} \tag{11.29}
$$

***Equal Couplings*** **scenario:**

$$
R(\boldsymbol{x};\Delta\kappa,\lambda) = 1 + A_2(\boldsymbol{x})\Delta\kappa + B_2(\boldsymbol{x})(\Delta\kappa)^2 + C_2(\boldsymbol{x})\lambda + D_2(\boldsymbol{x})(\lambda)^2 + E_2(\boldsymbol{x})\Delta\kappa\lambda \tag{11.30}
$$

***HISZ*** **scenario:**

$$
R(\boldsymbol{x};\Delta\kappa,\lambda) = 1 + A_3(\boldsymbol{x})\Delta\kappa + B_3(\boldsymbol{x})(\Delta\kappa)^2 + C_3(\boldsymbol{x})\lambda + D_3(\boldsymbol{x})(\lambda)^2 + E_3(\boldsymbol{x})\Delta\kappa\lambda \tag{11.31}
$$

#### 11.4.3.2 Re-weighting Function Coefficients

The re-weighting coefficients ($A_i, B_i, C_i, \ldots$) can be evaluated by constructing linear equations with a number of selected aTGC points. For instance, for *HISZ* scenario, which has 2 free parameters and 5 coefficients, 5 aTGC points (Table 11.7) are selected. The linear equations to solve the 5 coefficients are listed in Equation 11.32.

$$
\begin{aligned}
R1 &= 1 + C|\lambda| + D|\lambda|^2 \\
R2 &= 1 - C|\lambda| + D|\lambda|^2 \\
R3 &= 1 + A|\Delta\kappa| + B|\Delta\kappa|^2 \\
R4 &= 1 - A|\Delta\kappa| + B|\Delta\kappa|^2 \\
R5 &= 1 + A|\Delta\kappa| + B|\Delta\kappa|^2 + C|\lambda| + D|\lambda|^2 + E|\Delta\kappa\lambda|
\end{aligned}
\tag{11.32}
$$

The re-weighting coefficients for *No Constraint*, *LEP* and *Equal Couplings* scenarios are extracted in a similar way. Table 11.8 and 11.9 list the aTGC points selected to solve the re-weighting coefficients for *No Constraint* and *LEP* scenarios, respectively. The *Equal Couplings* scenario uses the same aTGC points in Table 11.7.

| re-weighting ratio | $R1$ | $R2$ | $R3$ | $R4$ | $R5$ |
|---|---|---|---|---|---|
| $\Delta\kappa$ | 0 | 0 | +0.5 | -0.5 | +0.5 |
| $\lambda$ | +0.4 | -0.4 | 0 | 0 | +0.4 |

Table 11.7: The 5 aTGC points selected to calculate the re-weighting coefficients for the *HISZ* and *Equal Couplings* scenario. $R1$ - $R5$ are obtained from Equation 11.25a.

| Re-weighting ratio | $R1$ | $R2$ | $R3$ | $R4$ | $R5$ | $R6$ | $R7$ | $R8$ | $R9$ | $R10$ |
|---|---|---|---|---|---|---|---|---|---|---|
| $\Delta\kappa^Z$ | +0.5 | -0.5 | 0 | 0 | 0 | 0 | 0 | 0 | 0 | 0 |
| $\lambda^Z$ | 0 | 0 | +0.4 | -0.4 | 0 | 0 | 0 | 0 | 0 | 0 |
| $\Delta g_1^Z$ | 0 | 0 | 0 | 0 | +0.5 | -0.5 | 0 | 0 | 0 | 0 |
| $\Delta\kappa^\gamma$ | 0 | 0 | 0 | 0 | 0 | 0 | +0.5 | -0.5 | 0 | 0 |
| $\lambda^\gamma$ | 0 | 0 | 0 | 0 | 0 | 0 | 0 | 0 | +0.4 | -0.4 |
| Re-weighting ratio | $R11$ | $R12$ | $R13$ | $R14$ | $R15$ | $R16$ | $R17$ | $R18$ | $R19$ | $R20$ |
| $\Delta\kappa^Z$ | +0.5 | +0.5 | +0.5 | +0.5 | 0 | 0 | 0 | 0 | 0 | 0 |
| $\lambda^Z$ | +0.4 | 0 | 0 | 0 | +0.4 | +0.4 | +0.4 | 0 | 0 | 0 |
| $\Delta g_1^Z$ | 0 | +0.5 | 0 | 0 | +0.5 | 0 | 0 | +0.5 | +0.5 | 0 |
| $\Delta\kappa^\gamma$ | 0 | 0 | +0.5 | 0 | 0 | +0.5 | 0 | +0.5 | 0 | +0.5 |
| $\lambda^\gamma$ | 0 | 0 | 0 | +0.4 | 0 | 0 | +0.4 | 0 | +0.4 | +0.4 |

Table 11.8: The 20 aTGC points selected to calculate the re-weighting coefficients for the *No Constraint* scenario. $R1$ - $R20$ are obtained from Equation 11.25a.

The re-weighting coefficients are calculated and stored for various form factors. It is straightforward to re-weight SM to any given aTGC point in the following steps: first, use the ME-level variables ($p_T^{\ell+}, p_T^{\ell-}, \not{E}_T^{rel}$) of an SM event to locate the 3-D space cell for the calculation of $R$ using Equations 11.28 - 11.31; then obtain the event weight

| Re-weighting ratio | $R1$ | $R2$ | $R3$ | $R4$ | $R5$ | $R6$ | $R7$ | $R8$ | $R9$ |
|---|---|---|---|---|---|---|---|---|---|
| $\Delta\kappa^Z$ | 0 | 0 | +0.5 | -0.5 | 0 | 0 | +0.5 | +0.5 | 0 |
| $\lambda$ | +0.4 | -0.4 | 0 | 0 | 0 | 0 | +0.4 | 0 | +0.4 |
| $\Delta g_1^Z$ | 0 | 0 | 0 | 0 | +0.5 | -0.5 | 0 | +0.5 | +0.5 |

Table 11.9: The 9 aTGC points selected to calculate the re-weighting coefficients for the *LEP* scenario. $R1$ - $R9$ are obtained from 11.25a.

for the given aTGCs by scaling the SM event weight with $R$. Note that, both ME- and reconstruction-level aTGC weights could be scaled from corresponding SM weights.

#### 11.4.3.3 Method Validations

To validate the 3-D re-weighting method, a set of kinematic distributions are compared between two sets of samples: the sample directly generated by **BHO** with aTGCs $\boldsymbol{\mu}$, and the sample re-weighted from SM to $\boldsymbol{\mu}$. Figures 11.3 and 11.4 show the $p_T^{\ell_1}$ distribution comparisons for various form factor $\Lambda$'s, with each scenario tested at different $\boldsymbol{\mu}$'s. The ratio plots shows self-consistency between directly generated aTGC points and SM re-weighted aTGC points for the 3-D parameterization in both full region and fiducial region.

While Equation 11.22 matches the coefficients $F^{ij}$ with **MC@NLO** built-in coupling weights very easily, the 3-D re-weighting method has to re-write its re-weighting formula from the form of 11.28 - 11.31 to the form of 11.25c accordingly. With 3-D parameterization, the re-weighting coefficients, as expressed by Equation 11.25b, could be obtained from **BHO** samples. To extract aTGC limits, `TGClim` program is used as well, with the same inputs as used in **MC@NLO** re-weighting methods except that the weights $w_0 \ldots w_{27}$, as expressed by Equation 11.25c, are not directly obtained from MC samples. Instead, they are converted by matching the coefficients for the same terms between Equation 11.25b and Equation 11.25c. In addition, for the purpose of suppressing statistical uncertainty in high-$p_T$ tail, the SM samples used for obtaining $w_0 \ldots w_{27}$ are not the directly generated one but are re-weighted from official aTGC samples, as in the case of **MC@NLO** re-weighting method. Table 11.10 lists the values of $w_0$ to $w_{27}$ obtained by the 3-D re-weighting method.

The SM samples used in the $w_0 \ldots w_{27}$ obtaining process are generated by **MC@NLO**, but the 3-D re-weighting coefficients are obtained from **BHO** generators. Therefore, it is important to check systematics from generator and **MC@NLO** self-reweighting. Figure 11.2 shows the $p_T^{\ell_1}$ distributions of different samples: the **BHO** SM sample, the high-statistics private **MC@NLO** SM sample, the official **MC@NLO** SM sample, the official

| $p_T^{\ell_1}$ (*GeV*) | 25-75 | 75-150 | 150-250 | 250-350 | 350-1000 |
|---|---|---|---|---|---|
| w0 | 2538.3511 | 580.6191 | 51.445 | 5.6007 | 1.1535 |
| w1 | 438.7857 | 585.6293 | 186.8445 | 43.9679 | 17.5143 |
| w2 | 2009.4443 | 7581.5474 | 5102.6034 | 1740.2584 | 1571.7922 |
| w3 | 3529.9578 | 21974.0164 | 15592.2389 | 6218.4736 | 5982.2154 |
| w4 | 0.0 | 0.0 | 0.0 | 0.0 | 0.0 |
| w5 | 342.9773 | 1490.3728 | 1019.4451 | 365.7732 | 366.6754 |
| w6 | 605.5428 | 4595.4982 | 3195.7329 | 1349.0118 | 1405.2140 |
| w7 | -10.8687 | -51.9752 | -6.6127 | -0.6348 | -0.1442 |
| w8 | -109.7604 | -222.0659 | -82.0642 | -12.9207 | -5.7168 |
| w9 | 88.2762 | 44.2816 | 19.2476 | 6.5967 | 7.7261 |
| w10 | 0.0 | 0.0 | 0.0 | 0.0 | 0.0 |
| w11 | -62.8050 | -106.2525 | -28.6680 | -7.2586 | -2.8779 |
| w12 | 10.8429 | 0.6799 | 3.5192 | -0.4431 | -0.8750 |
| w13 | 518.9738 | 720.5728 | 250.3745 | 62.9968 | 21.8032 |
| w14 | 637.9142 | 1332.0004 | 583.0990 | 115.5862 | 73.0757 |
| w15 | 0.0 | 0.0 | 0.0 | 0.0 | 0.0 |
| w16 | 80.9198 | 124.2226 | 47.7282 | 10.0910 | 6.3010 |
| w17 | 86.3953 | 181.3338 | 97.9049 | 24.7559 | 13.1611 |
| w18 | -48.3678 | -1083.4457 | -945.4161 | -128.7162 | -221.3528 |
| w19 | 0.0 | 0.0 | 0.0 | 0.0 | 0.0 |
| w20 | 347.0208 | 1262.6487 | 867.2372 | 307.0715 | 269.7145 |
| w21 | -13.1664 | -204.4220 | -223.3802 | -17.1787 | -51.1335 |
| w22 | 0.0 | 0.0 | 0.0 | 0.0 | 0.0 |
| w23 | -23.6429 | -73.3355 | -206.0210 | -16.6122 | -44.7209 |
| w24 | 614.0918 | 3731.3580 | 2846.1827 | 1064.5826 | 1083.9520 |
| w25 | 0.0 | 0.0 | 0.0 | 0.0 | 0.0 |
| w26 | 0.0 | 0.0 | 0.0 | 0.0 | 0.0 |
| w27 | -10.3011 | -219.1901 | -188.0310 | -32.4251 | -70.9133 |

Table 11.10: Signal anomalous coupling parameterization for *No Constraint* scenario using 3-D re-weighting method. The parameterization is given in bins of $p_T^{\ell_1}$ in the $e\mu$ channel only. The original $w_0$ obtained by this method is scaled bin by bin to be the $w_0$ in Table 11.2, and $w_1$ to $w_{27}$ are scaled by the factor of the ratio between them and the original $w_0$. Some rows are manually set to be 0 because they are converted from coefficients of the terms containing $g_1^\gamma$, while **BHO** generator has no parameterization for $\Delta g_1^\gamma$ (it assumes $\Delta g_1^\gamma = 0$). EW corrections are applied.

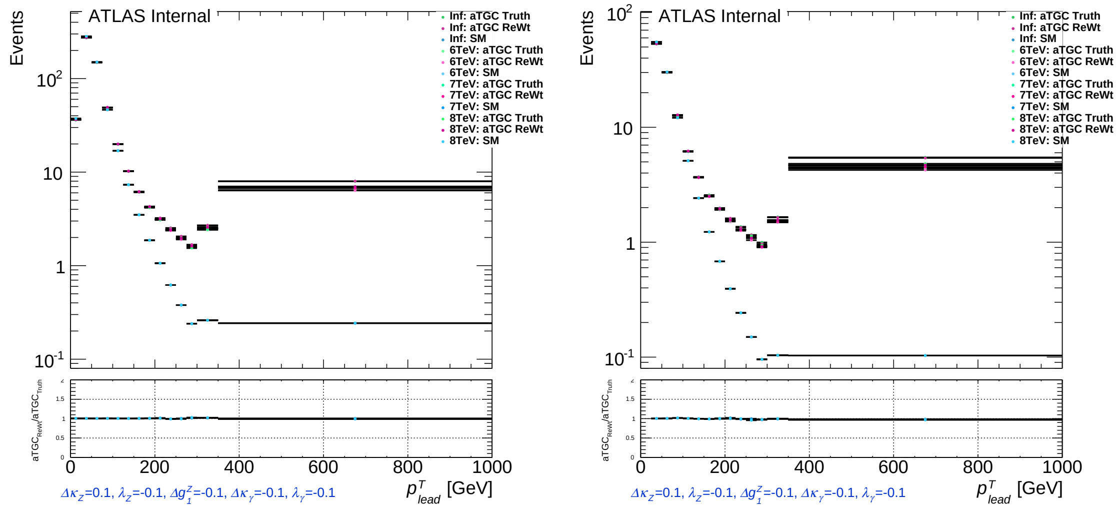


(a) *No Constraint* Scenario

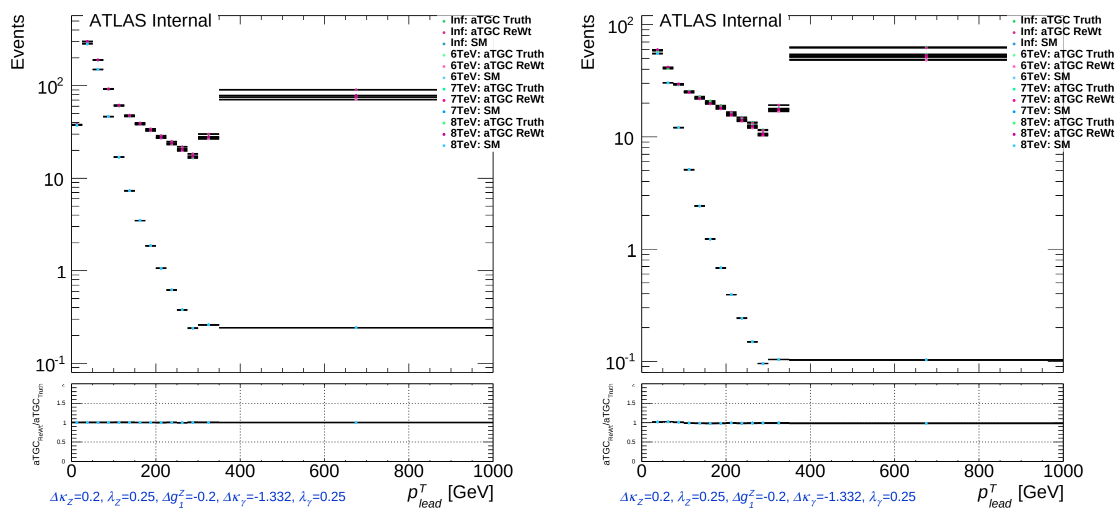


(b) *LEP* Scenario

Figure 11.3: Comparison of **BHO** ME-level $p_T^{\ell_1}$ distributions between directly generated events and self-reweighted events from SM (1). The plots on the left and right are in full and fiducial region, respectively. The ratio plots are between re-weighted plots and truth (directly generated) plots.

Powheg SM sample, the SM sample re-weighted from high-statistics private aTGC sample, and the SM sample re-weighted from official aTGC sample. The SM sample re-weighted from high-statistics private aTGC sample was skimmed, therefore the comparison with it is only available in fiducial region. From Figure 11.2, the generator systematics and **MC@NLO** self re-weighting systematics are observed to be at the same level if taking the official Powheg SM sample as benchmark (about 20% for the last bin).

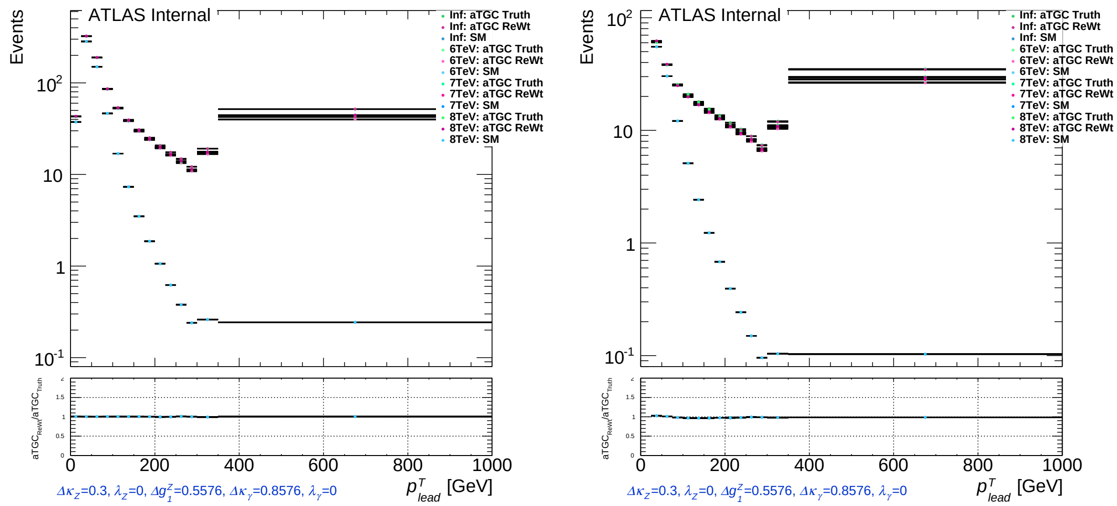


(a) *HISZ* Scenario

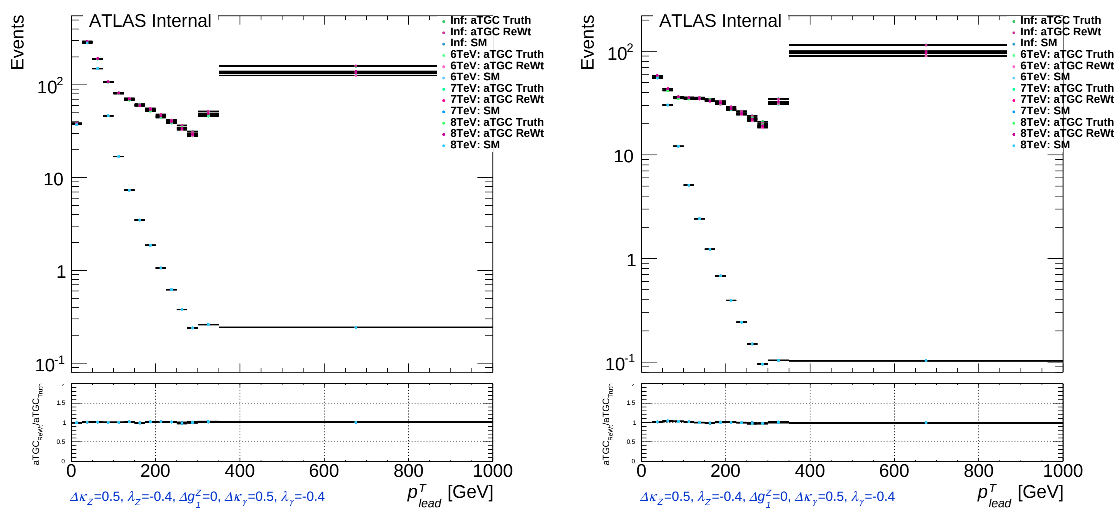


(b) *Equal Couplings* Scenario

Figure 11.4: Comparison of **BHO** ME-level $p_T^{\ell_1}$ distributions between directly generated events and self-reweighted events from SM (2). The plots on the left and right are in full and fiducial region, respectively. The ratio plots are between re-weighted plots and truth (directly generated) plots.

## 11.5 Results of aTGC Limits

The results of aTGC limit setting using the frequentist method are shown here. The baseline method is using **MC@NLO** for event re-weighting. The **BHO** re-weighting is an supporting method for cross checks, therefore only the *No Constraint* scenario results with infinite form factor is presented for comparison. Both methods use the same optimization, as well as the same statistical and systematic uncertainty ($\boldsymbol{\theta}$) input, with only the parameterization input different (see Table 11.2 and Table 11.10). The results of both methods show agreement within generator and parton shower uncertainties.

### 11.5.1 MC@NLO Parameterization Results

The results using **MC@NLO** re-weighting are fitted for $e\mu$ channel with the last 3 bins of $p_T^{\ell_1}$ (see Section 11.3.3) using the frequentist method. Table 11.11 gives the 1-D expected and observed 95% CL limits on aTGCs with infinite form factor applied, for the *No Constraint*, *LEP*, *HISZ*, and *Equal Couplings* scenarios.

| Scenario | Parameter | Expected | Observed |
|---|---|---|---|
| *No Constraint* | $\Delta g_1^Z$ | [-0.498,0.524] | [-0.215,0.267] |
| | $\Delta\kappa^Z$ | [-0.053,0.059] | [-0.027,0.042] |
| | $\lambda^Z$ | [-0.039,0.038] | [-0.024,0.024] |
| | $\Delta\kappa^\gamma$ | [-0.109,0.124] | [-0.054,0.092] |
| | $\lambda^\gamma$ | [-0.081,0.082] | [-0.051,0.052] |
| *LEP* | $\Delta g_1^Z$ | [-0.033,0.037] | [-0.016,0.027] |
| | $\Delta\kappa^Z$ | [-0.037,0.035] | [-0.025,0.020] |
| | $\lambda^Z$ | [-0.031,0.031] | [-0.019,0.019] |
| *HISZ* | $\Delta\kappa^Z$ | [-0.026,0.030] | [-0.012,0.022] |
| | $\lambda^Z$ | [-0.031,0.031] | [-0.019,0.019] |
| *Equal Couplings* | $\Delta\kappa^Z$ | [-0.041,0.048] | [-0.020,0.035] |
| | $\lambda^Z$ | [-0.030,0.030] | [-0.019,0.019] |
| EFT | $\frac{c_{WWW}}{\Lambda^2}$ | [-7.62,7.38] | [-4.61,4.60] |
| | $\frac{c_B}{\Lambda^2}$ | [-35.8,38.4] | [-20.9,26.3] |
| | $\frac{c_W}{\Lambda^2}$ | [-12.58,14.32] | [-5.87,10.54] |

Table 11.11: 95% CL expected and observed limits on aTGCs for *No Constraint*, *LEP*, *HISZ*, and *Equal Couplings* scenarios with $p_T^{\ell_1}$ bins of [150,250,350,1000] *GeV* in the $e\mu$ channel. The results are shown with $\Lambda = \infty$ for scenarios under the aTGCs framework. EW corrections have been applied to the SM only term.

Table 11.12 shows the limits on aTGCs with a 7 *TeV* form factor. 7 *TeV* is the upper bound to preserve unitarity for most aTGCs, the limits set with which represent the best estimates preserving the unitarity. Expected and observed limits with additional form factors are given in Tables 11.13, 11.14 and Figure 11.5.

Figure 11.6 shows the $p_T^{\ell_1}$ distributions re-weighted from SM to the best fit aTGCs

| Scenario | Parameter | Expected | Observed |
|---|---|---|---|
| *No Constraint* | $\Delta g_1^Z$ | [-0.519,0.563] | [-0.226,0.279] |
| | $\Delta\kappa^Z$ | [-0.057,0.064] | [-0.028,0.045] |
| | $\lambda^Z$ | [-0.043,0.042] | [-0.026,0.025] |
| | $\Delta\kappa^\gamma$ | [-0.118,0.136] | [-0.057,0.099] |
| | $\lambda^\gamma$ | [-0.088,0.089] | [-0.055,0.055] |
| *LEP* | $\Delta g_1^Z$ | [-0.035,0.041] | [-0.017,0.029] |
| | $\Delta\kappa^Z$ | [-0.041,0.038] | [-0.027,0.021] |
| | $\lambda^Z$ | [-0.033,0.033] | [-0.020,0.020] |
| *HISZ* | $\Delta\kappa^Z$ | [-0.028,0.033] | [-0.013,0.024] |
| | $\lambda^Z$ | [-0.033,0.034] | [-0.020,0.020] |
| *Equal Couplings* | $\Delta\kappa^Z$ | [-0.045,0.052] | [-0.021,0.037] |
| | $\lambda^Z$ | [-0.034,0.033] | [-0.020,0.020] |

Table 11.12: 95% CL expected and observed limits on aTGCs for *No Constraint*, *LEP*, *HISZ*, and *Equal Couplings* scenarios with $p_T^{\ell_1}$ bins of [150,250,350,1000] *GeV* in the $e\mu$ channel. The results are shown with $\Lambda = 7$ *TeV* for scenarios under the aTGCs framework. EW corrections have been applied to the SM only term.

| FF (*TeV*) | $\Delta g_1^Z$ | | $\Delta\kappa^Z$ | | $\lambda^Z$ | | $\Delta\kappa^\gamma$ | | $\lambda^\gamma$ | |
|---|---|---|---|---|---|---|---|---|---|---|
| 2 | -0.728 | 0.836 | -0.100 | 0.115 | -0.076 | 0.076 | -0.213 | 0.247 | -0.158 | 0.159 |
| 3 | -0.615 | 0.686 | -0.074 | 0.085 | -0.057 | 0.055 | -0.156 | 0.182 | -0.117 | 0.115 |
| 4 | -0.561 | 0.617 | -0.066 | 0.074 | -0.049 | 0.048 | -0.136 | 0.157 | -0.101 | 0.102 |
| 5 | -0.540 | 0.580 | -0.061 | 0.069 | -0.046 | 0.045 | -0.126 | 0.147 | -0.096 | 0.093 |
| 6 | -0.535 | 0.575 | -0.059 | 0.066 | -0.044 | 0.043 | -0.122 | 0.140 | -0.091 | 0.089 |
| 7 | -0.519 | 0.563 | -0.057 | 0.064 | -0.043 | 0.042 | -0.118 | 0.136 | -0.088 | 0.089 |
| 8 | -0.515 | 0.541 | -0.056 | 0.063 | -0.042 | 0.041 | -0.118 | 0.132 | -0.084 | 0.084 |
| 10 | -0.503 | 0.535 | -0.055 | 0.061 | -0.041 | 0.041 | -0.113 | 0.131 | -0.084 | 0.084 |
| 100 | -0.498 | 0.524 | -0.053 | 0.059 | -0.039 | 0.038 | -0.109 | 0.124 | -0.081 | 0.082 |

Table 11.13: 95% CL expected limits on aTGCs for *No Constraint* scenario with $p_T^{\ell_1}$ bins of [150,250,350,1000] *GeV* in the $e\mu$ channel under different form factors (FF). Here, $\Lambda = 100$ *TeV* is so high that it can be considered as $\Lambda = \infty$ or no form factor applied. EW corrections have been applied to the SM only term.

as well as the upper and lower 95% confidence interval bounds. Observed data and SM distributions are also presented for comparison.

To obtain the 2-dimensional limits on aTGCs, two of the parameters are fitted with all others fixed to 0. As an example, the 2-D 95% CL contours for the *LEP* scenario is shown in Figure 11.7.

| FF ($TeV$) | $\Delta g_1^Z$ | | $\Delta\kappa^Z$ | | $\lambda^Z$ | | $\Delta\kappa^\gamma$ | | $\lambda^\gamma$ | |
|---|---|---|---|---|---|---|---|---|---|---|
| 2 | -0.298 | 0.390 | -0.042 | 0.070 | -0.038 | 0.039 | -0.083 | 0.157 | -0.083 | 0.085 |
| 3 | -0.247 | 0.328 | -0.034 | 0.056 | -0.031 | 0.031 | -0.068 | 0.121 | -0.066 | 0.065 |
| 4 | -0.237 | 0.295 | -0.031 | 0.050 | -0.028 | 0.028 | -0.063 | 0.110 | -0.060 | 0.061 |
| 5 | -0.232 | 0.285 | -0.029 | 0.048 | -0.027 | 0.027 | -0.059 | 0.105 | -0.057 | 0.058 |
| 6 | -0.228 | 0.283 | -0.028 | 0.046 | -0.026 | 0.026 | -0.058 | 0.101 | -0.055 | 0.056 |
| 7 | -0.226 | 0.279 | -0.028 | 0.045 | -0.026 | 0.025 | -0.057 | 0.099 | -0.055 | 0.055 |
| 8 | -0.219 | 0.276 | -0.027 | 0.044 | -0.025 | 0.025 | -0.056 | 0.098 | -0.054 | 0.054 |
| 10 | -0.215 | 0.274 | -0.027 | 0.044 | -0.025 | 0.025 | -0.056 | 0.094 | -0.052 | 0.054 |
| 100 | -0.215 | 0.267 | -0.027 | 0.042 | -0.024 | 0.024 | -0.054 | 0.092 | -0.051 | 0.052 |

Table 11.14: 95% CL observed limits on aTGCs for *No Constraint* scenario with $p_T^{\ell_1}$ bins of [150,250,350,1000] $GeV$ in the $e\mu$ channel under different form factors (FF). Here, $\Lambda$ = 100 $TeV$ is so high that it can be considered as $\Lambda = \infty$ or no form factor applied. EW corrections have been applied to the SM only term.

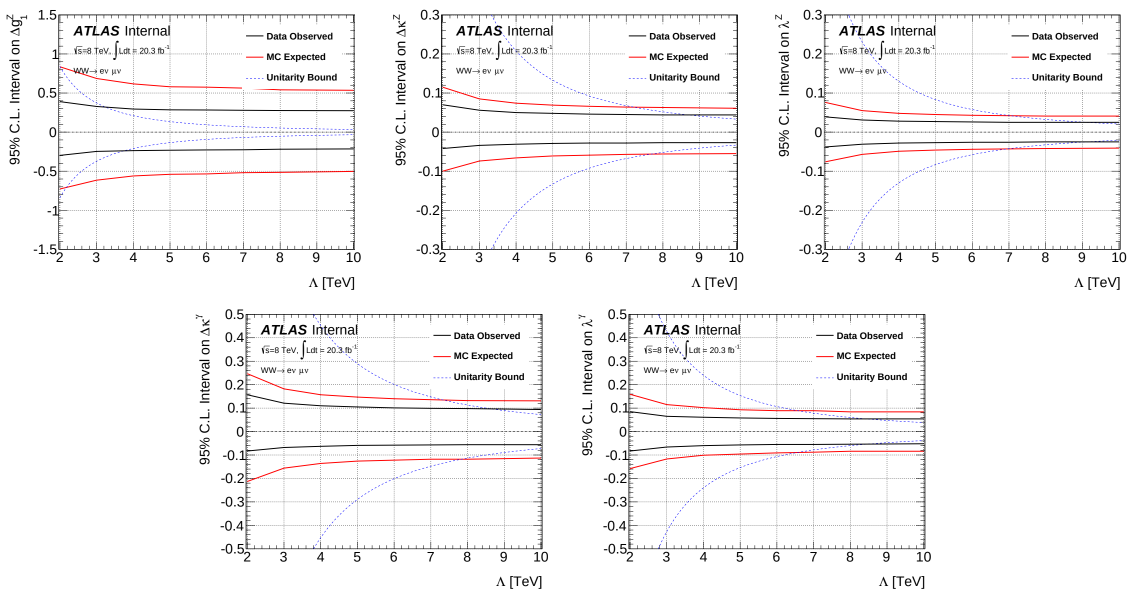


Figure 11.5: 95% CL limits with form factors with $\Lambda$ = 2 to $\Lambda$ = 10 $TeV$. The unitarity bounds (Equation 11.3) are given by the dashed blue lines.

### 11.5.2 BHO Parameterization Results

With the same process as described in Section 11.4.2, the 1-D expected and observed 95% CL limits on aTGCs with infinite form factor for the *No Constraint* scenario are presented in Table 11.15. The interval difference between Table 11.15 and Table 11.11 is presented in Table 11.16.

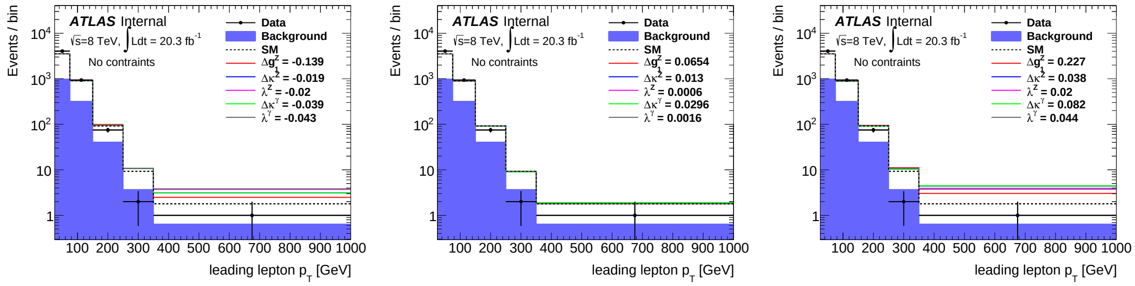


Figure 11.6: $p_T^{\ell_1}$ distributions in the $e\mu$ channel re-weighted from SM to the best fit aTGCs (middle) as well as the lower 95% bound (left) and the upper 95% bound (right). The values are obtained by fitting with the last 3 bins of $p_T^{\ell_1}$.

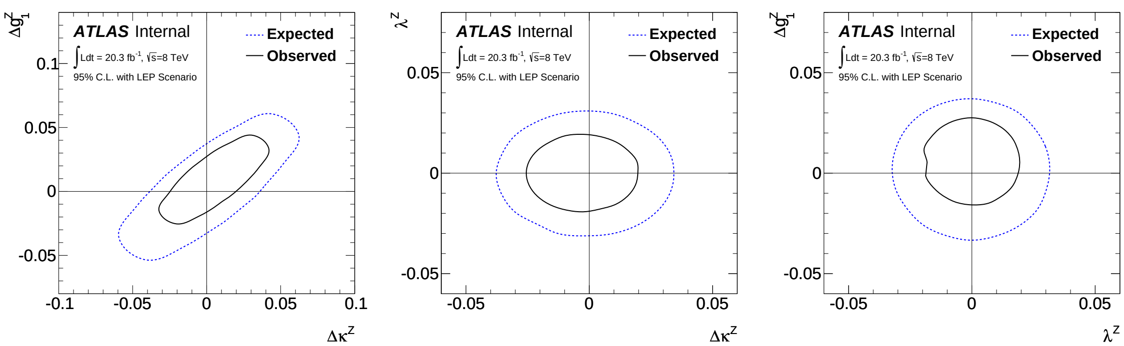


Figure 11.7: The two-dimensional 95% CL contours for the *LEP* scenario. The studied aTGCs are free with all others set to 0 during fitting.

| Scenario | Parameter | Expected | Observed |
|---|---|---|---|
| | $\Delta g_1^Z$ | [-0.504,0.533] | [-0.257,0.287] |
| | $\Delta\kappa^Z$ | [-0.059,0.065] | [-0.032,0.044] |
| *No Constraint* | $\lambda^Z$ | [-0.033,0.031] | [-0.021,0.019] |
| | $\Delta\kappa^\gamma$ | [-0.122,0.138] | [-0.067,0.095] |
| | $\lambda^\gamma$ | [-0.065,0.067] | [-0.042,0.043] |

Table 11.15: 95% CL expected and observed limits on aTGCs for *No Constraint* scenario with $p_T^{\ell_1}$ bins of [150,250,350,1000] *GeV* in the $e\mu$ channel. The results are obtained by the 3-D re-weighting methods with $\Lambda = \infty$. EW corrections have been applied to the SM only term.

| Scenario | Parameter | Expected | Observed |
|---|---|---|---|
| | $\Delta g_1^Z$ | 18.66% | 13.37% |
| | $\Delta\kappa^Z$ | 26.41% | 14.26% |
| *No Constraint* | $\lambda^Z$ | -8.15% | -16.27% |
| | $\Delta\kappa^\gamma$ | 25.84% | 14.77% |
| | $\lambda^\gamma$ | -9.93% | -16.26% |

Table 11.16: The interval difference between results obtained by **MC@NLO** re-weighting method in Table 11.11 and results obtained by 3-D re-weighting method in Table 11.15. Table 11.11 is used as the comparison basis.

## CHAPTER 12

# Summary

The $W^+W^-$ production cross section in $pp$ collisions at $\sqrt{s} = 8$ $TeV$ is measured using 20.3 $fb^{-1}$ of data collected by the ATLAS detector during 2012. The measurement is conducted using three $W^+W^-$ leptonic decay channels. A total of 6636 candidates is selected with an estimated background of 1547±325 events.

The measured total $W^+W^-$ production cross section is

$$\sigma(pp \to W^+W^-) = 71.0^{+1.1}_{-1.1}(\text{stat})^{+5.7}_{-5.0}(\text{syst})^{+2.1}_{-2.0}(\text{lumi})\ pb$$

This measured cross section is consistent with the SM prediction of 63.2 ± 2.0 $pb$ (the details of the calculations are given in Chapter 6). The difference between the measured cross section and the prediction is now $+1.1\sigma$, significantly reduced the discrepancies observed in previous measurements at 7 $TeV$ by both the ATLAS and CMS collaboration, where only the NLO calculation in theoretical prediction is used. This indicates that higher-order correction in theoretical calculations is important. It is necessary to point out here that the $W^+W^-$ production cross section through the gluon-fusion initial state has only been calculated at the leading order, which underestimates the $gg \to WW$ production rate significantly. This could account for that the measured cross section at 8 $TeV$ is still higher than the Standard Model prediction. Of course, the possibility for other possible new physics contributions could not be totally excluded. Therefore, the measurement of the $W^+W^-$ cross section at the LHC Run 2 at 13 $TeV$ remains a high-profile research topic.

The leading lepton $p_T$ distribution is used in the search for aTGC. Data is consistent with the couplings predicted by the SM. Therefore, the limits of anomalous couplings with different constraint scenarios are set at 95% C.L. in this analysis. The most stringent coupling parameter limit intervals are [-0.013,0.024] for $\Delta\kappa^Z$, and [-0.020,0.020] for $\lambda^Z$ at 95% CL for the *HISZ* scenario.

# BIBLIOGRAPHY


[1] ATLAS Collaboration, G. Aad et al., *Measurement of $W^+W^-$ production in pp collisions at $\sqrt{s}$=7 TeV with the ATLAS detector and limits on anomalous WWZ and WW$\gamma$ couplings*, Phys.Rev. **D87** no. 11, (2013) 112001, arXiv:1210.2979 [hep-ex].

[2] CMS Collaboration Collaboration, CMS Collaboration, *Measurement of the $W^+W^-$ cross section in pp collisions at $\sqrt{s}$ = 7 TeV and limits on anomalous $WW_\gamma$ and WWZ couplings*, Eur. Phys. J. C **73** no. arXiv:1306.1126. CMS-SMP-12-005. CERN-PH-EP-2013-075, (2013) 2610. 31 p, http://cds.cern.ch/record/1553554, Comments: Submitted to Eur. Phys. J. C.

[3] S. Weinberg, *The making of the standard model*. Springer, 2003.

[4] W. Pauli, *The connection between spin and statistics*, Physical Review **58** no. 8, (1940) 716.

[5] A. Bettini, *Charge conservation and symmetry*. UK: Cambridge University Press, 2008.

[6] P. Aurenche, *The Standard Model of particle physics*, Symmetries in Physics (1997) 169.

[7] K. Hagiwara, J. Woodside, and D. Zeppenfeld, *Measuring the WWZ coupling at the Fermilab Tevatron*, Physical Review D **41** no. 7, (1990) 2113.

[8] G. Azuelos, U. Baur, J. van der Bij, D. Bourilkov, O. Brein, R. Casalbuoni, A. Deandrea, S. De Curtis, D. De Florian, A. Denner, et al., *Electroweak physics*, arXiv preprint hep-ph/0003275v1 (2000).

[9] U. Baur and D. Zeppenfeld, *Unitarity constraints on the electroweak three vector boson vertices*, Physics Letters B **201** no. 3, (1988) 383–389.

[10] L. Evans and P. Bryant, *LHC machine*, Journal of Instrumentation **3** no. 08, (2008) S08001.

[11] R. Alemany-Fernandez, S. Redaelli, W. Venturini, M. Solfaroli Camillocci, A. Macpherson, L. Ponce, G. Papotti, J. Wenninger, A. Gorzawski, G. Roy, et al., *Operation and Configuration of the LHC in Run 1*, tech. rep., CERN, 2013.

[12] G. Aad, T. Abajyan, B. Abbott, J. Abdallah, S. A. Khalek, A. Abdelalim, O. Abdinov, R. Aben, B. Abi, M. Abolins, et al., *Improved luminosity determination in pp collisions at* $\sqrt{s} = 7$ *TeV using the ATLAS detector at the LHC*, The European Physical Journal C **73** no. 8, (2013) 1–39.

[13] G. Aad, E. Abat, J. Abdallah, A. Abdelalim, A. Abdesselam, O. Abdinov, B. Abi, M. Abolins, H. Abramowicz, E. Acerbi, et al., *The ATLAS experiment at the CERN large hadron collider*, Journal of Instrumentation **3** no. 08, (2008) S08003.

[14] L. Duguid, *Performance of the ATLAS Electron and Photon Trigger in pp Collisions at* $\sqrt{s} = 7$ *TeV in 2011*, tech. rep., ATL-COM-DAQ-2012-055, 2012.

[15] A. collaboration et al., *Performance of the ATLAS muon trigger in pp collisions at* $\sqrt{s} = 8$ *TeV*, arXiv preprint arXiv:1408.3179 (2014).

[16] *Recommended egamma trigger for 2012*, https://twiki.cern.ch/twiki/bin/viewauth/Atlas/TrigEgammaRecommendedTriggers2012.

[17] C. Anastopoulos, E. Benhar-Noccioli, A. Bocci, K. Brendlinger, F. Bhrer, M. Iconomidou-Fayard, L an Delmastro, O. Ducu, R. Fletcher, D. Froidevaux, T. Guillemin, S. Heim, F. Hubaut, M. Karnevskiy, J. Kretzschmar, J. Kroll, C. Lester, K. Lohwasser, J. B. Maurer, A. Morley, G. Pásztor, E. Richter-Was, A. Schaffer, T. Serre, P. Sommer, E. Tiouchichine, and H. Williams, *Supporting document on electron efficiency measurements using the 2012 LHC proton-proton collision data*, Tech. Rep. ATL-COM-PHYS-2013-1295, CERN, Geneva, Sep, 2013.

[18] D. Adams, R. Jones, D. Malon, D. Quarrie, S. Jarp, T. Wenaus, R. Hawkings, G. Poulard, D. Barberis, C. Bee, et al., *The ATLAS computing model*, tech. rep., CERN, 2004.

[19] ATLAS Collaboration, G. Duckeck et al., *ATLAS computing: Technical design report*,.

[20] H.-L. Lai, M. Guzzi, J. Huston, Z. Li, P. M. Nadolsky, J. Pumplin, and C.-P. Yuan, *New parton distributions for collider physics*, Phys. Rev. D **82** (2010) 074024, http://link.aps.org/doi/10.1103/PhysRevD.82.074024.

[21] A. Martin, W. Stirling, R. Thorne, and G. Watt, *Parton distributions for the LHC*, Eur.Phys.J. **C63** (2009) 189–285, arXiv:0901.0002 [hep-ph].

[22] R. D. Ball, V. Bertone, S. Carrazza, C. S. Deans, L. Del Debbio, et al., *Parton distributions with LHC data*, Nucl.Phys. **B867** (2013) 244–289, arXiv:1207.1303 [hep-ph].

[23] A. Buckley, J. Ferrando, S. Lloyd, K. Nordstrm, B. Page, et al., *LHAPDF6: parton density access in the LHC precision era*, Eur.Phys.J. **C75** no. 3, (2015) 132, arXiv:1412.7420 [hep-ph].

[24] T. A. Collaboration, *Determination of the Strange-Quark Density of the Proton from ATLAS Measurements of the $W \to \ell\nu$ and $Z \to \ell\ell$ Cross Sections*, Phys. Rev. Lett. **109** (2012) 012001, http://link.aps.org/doi/10.1103/PhysRevLett.109.012001.

[25] S. Alioli, P. Nason, C. Oleari, and E. Re, *A general framework for implementing NLO calculations in shower Monte Carlo programs: the POWHEG BOX*, JHEP **1006** (2010) 043, arXiv:1002.2581 [hep-ph].

[26] T. Binoth, M. Ciccolini, N. Kauer, and M. Kramer, *Gluon-induced W-boson pair production at the LHC*, JHEP **0612** (2006) 046, arXiv:hep-ph/0611170 [hep-ph].

[27] J. M. Campbell and R. K. Ellis, *An Update on vector boson pair production at hadron colliders*, Phys.Rev. **D60** (1999) 113006, arXiv:hep-ph/9905386 [hep-ph].

[28] M. L. Mangano, M. Moretti, F. Piccinini, R. Pittau, and A. D. Polosa, *ALPGEN, a generator for hard multiparton processes in hadronic collisions*, JHEP **0307** (2003) 001, arXiv:hep-ph/0206293 [hep-ph].

[29] S. Frixione and B. R. Webber, *Matching NLO QCD computations and parton shower simulations*, JHEP **0206** (2002) 029, arXiv:hep-ph/0204244 [hep-ph].

[30] B. P. Kersevan and E. Richter-Was, *The Monte Carlo event generator AcerMC versions 2.0 to 3.8 with interfaces to PYTHIA 6.4, HERWIG 6.5 and ARIADNE 4.1*, Comput.Phys.Commun. **184** (2013) 919–985, arXiv:hep-ph/0405247 [hep-ph].

[31] T. Gleisberg, S. Hoeche, F. Krauss, M. Schonherr, S. Schumann, et al., *Event generation with SHERPA 1.1*, JHEP **0902** (2009) 007, arXiv:0811.4622 [hep-ph].

[32] U. Baur, T. Han, and J. Ohnemus, *QCD corrections and nonstandard three vector boson couplings in $W^+W^-$ production at hadron colliders*, Phys.Rev. **D53** (1996) 1098–1123, arXiv:hep-ph/9507336 [hep-ph].

[33] T. Sjostrand et al., *High-energy physics event generation with PYTHIA 6.1*, Comput. Phys. Commun. **135** (2001) 238–259, arXiv:hep-ph/0010017.

[34] T. Sjostrand, S. Mrenna, and P. Z. Skands, *A Brief Introduction to PYTHIA 8.1*, Comput.Phys.Commun. **178** (2008) 852–867, arXiv:0710.3820 [hep-ph].

[35] G. Corcella, I. Knowles, G. Marchesini, S. Moretti, K. Odagiri, et al., *HERWIG 6.5: An Event generator for hadron emission reactions with interfering gluons (including supersymmetric processes)*, JHEP **0101** (2001) 010, arXiv:hep-ph/0011363v3 [hep-ph].

[36] M. Bahr, S. Gieseke, M. Gigg, D. Grellscheid, K. Hamilton, et al., *Herwig++ Physics and Manual*, Eur.Phys.J. **C58** (2008) 639–707, arXiv:0803.0883 [hep-ph].

[37] J. Butterworth, J. R. Forshaw, and M. Seymour, *Multiparton interactions in photoproduction at HERA*, Z.Phys. **C72** (1996) 637–646, arXiv:hep-ph/9601371 [hep-ph].

[38] ATLAS Collaboration,, *Further ATLAS tunes of PYTHIA6 and Pythia 8*,.

[39] ATLAS Collaboration,, *Summary of ATLAS Pythia 8 tunes*,.

[40] P. Golonka and Z. Was, *PHOTOS Monte Carlo: A Precision tool for QED corrections in Z and W decays*, Eur.Phys.J. **C45** (2006) 97–107, arXiv:hep-ph/0506026 [hep-ph].

[41] N. Davidson, G. Nanava, T. Przedzinski, E. Richter-Was, and Z. Was, *Universal Interface of TAUOLA Technical and Physics Documentation*, Comput.Phys.Commun. **183** (2012) 821–843, arXiv:1002.0543 [hep-ph].

[42] GEANT4 Collaboration, S. Agostinelli et al., *GEANT4: A Simulation toolkit*, Nucl.Instrum.Meth. **A506** (2003) 250–303.

[43] J. Allison, K. Amako, J. Apostolakis, H. Araujo, P. Dubois, et al., *Geant4 developments and applications*, IEEE Trans.Nucl.Sci. **53** (2006) 270.

[44] ATLAS Collaboration, *Performance of the ATLAS inner detector track and vertex reconstruction in the high pile-up LHC environment*, ATLAS Note (2012).

[45] T. Cornelissen, M. Elsing, S. Fleischmann, W. Liebig, E. Moyse, and A. Salzburger, *Concepts, Design and Implementation of the ATLAS New Tracking (NEWT)*, Tech. Rep. ATL-SOFT-PUB-2007-007. ATL-COM-SOFT-2007-002, CERN, Geneva, Mar, 2007. https://cds.cern.ch/record/1020106.

[46] ATLAS Collaboration, *Performance of primary vertex reconstruction in proton-proton collisions at $\sqrt{s} = 7$ TeV in the ATLAS experiment*, Tech. Rep. ATLAS-CONF-2010-069, CERN, Geneva, Jul, 2010. https://cds.cern.ch/record/1281344.

[47] ATLAS Collaboration, *Electron efficiency measurements with the ATLAS detector using the 2012 LHC proton-proton collision data*, ATLAS-CONF-2014-032. 2014.

[48] W. Lampl, S. Laplace, D. Lelas, P. Loch, H. Ma, S. Menke, S. Rajagopalan, D. Rousseau, S. Snyder, and G. Unal, *Calorimeter Clustering Algorithms: Description and Performance*, Tech. Rep. ATL-LARG-PUB-2008-002. ATL-COM-LARG-2008-003, CERN, Geneva, Apr, 2008. https://cds.cern.ch/record/1099735.

[49] R. Frühwirth, *Application of Kalman filtering to track and vertex fitting*, Nuclear Instruments and Methods in Physics Research Section A: Accelerators, Spectrometers, Detectors and Associated Equipment **262** no. 2, (1987) 444–450.

[50] T. Cornelissen, M. Elsing, I. Gavrilenko, J. Laporte, W. Liebig, M. Limper, K. Nikolopoulos, A. Poppleton, and A. Salzburger, *The global $\chi^2$ track fitter in ATLAS*,.

[51] ATLAS Collaboration Collaboration, ATLAS Collaboration, *Improved electron reconstruction in ATLAS using the Gaussian Sum Filter-based model for bremsstrahlung*, Tech. Rep. ATLAS-CONF-2012-047, CERN, Geneva, May, 2012. https://cds.cern.ch/record/1449796.

[52] J. Alison, K. Brendlinger, S. Heim, J. Kroll, and C. M. Lester, *Description and Performance of the Electron Likelihood Tool at ATLAS using 2012 LHC Data*, Tech. Rep. ATL-COM-PHYS-2013-378, CERN, Geneva, Apr, 2013. https://cds.cern.ch/record/1537410.

[53] D. Boline, K. Chen, J. Ebke, H. Feng, J. Gao, D. Hall, S. Hassani, C. Hays, J. Hejbal, J. Hobbs, O. Kepka, Y. Liu, E. Monnier, J.-F. Laporte, K. Lohwasser, M.-A. Pleier, F. Rättich, P. Sommer, D. Tsionou, Y. Wu, M. Xiao, L. Xu, M. Zeman, Z. Zhao, and B. Zhou, *Measurement of the WW Production Cross Section in Proton-Proton Collisions at $\sqrt{s} = 8$ TeV with the ATLAS Detector*, Tech. Rep. ATL-COM-PHYS-2013-1450, CERN, Geneva, Oct, 2013. https://cds.cern.ch/record/1612388. Supporting document for Run 1 8TeV WW Paper.

[54] G. Aad, B. Abbott, J. Abdallah, S. A. Khalek, O. Abdinov, R. Aben, B. Abi, M. Abolins, O. AbouZeid, H. Abramowicz, et al., *Electron and photon energy calibration with the ATLAS detector using LHC Run 1 data*, The European Physical Journal C **74** no. 10, (2014) 1–48.

[55] G. Aad, B. Abbott, J. Abdallah, S. A. Khalek, O. Abdinov, R. Aben, B. Abi, M. Abolins, O. AbouZeid, H. Abramowicz, et al., *Measurement of the muon reconstruction performance of the ATLAS detector using 2011 and 2012 LHC proton–proton collision data*, The European Physical Journal C **74** no. 11, (2014) 1–34.

[56] S. Hassani, L. Chevalier, E. Lancon, J. Laporte, R. Nicolaidou, et al., *A muon identification and combined reconstruction procedure for the ATLAS detector at the LHC using the (MUONBOY, STACO, MuTag) reconstruction packages*, Nucl.Instrum.Meth. **A572** (2007) 77–79.

[57] T. Lagouri, D. Adams, K. Assamagan, M. Biglietti, G. Carlino, et al., *A Muon Identification and Combined Reconstruction Procedure for the ATLAS Detector at the LHC at CERN*, IEEE Trans.Nucl.Sci. **51** (2004) 3030–3033.

[58] R. Nicolaidou, L. Chevalier, S. Hassani, J. Laporte, E. Le Menedeu, et al., *Muon identification procedure for the ATLAS detector at the LHC using Muonboy reconstruction package and tests of its performance using cosmic rays and single beam data*, J.Phys.Conf.Ser. **219** (2010) 032052.

[59] ATLAS Collaboration, K. Assamagan et al., *Muons in the calorimeters: Energy loss corrections and muon tagging*,.

[60] D. Adams, K. A. Assamagan, M. Biglietti, G. Carlino, G. Cataldi, et al., *Track reconstruction in the ATLAS Muon Spectrometer with MOORE 007*,.

[61] ATLAS Collaboration Collaboration, G. Aad et al., *Expected performance of the ATLAS experiment: detector, trigger and physics*. CERN, Geneva, 2009. https://cds.cern.ch/record/1125884.

[62] S. Tarem, Z. Tarem, N. Panikashvili, and O. Belkind, *MuGirl–Muon identification in the ATLAS detector from the inside out*, Nuclear Science Symposium Conference Record, 2006. IEEE **1** (2006) 617–621.

[63] G. Aad, T. Abajyan, B. Abbott, J. Abdallah, S. A. Khalek, A. Abdelalim, O. Abdinov, R. Aben, B. Abi, M. Abolins, et al., *Muon reconstruction efficiency and momentum resolution of the ATLAS experiment in proton–proton collisions at $\sqrt{s}$ = 7 TeV in 2010*, The European Physical Journal C **74** no. 9, (2014) 1–32.

[64] HSG3, HWW, *Object Selections in the $H \rightarrow WW(*)$ analysis with 20.3 $fb^{-1}$ of data collected with the ATLAS detector at $\sqrt{s} = 8\ TeV$*, Tech. Rep. ATL-COM-PHYS-2013-1504, CERN, Geneva, Nov, 2013. https://cds.cern.ch/record/1624408.

[65] ATLAS Collaboration, G. Aad et al., *Jet energy measurement and its systematic uncertainty in proton-proton collisions at $\sqrt{s}$ = 7 TeV with the ATLAS detector*, Eur.Phys.J. **C75** no. 1, (2015) 17, arXiv:1406.0076 [hep-ex].

[66] M. Cacciari, G. P. Salam, and G. Soyez, *The anti-$k_T$ jet clustering algorithm*, Journal of High Energy Physics **2008** no. 04, (2008) 063.

[67] M. Cacciari and G. P. Salam, *Dispelling the $N^3$ myth for the jet-finder*, Physics Letters B **641** no. 1, (2006) 57 – 61, http://www.sciencedirect.com/science/article/pii/S0370269306010094.

[68] ATLAS Collaboration, *Characterisation and mitigation of beam-induced backgrounds observed in the ATLAS detector during the 2011 proton-proton run*, Journal of Instrumentation **8** no. 07, (2013) P07004, http://stacks.iop.org/1748-0221/8/i=07/a=P07004.

[69] G. Aad, B. Abbott, J. Abdallah, A. Abdelalim, A. Abdesselam, O. Abdinov, B. Abi, M. Abolins, H. Abramowicz, H. Abreu, et al., *Jet energy measurement with the ATLAS detector in proton-proton collisions at $\sqrt{s} = 7\ TeV$*, The European Physical Journal C **73** no. 3, (2013) 1–118.

[70] G. Aad, T. Abajyan, B. Abbott, J. Abdallah, S. A. Khalek, A. Abdelalim, O. Abdinov, R. Aben, B. Abi, M. Abolins, et al., *Jet energy resolution in proton-proton collisions at* $\sqrt{s} = 7$ *recorded in 2010 with the ATLAS detector*, The European Physical Journal C **73** no. 3, (2013) 1–27.

[71] D. W. Miller, A. Schwartzman, and D. Su, *Pile-up jet energy scale corrections using the jet-vertex fraction method*, Tech. Rep. ATL-COM-PHYS-2009-180, CERN, Geneva, Apr, 2009. https://cds.cern.ch/record/1172636.

[72] A. collaboration et al., *Performance of missing transverse momentum reconstruction in ATLAS studied in proton-proton collisions recorded in 2012 at 8 TeV*, ATLAS-CONF-2013-082. 2013.

[73] T. Gehrmann, M. Grazzini, S. Kallweit, P. Maierhöfer, A. von Manteuffel, S. Pozzorini, D. Rathlev, and L. Tancredi, $W^+W^-$ *Production at Hadron Colliders in Next to Next to Leading Order QCD*, Phys. Rev. Lett. **113** (2014) 212001, http://link.aps.org/doi/10.1103/PhysRevLett.113.212001.

[74] LHC Higgs Cross Section Working Group Collaboration, S. Heinemeyer et al., *Handbook of LHC Higgs Cross Sections: 3. Higgs Properties*, arXiv:1307.1347 [hep-ph].

[75] M. Bonvini, F. Caola, S. Forte, K. Melnikov, and G. Ridolfi, *Signal-background interference effects for* $gg \to H \to W^+W^-$ *beyond leading order*, Phys.Rev. **D88** no. 3, (2013) 034032, arXiv:1304.3053 [hep-ph].

[76] A. Bierweiler, T. Kasprzik, J. H. Khn, and S. Uccirati, *Electroweak corrections to W-boson pair production at the LHC*, JHEP **1211** (2012) 093, arXiv:1208.3147 [hep-ph].

[77] M. Billoni, S. Dittmaier, B. Jager, and C. Speckner, *Next-to-leading-order electroweak corrections to* $pp \to WW \to 4$ *leptons in double-pole approximation at the LHC*, PoS **RADCOR2013** (2014) 018, arXiv:1311.5491 [hep-ph].

[78] B. Jager, C. Oleari, and D. Zeppenfeld, *Next-to-leading order QCD corrections to* $W^+W^-$ *production via vector-boson fusion*, JHEP **0607** (2006) 015, arXiv:hep-ph/0603177 [hep-ph].

[79] J. R. Gaunt et al., *Same-sign W pair production as a probe of double parton scattering at the LHC*, Eur.Phys.J. **C69** (2010) 53–65, arXiv:1003.3953 [hep-ph].

[80] B. Blok, Y. Dokshitzer, L. Frankfurt, and M. Strikman, *Perturbative QCD correlations in multi-parton collisions*, The European Physical Journal C **74** no. 6, (2014) 1–15.

[81] S. Dittmaier, S. Dittmaier, C. Mariotti, G. Passarino, R. Tanaka, et al., *Handbook of LHC Higgs Cross Sections: 2. Differential Distributions*, arXiv:1201.3084 [hep-ph].

[82] *Backgrounds To Higgs Boson Searches from Asymmetric- Internal Conversion*, arXiv:1110.1368 [hep-ph].

[83] https://twiki.cern.ch/twiki/pub/AtlasProtected/HSG3MC12Samples/8TeVCrossSections.pdf.

[84] J. Barreiro Guimaraes da Costa, A. Belloni, G. Conti, T. Dai, J. Ebke, J. Elmsheuser, J. Gao, D. Hall, C. Hays, J. Hejbal, R. Kehoe, O. Kepka, S. Li, J. Liu, L. Liu, Y. Liu, C. Mills, E. Monnier, A. Nagarkar, H. Peng, M.-A. Pleier, M. Schott, Y. Wu, H. Yang, M. Zeman, Z. Zhao, B. Zhou, J. Zhu, and Y. Zhu, *Measurement of the W+W- Production Cross Section in Proton-Proton Collisions at sqrt(s) = 7 TeV with the ATLAS Detector and Limits on the Anomalous Triple-Gauge-Boson Couplings*, Tech. Rep. ATL-COM-PHYS-2012-189, CERN, Geneva, Feb, 2012. https://cds.cern.ch/record/1425083. Supporting Document for the published WW Analysis at 7 TeV.

[85] M. Botje, J. Butterworth, A. Cooper-Sarkar, A. de Roeck, J. Feltesse, et al., *The PDF4LHC Working Group Interim Recommendations*, arXiv:1101.0538 [hep-ph].

[86] ATLAS Collaboration, G. Aad et al., *Observation and measurement of Higgs boson decays to $WW^*$ with the ATLAS detector*, Phys. Rev. **D92** no. 1, (2015) 012006, arXiv:1412.2641 [hep-ex].

[87] J. Baglio, L. D. Ninh, and M. M. Weber, *Massive gauge boson pair production at the LHC: A next-to-leading order story*, Phys. Rev. D **88** (2013) 113005, http://link.aps.org/doi/10.1103/PhysRevD.88.113005.

[88] A. Bierweiler, T. Kasprzik, and J. H. Khn, *Vector-boson pair production at the LHC to $O(\alpha^3)$ accuracy*, JHEP **1312** (2013) 071, arXiv:1305.5402 [hep-ph].

[89] S. Gieseke, T. Kasprzik, and J. H. Khn, *Vector-boson pair production and electroweak corrections in HERWIG++*, Eur. Phys. J. **C74** no. 8, (2014) 2988, arXiv:1401.3964 [hep-ph].

[90] C. F. Berger, C. Marcantonini, I. W. Stewart, F. J. Tackmann, and W. J. Waalewijn, *Higgs Production with a Central jet-veto at NNLL+NNLO*, JHEP **04** (2011) 092, arXiv:1012.4480 [hep-ph].

[91] F. James, *MINUIT Function Minimization and Error Analysis: Reference Manual Version 94.1*,.

[92] P. F. Monni and G. Zanderighi, *On the excess in the inclusive $W^+W^- \rightarrow l^+l^-\nu\bar{\nu}$ cross section*, JHEP **05** (2015) 013, arXiv:1410.4745 [hep-ph].

[93] P. Meade, H. Ramani, and M. Zeng, *Transverse momentum resummation effects in $W^+W^-$ measurements*, Phys. Rev. **D90** no. 11, (2014) 114006, arXiv:1407.4481 [hep-ph].

[94] D. Curtin, P. Jaiswal, and P. Meade, *Charginos Hiding In Plain Sight*, Phys.Rev. **D87** no. 3, (2013) 031701, arXiv:1206.6888 [hep-ph].

[95] B. Feigl, H. Rzehak, and D. Zeppenfeld, *New Physics Backgrounds to the $H \to WW$ Search at the LHC?*, Phys.Lett. **B717** (2012) 390–395, arXiv:1205.3468 [hep-ph].

[96] K. Rolbiecki and K. Sakurai, *Light stops emerging in WW cross section measurements?*, JHEP **1309** (2013) 004, arXiv:1303.5696 [hep-ph].

[97] H. Aihara, T. Barklow, U. Baur, J. Busenitz, S. Errede, et al., *Anomalous gauge boson interactions*, arXiv:hep-ph/9503425 [hep-ph].

[98] C. Degrande, N. Greiner, W. Kilian, O. Mattelaer, H. Mebane, T. Stelzer, S. Willenbrock, and C. Zhang, *Effective Field Theory: A Modern Approach to Anomalous Couplings*, Annals Phys. **335** (2013) 21–32, arXiv:1205.4231 [hep-ph].

[99] G. Gounaris et al., *Triple gauge boson couplings*, in *AGS / RHIC Users Annual Meeting Upton, New York, June 15-16, 1995*. 1996. arXiv:hep-ph/9601233 [hep-ph]. http://alice.cern.ch/format/showfull?sysnb=0215385.

[100] K. Hagiwara, S. Ishihara, R. Szalapski, and D. Zeppenfeld, *Low energy effects of new interactions in the electroweak boson sector*, Phys. Rev. D **48** (1993) 2182–2203, http://link.aps.org/doi/10.1103/PhysRevD.48.2182.

[101] G. Cowan, K. Cranmer, E. Gross, and O. Vitells, *Asymptotic formulae for likelihood-based tests of new physics*, Eur. Phys. J. **C71** (2011) 1554, arXiv:1007.1727 [physics.data-an], [Erratum: Eur. Phys. J.C73,2501(2013)].

[102] G. J. Feldman and R. D. Cousins, *A Unified approach to the classical statistical analysis of small signals*, Phys. Rev. **D57** (1998) 3873–3889, arXiv:physics/9711021 [physics.data-an].